

The Control of Turbulent Flows around Bluff Bodies by Means of Spanwise Sinusoidal Profiles

Andrew Alfred Antiohos

B.Eng. (Hons)

Submitted in fulfillment of the requirements for the degree of

Doctor of Philosophy



College of Engineering and Science

Victoria University

July 2014

© Copyright by Andrew Antiohos 2014

All Rights Reserved

To my dear wife Robabeh

The one who always pulls me through

ABSTRACT

Bluff bodies form ubiquitous components of many engineered structures. They are often exposed to turbulent flows, and the subsequent shedding of vortices gives rise to aerodynamic forces with large fluctuating components. As a result, significant oscillations are induced, which can lead to resonances and structural fatigue. To obviate these deleterious effects passive flow control mechanisms can be incorporated into the design of bluff bodies. However, to ensure the designs are effective and safe it is essential to understand and anticipate the behavior of the turbulent flows around bluff bodies.

The research reported in this thesis is inspired by the owl's book of aerodynamic wisdom. Owls' flight must be well controlled and silent, and this they achieve in part by the comb-like leading edges on the primary feathers of their wings. The leading edge comb is a passive flow control mechanism that exists in nature, and it is used in this research as a template for engineering designs to control the turbulent flows around bluff bodies. In this work, the comb-like features are idealised by spanwise sinusoidal profiles (SSPs) on the leading edges of bluff bodies. The research presented in this thesis is motivated by the possibility of utilising detailed numerical simulations of the flow control phenomena that occurs in nature, in an attempt to design more efficient aerodynamic structures.

To achieve this research objective, turbulent flows around square and rectangular cylinders are modelled numerically. Three-dimensional numerical predictions of the flow behaviour are obtained using the computational fluid dynamics (CFD) code – FLUENT[®], based on the mathematical approach of the large eddy simulation (LES)

turbulence model. The results have been validated against published experimental and numerical observations. Results are presented in the form of time-averaged quantitative observations of the turbulent flow fields and power spectral densities of the wakes at a Reynolds number of 2.35×10^4 . A significant practical finding of the research is that an SSP on the leading edge can reduce the mean drag force by up to 30% compared with a plain cylinder. Also, the lift force fluctuations can be reduced by up to 95%. Insights into the effectiveness of SSPs are gained by studying the topology of the flow field both within the boundary layers and wakes adjacent to the structures.

A parametric study that examines the role of the governing parameters of an SSP, namely the sinusoidal amplitude and wavelength, reveals that the flow regimes generated under turbulent flow differ from those of laminar flows. The wave steepness of the sinusoidal leading edge assumes more importance when controlling turbulent flow fields around bluff bodies, whereas the wavelength has a strong influence on laminar flow fields.

Investigations of the turbulent flow around bluff bodies with large aspect ratio, demonstrate that the proximity of the leading edge to the trailing edge does not profoundly influence the control of the flow field. In fact, the flow field and resulting wake generated by the SSP resembles that of a streamlined body. The sinusoidal perturbations are capable of largely dissipating the shear layers to form a narrow wake behind the elongated body. In addition, numerical simulations of the flow around square cylinders with partially imposed SSPs on the leading edges show that the passive flow control mechanism is able to locally control the flow field, in a similar manner to the leading edge comb on an owl's wing. In summary, an SSP is a very practical and important mechanism for reducing the aerodynamic forces on bluff bodies.

DECLARATION

“I, Andrew Antiohos, declare that the PhD thesis entitled ‘The Control of Turbulent Flow around Bluff Bodies by means of Spanwise Sinusoidal Profiles’ is no more than 100,000 words in length including quotes and exclusive of tables, figures, appendices, bibliography, references and footnotes. This thesis contains no material that has been submitted previously, in whole or in part, for the award of any other academic degree or diploma. Except where otherwise indicated, this thesis is my own work”.

Andrew Antiohos

Signed

14 / 10 / 13

Date

ACKNOWLEDGEMENTS

I would like to acknowledge the guidance, support and encouragement from my supervisor, Prof. Graham Thorpe. I am grateful for his advice and direction, which has enabled me to not only complete this dissertation but also become a better researcher. I would also like to sincerely thank Prof. Greg Baxter for his kind support during this work and the many helpful discussions.

I gratefully acknowledge the financial support provided through the Victoria University Postgraduate Research Scholarship. I thank Elizabeth Smith for her immense guidance and assistance throughout this journey. Thanks to Kylie Baggetto for always helping without hesitation to ensure that everything progressed smoothly. I would also like to thank the staff of the Graduate Research Office and the College of Engineering and Science. My gratitude also goes to Prof. Chris Perera for his kind support and understanding.

Special thanks to my colleagues who have shared this journey with me through its highs and lows. The encouragements, memories and friendships of Farial Jafar and Marija Gradinscak will always be remembered. To my family, thank you for the support during these years, I would not have the opportunities in life without the endless support and encouragements from my parents.

Finally, my deepest thanks and gratitude go to my grandfather, Dr. Alfred Grech, for whom I owe all my inspiration in life to pursue my education and follow my dreams.

TABLE OF CONTENTS

Abstract	iv
Declaration	vi
Acknowledgements	vii
Table of Contents	viii
List of Figures	xi
List of Tables	xxiii
Nomenclature	xxiv
1 Introduction	1
1.1 Passive Flow Control Mechanism	3
1.2 Objectives and Contributions of the Thesis	6
1.3 Thesis Outline	8
2 Technology of Owls' Silent Flight: A Bio-Inspired Spanwise Sinusoidal Profile	12
2.1 The Phenomena of Silent Flight	15
2.1.1 Leading Edge Comb.....	16
2.1.2 Trailing Edge Fringe	21
2.2 Scaling for Biomimicry.....	23
2.3 Practical Adaptations of Silent Flight Technology	26
2.4 The Spanwise Sinusoidal Profile (SSP).....	29
2.5 Summary	32
3 The Computational and Mathematical Models	34
3.1 Numerical Description	40
3.1.1 Mathematical Model	40
3.1.2 LES Boundary Conditions	48
3.2 Computational Domain	50
3.2.1 Boundary Conditions	54
3.3 Model Verification and Mesh Generation	57
3.3.1 Sizing Function and Near Wall Region	57

3.3.2	Grid and Time Step Independence	63
3.3.3	Solution Convergence	66
3.4	Comparisons in the Wake of Square SSP Cylinders	71
3.4.1	Model Comparisons in the Near Wake	71
3.4.2	Model Comparisons in the Intermediate Wake.....	76
3.4.3	Characteristic Comparisons of Aerodynamic Forces.....	79
3.5	Summary	81
4	Controlling Flow by Means of Spanwise Sinusoidal Profiles on the Leading Edge of Bluff Bodies	83
4.1	Effects of Spanwise Sinusoidal Profiles on Flow Fields	86
4.2	Turbulent Flow Field around a Square Cylinder SSP.....	90
4.3	A Parametric Study of Turbulent Flow Regimes.....	111
4.3.1	Performance of Aerodynamic Forces.....	111
4.3.2	Topologies of Wakes of Spanwise Sinusoidal Profiles.....	113
4.4	Summary	123
5	The Effect of Aspect Ratio on a Spanwise Sinusoidal Profile	125
5.1	Flow Field around an Elongated SSP Cylinder	126
5.1.1	Performance of Aerodynamic Forces of an Elongated SSP.....	129
5.1.2	Topology of the Flow Field around an Elongated SSP.....	134
5.2	Summary	144
6	Topology of the Flow Field around a Partial Spanwise Sinusoidal Profile	146
6.1	Effectiveness of a Partial Spanwise Sinusoidal Profile	147
6.1.1	Performance of Aerodynamic Forces of a Partial SSP	148
6.1.2	Topological Study by Means of Flow Visualisations	152
6.2	Summary	164
7	Conclusions and Future Work	165
7.1	Contributions of the Thesis	165
7.2	Suggestions for Future Work	167
	References	170

A	Correlation Analysis of the Boundary Layers around SSP Bluff Bodies	180
A.1	Boundary Layer Topology Analysis of a Square SSP	180
A.1.1	Correlations at the Leading Edge of the Square Cylinder.....	182
A.1.2	Correlations at the Trailing Edge of the Square Cylinder.....	191
B	Correlation Analysis of the Boundary Layer around an Elongated SSP	199
B.1	Boundary Layer Topology Analysis of an Elongated SSP	199
B.1.1	Correlations at the Leading Edge of the Elongated Cylinder.....	200
B.1.2	Correlations at the Trailing Edge of the Elongated Cylinder.....	208
C	Correlation Analysis of the Boundary Layer around a Partial SSP	217
C.1	Boundary Layer Topology Analysis of a Partial SSP.....	217
C.1.1	Correlations at the Leading Edge of the Partial SSP Cylinder.....	218
C.1.2	Correlations at the Trailing Edge of the Partial SSP Cylinder.....	233
D	Exploration of a Semi-Active Control Method for Vortex-Induced Resonance	248
D.1	Model Description	249
D.2	Numerical Observations.....	253
D.2.1	Uncontrolled Vortex Induced Resonance	253
D.2.2	Proposed Semi-Active Control	256
D.3	Practical Implementation	261
D.4	Summary	262

LIST OF FIGURES

2.1	Leading edge comb of a Barn Owl (<i>Tyto alba</i>) feather (Sieradzki 2008).....	18
2.2	Diagram of a Barn Owl's wing showing the primary and secondary feathers (Bachmann et al. 2007)	18
2.3	Leading edge comb shown on a Barred Owl (<i>Strix varia</i>) in flight (Kohut 2009)	19
2.4	Flight path of a Barn Owl during the day (top) and night (bottom) (Lilley 2009)	20
2.5	Trailing edge fringe of a Barn Owl (<i>Tyto alba</i>) showing detail of fibre extensions of the barbs of the feather (Bachmann et al. 2007)	22
2.6	Serrated fan blades of Liang et al. (2010), showing their four leading edge configurations.....	27
2.7	Serrated trailing edges showing (a) Saw-tooth schematic and (b) diagram of different saw-tooth configurations (Dassen et al. 1996)	29
2.8	Model of (a) a plain square cylinder (slender bluff body) and (b) a square cylinder with an SSP applied to the leading edge	31
3.1	Computational domain showing (a) domain schematic (left) and boundary conditions with computational mesh (right) and (b) Enlarged view illustrating the fine mesh adjacent to the cylinder	52
3.2	Computational model of (a) reference square cylinder ($W0$) and (b) square cylinder with an SSP applied ($W3$)	53
3.3	Experimental setup of Dobre <i>et al.</i> (2006) showing (a) top view of the wind tunnel section and (b) square cylinder model showing near and intermediate wake measurement points	54
3.4	Computational domain indicating the boundary conditions	55
3.5	Computational model of the square cylinder, $W3$, indicating the hollow cross-section to minimise grid elements	57
3.6	Symmetry boundary grid showing the uniform mesh expansion away from the geometry surface as a result of the sizing function	59

3.7	Enlarged view of the symmetry boundary plane showing the boundary layer mesh surrounding the square cylinder, $W3$	60
3.8	Semi-log representation of the near wall region showing y^+ within the buffer layer, between the law-of-the-wall and log-law regions (ANSYS 2009)	62
3.9	Schematic of the iterative time advancement solution method in FLUENT®	69
3.10	Square cylinder model showing the measurement points in the near wake; (a) $W0$; (b) $W3$	74
3.11	Comparisons of numerical and experimental (top, —, Dobre <i>et al.</i> (2006)) PSD of the v -component velocity spectra at peak (—) and valley (—) locations measured at $(x/D, y/D) = (2, 2)$ for (a) $W0$, (b) $W1$, (c) $W2$ and (d) $W3$	75
3.12	Comparisons of numerical and experimental (top, —, Dobre <i>et al.</i> (2006)) PSD of the u -component (—) and v -component (—) velocity spectra at the mid-peak location measured at $(x/D, y/D) = (9, 0)$ for (a) $W0$ and (b) $W3$	78
4.1	An adaptation of Darekar and Sherwin (2001b), of the three flow regimes produced in the wakes of wavy square cylinders at a Re of 100. The hatched upper-right area represents a physically invalid region for an SSP with a plain trailing edge. $W1$, $W2$ and $W3$ are SSP geometries associated with the three laminar regimes. The nine SSP geometries in this study are depicted in relation to the regimes. Geometries coincide with λ/D of 2.4, 3.2 and 5.2, and ω/λ of around 0.026, 0.105 and 0.195	88
4.2	A schematic representation of SSP bodies with a constant wavelength, λ/D , of 1 and wave steepnesses, ω/λ , of 0 (ω_0), 0.1 (ω_1), 0.2 (ω_2) and 0.3 (ω_3). All of these geometries give rise to Regime I when the flow is laminar at a Reynolds number of 100	89
4.3	A schematic representation of SSP geometries at a constant wavelength, λ/D , of 3, and wave steepnesses, ω/λ , of 0 (ω_0), 0.01 (ω_1), 0.1 (ω_2), 0.2 (ω_3), and 0.3 (ω_4). When the Reynolds number is 100, ω_0 and ω_1 result in Regime I, and ω_2 , ω_3 and ω_4 give rise to Regime III	89
4.4	Computational models of the plain and SSP square cylinders; (a) $W0$, (b) $W1$, (c) $W2$ and (d) $W3$. The wave height (peak-to-peak), ω , and wavelength, λ , of the sinusoidal leading can be depicted	91

4.5	Contours of the vorticity fields around (a) $W0$, (b) $W1$, (c) $W2$ and (d) $W3$; (left) vertical x - y planes coincident with peaks and valleys of the SSP, and (right) isometric views of the resulting flow field	93
4.6	Coefficient of drag, C_d , for the plain square cylinder, $W0$ (—), and the three SSP geometries, $W1$ (—), $W2$ (—) and $W3$ (—); highlighting a significant reduction of up to 32% in the mean drag and corresponding reduction of the fluctuations as a result of the SSP with wave steepness, ω/λ , of 0.195 associated with $W3$	95
4.7	Coefficient of lift, C_l , for the plain square cylinder, $W0$ (a, —), and the three SSP geometries, $W1$ (b, —), $W2$ (c, —) and $W3$ (d, —); highlighting the significant reduction in the fluctuations of lift as a result of the SSP with wave steepness, ω/λ , of 0.195 associated with $W3$	96
4.8	Distribution of the time-averaged pressure coefficient, C_p , on the upper and lower surfaces of the plain square cylinder, $W0$, and SSP cylinder, $W3$. Comparison is shown for a plain square cylinder between the current results and the numerical distribution of Yu and Kareem (1998), at $Re = 1 \times 10^5$	98
4.9	Distribution of the time-averaged pressure coefficient, C_p , in the wake of the plain square cylinder, $W0$, and the SSP cylinder, $W3$. Comparison is shown between the current results and the mean pressure distribution of Sohankar (2006), at $Re = 2.2 \times 10^4$	99
4.10	Contours of instantaneous vorticity magnitude in the wake of the SSP square cylinders. The flow field is shown in the mid-span vertical x - y plane coincident with a peak (left), and the mid-span vertical x - y plane coincident with a valley (right); (a) $W0$, (b) $W1$, (c) $W2$ and (d) $W3$	101
4.11	Velocity vectors demonstrating the channelling of flow at peaks of the SSP geometry as the wave steepness, ω/λ , increases from (a) ω/λ of 0, $W0$; (b) ω/λ of 0.026, $W1$; (c) ω/λ of 0.105, $W2$ and (d) ω/λ of 0.195, $W3$. The velocity is shown in a horizontal x - z plane that approaches the leading edge at $0.25D$ below the upper surface.....	103
4.12	Time-averaged streamwise velocity, \bar{u} , profile measured mid-span along the line $x/D = 0.5$, on the upper side of the plain and SSP cylinders, at $Re = 2.35 \times 10^4$, (a) $W1$, (b) $W2$ and (c) $W3$. Comparison is made between the averaged numerical velocity profile of Sohankar (2006), at $Re = 2.2 \times 10^4$	104

4.13	Time-averaged streamwise velocity, \bar{u} , profiles measured downstream from the trailing edge along the centerline of the wake of the plain, $W0$, and SSP, $W3$, cylinders, at $Re = 2.35 \times 10^4$; (a) $x/D = 0$, (b) $x/D = 0.5$, (c) $x/D = 1.5$, (d) $x/D = 3$, (e) $x/D = 4.5$, (f) $x/D = 6$, (g) $x/D = 7.5$, (h) $x/D = 9$, (i) $x/D = 10.5$, (j) $x/D = 12$	108
4.14	A schematic representation of SSP bodies demonstrating similarities in wave steepness (gradient), as indicated by the dashed lines; (a) SSP geometries with identical ω/λ of 0.1, and λ/D of 2.4 (—) and 5.2 (—); (b) SSP geometries with identical ω/λ of 0.2, and λ/D of 2.4 (—) and 5.2 (—).....	110
4.15	Contours of vorticity magnitude for the SSP geometries, (above) $W2$ ($\omega/\lambda = 0.105$ and $\lambda/D = 2.4$) and (below) $W2_A$ ($\omega/\lambda = 0.09$ and $\lambda/D = 5.2$); (a) vertical y - z plane coincident to the trailing edge and (b) spanwise vertical x - z planes coincident to peaks and valleys	114
4.16	Contours of vorticity magnitude for $W2$ (left) and $W2_A$ (right); (a) vertical x - y planes at peaks and (b) vertical x - y planes at valleys.....	115
4.17	PSD of the v -component velocity spectra at peak (—) and valley (—) locations measured at $(x/D, y/D) = (2, 2)$; (a) $W2$ ($\omega/\lambda = 0.105$ and $\lambda/D = 2.4$); (b) $W2_A$ ($\omega/\lambda = 0.09$ and $\lambda/D = 5.2$).....	117
4.18	Contours of vorticity magnitude for the SSP geometries, (above) $W3$ ($\omega/\lambda = 0.195$ and $\lambda/D = 2.4$) and (below) $W3_A$ ($\omega/\lambda = 0.18$ and $\lambda/D = 5.2$); (a) vertical y - z plane coincident to the trailing edge and (b) spanwise vertical x - z planes coincident to peaks and valleys	119
4.19	Contours of vorticity magnitude for $W3$ and $W3_A$; (a) vertical x - y plane coincident with a peak and (b) vertical x - y plane coincident with a valley	120
4.20	Contours of the vorticity fields around SSP square cylinders; (left) vertical x - y planes coincident with peaks and valleys of the SSP, and (right) isometric views of the resulting flow field. (a) SSP with $\omega/\lambda = 0.105$ and $\lambda/D = 3.2$ ($W2_B$), (b) SSP with $\omega/\lambda = 0.09$ and $\lambda/D = 5.2$ ($W2_A$).....	121
4.21	Contours of the vorticity fields around SSP square cylinders; (left) vertical x - y planes coincident with peaks and valleys of the SSP, and (right) isometric views of the resulting flow field. (a) SSP with $\omega/\lambda = 0.195$ and $\lambda/D = 3.2$ ($W2_B$), (b) SSP with $\omega/\lambda = 0.18$ and $\lambda/D = 5.2$ ($W2_A$).....	122

5.1	Computational models of the plain and SSP elongated cylinders; (a) $W0_E$ and (b) $W3_E$. The wave height (peak-to-peak), ω , and wavelength, λ , of the sinusoidal leading can be depicted.....	128
5.2	(a) Coefficient of drag, C_d , for the plain elongated cylinder, $W0_E$ (blue), and the elongated SSP geometry, $W3_E$ (red), which highlights the reduction of up to 10% in the mean drag and related reduction of the fluctuations as a result of the SSP. This is corroborated by the time-averaged contours of the pressure coefficient, C_p , for (b) $W0_E$ and (c) $W3_E$, taken on the upper horizontal surface of the geometries. $W3_E$ has greater percentage of high pressure across the surface, particularly the highly discernable larger base pressure that is associated with the decrease in mean drag.....	129
5.3	Coefficient of lift, C_l , for (a) the plain elongated geometry, $W0_E$, and (b) the elongated SSP geometry, $W3_E$; highlighting the significant reduction in the fluctuations of lift as a result of the SSP.....	130
5.4	Distribution of the time-averaged pressure coefficient, C_p , on the upper and lower surfaces of the plain and SSP elongated cylinders with aspect ratio, D_1/D , of 5. (a) Comparison for a plain elongated cylinder between the current numerical model at $Re = 2.35 \times 10^4$ and that of Yu <i>et al.</i> (2013) at $Re = 1 \times 10^5$, and (b) distributions measured at mid-span for the plain elongated cylinder, $W0_E$, and coincident to a peak and valley at the mid-span region for the SSP elongated cylinder, $W3_E$	132
5.5	Distribution of the time-averaged pressure coefficient, C_p , in the wake of plain elongated cylinder, $W0_E$, and the elongated SSP cylinder, $W3_E$	134
5.6	Contours of the vorticity fields around (a) $W0_E$ and (b) $W3_E$; (left) vertical x - y planes coincident with peaks and valleys of the SSP, and (right) isometric views of the resulting flow field.....	136
5.7	Pathlines highlighting the magnitude of vorticity for (a) $W0_E$ and (b) $W3_E$, observed from the top of the horizontal x - z plane coincident with the upper surface of the elongated cylinders.....	137
5.8	Perspective views of the vorticity field around $W0_E$ (left) and $W3_E$ (right); (a) mid-span vertical x - y plane coincident to a peak, and (b) mid-span vertical x - y plane coincident to a valley.....	139

5.9	Time-averaged streamwise velocity, \bar{u} , profiles measured at along the center of the span on the upper surface of the plain, $W0_E$, and SSP, $W3_E$, elongated cylinders, at $Re = 2.35 \times 10^4$; (a) $x/D = 0$, (b) $x/D = 1.25$, (c) $x/D = 2.5$, (d) $x/D = 3.75$ and (e) $x/D = 5$	141
5.10	Pathlines illustrating the time-averaged velocity field around (a) $W0_E$ and (b) $W3_E$. It can be depicted that an SSP causes the flow field to resemble that of a streamlined geometry	143
6.1	Schematic of the partial SSP geometries; (a) plain geometry, (b) $PSSP_1$, (c) $PSSP_2$ and (d) $PSSP_3$	148
6.2	Coefficient of drag, C_d , for the plain square cylinder, $W0$ (—), and the three partial SSP geometries, $PSSP_1$ (—), $PSSP_2$ (—) and $PSSP_3$ (—); highlighting the significant reduction in the mean drag and related reduction of the fluctuations as a result of the partial SSP with wave steepness, ω/λ , of 0.195 associated with $W3$	150
6.3	Coefficient of lift, C_l , for the plain square cylinder, $W0$ (a, —), and the three partial SSP geometries, $PSSP_1$ (b, —), $PSSP_2$ (c, —) and $PSSP_3$ (d, —); highlighting the significant reduction in the fluctuations of lift as a result of the partial SSP with wave steepness, ω/λ , of 0.195 associated with $W3$	151
6.4	Contours of vorticity magnitude for the TE plane (left) and spanwise peak and valley planes (right); (a) $PSSP_1$, (b) $PSSP_2$ and (c) $PSSP_3$	153
6.5	Vectors of the magnitude of velocity for the three partial SSP geometries; (a) $PSSP_1$, (b) $PSSP_2$ and (c) $PSSP_3$. The velocity is shown across a horizontal x - z plane coincident with the upper surface. At peaks along the span of the partial SSPs, it can be seen that the flow is channelled towards the center of the peaks. Adjacent to the intersecting plane, the flow coincident with the plain leading edge is channelled only slightly in the direction of the SSP	156
6.6	Pathlines highlighting the vorticity field approaching the leading edge of the three partial SSP geometries in a horizontal x - z plane coincident with the upper surface; (a) $PSSP_1$, (b) $PSSP_2$ and (c) $PSSP_3$	159

6.7	Above view of the three partial SSP geometries showing the pathlines of the vorticity field approaching the leading edge in a horizontal x - z plane coincident with the upper surface; (a) $PSSP_1$, (b) $PSSP_2$ and (c) $PSSP_3$	161
6.8	Contours of vorticity magnitude for $PSSP_1$ showing the spanwise flow transition in vertical x - y planes coincident to (a) the plain leading edge, (b) the intersecting plane, (c) a peak of the partial SSP, and (d) a valley of the partial SSP	163
A.1	Data points for the boundary layer topology analysis; (a) $W0$; (b) $W3$	181
A.2	Cross-correlation between u -velocity (—) and pressure (—) at the leading edge of point 1 for $W0$ (left) and $W3$ (right); (a) data history and (b) unbiased cross-correlation sequence	183
A.3	PSD of u -velocity (—), pressure (—) and unbiased cross-correlation function (—) at the leading edge of point 1 for (a, b, c) $W0$ and (d, e, f) $W3$	184
A.4	Cross-correlation between u -velocity (—) and pressure (—) at the leading edge of point 2 for $W0$ (left) and $W3$ (right); (a) data history and (b) unbiased cross-correlation sequence	185
A.5	PSD of u -velocity (—), pressure (—) and unbiased cross-correlation function (—) at the leading edge of point 2 for (a, b, c) $W0$ and (d, e, f) $W3$	186
A.6	Cross-correlation between u -velocity (—) and pressure (—) at the leading edge of point 3 for $W0$ (left) and $W3$ (right); (a) data history and (b) unbiased cross-correlation sequence	187
A.7	PSD of u -velocity (—), pressure (—) and unbiased cross-correlation function (—) at the leading edge of point 3 for (a, b, c) $W0$ and (d, e, f) $W3$	188
A.8	Cross-correlation between u -velocity (—) and pressure (—) at the leading edge of point 4 for $W0$ (left) and $W3$ (right); (a) data history and (b) unbiased cross-correlation sequence	189
A.9	PSD of u -velocity (—), pressure (—) and unbiased cross-correlation function (—) at the leading edge of point 4 for (a, b, c) $W0$ and (d, e, f) $W3$	190

A.10	Cross-correlation between u -velocity (—) and pressure (—) at the trailing edge of point 1 for $W0$ (left) and $W3$ (right); (a) data history and (b) unbiased cross-correlation sequence	192
A.11	PSD of u -velocity (—), pressure (—) and unbiased cross-correlation function (—) at the trailing edge of point 1 for (a, b, c) $W0$ and (d, e, f) $W3$	193
A.12	Cross-correlation between u -velocity (—) and pressure (—) at the trailing edge of point 2 for $W0$ (left) and $W3$ (right); (a) data history and (b) unbiased cross-correlation sequence	193
A.13	PSD of u -velocity (—), pressure (—) and unbiased cross-correlation function (—) at the trailing edge of point 2 for (a, b, c) $W0$ and (d, e, f) $W3$	194
A.14	Cross-correlation between u -velocity (—) and pressure (—) at the trailing edge of point 3 for $W0$ (left) and $W3$ (right); (a) data history and (b) unbiased cross-correlation sequence	195
A.15	PSD of u -velocity (—), pressure (—) and unbiased cross-correlation function (—) at the trailing edge of point 3 for (a, b, c) $W0$ and (d, e, f) $W3$	196
A.16	Cross-correlation between u -velocity (—) and pressure (—) at the trailing edge of point 4 for $W0$ (left) and $W3$ (right); (a) data history and (b) unbiased cross-correlation sequence	197
A.17	PSD of u -velocity (—), pressure (—) and unbiased cross-correlation function (—) at the trailing edge of point 4 for (a, b, c) $W0$ and (d, e, f) $W3$	198
B.1	Data points for the boundary layer and wake topology analysis; (a) $W0_E$; (b) $W3_E$	200
B.2	Histories of u -velocity (—) and pressure (—) at the leading edge locations of $W0_E$; (a) point 1; (b) point 2; (c) point 3; (d) point 4; (e) point 5	201
B.3	Unbiased cross-correlation between u -velocity and pressure at the leading edge locations of $W0_E$; (a) point 1; (b) point 2; (c) point 3; (d) point 4; (e) point 5	202

B.4	PSD of u -velocity (—), pressure (—) and unbiased cross-correlation function (—) at the leading edge of $W0_E$; (a) point 1; (b) point 2; (c) point 3; (d) point 4; (e) point 5.....	203
B.5	Histories of u -velocity (—) and pressure (—) at the leading edge locations of $W3_E$; (a) point 1; (b) point 2; (c) point 3; (d) point 4; (e) point 5	204
B.6	Unbiased cross-correlation between u -velocity and pressure at the leading edge of $W3_E$; (a) point 1; (b) point 2; (c) point 3; (d) point 4; (e) point 5.....	206
B.7	PSD of u -velocity (—), pressure (—) and unbiased cross-correlation function (—) at the leading edge of $W3_E$; (a) point 1; (b) point 2; (c) point 3; (d) point 4; (e) point 5.....	207
B.8	Histories of u -velocity (—) and pressure (—) at the trailing edge locations of $W0_E$; (a) point 1; (b) point 2; (c) point 3; (d) point 4; (e) point 5.....	209
B.9	Histories of u -velocity (—) and pressure (—) at the trailing edge locations of $W0_E$; (a) point 1; (b) point 2; (c) point 3; (d) point 4; (e) point 5.....	210
B.10	PSD of u -velocity (—), pressure (—) and unbiased cross-correlation function (—) at the trailing edge of $W0_E$; (a) point 1; (b) point 2; (c) point 3; (d) point 4; (e) point 5	211
B.11	Histories of u -velocity (—) and pressure (—) at the trailing edge locations of $W3_E$; (a) point 1; (b) point 2; (c) point 3; (d) point 4; (e) point 5.....	212
B.12	Unbiased cross-correlation between u -velocity and pressure at the trailing edge locations of $W3_E$; (a) point 1; (b) point 2; (c) point 3; (d) point 4; (e) point 5	213
B.13	PSD of u -velocity (—), pressure (—) and unbiased cross-correlation function (—) at the trailing edge locations of $W3_E$; (a) point 1; (b) point 2; (c) point 3; (d) point 4; (e) point 5	215
C.1	Data points for the boundary layer and wake topology analysis; (a) $PSSP_1$; (b) $PSSP_2$; (c) $PSSP_3$	218
C.2	Histories of u -velocity (—) and pressure (—) at the leading edge locations of $PSSP_1$; (a) point 1; (b) point 2; (c) point 3; (d) point 4; (e) point 5; (f) point 6; (g) point 7	220

C.3	Unbiased cross-correlation between u -velocity and pressure at the leading edge of $PSSP_1$; (a) point 1; (b) point 2; (c) point 3; (d) point 4; (e) point 5; (f) point 6; (g) point 7.....	221
C.4	PSD of u -velocity (—), pressure (—) and unbiased cross-correlation function (—) at the leading edge of $PSSP_1$; (a) point 1; (b) point 2; (c) point 3; (d) point 4; (e) point 5; (f) point 6; (g) point 7	224
C.5	Histories of u -velocity (—) and pressure (—) at the leading edge locations of $PSSP_2$; (a) point 1; (b) point 2; (c) point 3; (d) point 4; (e) point 5; (f) point 6; (g) point 7	225
C.6	Unbiased cross-correlation between u -velocity and pressure at the leading edge of $PSSP_2$; (a) point 1; (b) point 2; (c) point 3; (d) point 4; (e) point 5; (f) point 6; (g) point 7.....	227
C.7	PSD of u -velocity (—), pressure (—) and unbiased cross-correlation function (—) at the leading edge of $PSSP_2$; (a) point 1; (b) point 2; (c) point 3; (d) point 4; (e) point 5; (f) point 6; (g) point 7	228
C.8	Histories of u -velocity (—) and pressure (—) at the leading edge locations of $PSSP_3$; (a) point 1; (b) point 2; (c) point 3; (d) point 4; (e) point 5	229
C.9	Unbiased cross-correlation between u -velocity and pressure at the leading edge of $PSSP_3$; (a) point 1; (b) point 2; (c) point 3; (d) point 4; (e) point 5	231
C.10	PSD of u -velocity (—), pressure (—) and unbiased cross-correlation function (—) at the leading edge of $PSSP_3$; (a) point 1; (b) point 2; (c) point 3; (d) point 4; (e) point 5.....	232
C.11	Histories of u -velocity (—) and pressure (—) at the trailing edge locations of $PSSP_1$; (a) point 1; (b) point 2; (c) point 3; (d) point 4; (e) point 5; (f) point 6; (g) point 7	235
C.12	Unbiased cross-correlation between u -velocity and pressure at the trailing edge of $PSSP_1$; (a) point 1; (b) point 2; (c) point 3; (d) point 4; (e) point 5; (f) point 6; (g) point 7.....	236
C.13	PSD of u -velocity (—), pressure (—) and unbiased cross-correlation function (—) at the trailing edge of $PSSP_1$; (a) point 1; (b) point 2; (c) point 3; (d) point 4; (e) point 5; (f) point 6; (g) point 7	238

C.14 Histories of u -velocity (—) and pressure (—) at the trailing edge locations of $PSSP_2$; (a) point 1; (b) point 2; (c) point 3; (d) point 4; (e) point 5; (f) point 6; (g) point 7	240
C.15 Unbiased cross-correlation between u -velocity and pressure at the trailing edge of $PSSP_2$; (a) point 1; (b) point 2; (c) point 3; (d) point 4; (e) point 5; (f) point 6; (g) point 7.....	241
C.16 PSD of u -velocity (—), pressure (—) and unbiased cross-correlation function (—) at the trailing edge of $PSSP_2$; (a) point 1; (b) point 2; (c) point 3; (d) point 4; (e) point 5; (f) point 6; (g) point 7	243
C.17 Histories of u -velocity (—) and pressure (—) at the trailing edge locations of $PSSP_3$; (a) point 1; (b) point 2; (c) point 3; (d) point 4; (e) point 5	244
C.18 Unbiased cross-correlation between u -velocity and pressure at the trailing edge location of $PSSP_3$; (a) point 1; (b) point 2; (c) point 3; (d) point 4; (e) point 5	245
C.19 PSD of u -velocity (—), pressure (—) and unbiased cross-correlation function (—) at the trailing edge of $PSSP_3$; (a) point 1; (b) point 2; (c) point 3; (d) point 4; (e) point 5.....	246
D.1 Schematic representation of the elastically mounted circular cylinder in cross-flow	249
D.2 Showing (a) full computational domain with imposed boundary conditions and (b) enlarged view with concentrated computational nodes	253
D.3 Histories of the uncontrolled lift coefficient C_l (----) and cylinder displacement (----) for ζ of 0.01 and Re of (a) 800, (b) 850, (c) 900, (d) 1000 and (e) 1100.....	255
D.4 Histories of the controlled lift coefficient C_l (----) and cylinder displacement (—) for ζ of 0.01, Re of 850 and for actuation periods, T_c of (a) T_n , (b) $2T_n$, (c) $3T_n$, (d) $4T_n$, (e) $5T_n$ and (f) $6T_n$	257
D.5 Variation of the amplitude ratio, y/y_o with control period, T_c	259
D.6 Contours of vorticity magnitude for ζ of 0.01 and Re of 850 near t/T_n of 20; (a) Uncontrolled cylinder, (b) $T_c = T_n$ and (c) $T_c = 4T_n$	260

D.7 Frequency distribution for the uncontrolled cylinder (a, ----) and controlled cylinder at T_c of $4T_n$ (b, —) and T_n (c, —).....261

LIST OF TABLES

3.1	Grid independence check for a plain square cylinder at $Re = 2.35 \times 10^4$	65
3.2	Time step independence check for a plain square cylinder at $Re = 2.35 \times 10^4$	65
3.3	Numerical data for the mean drag coefficient, C_d ; comparison between current numerical data at $Re = 2.35 \times 10^4$ and reported numerical data of Darekar and Sherwin (2001) at $Re = 100$	80
3.4	Streamwise turbulence intensity data measured at $(x/D, y/D) = (2, 2)$; comparison between current numerical results and reported experimental observations of Dobre <i>et al.</i> (2006).....	80
4.1	The mean drag coefficient, C_d , and the mean absolute lift coefficient, C_l , and their standard deviations for SSPs with a range of ω/λ and λ/D	112
A.1	Summary of observations for the spanwise boundary layer topology analysis ...	190
A.2	Summary of observations for the spanwise boundary layer topology analysis ...	198
B.1	Summary of leading edge correlation observations for $W0_E$ and $W3_E$	208
B.2	Summary of trailing edge correlation observations for $W0_E$ and $W3_E$	216
C.1	Summary of leading edge correlation observations for the partial SSPs	233
C.2	Summary of trailing edge correlation observations for the partial SSPs	247

NOMENCLATURE

LIST OF SYMBOLS

C_d	drag coefficient
C_{ij}	cross-term stress tensor
C_l	lift coefficient
C_p	pressure coefficient
C_s	Smagorinsky constant
D	cylinder width [m]
d	characteristic distance to wall surface [m]
dt	time-step [s]
F_d	drag force [N]
F_l	lift force [N]
f_{vo}	vortex-shedding frequency [Hz]
G	filtering function
k	wave number, turbulent kinetic energy [N·m]
L_{ij}	Leonard stress tensor
L_s	sub-grid scale characteristic length
p	pressure [Pa]
\bar{p}	filtered pressure [Pa]
Re	Reynolds number
R_{ij}	sub-grid scale Reynolds stress tensor
St	Strouhal number
\bar{S}_{ij}	strain rate tensor
t	time [s]
U_0	free-stream velocity [m/s]
\bar{U}	local mean velocity [m/s]
u	velocity component in the x -direction [m/s]
\bar{u}	filtered velocity [m/s]
u_τ	friction velocity [m/s]

u^+	non-dimensional velocity
u_{lam}^+	laminar non-dimensional velocity
u_{turb}^+	turbulent non-dimensional velocity
V_c	computational cell volume [m ³]
v	velocity component in the y -direction [m/s]
w	velocity component in the z -direction [m/s]
x, y, z	Cartesian co-ordinates
y^+	non-dimensional wall adjacent cell distance
Γ	law-of-the-wall blending function
δ	filtered static pressure [Pa]
ε	turbulent energy dissipation rate [m ² /s ³]
κ	von Kármán constant
λ	wavelength of spanwise sinusoidal profile [m]
μ	Newtonian fluid viscosity [kg/m.s]
μ_t	turbulent viscosity [kg/m.s]
ρ	fluid density [kg/m ³]
σ	normal stress [N/m ²]
$\bar{\sigma}$	normal stress due to molecular viscosity [N/m ²]
τ	shear stress [N/m ²]
$\bar{\tau}$	sub-grid scale shear stress [N/m ²]
τ_{kk}	isotropic sub-grid scale shear stress [N/m ²]
τ_w	wall shear stress [N/m ²]
ν	kinematic viscosity [m ² /s]
Φ	variable operator
$\bar{\Phi}$	filtered variable operator
ω	peak-to-peak amplitude of spanwise sinusoidal profile [m]

ABBREVIATIONS

LES	Large Eddy Simulation
RANS	Reynolds Averaged Navier-Stokes
SKE	Standard k -epsilon
SSP	Spanwise Sinusoidal Profile

INTRODUCTION

Turbulent flows around three-dimensional obstacles occur frequently and they occur around communication towers, buildings, cylindrical support structures, bridges, vehicles and so on. The subsequent formation of turbulence and the transport of vortices in the wake of the bluff body give rise to aerodynamic forces with large fluctuating components. This affects their aerodynamic performance, and can induce significant structural oscillations (vortex-induced vibrations), which can lead to fatigue failures and resonances. This is detrimental to safety. Therefore, the three-dimensional flow around bluff bodies is important in engineering practice, as the forces generated must be accounted for in the design. As a result, structures may have to be strengthened or reinforced, leading to the design of the structures being quite robust. However, they may still be susceptible to fatigue failure. This approach to mitigating the effects of vortex shedding is likely to be wasteful of materials, and it may not be aesthetically pleasing. An alternative is to modify the aerodynamics of bluff bodies and obviate these drawbacks. For these reasons, it is essential to understand and anticipate the properties of turbulent flow around bluff bodies, to implement more effective, efficient and safe engineering designs (Shah and Ferziger 1997).

Control mechanisms can alleviate the deleterious effects on bluff bodies caused by turbulent flow. They can achieve this by modifying the flow field around the bluff

bodies or by adjusting the body's response to the flow; in either case, the large fluctuating forces are attenuated. The latter can include active feedback controllers that reduce the high amplitude oscillations of the body in response to the vortex induced vibrations. However, this can be an expensive solution as actuators and sensors are incorporated into the mechanism; furthermore, active controls are subject to high maintenance costs, and they generally consume energy. Hence, an active flow control method is not necessarily suitable to achieve an effective and sustainable engineering design. Passive control mechanisms may be preferable. The development of flow control mechanisms can provide insights to better understand the fluid-to-structure interactions. Anticipating the fluid dynamics of the flow field around bluff bodies will facilitate the design of structures that are not subjected to damaging forces.

Numerous approaches for the control of the flow around bluff bodies have been implemented successfully. It has been found that flow control techniques, such as passive mechanisms are more preferable than active control methods. Passive controllers are typically more effective when they are applied adjacent to the point of transition (i.e. laminar to turbulent flow) or the separation lines on the surface of the body (Anderson and Szewczyk 1997; Bushnell 1994). These correspond to regions in which flow instabilities increase rapidly and critical flow regimes exist. The approaches to controlling the flow around a bluff body, with the aim of improving the aerodynamic performance, must consider controlling the wall-bounded turbulence (i.e. the flow on the surface). There are two common categories of flow controls; these are free-shear controllers and wall-bounded controllers. A free-shear controller focuses on the flow that has separated from the surface, and can have restrictions reducing the surface drag force, as the wall-bounded flow is more important in this case. Hence, this research will focus on a wall-bounded passive controller.

1.1 Passive Flow Control Mechanism

In order to control the flow around a bluff body, passive controls are often preferred to active control methods, as they provide effective solutions and simplified designs, without the need for external energy resources. Passive control mechanisms usually involve modifications to the structural geometry. An example of the use of passive devices include the work of Bearman and Brankovic (2004), in which helical strakes and bumps are applied to circular cylinders, in order to control vortex shedding and therefore reduce vortex induced vibration. Their application proved effective when applied to a fixed cylinder. However, in the case of freely vibrating flexible cylinders, the system resonates when the value of the reduced velocity, U/N_oD , is in the range in which vortex induced resonance would occur if the cylinder were plain. Here U is the velocity of the fluid, D is the diameter of the cylinder, and N_o is the natural frequency in vacuo.

Passive control mechanisms have the potential to control the turbulent flow field. However, not all types of passive controllers are practical. For example, helical strakes and surface bumps, although effective in flow control with their ability to reduce the adverse effects of vortex shedding, can increase the drag force by up to 10% (Griffin and Ramberg 1982). If these devices are attached to say, cylindrical towers, the increase in drag loading can induce significant bending moments at the base.

More recently, Kumar *et al.* (2008) reviewed methods of achieving passive control by fitting helical strakes, bumps and streamline fairings to bluff bodies. They agreed that these devices provided effective control when applied to single structures. However, when individual structures form part of an array of structures, the flow field may be modified in a way that promotes vibrations as a result of the fluid-to-structure

interactions caused by interference. In addition, these particular modifications can significantly affect the fluid dynamic performance, installation and maintenance costs, and overall simplicity of the structure.

Van den Abeele *et al.* (2008) numerically modelled the effects of helical strakes and streamlined fairings on bluff bodies in turbulent flows. Their results agreed closely with the experimental observations of Bearman and Brankovic (2004) and Kumar *et al.* (2008). The numerical models demonstrated that the effectiveness of these passive devices is dependent on the direction and velocity of the flow. An example of a passive control with a dependence on both the free-stream velocity and flow direction is control cylinders located on either side of the wake (Saha *et al.* 2003). Not only does this type of control depend on the flow direction, but mechanical attachments that hold the control cylinders in place can exacerbate resonance of the structure, and they may be subject to fatigue failure. Considerations such as these may limit the applicability of these passive control systems and pose an economic impediment to their adoption.

An effective method of controlling vortex shedding and improving the aerodynamic performance of a bluff body is to modify its geometry by incorporating a periodic perturbation to the leading and trailing edges, after the manner of Tombazis and Bearman (1997), Bearman and Owen (1998) and Owen and Bearman (2001). They reported a reduction of up to 34% in the mean drag loading, due to fixed spanwise vortex dislocations. Complete mitigation of vortex shedding was also achieved for very mild perturbations, regardless of the flow direction (Bearman and Owen 1998). Both the mean and unsteady forces were reduced, in which there was independence of the angle of attack of the flow; this may be a useful attribute. In addition, reduced forces can be a result of stable three-dimensional shear layers that have been found to be associated

with a wavy cylinder (Xu *et al.* 2010). Darekar and Sherwin (2001a, b) determined that in laminar flows the drag on wavy cylinders that have a square cross-section and are sinusoidal in the direction transverse to the flow is about 30% less than the drag on the corresponding straight square cylinder. Importantly, vortices on the length scale of the height of the bluff body were absent. They also established that three distinct laminar flow regimes result from this geometry, depending on parameters such as the wavelength and amplitude of the sinusoidal perturbations along the cylinder.

Further examples of passive control applications have been reported by Naumann *et al.* (1996) and Dobre *et al.* 2006, in which periodic changes were applied to the separation lines of circular and square cylinders, respectively. It was demonstrated that this application mitigated vortex shedding at critical free-stream velocities. Dobre *et al.* (2006) demonstrated that a reduction of up to 78% in the turbulence intensity could be achieved in the wake, and this is reflected in a 30% reduction in the mean drag force. The vortices in the wake were also observed to decay more rapidly; hence vortices in the intermediate to far wake regions were less well defined. In addition, castellation of the trailing edge of bluff bodies results in a decrease in the drag loading of up to 64%, which is associated with increases in the trailing edge pressure (Tanner 1972). The imposition of periodic perturbations is a promising mechanism for passively controlling the flow around bluff bodies, and it offers a thriving field of fluid dynamics research to understand the phenomena associated with this control method.

Biomimicry provides inspiration to elucidate the phenomena of the controlled flow field around a bluff body. Nature itself can be a template for many engineered applications, specifically passive control mechanisms that exhibit periodic perturbations. One particular example is the leading edge comb that is located on owls'

wings; these account to their silent flight (Lilley 1998). The comb can be idealised as a spanwise sinusoidal profile (SSP) on the leading edge of a bluff body. In fact, the broad aspect ratio of an owl's wing makes this passive control mechanism applicable to bluff bodies, including those researched in this work. It is the leading edge comb that forms the inspiration of the research, and this is discussed in greater detail in the following chapters. An SSP provides a very practical and important mechanism for reducing aerodynamic and hydrodynamic forces on bluff bodies. Its commercial applications are only now being realised, and this renders the work reported in this thesis particularly timely.

1.2 Objectives and Contributions of the Thesis

The principal objective of this research is to use spanwise sinusoidal profiles on the leading edges of bluff bodies to control turbulent flow fields. This is achieved by using a validated numerical model to simulate the transport phenomena in the flow field. In so doing, the numerical analysis can refine the existing knowledge discussed briefly in Section 1.1. The research presented in this thesis is motivated by the possibility of utilising detailed numerical simulations of the flow control phenomena that occur in nature. In particular, it is bio-inspired by the silent flight of owls. The wings of owls have special features in the form of a leading edge comb and trailing edge fringe. These features have been found to suppress the noise during flight by controlling the wing aerodynamics (Lilley 2009). Hence, the mean drag force and lift force variance is reduced, and the possibility exists for suppressing vortex-induced resonance. The numerical simulations will provide further understanding of the flow dynamics that are

associated with applying a leading edge comb to a bluff body, and the SSP is considered a generic example, as it exhibits similar characteristics.

Few important parameters need to be addressed when designing a passive control mechanism such as the SSP. These parameters are the amplitude and the wavelength of the sinusoidal perturbations. To establish these parameters within an intellectual framework, the results of this study are expressed in terms of the Reynolds number, Re , the normalised wavelength, λ/D , and wave steepness, ω/λ , where D is the leading edge height of the bluff body, and λ and ω are the wavelength and wave height, respectively.

This research provides a step towards understanding the links between nature and engineering, in an attempt to design more efficient aerodynamic structures. To achieve this research objective the aerodynamic performance of square and rectangular cylinders is examined in detail numerically, and the results are verified against published experimental observations. Although the square and rectangular geometries are not a direct replication of an owl's wing, they represent an idealisation of the leading edge comb. This approximation is a key to unlocking the aerodynamic wisdom of the owl. Hence, modelling the turbulent transport of air travelling around the square and rectangular cylinders provides an additional step toward a significant understanding of the passive control application. The transport of fluid flow around uncontrolled and controlled square and rectangular section bodies is important in a general sense for engineering applications. The complexity of the physical phenomena renders this approach an excellent candidate for analysis using contemporary methods.

Three-dimensional numerical predictions are obtained with the computational fluid dynamics (CFD) code – FLUENT[®]. It is essential that the CFD code is validated against experimental data for all flow characteristics associated with the investigation in this

study. The research reported in this thesis contributes to the validation of a commercial CFD package against a range of phenomena associated with turbulence flow control. This includes topology of the flow field both adjacent to the structures and within the boundary layer. Hence, the wall adjacent flow and near wake flow have been studied in detail. The effects of the SSP on mean drag force and lift force variance with different arrangements have also been investigated. In the numerical predictions, the mathematical approach is based on the Large Eddy Simulation (LES) turbulence model, where the large scale flow structures are sufficiently resolved and the small scale structures are modelled.

1.3 Thesis Outline

This research has been contextualised in Section 1.1, and here a more detailed outline is provided. As mentioned beforehand, the motivation for the research is bio-inspired from the silent flight of the owl. Chapter 2 provides a literature review of the morphological adaptations that promote silent flight. This puts the research into perspective. Discussion is made specifically on the leading edge comb, in order to elaborate on the results to be presented in following chapters, and demonstrate the connection between natural phenomena and engineered applications.

The research presented in this thesis is purely numerical, and the current results have been validated against existing experimental and numerical data. The governing mathematical equations, physical assumptions and details of the numerical techniques are detailed in Chapter 3. The computational domain and mesh generation is discussed, and the model validation and setup for experimental comparisons are outlined. A validation of the numerical approach using LES is demonstrated. Results from the

current numerical data for the turbulent flow around the bluff bodies are shown to agree well with other numerical and experimental observations reported in literature.

The numerical tool has enabled an investigation of physical phenomena that have not been previously reported in the literature. Details emerge of the flow field around a bluff body that has a spanwise sinusoidal profile attached to the leading edge. In Chapter 4, the phenomena of the controlled flow field are elucidated for contrasting configurations of an SSP imposed on square cylinders. Results are presented in the form of time-averaged quantitative observations for both uncontrolled and controlled flows, as well as the power spectral densities of the wake. These results are in good agreement with previously published studies. They are interpreted with the help of flow visualisations. The aerodynamic forces and their fluctuations acting on a square cylinder can be greatly reduced if an SSP is imposed on the leading edge. This is particularly the case when the wave steepness, ω/λ , is 0.2 and the normalised wavelength, λ/D , is between 2.4 and 5.6.

In addition, a parametric study is conducted in Chapter 4 to examine the role of the governing parameters of the SSP, namely the amplitude and wavelength. The motivation for the parametric study is that the literature suggests that the normalised wavelength plays an important role in controlling laminar flow fields. In contrast, the parametric study suggests that the wave steepness assumes more importance when controlling turbulent flow fields. It is to be noted that Chapter 4 establishes the setting for future chapters. Hence, the investigation and length of this chapter is larger than other chapters in this thesis.

Many practical applications involve bluff bodies with large aspect ratio, in which the geometries are elongated in the direction of the flow. Furthermore, owls' wings have

broad aspect ratio, which provides a further motivation for the investigation into elongated bluff bodies. An investigation of the spanwise sinusoidal profile applied on the leading edge of elongated cylinders is conducted in Chapter 5. The cylinders are elongated forms of the SSP geometries that are explored in Chapter 4. This chapter focuses on the effect of the behaviour of the shear layers associated with flat plates, namely the separating and reattaching phenomena along the surface. The results given in the form of flow visualisations and time-averaged physical quantities demonstrate that the aerodynamic forces acting on an elongated bluff body can be greatly reduced with an SSP imposed on the leading edge. The flow field and wake of the elongated SSP body resembles that of a streamlined body. Additionally, the proximity of the SSP leading edge to the trailing edge does not profoundly influence the control of the flow field. The sinusoidal perturbations are capable of largely dissipating the shear layers, and forming a narrow wake behind the elongated body.

The spanwise sinusoidal profile on the entire leading edge is a very effective passive flow control mechanism. However, in some practical cases, the deleterious effects that result from the surrounding flow may only exist at local regions on the span of the structure. In these cases, the full span SSP may be considered impractical. Furthermore, the leading edge comb is located on only the primary feathers of an owl's wing. Hence, Chapter 6 explores the effectiveness of SSPs applied on only part of the spans of square cylinders. In other words, the leading edges experience combinations of interrupted regions of plain (uncontrolled) and SSP (controlled) spans. The investigations are carried out with the most efficient SSP design that is obtained in the previous chapters. Flow visualisations and results of the time-averaged flow data are provided. Chapter 7 concludes the research and discusses possible future research opportunities.

A quantitative topological analysis of the boundary layers for the square, elongated and partial SSP cylinders is provided in Appendix A. A cross-correlation analysis of the time-averaged velocity and pressure measured at points located on both the leading and trailing edges is discussed in detail. The data are provided as an Appendix because a refined study is suggested as future work.

A proposal for a semi-active parameter control mechanism to control the turbulent flow surrounding a circular cylinder, and suppressing vortex-induced vibration is investigated in Appendix B. Although a passive control is the main focus of the thesis, the semi-active parameter control demonstrates an efficient mechanism as an alternative approach for flow control. This was investigated at the early stages of the research to contrast with the passive control. Through variations in the effective length, and based on knowledge of the turbulent flow environment, the control condition can be predetermined. This eliminates the need for computing and sensing equipment that is usually included with active controls. Hence, the proposed technique provides an efficient and reliable alternative.

TECHNOLOGY OF OWLS' SILENT FLIGHT: A BIO-INSPIRED SPANWISE SINUSOIDAL PROFILE

The history of technological development has generally been portrayed through engineering designs that are products of our sole understandings of engineering principles. For example, the development of efficient and safe road vehicles relies on the understanding of energy, combustion and mechanics. Furthermore, the design of superior commercial aircraft involves knowledge of aerodynamics, material science and hydraulics. In recent history however, the application of engineering towards the improvement of technology has opened the door to the broad field of biomimetics (Benyus 1997; Bar-Cohen 2006; Mueller 2008). Engineering principles have largely been used to explain phenomena in biological specimens; however, the case now rests on nature itself as a template for many engineered applications and the advancement of technology.

Nature itself holds the key for many, if not all, engineering principles. Even though the field of biomimetics is not new, engineers still have much to learn about nature in order to unlock and harness all its phenomena. In this research, focus is on aerodynamic phenomena, in particular, controlling turbulent flows around bluff bodies. When bluff bodies are located in a turbulent flow field, they experience unacceptably large and time

varying forces that result from their shedding vortices. In this case, the structure is susceptible to fatigue failure, and the fluctuating forces can create significant aerodynamic noise. To mitigate the forces on the bluff bodies, bio-inspired passive mechanisms can be employed as an effective solution, in which the aerodynamics are modified to obviate these drawbacks.

Passive mechanisms through biomimicry relate to morphological adaptations that control the flow around the body. There exist numerous types of passive controls in nature; one example is the drag reducing streamline shape that can be observed in many marine mammals, such as cetaceans (Bushnell and Moore 1991; Curren, Bose and Lien 1994; Wolfgang et al. 1999; Pavlov 2006). Their ability to swim efficiently is accountable to the fusiform shape of their bodies, flippers, flukes and the dorsal fin; these can resemble the shape of airfoils or fuselage found on aircraft. The purpose of these streamlined geometries is to maintain an attached smooth flow (boundary layer) across the surface, resulting in the lower drag force. Streamlining has been implemented on bluff bodies, in which fairings are attached to oil and gas submarine pipelines and catenary risers (Kumar *et al.* 2008; Van den Abeele *et al.* 2008). This passive control mechanism proved effective in most cases; although, it was found to be highly dependent on the direction of the flow. Marine mammals are living systems and therefore, have the ability to change their direction to the flow as they swim. Hence instead, mechanical devices were fixed to the streamline fairing to allow it to rotate streamwise around the structure. However, passive control methods are usually favoured over such active control methods because active controls require the use of mechanical devices which consume energy and can be susceptible to fatigue failure.

That a fusiform surface improves the aerodynamic performance of a geometry results in it being considered an exceptional means of passively controlling the flow. However, there exists other morphological adaptations that can control the flow and improve performance quite remarkably, which may not at first be expected to do so. These components of the body are eccentric features that create turbulent flow around the surface of the body rather than preserving laminar (smooth) flow. In other words, they force (trip) the boundary layer to prematurely transition from laminar to turbulent flow, in which the higher energy of the flow keeps it attached to the surface. Examples of such devices are the bumps that can be depicted on the surface of the pectoral flipper of a humpback whale (*Megaptera novaeangliae*) and the dorsal fin of porpoises (*Phocoena dioptrica*) (Winn and Reichley 1985; Evans, Kemper and Hill 2001; Watts and Fish 2001; Custodio 2007; Fish, Howle and Murray 2008). In addition, the eccentric morphological adaptations are not limited to marine mammals and are also found on the wings of birds such as the owl (*Strigiformes*) in the form of leading edge combs; these can be accountable to their silent flight (Lilley 1998). In fact, the broad aspect ratio of an owl's wing makes this passive control applicable to bluff bodies, and previous studies have been conducted to apply this silent flight technology to aircraft, in order to reduce airport noise during planes takeoff and landing (Roach 2004; Jaworski and Peake 2012).

Surface modifications, in particular leading edge modifications, prove to be an effective passive control mechanism, such as a sinusoidal leading edge (Bearman and Owen 1998; Owen *et al.* 2001; Darekar and Sherwin 2001; Dobre *et al.* 2006). A sinusoidally modulating leading edge generally results in flows in the wake of bluff bodies becoming incoherent. Hence, the flow field exhibits three-dimensional

characteristics which prevent a uniform bulk flow from forming the roll-up of large scale vortices. Indeed, the abovementioned corroborates the need to incorporate biomimetics of morphological adaptations to control the flow around bluff bodies in an effort to reduce the deleterious effects of vortex shedding.

The aims of this chapter are to highlight the phenomena of the silent flight of owls', which motivates the main research in this thesis; a bio-inspired spanwise sinusoidal profile (SSP) to control the turbulent flow around bluff bodies. Taking inspiration from the owls' book of aerodynamic wisdom, the SSP represents a simple form of the primary flow control mechanism found on an owl's wing; the leading edge comb. The features of the passive control mechanisms on owls' wings are explored in detail before elucidating the structure of the flow field around a bluff body with and without an SSP in later chapters. Hence, this chapter will focus on providing a detailed background on the owl, and will identify some practical applications of the technology of owls' silent flight, to demonstrate the potential use on bluff bodies.

2.1 The Phenomena of Silent Flight

Most birds of prey depend on their capability to fly at great speeds to capture their prey. Owls however, flying at relatively lower speeds, require a different strategy to hunt successfully. Owls are usually perched close to the ground, at approximately 3 to 6 m, therefore relying on stealth to remain undetected by its prey. The mice and voles hunted by owls have hearing that is most sensitive between 2 and 20 kHz, and the owl's bi-aural sensing system has a frequency range between 3 and 6 kHz (Lilley 2009). Hence, owls must remain relatively quiet above a frequency of 2 kHz, if they are not to interfere with both the preys' and their own hearing system.

An early work to explore how owls differed from other species of bird was that of Lieutenant Commander Graham R. N. (1934). It was observed in this work that the key features providing the owl with its stealth attribute are on the wing itself, and can be characterised by a leading edge comb, trailing edge fringe and velvety down feathers on the upper surface. This chapter will focus on the leading edge comb and trailing edge fringe, as we will later explore how these features allow the ability to control aerodynamic flows. Furthermore, results from current research presented in following chapters demonstrate the effectiveness of the leading edge comb applied to square and rectangular bodies in the simple form of a spanwise sinusoidal profile (SSP).

2.1.1 Leading Edge Comb

The leading edge comb is a hard comb-like structure, located at the front of every feather that acts as a leading edge of the wing. The combs are at most approximately 4 mm long with a spacing of 0.75 mm, and these parameters vary between species of owl (Graham 1934). An enlarged view of a leading edge comb from a Barn Owl (*Tyto alba*) is shown in Figure 2.1, where the hard shape and structured comb-like pattern can be depicted. That the parameters of the comb differ between species of owl, but nonetheless remain fixed for any given wing, suggest that the spacing and height of the teeth play an important role in controlling the flow field. In following chapters it is found that both the sinusoidal wavelength and amplitude of an SSP are significant parameters in effectively controlling the flow field around a bluff body.

For the Barn Owl, the leading edge comb appears only on the primary wing feather, from near the tip of the feather to the root, and has direct contact with the oncoming airstream. A diagram indicating the primary and secondary feathers of an owl's wing is

given in Figure 2.2. Lt. Cmdr. Graham (1934) suggested that the leading edge comb provides a silencing mechanism for noise generated by fluctuations in the air. The leading edge comb can be found on other adjacent primary feathers for other owl species, such as the Barred Owl (*Strix varia*); however, it is only present on the part of the wing that interacts with the free-stream flow (Bachmann et al. 2007). A Barred Owl in flight is displayed in Figure 2.3 and shows the leading edge comb only on all leading edge regions of the feathers that interact directly with the free-stream.

The leading edge comb of a Barn Owl is in such a way that each tooth is directed upward at an angle of approximately 45 degrees towards the tip of the wing (Graham 1934). This detail is clearly evident in Figure 2.1. In flight, when the wing is angled and cambered to the oncoming flow, initial interaction between the flow and wing may be concentrated towards the underneath of the leading edge. In this case, the upward extension of the leading edge teeth may allow the free-stream flow to firstly interact with the passive control by forcing the airstream to travel between the combs before reaching the true leading edge of the wing. Therefore, this slows the flow and reduces the effect of the sudden decrease in pressure within the upper boundary layer. The inclination of the comb deflects the flow in such a way that the boundary layer is much thinner on the upper surface (suction surface) than on a conventional wing without a comb. Hence, the upper surface boundary layer contains a pattern of small longitudinal (streamwise) vortices as a result of the comb (Lilley 2009). The flow remains attached along the cord of the wing, producing a stabilised flow on the upper surface during flight, as well as preventing the emission of sound from scattered turbulent flow.

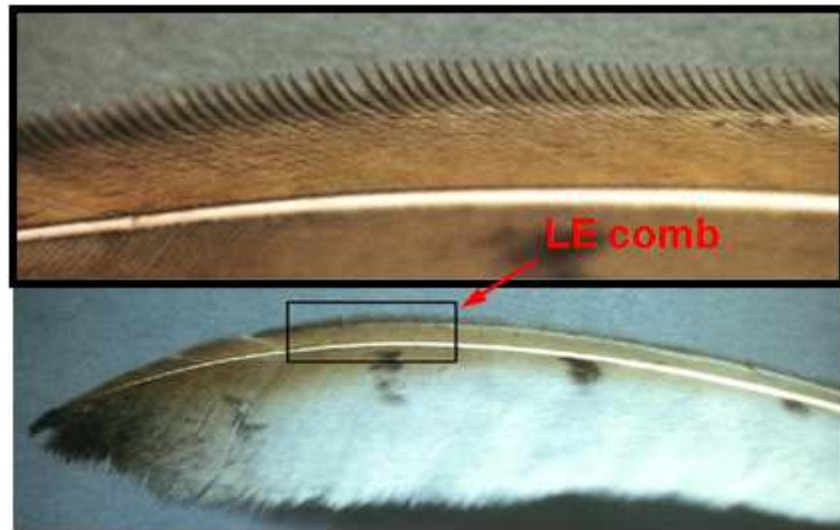


Figure 2.1: Leading edge comb of a Barn Owl (*Tyto alba*) feather (Sieradzki 2008).

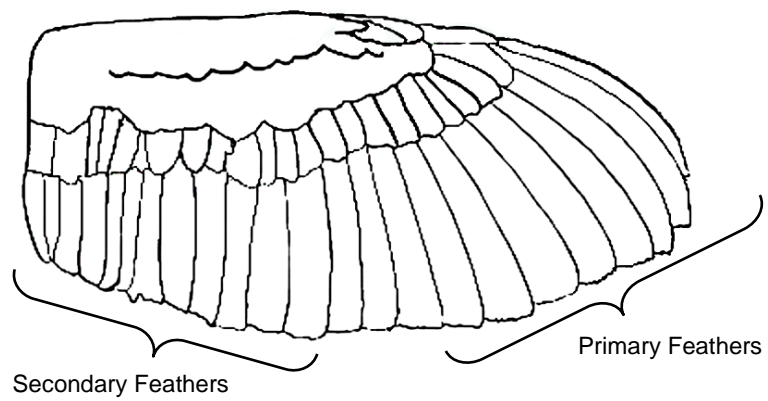


Figure 2.2: Diagram of a Barn Owl's wing showing the primary and secondary feathers (Bachmann et al. 2007).

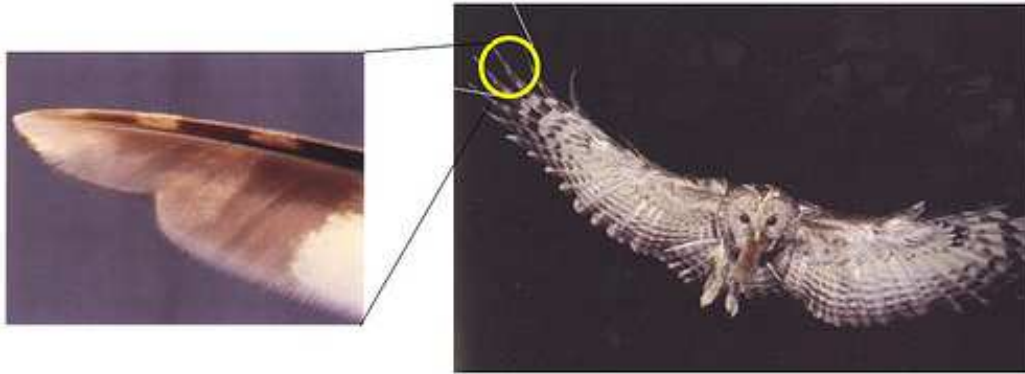


Figure 2.3: Leading edge comb shown on a Barred Owl (*Strix varia*) in flight (Kohut 2009).

An owl does not have a comparable flight speed to other bird species such as an eagle or peregrine. Furthermore, the shape of an owl's wing is rounded with a very broad aspect ratio, allowing the owl to glide slowly. At an average Reynolds number of approximately 1.5×10^5 corresponding to a flight velocity of 6 to 8 ms^{-1} , the owl flies quite steeply towards its prey at approximately 24 degrees to the horizontal. Adding to that, the wings are highly cambered during a rapid acceleration from the perched position, and a sudden deceleration when catching the prey (Lilley 1998). In Figure 2.4, a typical steep flight profile of a Barn Owl is shown, demonstrating the positioning of the wings during an approach to its prey. This typical flight behaviour of an owl would produce a stalled flow on the upper surface of the wings, hindering the owl's ability to maintain flight. The leading edge comb is a mechanism that provides effectiveness in flow control by stabilising and quietening the flow around the wings, allowing the owl to maintain its flight and hunt accurately and successfully.

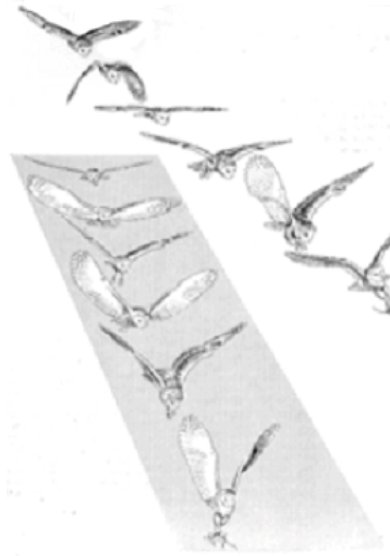


Figure 2.4: Flight path of a Barn Owl during the day (top) and night (bottom) (Lilley 2009).

Lilley (1998) conducted a study of owls silent flight, based on the work of Kroeger, Grushka and Helvey (1972) to confirm the owls' remarkable abilities. Kroeger et al. (1972) studied the flight behaviours of the Barred Owl both with and without a leading edge comb. They found that without the leading edge comb, the Barred Owl experienced difficulty maintaining straight flight, and was not able to capture its prey accurately. The acoustic range of the owl was well above 10 kHz, which is similar to all other birds. The higher frequencies produced during these observations can also be a contribution to the Barred Owl's inability to maintain its approach trajectory, as the noise would interfere with the bi-aural sensing system. However, as the Barred Owl of Kroeger et al. (1972) was trained to hunt its imitation prey for the experiments, the difficult flight could very well be the result of stalled flow on the wings.

The observations of Kroeger et al. (1972) and further work of Lilley (1998) can be considered a confirmation of the theory that the flow is stalled across the wing without a

leading edge comb, while identifying the prevention of laminar separation along the wing upper surface when the leading edge comb is attached. In fact, the observations demonstrate how the leading edge comb not only reduces noise levels, but also allows a pseudo-turbulent flow at low Reynolds number to remain attached across the wing surface (Lilley 1998). Furthermore, when Kroeger et al. (1972) conducted the experiments for the normal Barred Owl, the noise was dominant at frequencies well below 2 kHz, demonstrating the owl's silent flight mechanism. This substantiates the motivation to apply a form of the leading edge comb to the leading edge of a bluff body in order to control the flow across the surface. By maintaining an attached flow, the flow field around the bluff body would exhibit the characteristics associated with the flow field around streamlined (fusiform) bodies.

2.1.2 Trailing Edge Fringe

The trailing edge (TE) fringe consists of fibres that extend from the trailing edge of each primary feather and the main wing. They are formed from the tips of the barbs (strands) that make up the feathers (Bachmann et al. 2007). Barbs can be identified as hair strands that are combined together to form the surface of the feather. The length of the trailing edge fringes are approximately 5 mm in the case of large owls and the spacing is non-uniform (Graham 1934). A trailing edge fringe is shown in Figure 2.5, where the similarity to fibres can be depicted. Each barb throughout the feather is connected by microscopic secondary branches called hook radiates (Bachmann et al. 2007). These radiates contain small hooks that connect to the hooks of adjacent radiates and hence connect the barbs. At the trailing edge of the feather, the barbs are thinner and lack the

small hooks. Hence, this characteristic forms the fibres, as the barbs exist independently to form the fringe.

One can suggest that the non-uniform nature of the trailing edge fringe and random fibre lengths, shown in Figure 2.5, are able to absorb the non-uniform pseudo-turbulent flow features that exist within the boundary layers by applying a porous medium to the feathers. As the flow along the upper and lower surfaces of the wing sheds from the trailing edge, the small turbulent eddies present on each surface and created by the presence of the leading edge comb, interact with each other. For a normal wing without a trailing edge fringe, the mixing of the upper and lower boundary layers can generate vortex shedding and noise. Graham (1934) suggests that as the flow travels through the trailing edge fringe, the interaction process is delayed by the porosity of the trailing edge fringe, and the resulting near wake stream is smoothed and vortex shedding suppressed.

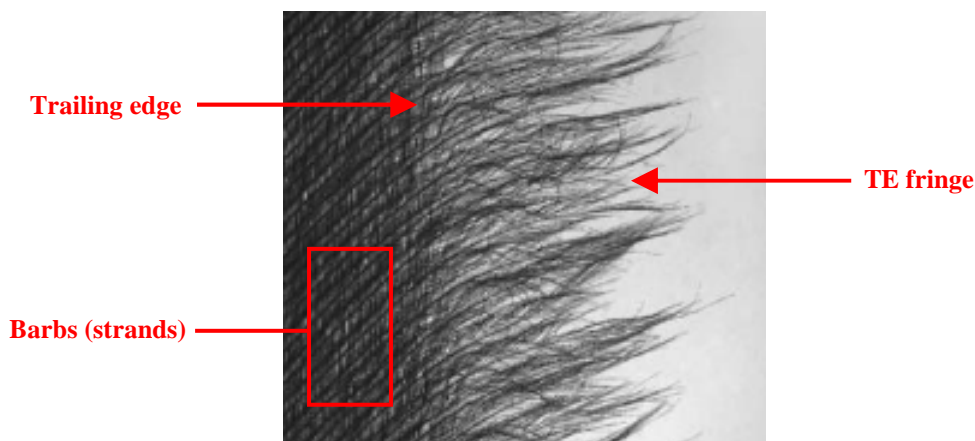


Figure 2.5: Trailing edge fringe of a Barn Owl (*Tyto alba*) showing detail of fibre extensions of the barbs of the feather (Bachmann et al. 2007).

Another suggestion from Graham (1934) is that the trailing edge fringe also behaves as an absorber to fluttering caused by flow induced vibrations at the trailing edge, therefore, suppressing the scattered turbulent noise. This suggestion is based on the observation that the trailing edge fringe is not only present along feathers that behave as a trailing edge, but also overlapping primary feathers. The reason, as an owl glides through the air the wing feathers space evenly to allow the air to travel between each feather in order to maintain gliding flight. An example of this feather spacing can be seen in Figure 2.3 for the Barred Owl.

Interestingly, Bachmann et al. (2007) also noted a fringe along the leading edge of each feather. However, it was not present on the true leading edge of the initial primary feather and this fringe was shorter and mostly parallel to the leading edge. It might be reasonable to suggest that this additional fringe can be associated with reducing friction between the feathers, as well as absorbing turbulence not absorbed by adjacent feathers. The current research does not cover a complete study into the effectiveness of the trailing edge fringe on bluff bodies, however, it is thought necessary to introduce background on this silent flight mechanism as it is plausible to include in future research. Hence, following sections in this chapter will briefly demonstrate the practical applications of a trailing edge fringe.

2.2 Scaling for Biomimicry

Passive adaptations such as the leading edge comb and trailing edge fringe allow the owl to fly relatively silently by altering the surrounding flow. Indeed, these devices can be implemented to enhance the aerodynamics around bluff bodies. An effective transition of such biological design to engineering applications requires the use of

proper scaling. For example, a particular case of a technological system may be larger in size and also operating at a faster speed as compared to that of a biological system; this example can exist between a bluff body and an owl. Hence, to obtain the same degree of effectiveness in control of the flow field on a bluff body as that of an owl, an overlap in performance criteria between the two cases can be established (Fish et al. 2011).

Examination of the steep approach path of an owl of approximately 24 degrees to the horizontal reveals this to be typical of most owls, and resembles the trajectory of commercial aircraft during landing (Lilley 2009). The large angle of attack of the flow field upon a leading edge can also coincide with conditions on bluff bodies that are manifest in a myriad of many engineered structures and applications. Furthermore, an additional overlap can exist by comparing the flow speeds. Taking the Reynolds number as $Re = (\rho UD)/\mu$, where ρ , U , D and μ , are respectively the fluid density, streamwise velocity, wing cord (width) and dynamic viscosity, an owl flying at a Reynolds number of 1.5×10^5 can produce and maintain attached flow across the wing with a coefficient of lift, C_l , of 1. In the case of a conventional wing or blade operating at the same speed, flow separation will be experienced at C_l of 0.6 (Lilley 2009). As Kroeger et al. (1972) discovered, the inclusion of the leading edge comb provides the owl with stable flight by applying the effect of co-rotating vortex generators across the upper surface of the wing. The resulting decrease in surface drag prevents a stalled flow from occurring and also reduces scattered turbulent noise. In this case, an owl's wing containing a broad length/cord (L/D) ratio and lower streamwise velocity, U , resulting in a lower flight Reynolds number, can achieve a much higher performance in lift. Hence, the limitations of performance placed on conventional geometries can be significantly improved.

Lilley (1998) derived that the far-field sound intensity was proportional to the amount of turbulence crossing the trailing edge of the wing. Therefore, for a highly turbulent flow passing over the surface of the wing, a high intensity of sound is also expected; the increase of sound can equate to lower aerodynamic performance. Reducing the boundary layer thickness across the upper and lower surfaces of the wing reduces the turbulent flow and hence, the sound intensity and surface drag.

The leading edge comb contains uniform spacing between teeth, which produces a thin boundary layer on the surface of the wing. Lilley (1998; 2009) deduced that the uniform tooth spacing produces a streamwise vorticity field across the surface, maintaining an attached flow up to the trailing edge, which mitigates the interaction of turbulence intensity at the trailing edge of the wing. He related the even spacing of the comb teeth to a non-dimensional spanwise spacing,

$$z^* = \frac{u_\tau \Delta z}{\nu} \quad (2.2.1)$$

which is accountable for optimal drag reduction, where u_τ is the local shearing velocity at the leading edge and Δz is the uniform spacing between each tooth. The value of z^* for the leading edge comb is approximately 18, determined through experiments, and is near the value for maximum drag reduction (Lilley 2009). Similarly, Bachmann et al. (2007) measured the density of the leading edge comb to be approximately 18 per cm, which is equivalent to the density of the barbs abovementioned in Section 2.1.1. Hence, it can be anticipated that the non-dimensional spacing of the leading edge comb plays an important role in obtaining a controlled flow field, and is also a significant parameter in providing an overlap between the biological phenomena of the owl and an engineered

application; this will be the focus of the research and demonstrated by the spanwise sinusoidal profiles on the bluff bodies.

2.3 Practical Adaptations of Silent Flight Technology

The technology associated with silent flight was proposed by Graham (1934) to be used for silencing airscrew blades, that is, propellers and turbines. However, it was concluded that the light wing-loading of the owl and the slow speed in comparison to propellers might prevent the modifications from being applied, but the noise characteristics are still worthy of investigating. Nevertheless, silent flight technology, or preferably referred owl technology, has been utilised by Liang et al. (2010) to investigate noise reduction of fan vanes, while attempting to increase both air flow and efficiency. This work involved experiments with the application of a saw-tooth serration along the tip region on the leading edge of the fan blades. The serrated fan blades of Liang et al. (2010) are shown in Figure 2.6.

Considering owls' wing structure, shape and distribution of the leading edge comb, Liang et al. (2010) decided the key parameters for designing the saw-tooth leading edge were the number of teeth, height of the teeth, and the circular pitch (spacing) of the teeth. It was found that a fan blade with less teeth, but large pitch and height, achieved the best performance. This configuration is shown in the image on the far left of Figure 2.6. That the application of a leading edge comb improves the performance of a streamlined body (i.e. fan vane), which would already contain good performance criteria without any modification, justifies the motivation to investigate this use on bluff bodies. Indeed, the abovementioned findings corroborate the current research results for a bluff body, which is presented in the following chapters.

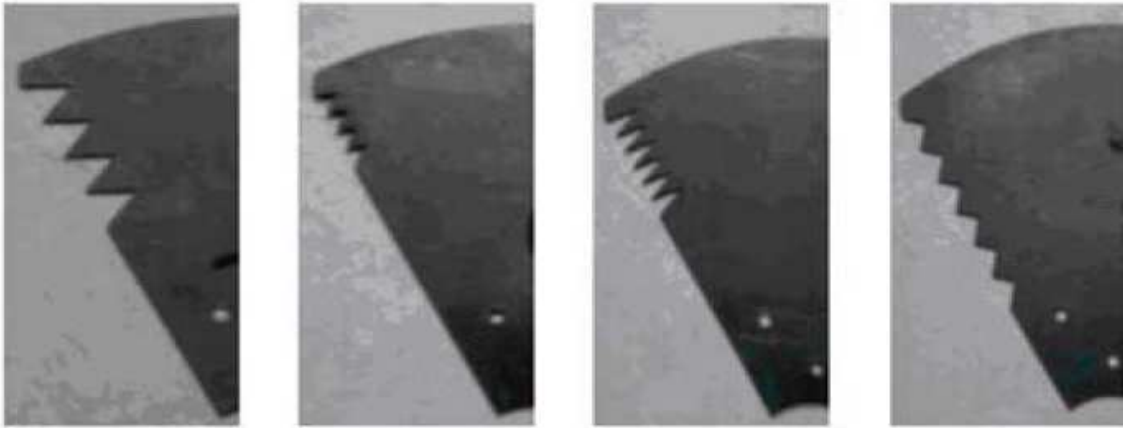


Figure 2.6: Serrated fan blades of Liang et al. (2010), showing their four leading edge configurations.

Dassen et al. (1996) performed acoustic experiments with different planforms and orientations of a saw-tooth trailing edge attached to a semi-infinite flat plate and a symmetrical NACA0012 airfoil. A schematic representation of each of their models investigated is shown in Figure 2.7. Each model contained a saw-tooth edge 50 mm long with tooth spacing of 5 mm. The most significant noise reduction was found to be above 5 dB for both the flat plate and airfoil containing a trailing edge in the same plane and parallel to the leading edge, depicted as their FP2 in Figure 2.7. Other configurations produced only a slight decrease in noise levels. A trailing edge fringe configured at an angle of 15 degrees with the chord (i.e. FP2_15) increased the sound level by 10 dB. However, each configuration did not decrease the performance of the models, regardless of the orientation, and had made slight improvements to the aerodynamic performance overall.

The experiments of Dassen et al. (1996) also deduced that the noise reductions obtained were not dependent on free stream velocity and are therefore Reynolds number independent. These findings were strongly agreed with by Herr (2006), who conducted

trailing edge experiments with flexible polypropylene fibres. Herr (2006) suggests that the reduction in noise is a result of viscous damping of unsteady turbulent eddies passing over the trailing edge.

Both the investigations of Dassen et al. (1996) and Liang et al. (2010) demonstrate the effects of owl technology in a practical sense. Although the experiments of Liang et al. (2010) do not report the Reynolds number, it is nonetheless evident that both investigations discovered that the principal phenomena of the technology are applicable to similar applications at high and low Reynolds numbers. An important aspect of the experiments of Dassen et al. (1996) and Liang et al. (2010) is that having either just a trailing edge fringe or leading edge comb would allow an understanding of the separate mechanisms of owl technology. If analysis were to be conducted with a combination of both the leading edge comb and trailing edge fringe, the separate mechanisms may not be as apparent. Hence, their findings provide a lead into this field of research.

It is apparent that achieving significant aerodynamic performance for a particular system relies purely on controlling the flow field effectively at the leading edge. Any modifications to the flow field at the trailing edge relates to improving the far-field noise characteristics of the system. It goes hand-in-hand that controlling the turbulence at the leading edge enhances the mitigation of noise propagation at the trailing edge. Hence, to achieve the latter, it is important to establish a complete understanding of the phenomenological aspects of the leading edge comb, in which the flow field can be precisely controlled for any given application.

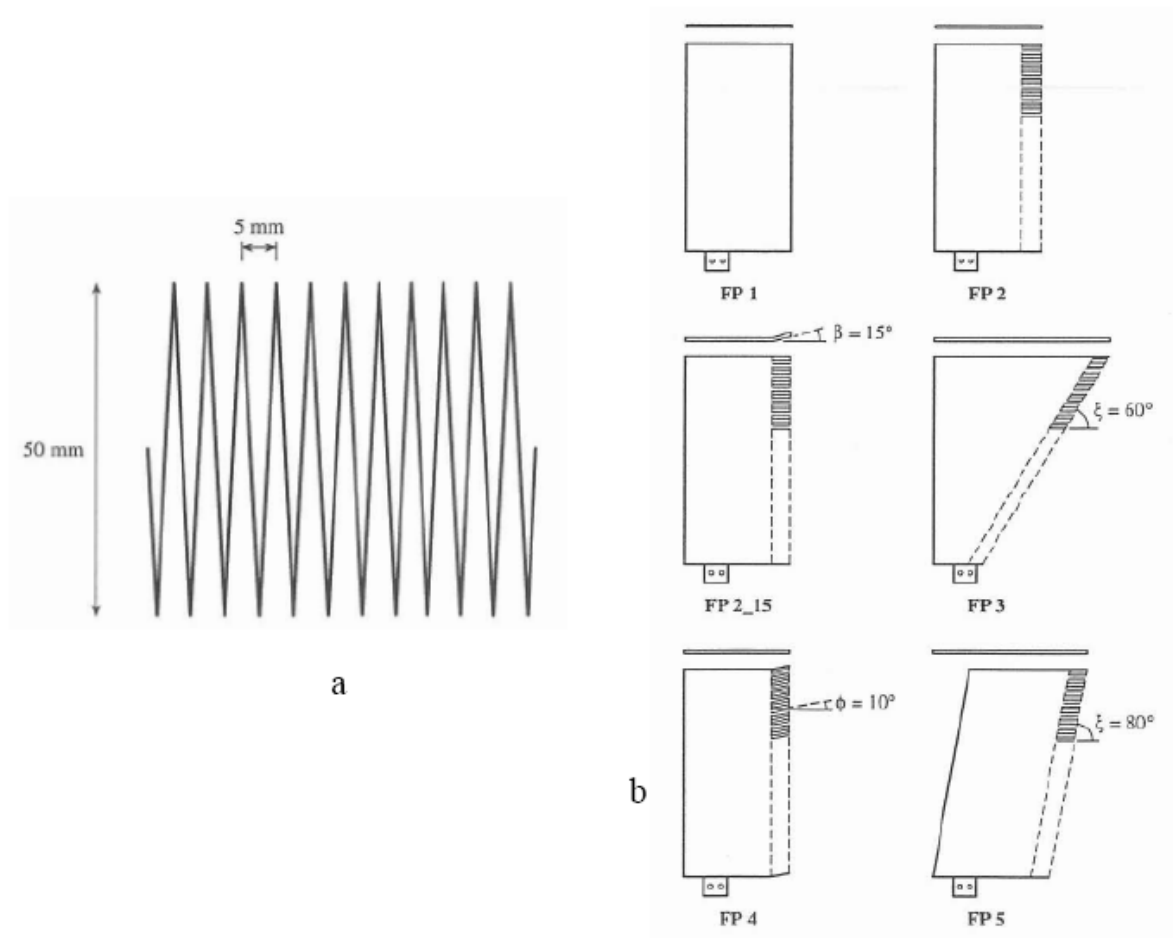


Figure 2.7: Serrated trailing edges showing (a) Saw-tooth schematic and (b) diagram of different saw-tooth configurations (Dassen et al. 1996).

2.4 The Spanwise Sinusoidal Profile (SSP)

Flow around a bluff body has drawn out significant interest due to its substantial practicality, i.e. flow around communication towers, oil rigs, support structures, buildings, and so on. The flow field in the wake behind a bluff body and the resulting transport of the vortical structures contain many significant and practical implications; examples include vortex-induced vibration and noise. Hence, to control the flow field around a bluff structure is quite an important concept. In addition, understanding the

phenomena that is associated with flow control so as to implement the concept onto the myriad of practical applications, will achieve a significant milestone in engineering. Of course, this cannot be realised without the use of biomimicry.

The leading edge comb can be simply represented by a spanwise sinusoidal profile (SSP) applied to the leading edge of a slender bluff body. An example of an SSP geometry is shown in Figure 2.8. In an analogous manner to the comb, an SSP can control the deleterious effects associated with turbulent flow and vortex shedding. To elucidate the mechanisms of the controlled flow arising from an SSP, a comprehensive description of the near wake topology of the vorticity field around square and rectangular cylinders with and without an SSP is researched.

The geometry of a spanwise sinusoidal profile is governed by two dimensionless parameters, namely a normalised wavelength, λ/D , and the wave steepness, ω/λ , where ω and λ are respectively the sinusoidal amplitude and wavelength (Darekar and Sherwin 2001). Hence, these two parameters represent the tooth length and tooth spacing of the leading edge comb, respectively. What will be demonstrated in following chapters is the dependency of the configuration of the flow that is present in the wake of an SSP on the values generated of ω/λ and λ/D . There may exist a dependence on the wavelength similar to the relationship deduced by Lilley (2009) in equation 2.2.1. Under turbulent flow conditions, a two-dimensional wake exists when maintaining λ/D constant and having low values of ω/λ ; hence there is no effect on the flow, and the wake remains essentially similar to a plain geometry. Increasing ω/λ obtains substantial spanwise incoherence in the wake. Hence, the modified flow field in the form of high three-dimensionality in the wake is said to be controlled flow. An intermittent wake is produced for values of ω/λ in between those associated with control and no control.

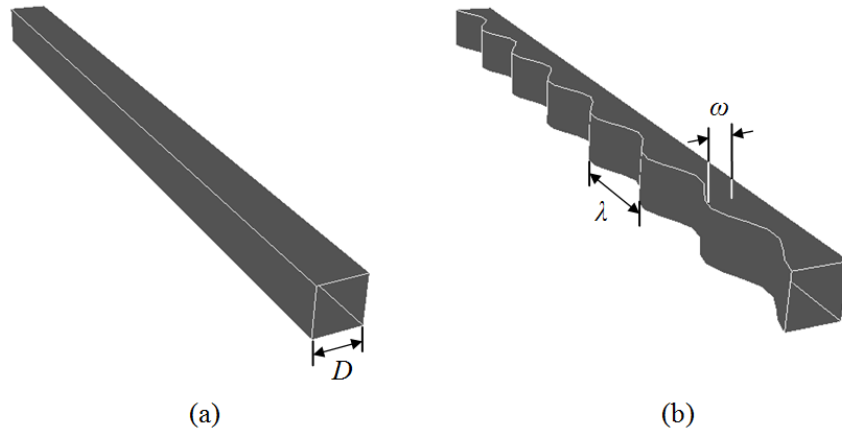


Figure 2.8: Model of (a) a plain square cylinder (slender bluff body) and (b) a square cylinder with an SSP applied to the leading edge.

In this research, several geometries of an SSP are studied that represent geometries that do not control, intermittently control, and highly control the flow field. The topology of the flow field is obtained by utilising numerical simulations to capture and extract the inherently transient features of the flow using a method called large eddy simulation (LES). This computational method is beneficial in aiding an understanding of the fluid-to-structure interactions associated with an SSP. It is believed that such details of the flow around SSP geometries have not hitherto reported in the literature. The mathematical and numerical models are discussed in detail in the next chapter. To demonstrate the effectiveness of the SSP, three contrasting levels of the SSP are presented and compared on square cylinder geometries. Secondly, the flow around slender rectangular geometries is presented as a basic representation of an owls' wing.

2.5 Summary

In this chapter, the mechanisms of owls' silent flight have been explored through a literature summary on the Barn Owl (*Tyto alba*) and Barred Owl (*Strix varia*). Firstly, the effects of a leading edge comb were investigated. This feature of the owl is located on all the primary flight feathers that behave as leading edges to the upstream flow. The main mechanism of the leading edge comb is to provide the wing with the effect of co-rotating vortex generators, which creates a surface vorticity field maintaining an attached boundary layer across the upper surface of the wing. As owls are known for flying in steep trajectories with a relatively low Reynolds number, the flow attachment stabilises an owl's flight. This stabilisation not only controls the owls' flight, but also minimises the energy of turbulence that approaches the trailing edge, therefore reducing scattered noise, and can significantly reduce drag and vortex-induced vibrations of bluff bodies.

Secondly, the trailing edge fringe of owls' feathers was investigated. Being located along all trailing edges of the primary and secondary feathers, this porous feature enhances the reduction of scattered noise by delaying the interaction between the upper and lower flows of the wing, preventing vortices from occurring and hence further preventing vortex shedding noise and vibration.

Several examples of the technology applied to aerodynamic models have been given, in order to facilitate an understanding of the effectiveness of the mechanism in controlling flow in a practical situation. These models included symmetric airfoils and semi-infinite flat plates, which demonstrated the possible application to bluff bodies. Specific details of the independent qualities of both the leading edge comb and trailing

edge fringe have been given, and these details suggest several avenues of future research.

The following chapters will explore the effectiveness of owl technology, through both a quantitative and qualitative investigation. Numerical analysis of a bio-inspired spanwise sinusoidal profile (SSP) that represents a leading edge comb applied to square and rectangular sections, will provide details of the phenomenal characteristics of owl technology. These findings will validate previous experimental observations, as well as provide new understandings of the fluid dynamics of owl technology.

THE COMPUTATIONAL AND MATHEMATICAL MODELS

The power of computer aided technology, particularly within computational fluid dynamics (CFD), has improved substantially over time. In early CFD days, the processing speeds of most computers limited numerical analysis to simple investigations. Now at present, processing speeds are seemingly limitless, and parallel computing opens the door to explore complex problems. The area of CFD is pushing the boundaries on the way fluid dynamics problems are able to be solved (Slagter 2011). With this in mind, it is not difficult to imagine the many exciting opportunities involving CFD. The field of fluid mechanics in aerodynamics and wind engineering can benefit greatly from this advancement in technology, as the power of CFD has allowed numerical modelling to be a more productive method than experimental analysis alone. The work in this thesis is purely numerical, containing verification against existing experimental data. Before describing the numerical setup, it is felt necessary to firstly discuss some background on numerical modelling, in order to establish the effectiveness of this methodology and the foundation for selecting this analytical approach.

Until the advent of readily available computer resources, the theory and application of fluid dynamics were quite limited. However, engineering resources are developing in a way that enables us to study physical phenomena, such as turbulence, in ever

increasing temporal and spatial detail. For example, in preceding times, both experimental and theoretical methodologies have widely been employed to explore fluid flow. Physical systems are easily represented by deriving and solving equations using a theoretical procedure, and these governing equations contain assumptions to provide results that have a valid description of the system. The phenomenon of turbulent flow however, contains governing equations that are coupled and multi-dimensional. Consequently, without sufficient resources, the analytical solutions to a theoretical approach can only be obtained for simple cases, limiting the possible case studies greatly.

Experiments have a broad scope, as the multi-dimensional nature of turbulent flow can be practically represented. By ensuring the measurements are recorded without difficulty and the physical conditions are accurately represented, this methodology can provide a complete description of the physical system. However, this is not always the case, for some systems, such as flow around complex bluff bodies, can be difficult to represent and the measurements must also be obtained in a way as to not interrupt the flow. Therefore, experimental procedures can be expensive, and some techniques may even provide solutions that are not sufficiently detailed (Shah and Ferziger 1997).

The ability of CFD to simulate fluid flow calculations and accurately interpret the physical system has allowed this methodology to become the new powerful tool in flow investigations. For a computational procedure, the theoretical governing equations are solved at discrete locations in both space and time. Hence, spatial and temporal discretisation is employed using approximate methods to approximate the system derivatives (Wilcox 1996). If a sufficient number of discrete points are defined while

setting up the problem, the solution can reach an accurate value that would otherwise be obtained if an analytical solution of the theoretical methodology is utilised.

Benefits of employing CFD to solve fluid flow problems include being able to obtain analytical solutions to time-dependent and multi-dimensional problems that have great practical significance. The governing equations for the flow represent the theoretical side of CFD, and the application of the numerical procedure and the solution validation represents the experimental side of CFD. Hence, utilising CFD surmounts the difficulties for the individual approaches discussed above. Provided that suitable initial conditions are chosen and boundary conditions are considered appropriately, the numerical model can closely represent a physical system. Virtual monitors can be placed at any location throughout the computational domain, eliminating any interference to the surrounding flow. Throughout computations, changes to the flow parameters can be made both before and during the analysis. CFD has benefits as a flow solving methodology, by providing an accurate representation of the flow conditions. Computational fluid dynamics is therefore, a suitable choice to consider when conducting research in fluid dynamics. Hence, it is the reason for choosing this methodology to conduct the work in this thesis.

Significant attention to detail is required when employing CFD, as a drawback of this methodology is the amount of care required to ensure the desired accuracy. For an approach to CFD, such as the study of flow around a bluff body, the designer should firstly consider the expected results that are to be obtained from the simulation. Keeping this in mind, the computational domain and its associated mesh must be created to acquire the desired results. One consideration is the domain to be designed in such a way to accommodate the flow adequately. The computational mesh should be refined in

the regions where steep gradients exist, for accurate approximations, and can be less refined in surrounding regions where accuracy is not greatly required (Saha *et al.* 2001). Steep gradients generally occur along wall surfaces. Secondly, the designer should consider the physics involved, which includes whether the flow is turbulent or laminar, incompressible or compressible. The dynamics are quite different for each problem; therefore, specific solvers are employed to solve a particular tailored problem (Tinoco, Lindqvist and Frid 2010). Such considerations are employed to generate the models throughout this study. For the work in this thesis, the flow is incompressible and turbulent.

At present, flow around a bluff body has elicited significant interest due to both its theoretical and practical importance. The turbulence that is formed in the wake behind the body and resulting transport of the turbulent structures contain many significant and practical implications. Turbulent flow contains irregular and unsteady three-dimensional eddies (currents) of varying sizes (Wilcox 1992). Essentially, the size of the large scale turbulent eddies is similar to the characteristic length scale, such as the leading edge height of the body. The smallest scales of turbulence can be several orders of magnitude smaller than their larger counterparts (Landahl and Mollo-Christensen 1992). The small scales are generally isotropic at higher flow velocities and acquiescent to modelling, whereas the large scales are generally anisotropic. In turbulent flows, the energy is transferred from the large scales to the smaller scales. The larger eddies interact and extract the energy from the mean flow. Therefore, the large turbulent scales depend on the geometry, the particular boundary conditions and loading forces that act on the geometry (the large scales are amenable). Hence, turbulent flow is dependent on the larger scales of motion, and in order to accurately resolve the turbulence scales, a solution to the governing equations is obtained with a numerical model.

The numerical model that solves the governing equations in such a way as to compute the larger turbulent eddies explicitly, while modelling the smaller scales, is known as the Large Eddy Simulation (LES) turbulence model. This turbulence model is well suited to wind engineering and aerodynamic studies, as the forces, moments and the fluctuations within turbulent flow are dependent on the large scales of transport (Shah and Ferziger 1997). In order to achieve the LES approach to the numerical treatment of turbulence, a spatial filtering operation is employed that separates the large and small eddies. The interactions between the large resolved scales and the smaller unresolved scales are determined through sub-grid scale (SGS) models. Through a finite volume method, the time-dependent and spatially filtered governing equations are solved across control volumes, including the equations to the SGS model that contains the unresolved sub-grid stresses.

Sufficient grid density and time-step sizing is essential for LES, consequently making the computing power expensive. Compared to LES, a Reynolds Averaged Navier-Stokes (RANS) turbulence model requires much less computing. However, a RANS model is not universal, and usually requires empirical adjustments to produce accurate results. RANS models are also not preferred for solving turbulent flows, as turbulence quantities are not modelled in this approach. A direct numerical simulation (DNS) can capture the smallest scales of turbulence. However, as the scales of motion decrease with increasing Reynolds number, DNS requires much finer meshing and time-steps than LES, as this approach does not employ SGS models. To minimise computing expense, DNS is limited to low Reynolds number flows, and therefore also limited when applied to practical problems. LES is a universal turbulence model and achieves reliable simulations of turbulent flow.

Through the advantages that CFD offers as compared to the more traditional methods of resolving fluid flow problems, such as experimental and theoretical approaches, it is clear that advances in the available tools are improving the pursuit of a common methodology. The computing requirements of LES are so expensive that simulations are limited to simple geometries (Kato and Ikegawa 1991; Lu *et al.* 1997a; Lu *et al.* 1997b; Jordan and Ragab 1998; Kravchenko and Moin 2000). Nevertheless, as LES resolves the larger scale turbulence, the numerical solution can provide detailed information regarding the physics of the flow surrounding a bluff body. Also, for the fundamental fluid study of spatial turbulent transition in the boundary layer, LES agrees well with both experiments and empirical laws for transitional flow (Xiyun and Guocan 2002).

In this chapter, the numerical model and procedure are discussed for simulating the flow around square and rectangular cylinders with and without the attachment of a passive control device on the leading edges. These geometries are a representation of the leading edge comb found on owls' wings. The passive control device is a spanwise periodic perturbation essentially containing the structure of a spanwise sinusoidal profile (SSP). The SSP in this study involves the modification of the leading edge in the form of a sinusoidal indentation. In the following, the computational domain is presented, and the boundary conditions and mesh generation are detailed. The numerical description for LES is provided, giving a detailed insight to this methodology. Reference to an experimental model is given within the numerical explanation, in order to provide details for establishing a close approximation to an experimental setup for model verification. Throughout this study, the computational fluid dynamics (CFD) code, FLUENT[®] is employed.

3.1 Numerical Description

The large scale turbulent structures are responsible for loading forces, moments and turbulent fluctuations, and momentum and energy are also obtained through the transport of large turbulent structures. Therefore, it is necessary to obtain flow details at this scale, in order to assist in understanding the fluid dynamics of the passive control application. The CFD code, FLUENT[®] has been used to perform the numerical simulations using large eddy simulation (LES) (ANSYS 2009). The decision to utilise the LES turbulence model is due to its ability to accurately resolve the large scale eddies present in the flow explicitly, while sufficiently modelling the small scale eddies (Shah and Ferziger 1997). This section will discuss the methodology behind the LES turbulence model and the subsequent choice for the supporting sub-grid scale models. Available knowledge in LES will be presented; however, the details will explain the relevance to the numerical model.

3.1.1 Mathematical Model

Throughout the numerical simulations, the flow is considered three-dimensional, unsteady and incompressible. The modelling of flow through the domain is governed by the fundamental equation of continuity, and three-dimensional Navier-Stokes equations of momentum for constant density and viscosity given as

- Continuity equation:

$$\frac{\partial u}{\partial x} + \frac{\partial v}{\partial y} + \frac{\partial w}{\partial z} = 0 \quad (3.1.1)$$

- Three-dimensional differential momentum equations:

$$\frac{du}{dt} = -\frac{1}{\rho} \frac{\partial p}{\partial x} + \nu \left(\frac{\partial^2 u}{\partial x^2} + \frac{\partial^2 u}{\partial y^2} + \frac{\partial^2 u}{\partial z^2} \right) \quad (3.1.2)$$

$$\frac{dv}{dt} = -\frac{1}{\rho} \frac{\partial p}{\partial y} + \nu \left(\frac{\partial^2 v}{\partial x^2} + \frac{\partial^2 v}{\partial y^2} + \frac{\partial^2 v}{\partial z^2} \right) \quad (3.1.3)$$

$$\frac{dw}{dt} = -\frac{1}{\rho} \frac{\partial p}{\partial z} + \nu \left(\frac{\partial^2 w}{\partial x^2} + \frac{\partial^2 w}{\partial y^2} + \frac{\partial^2 w}{\partial z^2} \right) \quad (3.1.4)$$

In equations 3.1.1 to 3.1.4, the variables u , v and w are the Cartesian x , y and z velocity components, respectively. The variable ρ is the fluid density, p is the fluid pressure and t represents time. It should be noted that the term for gravitational force is not included in the momentum equations.

In the numerical treatment of turbulence for LES, a spatial filtering function is applied to the time-dependent incompressible Navier-Stokes equations, in order to separate the large and small structures. The filtered momentum equations explicitly resolve the large scale turbulence, while the small scale turbulent structures are modelled (Shah and Ferziger 1997; Versteeg and Malalasekera 2007; Wilcox 1993). This spatial filtering process selects the minimum filter size of the large scale turbulent structures equivalent to the minimum grid size within the computational mesh. Hence, the large scale structures are resolved on the length scale of the mesh. The filtering operation neglects turbulent scales that are smaller than the mesh size while resolving the remaining larger scales. Hence, it is necessary to define a relatively fine

computational grid near regions of steep gradients, such as a wall, when employing the turbulence model.

Information related to the filtered smaller scales is not considered through the spatial filtering algorithm. Therefore, the interaction effects between the larger resolved turbulent scales and smaller unresolved scales introduce sub-grid scale stresses, which effect on the resolved flow is determined through a sub-grid scale (SGS) model (Versteeg and Malalasekera 2007). It is usually typical for a turbulence model to contain numerical uncertainty and error, as more scales are modelled rather than solved. Reynolds averaged Navier-Stokes (RANS) models are widely applied in practical situations because they make modest demands on computer resources. However, when phenomena are averaged there is an inevitable loss of information. An advantage of LES is that it retains important temporal details of the flow. The filtering process is as follows.

- Filtering function:

$$G(\mathbf{x}, \mathbf{x}') = \frac{1}{\Delta^3} \quad (3.1.5)$$

where: $\Delta = \sqrt[3]{\Delta x \Delta y \Delta z}$ is the cube root of the grid cell volume.

hence: $\Delta^3 = V_C$ is the grid cell volume. (3.1.6)

For finite volume discretisation in LES, equation 3.1.5 is called a box filter and is the preferred method for spatial filtering (Wilcox 1993). This is a simple form of spatial

filtering functions and is typical for three-dimensional simulations of LES. The limits of the box filtering function states

- Box filter limits:

$$G(x, x', \Delta) = \begin{cases} 1/V_c & |x - x'| \leq \frac{\Delta}{2} \\ 0 & |x - x'| > \frac{\Delta}{2} \end{cases} \quad (3.1.7)$$

The box filter function provides the definition to the spatial discretisation and separates the resolvable scales from the sub-grid scales. The filtering operation then defines the governing equations for the resolvable scales.

- Filtering operation:

$$\bar{\Phi}(x) = \frac{1}{V_c} \int_v \Phi(x') dx', \quad x' \in v \quad (3.1.8)$$

where: $\Phi(x')$ is a given unfiltered flow variable.

In equation 3.1.8, the time dependent flow variables are spatially filtered and solved across control volumes, v , in the computational domain. The overbar denotes a filtered variable. The spatial filtering operation is linearly three-dimensional. It can be assumed that the filter function, G , is constant and independent of the grid position. This allows commutation of the filtering and differentiation for both temporal and spatial discretisation (Krajnovic and Davidson 2002). Bearing in mind this uniform filter

function, simplifies the algebra when solving for the filtered momentum equations for homogeneous flow. Applying equation 3.1.8, the generic form of the filtered momentum equations is given.

- Filtered incompressible Navier-Stokes equations:

$$\frac{\partial \bar{u}_i}{\partial t} = -\frac{1}{\rho} \left(\frac{\partial \bar{p}}{\partial x_i} + \frac{\partial \bar{\tau}_{ij}}{\partial x_j} \right) - \frac{\partial \bar{u}_i \bar{u}_j}{\partial x_j} + \frac{\partial}{\partial x_j} \left(\nu \frac{\partial \bar{\sigma}_{ij}}{\partial x_j} \right) \quad (3.1.10)$$

$$\text{where:} \quad \bar{\sigma}_{ij} \equiv \left[\mu \left(\frac{\partial \bar{u}_i}{\partial x_j} + \frac{\partial \bar{u}_j}{\partial x_i} \right) \right] - \frac{2}{3} \mu \cdot \delta_{ij} \frac{\partial \bar{u}_l}{\partial x_l} \quad (3.1.11a)$$

$$\bar{\tau}_{ij} \equiv \rho \overline{u_i u_j} - \rho \bar{u}_i \bar{u}_j \quad (3.1.11b)$$

- Filtered incompressible continuity equation:

$$\frac{\partial \bar{u}_i}{\partial x_i} = 0 \quad (3.1.12)$$

Applying the filter function, G , to a given flow variable, Φ , in the Navier-Stokes equations, introduces the additional stress tensors. These are the stress due to molecular viscosity, $\bar{\sigma}_{ij}$, and sub-grid scale stress, $\bar{\tau}_{ij}$, given in equation 3.1.11. In equations 3.1.9 through to 3.1.12, i and j can assume the values 1, 2, and 3.

As a result of the interactions between the sub-grid scale turbulences, $\bar{\tau}_{ij}$ is responsible for the convective momentum transport (Wilcox 1993). If a flow variable, $\Phi(x)$, is considered as the sum of a filtered variable resolved by the LES, $\bar{\Phi}(x)$, and a sub-grid scale variable containing spatial variations, $\Phi'(x)$, it can be determined that

the sub-grid scale stresses of LES contain additional contributions to the small scale turbulence. Hence, equation 3.1.11b can be expressed as

- SGS stress:

$$\bar{\tau}_{ij} = \rho \overline{u_i u_j} - \rho \bar{u}_i \bar{u}_j = \rho \left((\overline{u_i u_j} - \bar{u}_i \bar{u}_j) + \overline{u_i u'_j} + \overline{u'_i u_j} + \overline{u'_i u'_j} \right) \quad (3.1.13)$$

such that:

$$\begin{aligned} \rho \overline{u_i u_j} &= \rho \overline{(\bar{u}_i + u'_i)(\bar{u}_j + u'_j)} = \rho (\overline{u_i u_j} + \overline{u_i u'_j} + \overline{u'_i u_j} + \overline{u'_i u'_j}) \\ &= \rho (\bar{u}_i \bar{u}_j + (\overline{u_i u_j} - \bar{u}_i \bar{u}_j) + \overline{u_i u'_j} + \overline{u'_i u_j} + \overline{u'_i u'_j}) \end{aligned}$$

where:

$$\rho (\overline{u_i u_j} - \bar{u}_i \bar{u}_j) = L_{ij} \quad (3.1.14a)$$

$$\rho (\overline{u_i u'_j} + \overline{u'_i u_j}) = C_{ij} \quad (3.1.14b)$$

$$\rho \overline{u'_i u'_j} = R_{ij} \quad (3.1.14c)$$

In equation 3.1.14, the additional contributions to the sub-grid scale turbulent stresses are, the Leonard stress, L_{ij} , the cross-term stress, C_{ij} , and the LES sub-grid scale Reynolds stress, R_{ij} . The Leonard stress is due to the resolved scales and is implicitly represented at moderate Reynolds number for a second-order finite volume method of computation. The cross-term stress is due to the interactions between the large resolved structures and the sub-grid scale structures, and the Reynolds stress is due to the convective momentum transport.

Solving for the sub-grid scale stresses, equation 3.1.13 requires modelling. For this reason, sub-grid scale (SGS) turbulence models are employed in conjunction to the LES. Each of these models utilises a Boussinesq eddy-viscosity approximation to resolve the stress components. This hypothesis states that the turbulent stresses are proportional to the mean rate of strain. The relationship would hold true if the turbulent stresses remain isotropic. Hence, due to the isotropic nature of the sub-grid scales, the local sub-grid scale stresses of equation 3.1.13 can be considered proportional to the local rate of strain (Xiyun and Guocan 2002; Krajnovic and Davidson 2002; Versteeg and Malalasekera 2007). The sub-grid scale turbulence model is given as

- Sub-grid scale turbulence model:

$$\bar{\tau}_{ij} - \frac{1}{3}\tau_{kk}\delta_{ij} = -2\mu_t\bar{S}_{ij} \quad (3.1.15)$$

$$\text{if:} \quad i = j, \delta_{ij} = 1 \quad ; \quad i \neq j, \delta_{ij} = 0$$

$$\text{where:} \quad \bar{S}_{ij} \equiv \frac{1}{2} \left(\frac{\partial \bar{u}_i}{\partial x_j} + \frac{\partial \bar{u}_j}{\partial x_i} \right) \quad (3.1.16)$$

The variables δ_{ij} and τ_{kk} , represent the terms for filtered static pressure, and the isotropic component of the sub-grid scale stresses, respectively. These two terms are grouped together with the Reynolds stresses for the LES. In equations 3.1.15 and 3.1.16, the variable \bar{S}_{ij} , is the local rate of strain tensor of the resolved flow. There are four distinctive classes of sub-grid scale turbulence models available in LES. In addition to solving for the stresses, the turbulence models are applied primarily to resolve the

turbulent sub-grid scale viscosity, μ_t . For the purpose of the numerical simulations in this study, the Smagorinsky-Lilley SGS turbulence model was chosen. This model is the most basic of the available turbulence models within LES and models the SGS turbulent viscosity given the equation below.

- Smagorinsky-Lilley SGS turbulence model:

$$\mu_t = \rho L_s^2 |\bar{s}| \quad (3.1.17)$$

$$\text{where:} \quad |\bar{s}| \equiv \sqrt{2 \bar{s}_{ij} \bar{s}_{ij}} \quad (3.1.18a)$$

$$L_s^2 = \min(\kappa d, C_s V_c^{1/3}) \quad (3.1.18b)$$

The definition provided herein is essentially resolving the sub-grid scale stresses by defining them to the resolved scales of the fluid dynamics. In the Smagorinsky-Lilley definition, L_s , is the characteristic mixing length of the sub-grid scales, and C_s is the Smagorinsky constant. The variables κ and d represent the von Kármán constant and the distance to the cylinder surface, respectively. Equation 3.1.17 essentially determines the SGS turbulent kinematic viscosity based on a local equilibrium between the transport of turbulent sub-grid scale energy and the transmission of this energy. A fixed value for the Smagorinsky constant, C_s , equal to 0.1 (Liang and Papadakis 2007; Lam and Lin 2008; Sohankar 2008; Lam *et al.* 2010) was used to determine the turbulent viscosity. Deardorff (1970) and Breuer (1998) determined this value of the Smagorinsky constant provides the best results when large scale fluctuations in the

transitional flow exist near wall boundaries, as well as containing shear flow fluctuations.

Applying a higher order dynamic SGS model will result in the value of C_s fluctuating with the given instantaneous resolved scales. This approach can lead to numerical instability, as C_s can increase in value to a maximum of 0.23. In contrast, compared to the chosen value of C_s , a small increase to 0.17 introduces significant damping of the fluctuations mentioned above. In order to increase the numerical throughput, it is considered suitable to avoid additional requirements, such as dynamic sub-computations. Due to the transient conditions of the current numerical simulations in this work, the choice for the Smagorinsky constant is appropriate.

3.1.2 LES Boundary Conditions

Specifying the inlet boundary conditions in FLUENT[®] is straight forward with the large eddy simulation turbulence model. To obtain additional knowledge of the flow conditions occurring when being obstructed by a bluff body, especially with the SSP, it is desirable to maintain minimal levels of turbulence at the inlet conditions. This ensures that only the obstructions to the flow create the turbulence and that the fluid-structure interactions are revealed clearly.

The experimental setup of Dobre *et al.* (2006) contained less than 0.5% streamwise turbulence intensity and less than 0.3% cross-stream turbulence intensity. As a steady velocity inlet boundary condition is established for the upstream boundary of the computational domain, a *No Perturbations* option is selected in the LES at this boundary, in order to set negligible turbulence. The employment of this boundary condition sets the instantaneous velocity components equal to the mean velocity at the

inlet location. This provides the foundation for obtaining the correct fluid-to-structure interactions, and is a similar approach to that of Krajnovic and Davidson (2002). Therefore, neglecting the turbulence at the inlet during the simulations ensured a comparative model setup between the experimental and numerical investigations.

As will be discussed in Section 3.3, the lateral boundaries are assigned as symmetry boundary conditions, in order to assume a virtual infinite cylinder span. Hence, the symmetry surfaces are treated as *slip* surfaces to give zero flux such that

$$\frac{\partial u}{\partial z} = \frac{\partial v}{\partial z} = w = 0 \quad (3.1.19)$$

For the pressure outlet boundary condition specified for the downstream boundary, a zero gradient condition is implemented for the mean flow, U_0 , and convective conditions are applied to extrapolate the fluctuating properties. Hence, the outflow conditions are such that

$$\frac{\partial u_i}{\partial t} + U_0 \frac{\partial u_i}{\partial x} = 0 \quad (3.1.20)$$

The fluid-structure interactions are quantitatively studied within the near wall boundary layers throughout this research. Therefore, as the filtered Navier-Stokes equations are to be integrated to the wall, a *no-slip* boundary condition is applied to the geometry walls during the LES. This generally requires fine near wall grids with $y^+ \leq 1$. As the free-stream flow throughout this study contains moderate to high Reynolds number, it is feasible to employ a wall function (Versteeg and Malalasekera 2007). The application of a wall function is discussed in Section 3.3.1.

3.2 Computational Domain

When creating a computational domain for simulating flow around a bluff body, considerations are required to ensure that the boundaries of the domain are not too close to the body. It is important to allow the free-stream flow to travel through the domain and around the bluff body without added effects from surrounding domain boundaries or walls. These added effects are known as ‘blockage effects’. Taking this into consideration for the current models, an example of the full computational domain for the numerical simulations in this study is presented in the left of Figure 3.1(a). The resulting computational mesh is shown in the right of Figure 3.1(a). The domain is similar to that used by Saha *et al.* (2003), Shah and Ferziger (1997) and Krajnovic and Davidson (2002), as it ensures sufficient space for the downstream wake development, as well as minimising any blockage effects due to the top and bottom boundaries in the vertical y -direction. Taking the height of the body as D , measured in meters, the domain extends from the center of the body a distance of $7D$ both upstream and along the vertical y -direction, and a distance of $15D$ downstream. Hence, the overall dimensions of the numerical domain are a length of 0.704 m, width of 0.224 m and a height of 0.448 m.

To represent a basic model of an owl’s wing and the leading edge comb, models of both square and rectangular cylinders with a leading edge height, D , of 0.032 m are considered for numerical analyses. The square models are similar to the experimental models of Dobre *et al.* (2006). These models are a plain square cylinder (for reference comparisons) and three additional models, each with a different configuration of the spanwise sinusoidal profile (SSP) applied to the leading edge (LE). The SSP in this study involves a sinusoidal indentation applied to the leading edge. Similar to Dobre *et*

al. (2006), the three SSP configurations are referred to as $W1$, $W2$ and $W3$ containing peak-to-peak sinusoidal amplitudes, ω , of 2, 8 and 15 mm, respectively. $W0$ refers to the plain reference square cylinder. The reason for selecting such parameters is discussed in detail in a following chapter. The numerical models of $W0$ and $W3$ are presented in Figure 3.2, in order to demonstrate the plain reference square cylinder in Figure 3.2(a), and the resulting square cylinder with the SSP in Figure 3.2(b), respectively. The parameters, the peak-to-peak amplitude, ω , and spanwise wavelength, λ , indicated in Figure 3.2, are the two key parameters in this study for designing the passive control. These parameters are also discussed in following chapters.

The numerical models studied in this work were generated using DesignModeler[®] to develop the geometries with alternating configurations of the SSP. The meshing of the computational domain was performed Using GAMBIT[®]. Both DesignModeler[®] and GAMBIT[®] are computer aided design (CAD) softwares, which are effective for creating basic three-dimensional models. In order to create the sinusoidal leading edge for each model, the process adapted was the ‘bottom-up’ technique. This technique required the least amount of effort to generate the models, allowing rapid development and modifications. Primarily, nodes are distributed across the three-dimensional field at the locations of the minimum and maximum of the leading edge sine function. Additional nodes are placed across the field at the locations of all intersections and points of interest throughout the computational domain. Essentially, the nodes are placed in order to represent the model shown in Figure 3.1(a). Therefore, the remaining process for the bottom-up technique required connecting all nodes to create the edges (lines) of the domain. The edges are then grouped to form faces (surfaces), and then the volumes for the domain are formed similarly by grouping the faces. Once creating all the domain volumes, Boolean operations are employed to subtract the volume of the cylinder from

the surrounding volumes (Modelling and Meshing Guide 2009). The surrounding volumes are then grouped and assigned as the fluid domain. To model the square cylinder as a hollow section and define only the cylinder walls eliminates the need to assign both solid and fluid interfaces for the simulations. This process reduces the computational demand, as only a fluid interface is required to be interpreted. Considering the computational domain as a rectangular prism, as shown in Figure 3.1(a), allows the boundary conditions to be simply applied to the six outer faces.

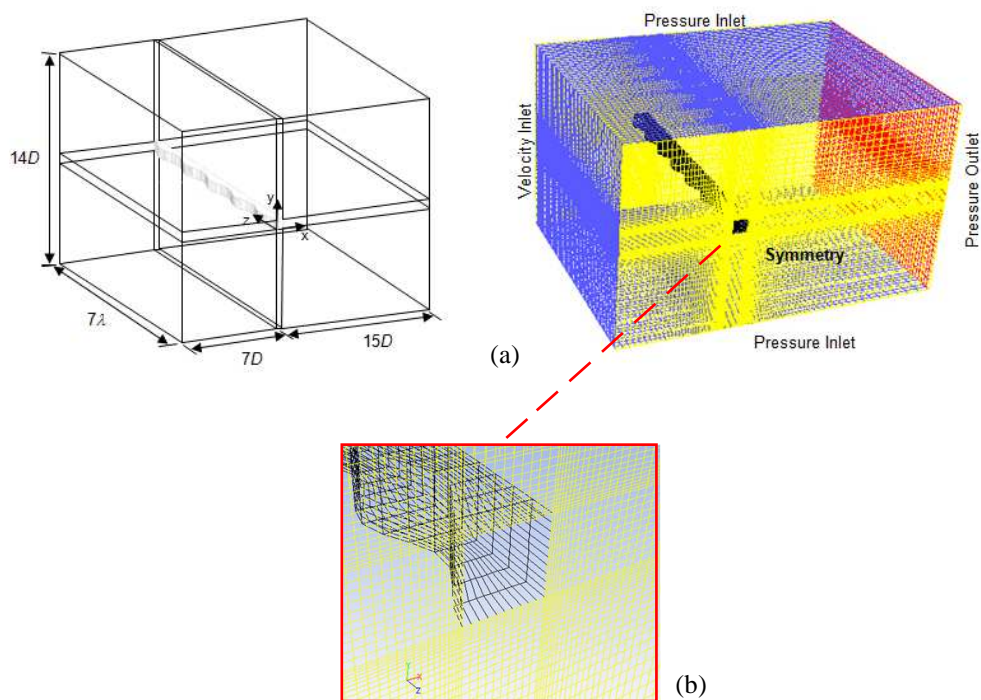


Figure 3.1: Computational domain showing (a) domain schematic (left) and boundary conditions with computational mesh (right) and (b) Enlarged view illustrating the fine mesh adjacent to the cylinder.

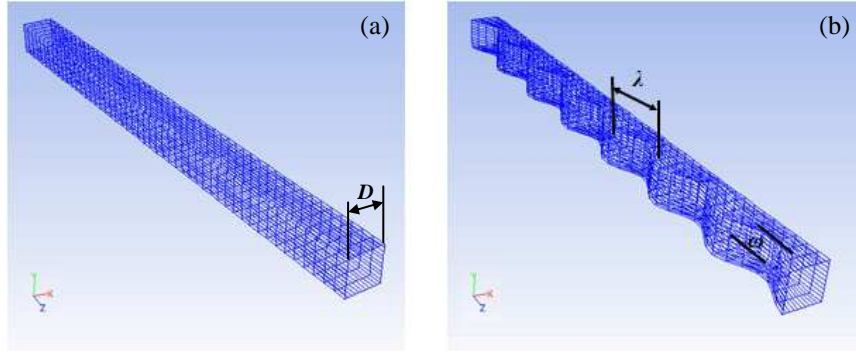


Figure 3.2: Computational model of (a) reference square cylinder ($W0$) and (b) square cylinder with an SSP applied ($W3$).

In Figure 3.3, the experimental setup of Dobre *et al.* (2006) is given, showing the top view of their wind tunnel model attached to side end plates at a fixed span of 14λ , in Figure 3.3(a). There was no control methods reported for the end effects created by the side end plates. Therefore, in order to neglect this factor in the numerical model, symmetry boundaries are applied to the ends of the numerical square cylinder. The application of symmetry boundaries allows the numerical model to have an infinite virtual span, removing any side wall blockage effects. Free-stream velocity, U_o , in both the numerical and experimental models is from left to right along the positive x -direction. As the leading edge is directed left (upstream, negative x -direction), the downstream amplitude of the SSP is referred as a peak and the upstream amplitude referred as a valley. This definition will be used throughout this study. This is demonstrated in Figure 3.3(b). The spanwise wavelength, λ , of the SSP is initially fixed at a value of 76.8 mm for each configuration, also shown in Figure 3.3(a). This value is later varied to research the effects of both ω and λ , and discussed in following chapters. Therefore, $W1$, $W2$ and $W3$ contain steepness ratios, ω/λ , of 0.026, 0.104 and 0.195, respectively. Details regarding the selection of these parameters are given in Chapter 4.

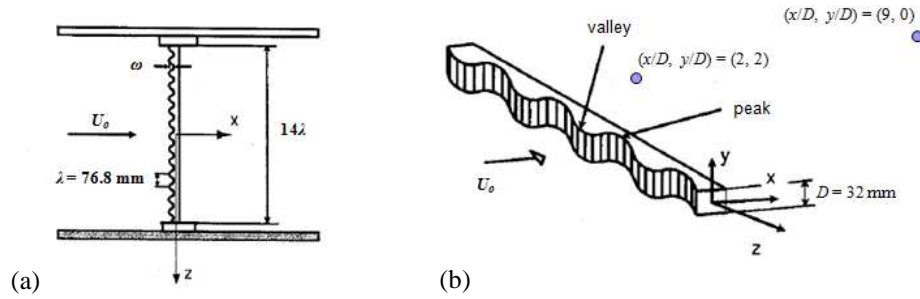


Figure 3.3: Experimental setup of Dobre *et al.* (2006) showing (a) top view of the wind tunnel section and (b) square cylinder model showing near and intermediate wake measurement points.

3.2.1 Boundary Conditions

In order to establish correct observations, one consideration required when creating the numerical model is the careful application of boundary conditions. Thought has to be given for the type of flow being studied, and more importantly, the expected results that are to be obtained. The selection of boundary conditions is ideally based on physical and practical conditions, in which effects from external sources exist. These external sources can include turbulence intensities, pressure gradients and temperature changes. A numerical simulation operates under ideal conditions where external sources can either remain constant or are negligible. Therefore, in order to account for the practicality of the solution, factors are placed on the boundary conditions. Although the numerical model presented in this study is not complex in nature, it is three-dimensional and must closely represent the conditions of an experimental model. The flow is to be driven and directed across the computational domain similar to a wind tunnel test section. Hence, the boundary conditions are set to ensure this effect.

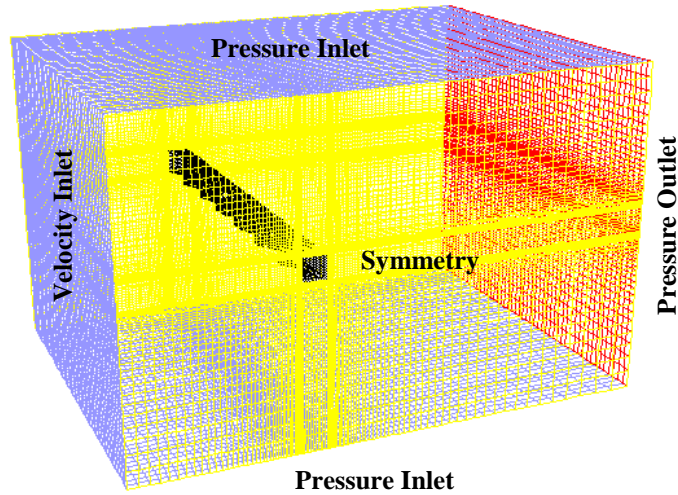


Figure 3.4: Computational domain indicating the boundary conditions.

The boundary upstream from the leading edge of the cylinder is assigned a velocity inlet boundary condition, shown in Figure 3.4, as well as Figure 3.1(a). The value of the free-stream velocity was set at a fixed value of $U_o = 11 \text{ ms}^{-1}$. This corresponds to a Reynolds number based on the cylinder height, Re , of 2.35×10^4 . The definition for Reynolds number used throughout this work is

$$Re = \frac{U_o D}{\nu} \quad (3.2.1)$$

where, ν is the kinematic viscosity of air. This inlet condition is equivalent to the experimental inlet condition of Dobre *et al.* (2006). While the free-stream flow is force driven, the flow still requires being pressure driven along the domain, in order to remain streamwise along the positive x -direction. Therefore, to direct the flow as needed, both the top and bottom boundaries of the computational domain were assigned a pressure inlet boundary condition, and the downstream boundary from the cylinder was assigned

a pressure outlet boundary condition. These details are shown in Figure 3.4, showing the inlet and outlet boundaries represented by the blue and red surfaces, respectively.

One method to reduce the computational requirements of the simulations is to have a computational domain that is small as possible. The computed span of the cylinder models in this study is chosen to be 7λ . This span corresponds to half the span of 14λ in the experimental models used by Dobre *et al.* (2006), and contains sufficient length of the SSP to conduct accurate analysis. In order to prevent spanwise wall effects, the vertical end planes, shown in Figures 3.4 and 3.1(a) as yellow surfaces, were treated as symmetry boundaries. Hence, as discussed above, the model contains axial symmetry along the horizontal z -direction, eliminating wall effects by assuming a virtual infinite span beyond the symmetry boundaries. In addition, Shan *et al.* (2008) investigated flow controls for an airfoil using similar symmetry boundary conditions and a spanwise domain length of only $0.1c$, where c is the chord length of the geometry.

Another method to reduce the computational requirements of the simulations is modelling the square cylinder as a hollow structure and not as a solid. This was briefly discussed in Section 3.2, and shown in Figure 3.5. As the flow travels around the cylinder and not inside the cylinder, it is not necessary to model the cylinder internally. This consideration assists in minimising the grid elements within the domain for faster simulations, as only a fluid interface is imported into the numerical software, and less computational memory is required. In later chapters, numerical experiments are conducted for different geometries of the SSP, including geometries with a rectangular (elongated) cross-section. The generation of these additional computational models follow a similar approach towards the details discussed in this chapter.

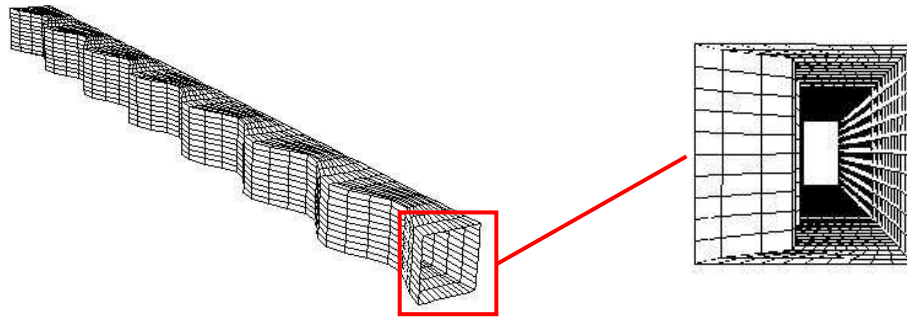


Figure 3.5: Computational model of the square cylinder, $W3$, indicating the hollow cross-section to minimise grid elements.

3.3 Model Verification and Mesh Generation

Having established the governing mathematical equations and their boundary conditions, they must be solved. In this section, the methodology employed to obtain a numerical solution is discussed. As the small scale turbulence is modelled throughout the numerical analysis, the computational domain can contain a larger overall grid size, therefore reducing the computational requirements (Shah & Ferziger 1997). However, employing the LES turbulence model still requires a relatively fine mesh to solve the filtered Navier-Stokes equations. The filtering operation allows the flow scales larger than the grid sizing to be resolved. For this reason, a balance must be established to ensure the computational grid remains fine enough to resolve a large quantity of flow scales and still maintain minimal modelling expense.

3.3.1 Sizing Function and Near Wall Region

To obtain an accurate result using limited computing resources requires a judicious approach to meshing the computational domain. In order to develop a fine mesh while

still aiming to reduce the computational costs, the mesh was generated with a high density of grid elements where the gradients are steep (geometry surface) and a lower density elsewhere. A function referred as a sizing function is applied to the mesh in order to construct the grid of the computational domain. The sizing function allows a concentration of grid elements adjacent to the geometry wall and a consistent growth in the spacing between elements moving in a direction away from the wall. Hence, the computational grid can begin with a very fine mesh at the surface, which then grows coarser gradually with distance. The computational mesh near the surface of the geometries allows the results to capture and measure the flow details accurately to the wall. The detail of the sizing function is shown in Figure 3.6, indicating the meshed region surrounding the square cylinder of $W3$ and the uniform mesh growth away from the cylinder.

Near solid surfaces where velocity gradients are steep, the flow field must be highly resolved. The near wall region shown in Figure 3.1(b) is meshed utilising a boundary layer technique. In the boundary layer technique, a structured quadrilateral mesh that is six layers in depth is placed around the geometry. This is shown in Figure 3.7. Each layer has a growth factor of 1.1 with a size limit of 1, and an initial layer height of 0.001 m. This initial layer height of 0.001 m is sufficiently small to capture details of the flow, and corresponds to 3% of the cylinder height, D , in agreement with the initial cell height of Sohankar *et al.* (2000). Hence, the boundary layer mesh controls the growth factor of the sizing function, while ensuring the LES can resolve the near wall features. The growth of the sizing function was chosen such that the near mesh downstream of the geometry is fine enough to also measure the near wake data. Similarly, the upstream mesh ensures no disturbance to the steady free-stream flow impacting the leading edge of the geometry.

To allow the mesh to expand uniformly in all directions normal to the surface of the geometries, four meshed faces were generated in each symmetry boundary, located perpendicular to the front, upper, back and lower surfaces of the geometry. These four faces form the cross pattern within the symmetry planes that are depicted in Figure 3.6, and identified as faces 1, 2, 3 and 4. The sizing function exists along the edges of these faces, extending from the geometry surface. Therefore, as can be seen in Figure 3.6, a high concentration of grid elements exists around the geometry to the normal directly above and below, as well as directly upstream and downstream of the geometry.

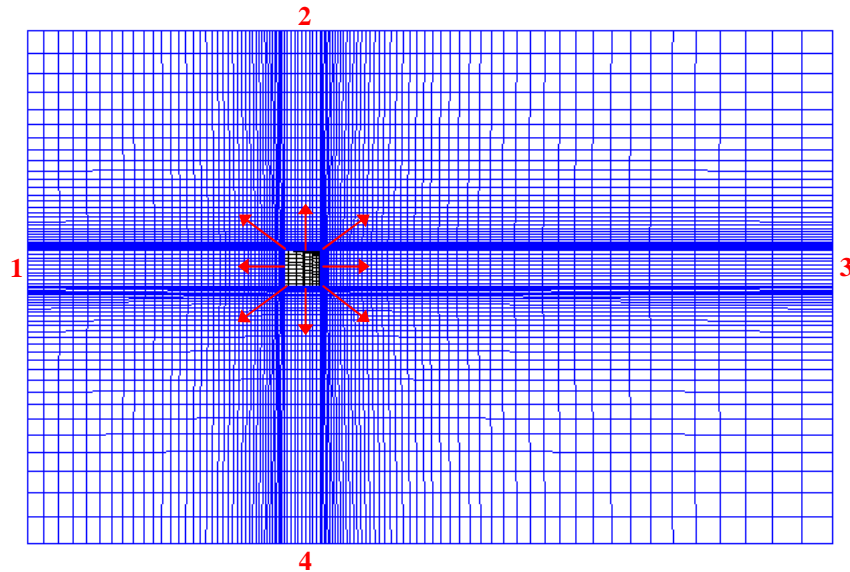


Figure 3.6: Symmetry boundary grid showing the uniform mesh expansion away from the geometry surface as a result of the sizing function.

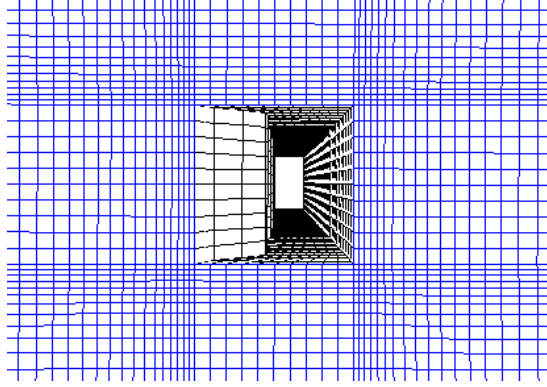


Figure 3.7: Enlarged view of the symmetry boundary plane showing the boundary layer mesh surrounding the square cylinder, W3.

Three sub-layers exist within the flow most adjacent to the geometry wall, which form the inner region of the boundary layer. The log-linear relationship between these three boundary layer sub-layers is shown in Figure 3.8 (ANSYS 2009). The mean velocity at the near wall region can be expressed in a form that is independent of the Reynolds number and geometry in the case where the velocity and distance from the wall are normalised by the wall shear stress. Defined as the non-dimensional distance to the wall, proportional to the friction velocity along the geometry surface, the wall y^+ characterises the law-of-the-wall. As the boundary layer governs the parameters of the sizing function and the near wall region is of particular interest in this work, the value of y^+ must be checked.

Closest to the cylinder wall is the laminar viscous sub-layer ($y^+ < 5$). This law is indicated by the curved linear function in Figure 3.8, and in this sub-layer the non-dimensional velocity, u^+ , is equal to y^+ for incompressible flow. Turbulent motions are considered negligible in this region. The second sub-layer is a transitional layer or buffer layer ($5 < y^+ < 30$) between the laminar viscous sub-layer and third inertial turbulent sub-layer. In this layer, identified as the logarithmic function in Figure 3.8, the

molecular viscosity and turbulence are equally important. The inertial sub-layer is formally known as the log-law-of-the-wall region ($30 < y^+ < 200$). In this outer logarithmic region, the flow is fully turbulent and viscous effects are negligible. Calculating the friction velocity throughout the simulations, the average value of wall y^+ is between 11 and 16 for the configurations W0 to W3. According to the theory on boundary layer flow over a smooth flat plate, this means that the value of y^+ corresponds to the buffer layer. The definition is given below.

- Wall y^+ definition:

$$y^+ \equiv \frac{u_\tau y}{\nu} \quad (3.3.1)$$

$$\text{where:} \quad u_\tau = \left(\frac{\tau_w}{\rho} \right)^{\frac{1}{2}} \quad (3.3.2)$$

In equation 3.3.1, y is the distance between the wall and adjacent cell centroid, and u_τ is the friction velocity at the wall. The variable τ_w is the wall shear stress. The relationship for the velocity profile within the near wall region is given in equation 3.3.3. The near wall velocity profile is equivalent for typical turbulent flow near a wall, and any profile variation is mostly due to low Reynolds number. At higher Reynolds numbers, the velocity profile will remain constant in the law-of-the-wall and buffer layer regions up until approximately y^+ of 500. Beyond the logarithmic region, the velocity profile resembles that of free shear flow (White 2003).

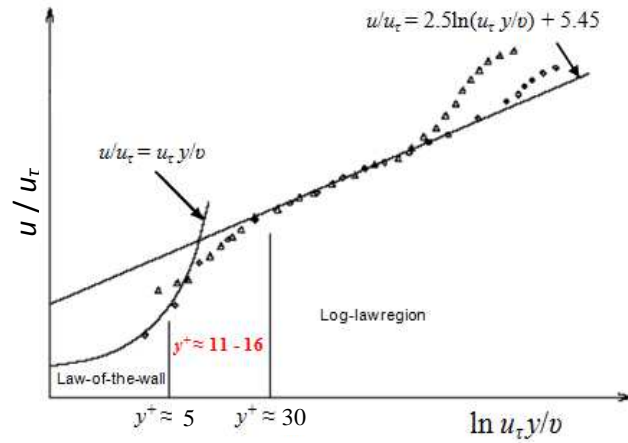


Figure 3.8: Semi-log representation of the near wall region showing y^+ within the buffer layer, between the law-of-the-wall and log-law regions (ANSYS 2009).

- Near wall velocity profile:

$$u^+ = \frac{u}{u_\tau} = \begin{cases} y^+, & y^+ < 5 \\ \frac{1}{\kappa} \ln y^+ + b, & 30 < y^+ < 500 \end{cases} \quad (3.3.3)$$

where: $\kappa \cong 0.4$; $b \cong 5.45$

As y^+ for the geometries in this research is within the buffer layer ($y^+ \approx 11$ to 16), a wall function needs to be applied, in order to blend the law-of-the-wall and log-law regions. An enhanced wall function in FLUENT[®] relates u^+ to y^+ as given below.

- Law of the wall blending function:

$$\Gamma = -\frac{0.01(y^+)^4}{1+5y^+} \quad (3.3.4)$$

- Enhanced wall function:

$$u^+ = e^{\Gamma} u_{lam}^+ + e^{\frac{1}{\Gamma}} u_{turb}^+ \quad (3.3.5)$$

The purpose of this enhanced wall function is to create a link between the viscosity dependent region and the fully turbulent region of the boundary sub-layers (Moin 2002; Catalano *et al.* 2003). Hence, as the computational mesh is fine enough to resolve the boundary layer; it is not fine enough to resolve the flow all the way within the viscous sub-layer. Resolving the boundary layer all the way to the cylinder surface would require a very fine mesh. This would create significant computational demand. Therefore, applying the wall function provides the LES turbulence model with an accurate description of the velocity profile within the wall adjacent sub-layer. The depiction from the wall function is dependent on the correct behaviour of y^+ values within the buffer layer (ANSYS 2009). For this reason, the correct application of the boundary layer technique and sizing function is essential. In equation 3.3.5, u_{lam}^+ and u_{turb}^+ are the non-dimensional velocities within the laminar law-of-the-wall ($y^+ < 5$) and turbulent log-law-of-the-wall ($y^+ > 30$) regions, respectively.

3.3.2 Grid and Time Step Independence

Performing extensive CFD simulations to solve turbulent flow problems, it is important to establish the validity of the numerical model, in order to determine the numerical error from the turbulence model (LES) error (Wilcox 1993). A common way to establish model validity is to perform both grid and time step independence checks. In this section, the independence checks have been performed for the 3D LES with a constant Reynolds number based on the geometry height, Re , of 2.35×10^4 . The

maximum absolute lift coefficient, C_l , mean drag coefficient, \bar{C}_d , and mean of the streamwise velocity fluctuations, \bar{u} , are observed. It is to be noted that the study was conducted only for the plain square cylinder, $W0$. The coefficients of lift and drag are defined in Equations 3.3.6 and 3.3.7, where F_l and F_d are the fluid forces.

- Coefficients of lift and drag:

$$C_l = \frac{F_l}{0.5\rho U_0^2 D} \quad (3.3.6)$$

$$C_d = \frac{F_d}{0.5\rho U_0^2 D} \quad (3.3.7)$$

For the grid independence check, three grid sizes were considered, containing 1.73×10^5 , 2.54×10^5 and 3.45×10^5 elements. The computational observations are presented in Table 3.1. The results show that suitable convergence is obtained for the flow solutions as there is no significant impact on the simulation results with different number of elements, where the largest differences are 2.9%, 0.5% and 2.02% for C_l , \bar{C}_d and \bar{u} , respectively. Hence, a grid size of 3.45×10^5 elements is chosen with confidence for the simulations conducted in this thesis. This corresponds to approximately 10 elements per sinusoidal wave in the spanwise direction.

The form of the computational grid for all models in this study is a structured hexahedron mesh. The commutation of the filtering operation as discussed in Section 3.1.1 is essentially valid with temporal and spatial discretisation for uniform computational grids (Xiyun and Guocan 2002). It should be noted that the chosen grid size is near the maximum allowable grid size that can be facilitated with the available computer resources. Krajnovic and Davidson (2002) performed LES for flow around a

square cube with a very coarse computational grid containing only approximately 2.7×10^5 elements. They found that applying simple inlet boundary conditions with a coarse mesh and one-equation SGS model produced accurate results in close agreement to experimental observations.

To check for time step independence, using the chosen grid size, the 3D LES were conducted for two time step sizes, dt , of 1×10^{-4} s and 1×10^{-5} s. The observations for the maximum absolute lift coefficient, C_l , mean drag coefficient, \bar{C}_d , and mean of the streamwise velocity fluctuations, \bar{u} , are presented in Table 3.2. There is no significant affect on the numerical results with different time step size, as the largest differences are 2.14%, 0.08% and 1.51% for C_l , \bar{C}_d and \bar{u} , respectively. Hence, a time step size, dt , of 1×10^{-4} s is chosen. However, both time step sizes used in the independence check are required to achieve proper solution convergence of the LES. This is discussed in Section 3.3.3. Further validations of the current numerical results are presented in following chapters.

Table 3.1: Grid independence check for a plain square cylinder at $Re = 2.35 \times 10^4$.

Total Number of Cells	Absolute C_l	Mean \bar{C}_d	\bar{u} [ms^{-1}]
1.73×10^5	2.025	2.406	14.06
2.54×10^5	2.037	2.415	14.28
3.45×10^5	2.085	2.418	14.35

Table 3.2: Time step independence check for a plain square cylinder at $Re = 2.35 \times 10^4$.

Time Step Size [s]	Absolute C_l	Mean \bar{C}_d	\bar{u} [ms^{-1}]
1×10^{-4}	2.076	2.416	14.217
1×10^{-5}	2.105	2.418	14.434

3.3.3 Solution Convergence

A fine computational grid and sufficiently small time step are key requirements to ensure the computations can resolve the unsteady momentum and energy equations, and accurately capture the flow phenomena. This requirement, along with the grid density, results in an extensive computing time. All CFD simulations need a considerable numerical accuracy, while also considering the demand on computing resources (Roache 1990). One method of determining the numerical accuracy is by monitoring the solution iterations for convergence. The convergence is evaluated based on the difference between the current iterate solution and the exact solution to the flow differential equations. However, computations that involve turbulence modelling are more irregular and essentially slower to achieve iteration convergence, due to the complex nature of these computations. Hence, turbulence models require more precise convergence criteria.

Wilcox (1993) has shown that the actual solution error for simulations involving turbulence can be measured as the difference between the exact solution to the discretised equations and the numerical solution at the current iteration. This approach demonstrates that the actual solution error is larger than the difference between successive iterations. Hence, for a turbulence model containing slow rate of convergence, the iteration convergence is achieved if sufficiently small difference exists between iterates.

In this sub-section the methodology for determining and maintaining convergence when utilising LES is discussed. As LES requires sufficiently high computational demand, therefore slower rate of convergence, it is desirable to establish an approximation of the flow field on which an LES solution can be based, and improve

the computational rate. If the solution to a time-dependent flow problem is dependent on the initial conditions, it is essential to accurately indicate the initial conditions that have been established from other sources (Versteeg and Malalasekera 2007).

In order to obtain initial conditions before commencing the LES simulations, an approximation of the flow field was achieved by modelling a steady-state flow field using a Standard $k\epsilon$ (SKE) turbulence model. The SKE turbulence model is a semi-empirical; two-equation Reynolds averaged Navier Stokes (RANS) formulation. It is based on the transport equations for the turbulent kinetic energy, k , and the turbulent energy dissipation rate, ϵ . Therefore, in this way an initial flow field was established. For the purpose of brevity, only brief explanation is given regarding the employment of the SKE turbulence model, however the details given are suitable for addressing the procedure.

The solution for the SKE simulations of the initial flow field in this work converges at approximately 2000 iterations. This is achieved firstly by implementing an enhanced wall treatment during the SKE simulations. Similar to the enhanced wall function discussed in Section 3.3.1, the wall treatment formulates the laws-of-the-wall as one wall law for the RANS solution (ANSYS 2009; Moin 2002). This procedure is accurate and suitable to increase the rate of initial convergence for the reasonably high Reynolds number flow utilised in this study. Secondly, to resolve the pressure-velocity coupling, the SIMPLE pressure-based segregated algorithm is employed. This algorithm maintains the continuity equation simply by approximating the pressure-velocity corrections through a correction of the face flux in each computational cell. For the spatial discretisation of the momentum and energy equations, a second-order upwind scheme is employed, which provides sufficient accuracy for obtaining the initial flow

field. The SKE turbulence model is not time dependent, being run at a steady state, therefore FLUENT[®] calculates the flow field based on an explicit iterative process to be accurate within defined error bounds. To assess the iteration convergence, the lift coefficient, drag coefficient and streamwise velocity are monitored for reaching a steady state.

Having achieved convergence through the Standard – $k\varepsilon$ turbulence model, the instantaneous velocity field provides the initial conditions. LES is intrinsically unsteady (transient) and the formulation of spatial derivatives is implicitly second-order. For the LES turbulence model, the spatial discretisation scheme utilised for the convection of momentum and energy is a bounded central-differencing scheme of second-order accuracy (Krajnovic and Davidson 2002; Xiyun and Guocan 2002). Applying a central-differencing scheme is found to provide better agreement with experimental data. A bounded central-differencing scheme interpolates the cell center scalar values accurately for calculating the face scalars required for convection terms.

Initially, the time-step selected for the LES was 1×10^{-5} s. Convergence for this turbulence model with the computational considerations explained in this chapter is achieved at approximately 0.1 s of simulation run time. As FLUENT[®] employs an iterative time advancement solution method, convergence for the first 0.1 s is determined based on the number of iterations required per time-step. As discussed above, obtaining sufficiently small difference between successive iterates minimises the number of iterations required per time-step. A schematic representing the iterative process of the LES simulations is provided in Figure 3.9. Within the solver, the maximum number of iterations per time-step can be set, in order to not exceed a certain limit of calculations. The maximum allowable iterations throughout the simulations are

set to 50. The reason for this choice is based on convergence criteria for FLUENT[®] (ANSYS 2009). Solution convergence is also assessed based on statistically completing the flow residence time. The residence time is defined as the ratio between the characteristic length of the computational field, L , and the free-stream velocity, U_0 . The first 0.1 s of the simulation corresponds to approximately double the flow residence time.

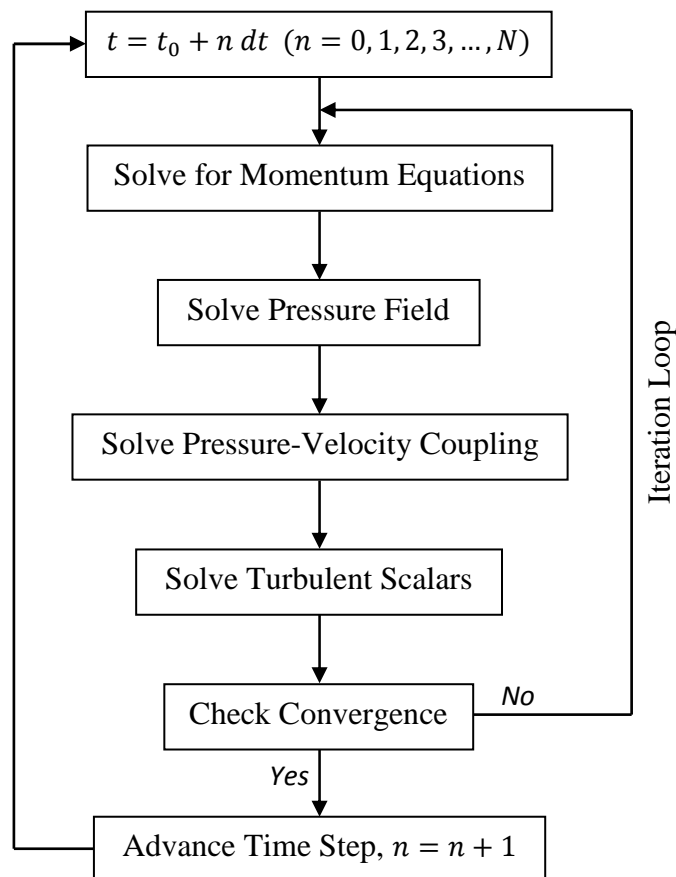


Figure 3.9: Schematic of the iterative time advancement solution method in FLUENT[®].

When selecting the time-step, the maximum simulated iterations should not exceed 10. If exceeded, the time-step should be made smaller, as the solution is not accurate enough and hence, not reaching convergence due to the large difference between iterates (Wilcox 1993). If the simulated iterations remain less than 10, the time-step chosen is adequate and the solution can be considered converged. The number of simulated iterations for the first 0.1 seconds is 2 iterations.

As the time-step can be increased if less than 10 iterations are required per time-step, the time-step is made 1×10^{-4} s for the remaining time of the simulations. However, before adjusting the time-step, the initial flow statistics are made the new initial conditions. For this larger time-step, the maximum number of simulated iterations per time step remained 9 iterations. It is to be noted that several expensive simulations were conducted, in order to determine the correct selection for the time-step size.

The data is considered to become statistically steady in FLUENT[®] once achieving a total simulation run time equal to a considerable multiple of the mean flow residence time. The value of mean flow residence time for the models developed in this study is approximately 0.064 s. Therefore, due to this theoretical residence time being small, it is considered appropriate to average the time statistics over a substantial simulation run time. Hence, the large eddy simulations are considered complete when achieving a total simulation time no less than approximately 2 s.

This overall process for convergence and time-step choice improves the performance of the simulations, while still ensuring suitable accuracy is obtained within the solution. The methodology is similar to that of Xiyun & Guocan (2002) in obtaining faster convergence for LES. Convergence was checked throughout this research by monitoring the number of iterations required per time-step and through monitoring the

solution residuals. Global convergence is ensured through mesh independence checks when creating the numerical models.

3.4 Comparisons in the Wake of Square SSP Cylinders

It is essential that the numerical model developed in this research generates results that accurately reflect reality. Hence, the model is validated by replicating the experimental conditions reported by Dobre *et al.* (2006). Comparisons are made of the computed and experimentally observed power spectral densities (PSDs) of the flow fields in the near and intermediate wakes produced by bluff bodies with and without SSPs. The model is also validated against published drag forces and streamwise turbulence intensities.

The characteristics of power spectral densities generated by bluff bodies are excellent indication of the degree of flow control. This arises because the absence of a dominant frequency in the wake is congruent with small fluctuations in the aerodynamic forces. Furthermore, the lack of a dominant frequency is associated with a reduction in the drag force.

3.4.1 Model Comparisons in the Near Wake

PSDs in the near wakes generated by square cylinders with and without spanwise sinusoidal profiles (SSPs) were measured and analysed by Dobre *et al.* (2006). Their monitoring point was located at $(x/D, y/D) = (2, 2)$ as indicated in Figure 3.10. The monitor location in the near wake corresponds to the border of the formation region of the streamwise Kármán vortices and was determined to have qualitative similarities at both low and high Reynolds numbers (Dobre *et al.* 2006). In the case of a square cylinder with a plain leading edge, $W0$, the monitoring point was located in a vertical

plane co-planar with the mid-span, as shown in Figure 3.10(a). In the cases of square cylinders on which SSPs are imposed on the leading edge, cases $W1$, $W2$ and $W3$, Dobre *et al.* (2006) located the near wake monitoring points downstream of the central peak and valley as indicated in Figure 3.10(b).

Power spectral densities (PSD) of the v -velocity fluctuations are presented in Figure 3.11. The numerical results compare very well with the experimental observations. Both numerical and experimental observations show larger reductions in velocity fluctuations co-planar with a valley, shown in green for the numerical data and the lower black spectra for the experimental data. The computed results agree clearly with those of the experiments, demonstrating the effectiveness of the SSP as steepness ratio increases from $W0$ to $W3$, as indicated by the decreasing magnitude of the fundamental harmonic in Figures 3.11(a) to 3.11(d). In Figure 3.11(a), both experimental and numerical PSD of the reference square cylinder, $W0$, indicate a fundamental harmonic at approximately 47 Hz, corresponding to the vortex shedding frequency, f_{vo} . Therefore, the Strouhal number, St , defined in Equation 3.4.1 for the square cylinder at a Reynolds number of 2.35×10^4 is 0.14. Recall that D is the cylinder height, and U_0 is the free-stream velocity.

$$St = \frac{f_{vo}D}{U_0} \quad (3.4.1)$$

A Strouhal number of 0.14 is in good agreement with typical values of St for a square cross-section (Blevins 2009). The Strouhal number is a non-dimensional parameter that relates the free-stream velocity to the vortex shedding frequency caused by the blockage of a body. Hence, the Strouhal number is also dependent on the

characteristic length of the body. In this case, it is the square cylinder height, D . The presence of a second harmonic in Figures 3.11(a), 3.11(b) and 3.11(c) indicates some radial asymmetry of the vortices in the near wake, corresponding to $W0$, $W1$ and $W2$, respectively (Dobre *et al.* 2006). Both spectral peaks are suppressed for $W3$ in Figure 3.11(d).

The v -velocity spectra for both experimental and numerical results follow the negative $5/3$ slope corresponding to the well known Kolmogorov's law (Wilcox 1993). This region of local isotropy is indicated by the straight black and red lines above the experimental and numerical spectra, respectively. This law was formulated through a dimensional analysis, in order to derive the energy distribution in a turbulent flow. The formulation of the energy spectrum relates the wave number, k , to the turbulent energy dissipation rate, ε , such that

$$E(k) = C \varepsilon^{2/3} k^{-5/3} \quad (3.4.2)$$

where, C is a constant with a value approximately equal to 1. The wave number, k , can be considered a frequency component of the local mean velocity, \bar{U} . Hence, as can be seen in Figure 3.11, Kolmogorov's law states that the turbulent kinetic energy decreases along a negative $5/3$ slope with frequency (or wave number).

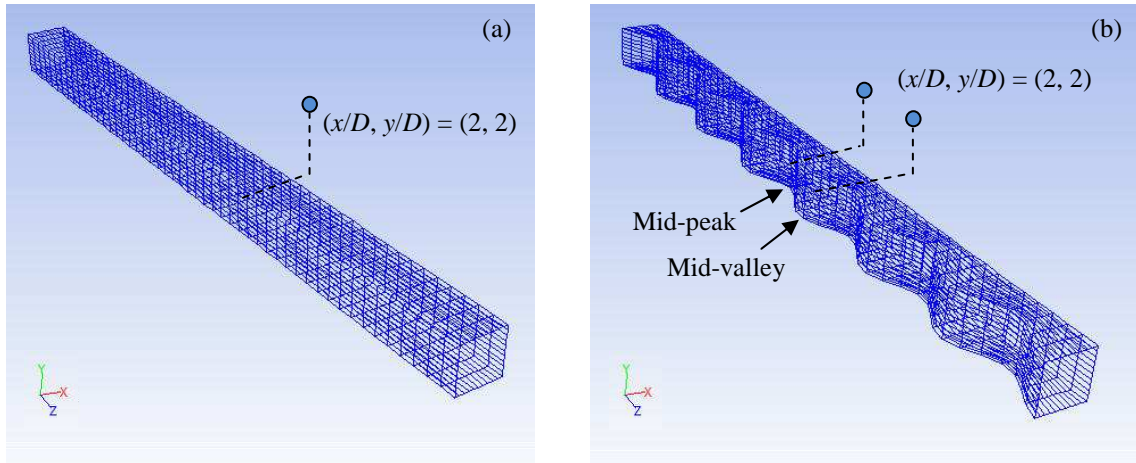


Figure 3.10: Square cylinder model showing the measurement points in the near wake; (a) $W0$; (b) $W3$.

The resolution of the power spectral densities between the numerical and experimental observations is different. However, this is due to the difference in sampling rates between the two comparisons. An order of magnitude difference exists between the two data sets; nevertheless, the effects of applying an SSP to represent the leading edge comb are clearly observed. As discussed earlier, considerations are required to obtain efficient computations, while ensuring the important flow details are still being captured. Consequently, it is shown in this section that the key flow characteristics are clearly observed, with close agreement between the numerical and experimental cases. In addition, finer detail is captured in the numerical observations, depicted in the numerical spectra of Figure 3.11 by the spectral content that appears below the distribution. The LES is sensitive to the finer small scale turbulences that are present within the flow as a result of the sub-grid scale turbulence. This close agreement corroborates the suitability of the LES turbulence model for analysing the adjacent flow field and near wake of the SSP models in this research.

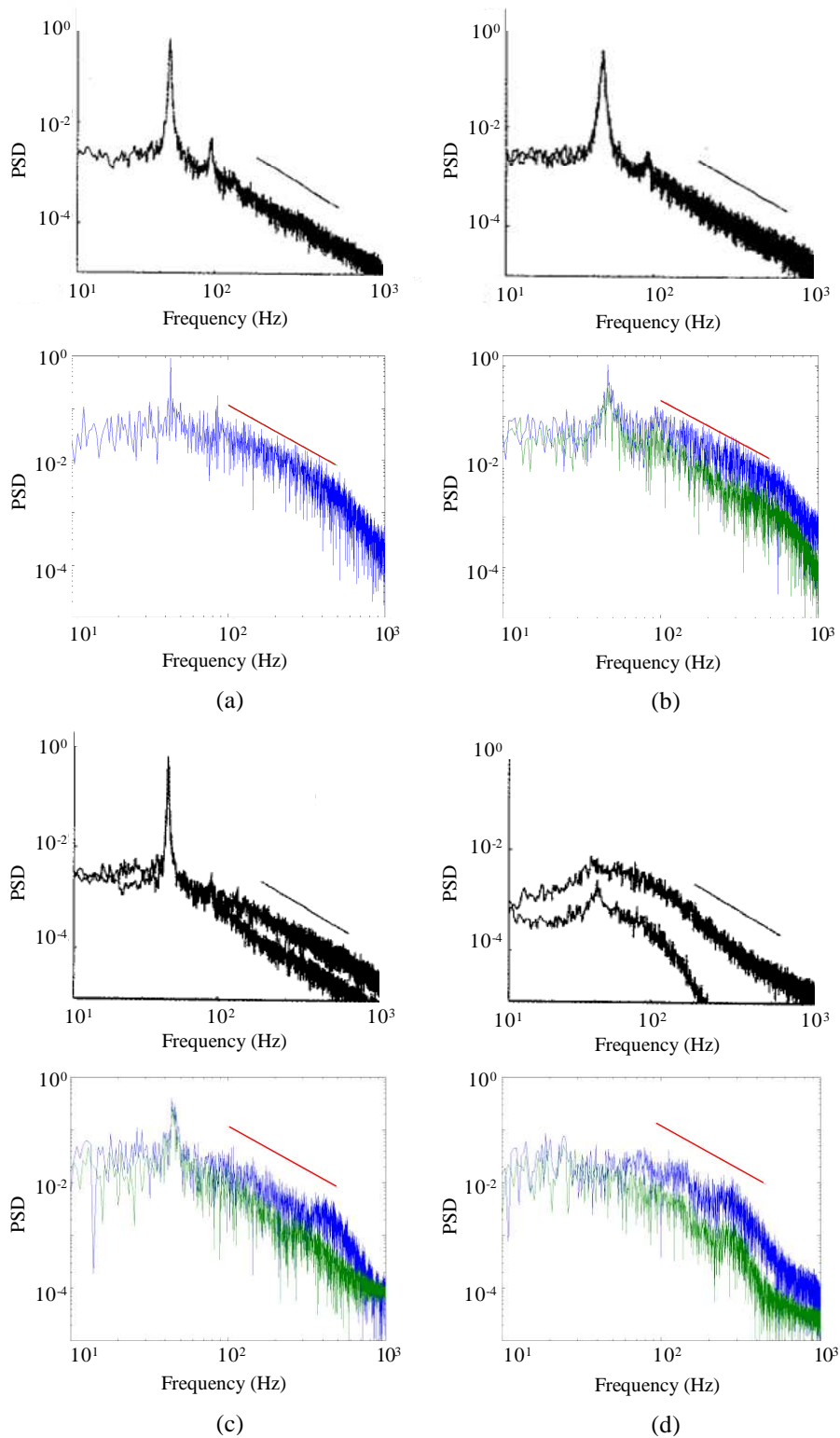


Figure 3.11: Comparisons of numerical and experimental (top, —, Dobre *et al.* (2006)) PSD of the v -component velocity spectra at peak (—) and valley (—) locations measured at $(x/D, y/D) = (2, 2)$ for (a) W0, (b) W1, (c) W2 and (d) W3.

3.4.2 Model Comparisons in the Intermediate Wake

It is essential that numerical models are validated against experiments. In this work, the validation is achieved by comparing flow observations in the posterior direction to the leading edge. Although the discussion throughout this research focuses within the boundary layer and near wake regions, verification in these regions is just one check to determining the validation of the numerical technique. In order to obtain an additional validation, comparisons between numerical and experimental observations within the intermediate wake are discussed in this section.

Experimental measurements were carried out by Dobre *et al.* (2006) in the intermediate wake corresponding to a downstream location of $(x/D, y/D) = (9, 0)$. The monitor location in the intermediate wake was chosen to measure and determine the rate of vorticity decay downstream of the square cylinder (Dobre *et al.* 2006). Spanwise (z -direction) homogeneity between the peak and valley planes occurs both experimentally and numerically at this location. Hence, the data collected at the central peak is discussed, for brevity. Furthermore, comparisons in the intermediate wake are provided only between $W0$ and $W3$, as the PSD in Section 3.4.1 showed the best contrast of the frequency spectra for these two square cylinders.

The power spectral densities of the u and v -velocity fluctuations in the intermediate wake between the experimental observations of Dobre *et al.* (2006) and the current numerical results are presented in Figure 3.12(a) for $W0$ and Figure 3.12(b) for $W3$. The spectral distribution of the u -velocity fluctuations are represented in blue, and the v -velocity fluctuations are represented in green. The red and black lines above the distributions correspond to the $-5/3$ Kolmogorov's law discussed in Section 3.4.1.

Minor discrepancies exist between the experimental and numerical comparisons; however, the principal features of the flow are captured. It is important to note the large distance between the monitoring point and the trailing edge. In Figure 3.12(b), it can be seen that the re-emergence of a fundamental peak appears in the intermediate wake of $W3$. This occurs for the numerical observations at a lower frequency than that of the experimental observations, corresponding to approximately $1/2f_{vo}$. As the computational grid is coarse in the intermediate wake region, it can be speculated that the LES was unable to capture the true frequency of velocity fluctuations at the measurement location. However, it is depicted in Figure 3.12(a) that for $W0$ the fundamental peak occurs at the vortex shedding frequency of approximately 47 Hz. Hence, the LES is indeed capable of capturing the correct features of the flow within the coarse mesh region. Grid independence studies have been discussed in Section 3.3.2. The reason for the frequency shift from the natural shedding frequency is not completely understood. Nevertheless, the occurrence of the peak is due to the interaction between the top and bottom shear layers. An interaction of this form is expected within the region defined as the intermediate wake, as a restructuring of the von Kármán vortices will develop at approximately the location of the measuring point (Dobre *et al.* 2006).

The fundamental peak for $W3$ indicates significant three-dimensionality within the wake, due to the broad nature of the spectral peak. A sharp spectral peak, as in Figure 3.12(a) for $W0$, demonstrates a clearly organised two-dimensional structure. The definition of a two-dimensional wake is that it contains only structures that are streamwise and normal to the flow (i.e. variables in the x and y -directions); a broad spectral peak indicates the presence of a weakened structure due to three-dimensional interactions (i.e. flow in the x , y and z -directions). In this work, two-dimensional flow is referred as uncontrolled flow, and three-dimensional flow is referred as controlled flow.

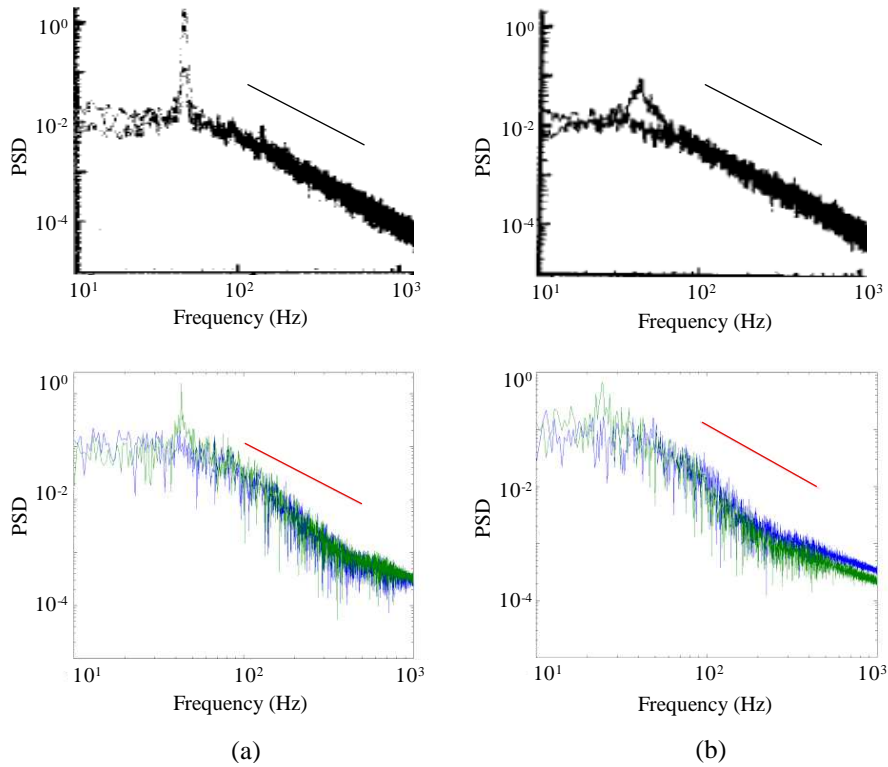


Figure 3.12: Comparisons of numerical and experimental (top, —, Dobre *et al.* (2006)) PSD of the u -component (—) and v -component (—) velocity spectra at the mid-peak location measured at $(x/D, y/D) = (9, 0)$ for (a) $W0$ and (b) $W3$.

In the experimental observations, the reduction in magnitude of the fundamental peak for $W3$ in Figure 3.12(b) as compared to $W0$ is an indication of the lower energy of the vortices (Dobre *et al.* 2006). This is also evident in the PSD generated for the numerical data. This confirms that the numerical data captures the relevant flow structures that are also evident in the experimental data, and provides further confidence in the accuracy of the numerical model.

The reason for the apparent lower energy of the vortices and flow three-dimensionality in the intermediate wake of $W3$ is due to interactions between primary and secondary vortex structures occurring for $W0$ (Dobre and Hangan 2004; Dobre *et*

al. 2006). These structures are the spanwise Kármán vortices and streamwise interconnecting ribs, respectively.

3.4.3 Characteristic Comparisons of Aerodynamic Forces

Comparisons of the drag coefficient, C_d , and streamwise turbulence intensity, u/\bar{U} , provide an additional avenue for comparing experimental and numerical data, in order to obtain a validation of the numerical model. The numerical data obtained in this study for the coefficient of drag, C_d , are provided in Table 3.3. Comparisons are made between the current numerical data at $Re = 2.35 \times 10^4$ and the reported numerical data of Darekar and Sherwin (2001) at $Re = 100$. The data in Table 3.3 agree well; they indicate that average values of C_d decrease with increasing wave steepness. However, the reduction in drag becomes significant only for large wave steepness. For example, in the current numerical results between the configurations *W1* and *W2* a decrease of only 12.2% exists with ω/λ of 0.026 and 0.105, respectively. The decrease in drag is 9.6% in the published data.

Reductions in C_d of up to 30% are recorded in previous works when applying the SSP with a wave steepness, ω/λ , in excess of 0.09 (Bearman and Owen 1998; Dobre *et al.* 2006). The present numerical results agree well with these observations; a wave steepness, ω/λ , equal to 0.195, corresponding to *W3* causes a reduction in C_d of 33.3% from the drag force of the reference square cylinder. This is a significant improvement in drag reduction once introducing large wave steepness, and in good agreement with previous works. As an additional verification of the current numerical model, a comparison of C_d is made with the reported data of Sohankar *et al.* (2000). They performed LES using a Smagorinsky sub-grid scale turbulence model at $Re = 2.2 \times 10^4$,

and recorded an average value of C_d for a plain square cylinder to be 2.22. This is in good agreement with the current LES results for the plain square cylinder, $W0$; the average value of C_d given in Table 3.3 is 2.4 at $Re = 2.35 \times 10^4$.

Numerical data for the streamwise turbulence intensity, u/\bar{U} , measured at the peak and valley locations within the near wake at $(x/D, y/D) = (2, 2)$, is provided in Table 3.4. The average value of u/\bar{U} is slightly higher along the peak plane than the valley plane, hence larger reductions in turbulence intensity are observed in a plane that is coincident with a valley. It is interesting to note that an increase in u/\bar{U} of approximately 31.8% is observed at the peak location for $W1$, and only marginal reductions of approximately 6.7% are obtained at a valley location. Both $W2$ and $W3$ contain expected trends in the reductions in streamwise turbulence intensity with a significant 85.3% decrease obtained at the valley location for $W3$, and 72.7% at a peak location.

Table 3.3: Numerical data for the mean drag coefficient, C_d ; comparison between current numerical data at $Re = 2.35 \times 10^4$ and reported numerical data of Darekar and Sherwin (2001) at $Re = 100$.

Configuration	Numerical, $Re = 2.35 \times 10^4$		Numerical, $Re = 100$	
	Average C_d	C_d Reduction [%]	Average C_d	C_d Reduction [%]
$W0$ ($\omega/\lambda = 0$)	2.4	-	1.48	-
$W1$ ($\omega/\lambda = 0.026$)	2.3	4.2	1.45	2.03
$W2$ ($\omega/\lambda = 0.105$)	2.02	15.8	1.31	11.5
$W3$ ($\omega/\lambda = 0.195$)	1.6	33.3	1.29	12.8

Table 3.4: Streamwise turbulence intensity data measured at $(x/D, y/D) = (2, 2)$; comparison between current numerical results and reported experimental observations of Dobre *et al.* (2006).

Configuration	Peak				Valley			
	Numerical		Experimental		Numerical		Experimental	
	Average u/\bar{U}	u/\bar{U} Reduction [%]						
W0	0.15	N/A	0.17	N/A	0.15	N/A	0.17	N/A
W1	0.22	- 31.8	0.16	6.4	0.14	6.7	0.158	8.04
W2	0.11	26.7	0.162	5.7	0.083	44.7	0.13	23.8
W3	0.041	72.7	0.085	50.5	0.022	85.3	0.04	77.04

3.5 Summary

The objective of this chapter is to describe the effective procedure developed to conduct three-dimensional numerical investigations of the bluff body flow for a square cylinder with and without a passive control device; a spanwise sinusoidal profile (SSP). A large eddy simulation (LES) turbulence model, in conjunction to the computational fluid dynamics (CFD) code, FLUENT[®] is adopted to conduct the analysis throughout this thesis. Detailed discussion has been provided for the methodology and the considerations employed to develop the numerical models, while establishing close approximation to an experimental model. The computational domain, mesh generation, model verification and numerical procedure have been provided.

In order to improve the computational demand for conducting a LES, it is coupled with a sub-grid scale (SGS) turbulence model to resolve the small scale structures present in the flow. Suitable selection of the SGS model provides significant influence on the three-dimensional flow at moderate to high Reynolds numbers, and allows

accurate prediction of the flow physics for bluff body flow. Initial convergence is achieved through a steady state Reynolds averaged Navier-Stokes (RANS) solution.

Spatial filtering of the governing flow equations for momentum and energy accurately resolves the large scale motion. Hence, the LES turbulence model is well suited to study flow problems in wind engineering and aerodynamic applications, as forces, moments and their fluctuations are governed by the large scales. For the case of bluff body flow in this study, LES is a suitable approach for determining the common three-dimensional characteristics, boundary layer separation and large scale unsteadiness. It has been demonstrated in this chapter that the LES turbulence model is a strong tool for capturing the structures of the flow field, and provides a means to analyse flow control methods such as the spanwise sinusoidal profile (SSP). Future chapters will develop the LES of turbulent flow and scalar transport mechanisms for the control of bluff body flow. The results will provide details of the fluid-structure interactions not presently available.

CONTROLLING FLOW BY MEANS OF SPANWISE SINUSOIDAL PROFILES ON THE LEADING EDGE OF BLUFF BODIES

Bluff bodies are manifest in a myriad of structures and artefacts such as communication towers, oil rigs, cylindrical support structures, louvres, gates and fences, fans, air conditioning components and so on. When located in a fluid flow field, bluff bodies may experience unacceptably large and time varying forces that result from their shedding vortices. As a result, structures may have to be strengthened or reinforced, and in these cases they may still be susceptible to fatigue failure. An alternative is to modify the aerodynamics of bluff bodies and obviate these drawbacks. To achieve this, passive flow control mechanisms are embodied into the design of bluff bodies. A fairly simple and well established passive approach to reducing the forces on bluff bodies, in particular the drag force, is to streamline them, but in some circumstances manufacturers may find this an expensive solution. Furthermore, streamlining is directional (Van den Abeele *et al.* 2008).

An alternative is to fit helical strakes and bumps to the body in a manner similar to Bearman and Brankovic (2004). These devices reduce the vortex shedding induced vibrations. Their application proved effective when applied to a fixed cylinder. However, in the case of freely vibrating flexible cylinders, the system resonates when

the value of the reduced velocity is in the range in which vortex induced resonance would occur if the cylinder were plain. Although helical strakes may reduce the adverse effects of vortex shedding, they can increase the drag coefficient by up to 10% (Griffin and Ramberg 1982; Kumar *et al.* 2008).

An effective method of controlling vortex shedding and improving the aerodynamic performance of a bluff body is to embody a spanwise sinusoidal profile (SSP) to the leading edge. Bearman and Owen (1998) and Owen and Bearman (2001) experimentally reported a reduction of up to 30% in the mean drag and a suppression of vortex shedding when applying a sinusoidal leading edge. Hence, both the mean and unsteady forces were reduced, and there was independence on the angle of attack.

Darekar and Sherwin (2001a, b) determined that in laminar flows the drag on wavy square cylinders is about 30% less than the drag on the corresponding straight square cylinder. They established that three laminar flow regimes result from this geometry, depending on parameters such as the wavelength and amplitude of the sinusoidal perturbations along the span. Dobre *et al.* (2006) conducted experimental investigations of the flow over square cylinders fitted with a sinusoidally perturbed leading edge and straight trailing edge. Their work demonstrated that a reduction of up to 78% in the turbulence intensity could be achieved in the wake, and this is reflected in a 30% reduction in the mean drag force. A sinusoidal leading edge also causes the vortices in the wake to decay more rapidly; hence vortices in the intermediate to far wake regions are less well defined.

The studies conducted on a sinusoidal periodic perturbation by Darekar and Sherwin (2001a, b) were limited to laminar flows. In addition, they carried out the analysis on square cylinders that were sinusoidal in the spanwise direction; i.e. both the

leading and trailing edges undulated sinusoidally. Their work established that three laminar flow regimes result from this geometry. However, most practical flow conditions are turbulent. Although, Bearman and Owen (1998), Owen and Bearman (2001) and Dobre *et al.* (2006) studied the wake behaviour downstream of several geometries subject to turbulent flows, some aspects of the resulting flow fields remain obscure, and there is still much to explore regarding an SSP. For example, what are the critical parameters of an SSP to effectively target the fluctuating drag and lift forces, and what phenomena constitute a controlled flow field?

The research presented in this chapter demonstrates that spanwise sinusoidal profiles (SSPs) have profoundly beneficial effects on reducing the aerodynamic forces on bluff bodies. The reasons for this are investigated by numerically modelling the flow fields generated by square cylinders with and without SSPs imposed on their leading edges. This is achieved by interpreting the vorticity magnitude distributions and pathlines of the flow around the bodies, which capture the features of the near wake topology. In addition, time-averaged flow properties are recorded. These numerical studies indicate that turbulent flows in the wakes of bluff bodies with sinusoidal perturbations on their leading edges have topologies that are quite different from those generated by plain square cylinders. Furthermore, the wakes generated by an SSP geometry are dependent on the physical parameters of the sinusoid, and this will be explored.

Two principal findings are presented in this chapter, namely,

- 1) The aerodynamic forces (i.e. drag and lift) and their fluctuations acting on a square cylinder can be greatly reduced if an SSP is imposed on the leading edge.

This is particularly the case when the wave steepness, ω/λ , is 0.2 and the normalised wavelength, λ/D , is between 2.4 and 5.6.

2) Previous studies suggest that the normalised wavelength plays an important role in controlling laminar flows. In contrast, the research presented herein suggests that the wave steepness assumes more importance when controlling turbulent flows.

4.1 Effects of Spanwise Sinusoidal Profiles on Flow Fields

The effective control of a flow field depends on the geometry of the SSP bluff body and its effect on vortex shedding. As discussed briefly in earlier chapters, a square cylinder that has an SSP leading edge is capable of controlling flows. This has been reported in the literature for laminar flows and is also evident under turbulent flows in the current work (Antiohos *et al.* 2010). The basic features of an SSP, along with those of a square cylinder are portrayed in Figure 3.2 of Chapter 3. Recall that the geometry of an SSP is defined by two parameters, namely the sinusoidal amplitude, ω , and the wavelength, λ , depicted in Figure 3.2. The wave steepness is defined by ω/λ , and a normalised wavelength by λ/D .

At a Reynolds number of 100, the flow is laminar and the geometries of the SSP promote distinctive flow regimes within the wake of the bluff body (Darekar and Sherwin 2001a, b). The flow regimes in the wake are characterised by being either predominantly two-dimensional coherent flow fields, i.e. the flow field is uniform in the spanwise direction, or as giving rise to incoherent three-dimensional flow fields. The former, coherent case is associated with flow around a plain square cylinder and the latter is the result of applying an SSP to bluff bodies. However, the geometry of the SSP must satisfy defined constraints to be effective.

Darekar and Sherwin (2001a, b) reported three principal flow regimes that obtain in the wake of an SSP under laminar flow conditions and they are governed by ω/λ and λ/D . The three flow regimes are designated as Regimes I, II and III, and they are depicted in Figure 4.1. Regimes I and III represent the two distinct regions that respectively correspond to no control and control of the flow field. Between these two regions exists Regime II, in which the wake is unsteady such that there is spanwise incoherence, but vortices are nonetheless shed. It should also be noted that Regime III contains two sub-regimes, namely Regimes IIIa and IIIb, which correspond respectively to highly controlled flow, and highly controlled flow that intermittently displays features of Regime II (Darekar and Sherwin 2001b).

Geometries of an SSP that give rise to Regime I-type flows at $Re = 100$ are shown in Figure 4.2. Each of the three cases depicted is characterised by having a normalised wavelength, λ/D , of unity and the three values of the wave steepness, ω/λ , are 0.1, 0.2 and 0.3, as well as zero that corresponds to a straight leading edge. The key issue associated with the geometries shown in Figure 4.2 is that they do not control the flow as indicated by Figure 4.1, and coherent vortices are shed synchronously from the trailing edge. The leading edge approaches planarity, in which the wave height, ω , and wavelength, λ , are too small and are therefore unable to affect the flow field. Further insights into geometries that lead to the control of the flow field at $Re = 100$ can be gained from Figure 4.3 which includes the conditions that result in desired control of the flow. A series of sinusoidally spatially periodic leading edges is shown, each with λ/D of 3. In the cases when $\omega/\lambda = 0$ (ω_0) or $\omega/\lambda = 0.01$ (ω_1) the flow is not controlled and it produces Regime I-type flow; however, when ω/λ is 0.1 (ω_2), 0.2 (ω_3) or 0.3 (ω_4), Regime IIIa prevails and vortices are not shed coherently. In these latter cases, the

values of ω and λ are large enough to result in a high wave steepness, which disturbs the flow approaching the leading edge.

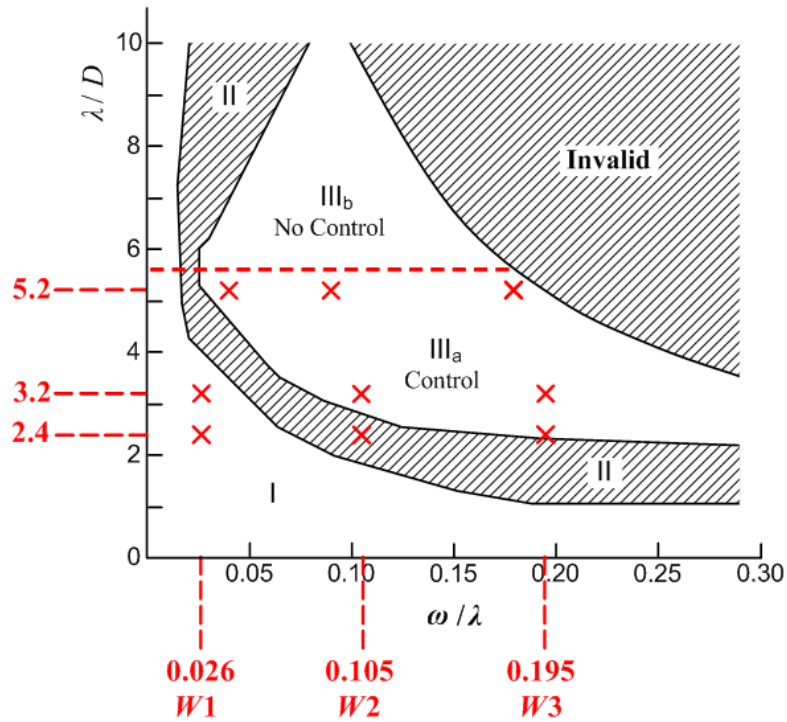


Figure 4.1: An adaptation of Darekar and Sherwin (2001b), of the three flow regimes produced in the wakes of wavy square cylinders at a Re of 100. The hatched upper-right area represents a physically invalid region for an SSP with a plain trailing edge. $W1$, $W2$ and $W3$ are SSP geometries associated with the three laminar regimes. The nine SSP geometries in this study are depicted in relation to the regimes. Geometries coincide with λ/D of 2.4, 3.2 and 5.2, and ω/λ of around 0.026, 0.105 and 0.195.

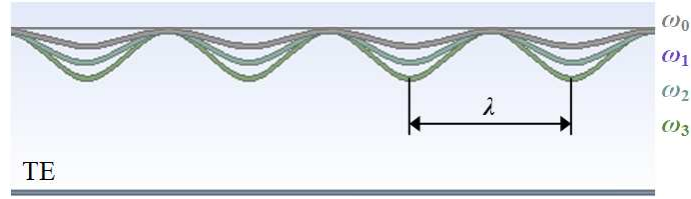


Figure 4.2: A schematic representation of SSP bodies with a constant wavelength, λ/D , of 1 and wave steepnesses, ω/λ , of 0 (ω_0), 0.1 (ω_1), 0.2 (ω_2) and 0.3 (ω_3). All of these geometries give rise to Regime I when the flow is laminar at a Reynolds number of 100.

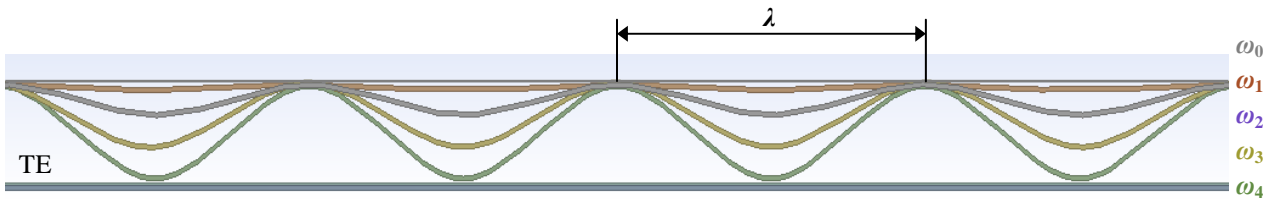


Figure 4.3: A schematic representation of SSP geometries at a constant wavelength, λ/D , of 3, and wave steepnesses, ω/λ , of 0 (ω_0), 0.01 (ω_1), 0.1 (ω_2), 0.2 (ω_3), and 0.3 (ω_4). When the Reynolds number is 100, ω_0 and ω_1 result in Regime I, and ω_2 , ω_3 and ω_4 give rise to Regime III.

It is to be noted that the work of Darekar and Sherwin (2001b) was carried out with a wavy square cylinder; i.e. both the leading and trailing edges have SSPs. However, in this research, a square cylinder with only the leading edge consisting of an SSP has been considered. Therefore, the wave height, ω , cannot physically exceed the width, D , of the square cylinder, such that

$$\frac{\omega}{\lambda} \cdot \frac{\lambda}{D} = \frac{\omega}{D} < 1 \quad (4.1.1)$$

where values of $\omega/D \geq 1$ correspond to the physically invalid region (hatched area) in the upper right of Figure 4.1. This region limits the selection of the parameters of the SSP that coincide with Regime IIIa. It is worthwhile to consider the impact of ω/λ and λ/D on the geometry of the leading edge alone for turbulent flow.

4.2 Turbulent Flow Field around a Square Cylinder SSP

As discussed in Chapter 2, the comb located on the leading edge of an owl's wing can be idealised by a spanwise sinusoidal profile (SSP). In an analogous manner to the comb, an SSP can control the deleterious effects associated with the shedding of vortices from the trailing edge and the resulting turbulent flow. To elucidate the mechanisms of the controlled flow arising from an SSP, a comprehensive description of the near wake topology of the vorticity field around square cylinders with and without an SSP is researched in this chapter. The effectiveness of the SSP is demonstrated by comparing the aerodynamic performance of three contrasting configurations of the SSP and a plain square cylinder.

Three configurations of the square cylinder SSPs that are considered are referred to as $W1$, $W2$ and $W3$, and each has a normalised wavelength, λ/D , of 2.4 and wave steepnesses, ω/λ , of 0.026, 0.105 and 0.195, respectively. $W0$ represents a plain cylinder (i.e. $\omega/\lambda = 0$). These geometries are similar to those studied by Dobre *et al.* (2006). The computational models are shown in Figure 4.4. The SSPs represent geometries that respectively do not control, intermittently control, and effectively control the flow field. A comparison between $W0$ and $W3$ provides the most marked contrast of uncontrolled and controlled flow; comparisons between $W1$ and $W2$ provide insights to the nature of the transition of flows generated by SSPs that are intermediate between $W0$ and $W3$.

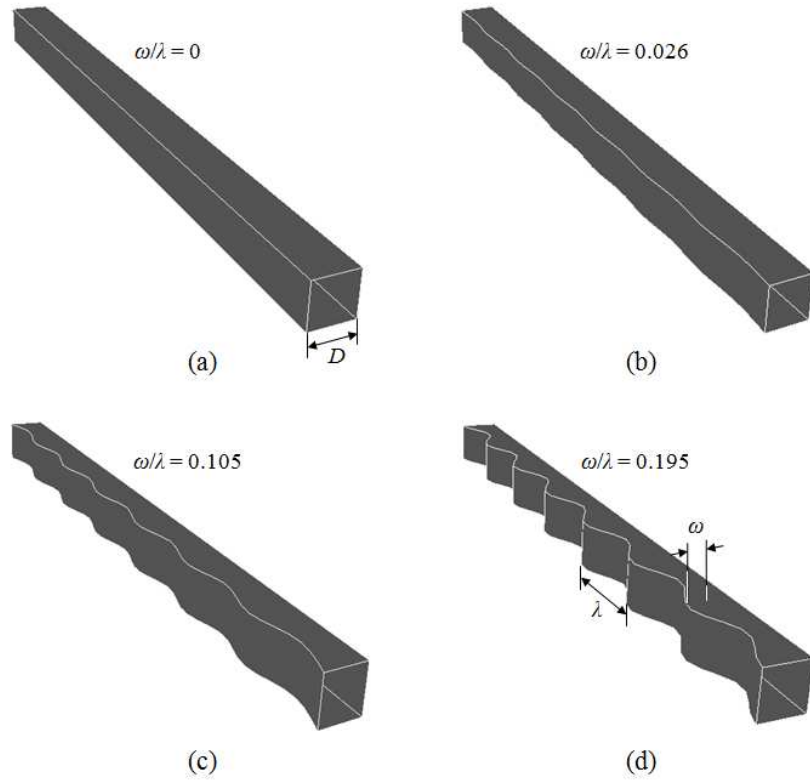


Figure 4.4: Computational models of the plain and SSP square cylinders; (a) W_0 , (b) W_1 , (c) W_2 and (d) W_3 . The wave height (peak-to-peak), ω , and wavelength, λ , of the sinusoidal leading can be depicted.

The flow fields of vorticity magnitude are shown for W_0 , W_1 , W_2 and W_3 in Figure 4.5; the flow is from left to right. In the left column of Figure 4.5, isometric views of the cylinders are shown to detail the phenomena of the flow in vertical planes across the span that coincides with peaks and valleys of the SSP. The vorticity demonstrates the flow field is increasingly incoherent as the wave steepness increases (i.e. examining Figure 4.5(a) through to 4.5(d)). The figures on the right of Figure 4.5 show the resulting flow field for each case. The flow approaches the leading edge coincident with a plane $0.25D$ below the upper surface. Recall that in this work an SSP leading edge is defined in the direction of the free-stream flow; peaks are points on the SSP that are furthest downstream, and valleys are regions of the SSP that are furthest upstream.

The vortices shed from a plain square cylinder, $W0$, depicted in Figure 4.5(a), retain their coherence in the wake of the cylinder. This coherence forms a predominantly two-dimensional flow field that is typical for a square bluff body. The shedding of vortices is quite uniform in the spanwise direction; i.e. there are only small phase differences along the length of the cylinder. Similar coherence to that of a plain cylinder can be discerned for $W1$, although a spanwise structure is somewhat evident, as shown by the slight irregularity of vorticity. Nonetheless, vortex shedding is clearly illustrated in the wake of this very mild SSP geometry. It can be seen in Figure 4.5(b) that a spanwise variation of the phase between vortices is more definitive for $W1$ than that of $W0$. However, it is clear that the flow field has not been significantly affected with the small wave steepness, ω/λ , of 0.026.

The flow field around $W2$ demonstrates vortices being somewhat detached from the upper and lower surfaces at the peaks of the SSP, while the vortices remain adjacent to the surfaces at the valleys. It would appear that an interruption to the coherence of the flow field has been introduced and hence a degree of control achieved; however, vortex shedding is clearly shown in the vertical x - y planes coincident with the peaks and valleys. In fact, two distinct structures are present in the wake of a mildly sinusoidal profile. Kármán vortex shedding is evident, but a stretching of the upper and lower boundary layers exists at valleys; whereas, the roll-up of the boundary layers occurs much closer to the trailing edge at peaks. It is these phenomena that cause vortices in the spanwise direction to be quite incoherent, but distinct vortices are nonetheless shed from the cylinder. A mild level of this passive control marks a transition between the flow field of a plain cylinder and a completely controlled wake.

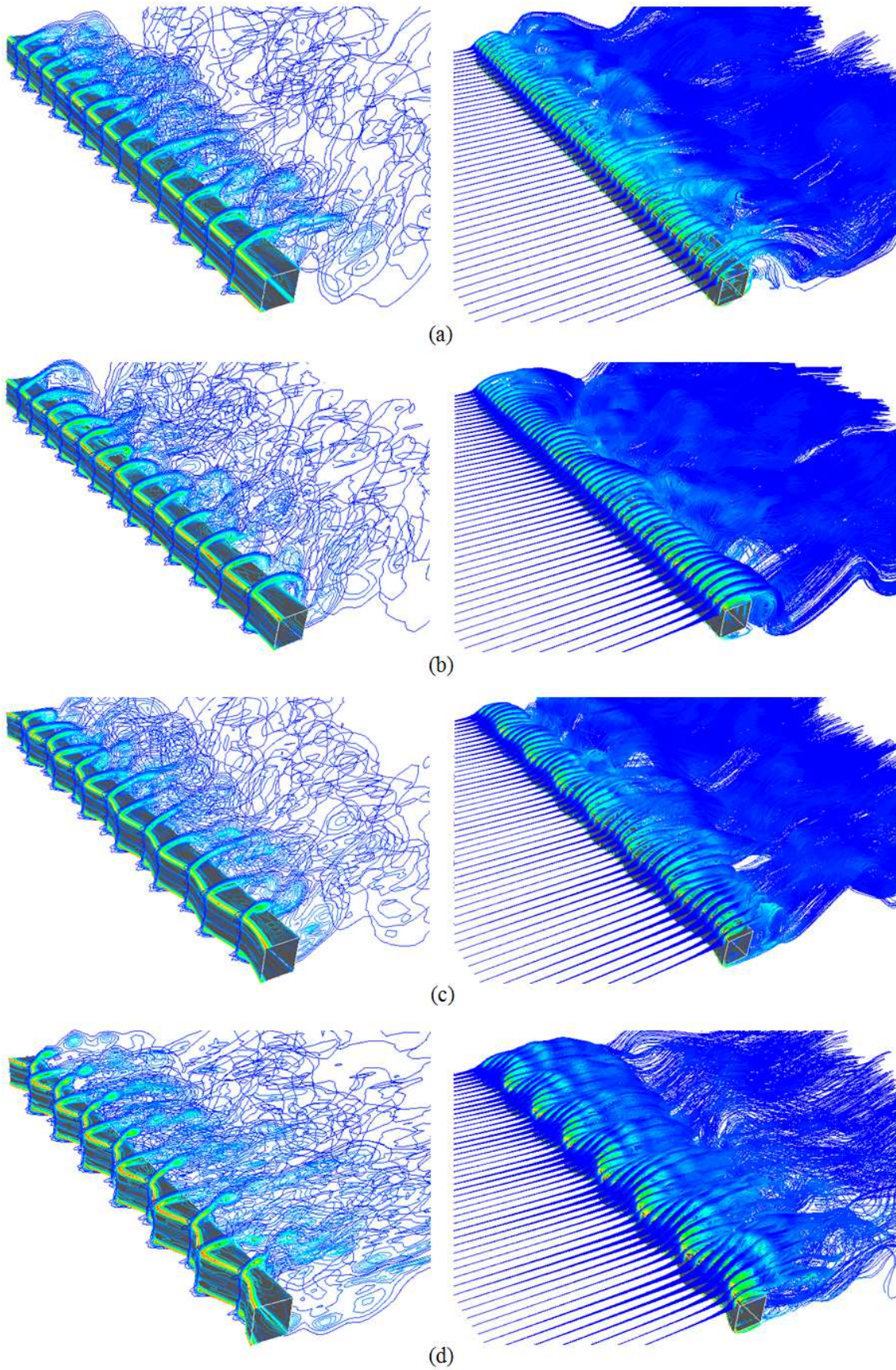


Figure 4.5: Contours of the vorticity fields around (a) W_0 , (b) W_1 , (c) W_2 and (d) W_3 ; (left) vertical x - y planes coincident with peaks and valleys of the SSP, and (right) isometric views of the resulting flow field.

The vorticity field shown in Figure 4.5(d) provides striking evidence of a dissipated vorticity field around the SSP geometry, *W3*. It can be seen that the flow field exhibits a well defined spanwise structure, in which the wake displays a three-dimensional nature that arises from the sinusoidal shape of the leading edge. The flow is detached from the upper and lower surfaces, depicted in *x-y* planes corresponding to peaks. This is due to the flow being channelled towards the center of the peaks as the flow is forced to travel obliquely at the leading edge. This will be discussed in more detail. As a result, small scale streamwise vortices exist coincident to the peaks, in a manner similar to the flow field across an owl's wing as observed by Lilley (2009). These small scale vortices depicted in Figure 4.5(d) are essentially the commonly known Kelvin-Helmholtz instabilities (Bloor and Gerrard 1966).

At the valleys, the flow remains close to the surfaces, in which separation is delayed up to the trailing edge. This is due to significantly lower local adverse pressure gradient; as a result of the leading edge geometry, the flow diverges from the valleys towards the peaks. This pattern emerges in the resulting flow field in Figure 4.5(d) that reflects the sinusoid of the SSP, and it is these phenomena that lead to the spanwise incoherence of the wake. The flow remaining attached to the upper and lower surfaces of *W3* at the valleys enhances the aerodynamic performance of the bluff body by increasing the base pressure and reducing the drag forces. Hence, analogous to features of an owl's wing, the conventional properties of the bluff body are significantly improved.

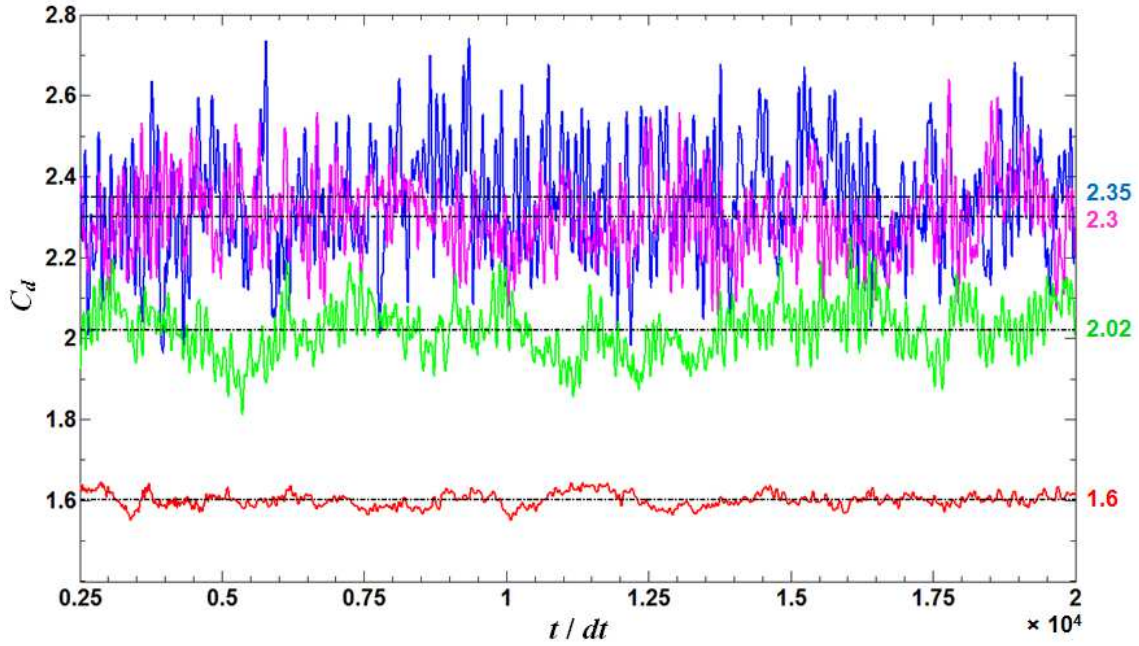


Figure 4.6: Coefficient of drag, C_d , for the plain square cylinder, $W0$ (—), and the three SSP geometries, $W1$ (—), $W2$ (—) and $W3$ (—); highlighting a significant reduction of up to 32% in the mean drag and corresponding reduction of the fluctuations as a result of the SSP with wave steepness, ω/λ , of 0.195 associated with $W3$.

It is important to address the impact of the SSP on the performance of bluff bodies, namely the effect on lift and drag. The coefficient of mean drag, C_d , is plotted against the non-dimensional time, t/dt , for the SSP geometries, $W0$, $W1$, $W2$ and $W3$; this is shown in Figure 4.6. It would be expected from the vorticity fields of each geometry shown in Figure 4.5 that the mean drag will decrease monotonically with the SSP geometries. The value of mean drag is respectively 2.35, 2.3, 2.02 and 1.6 for each case, demonstrating significant reduction in the mean drag observed for $W3$, in which a decrease of up to 32% is achieved. This is associated with a significant reduction of the fluctuations about the mean drag; approximately, 88% reduction in the standard deviation is achieved.

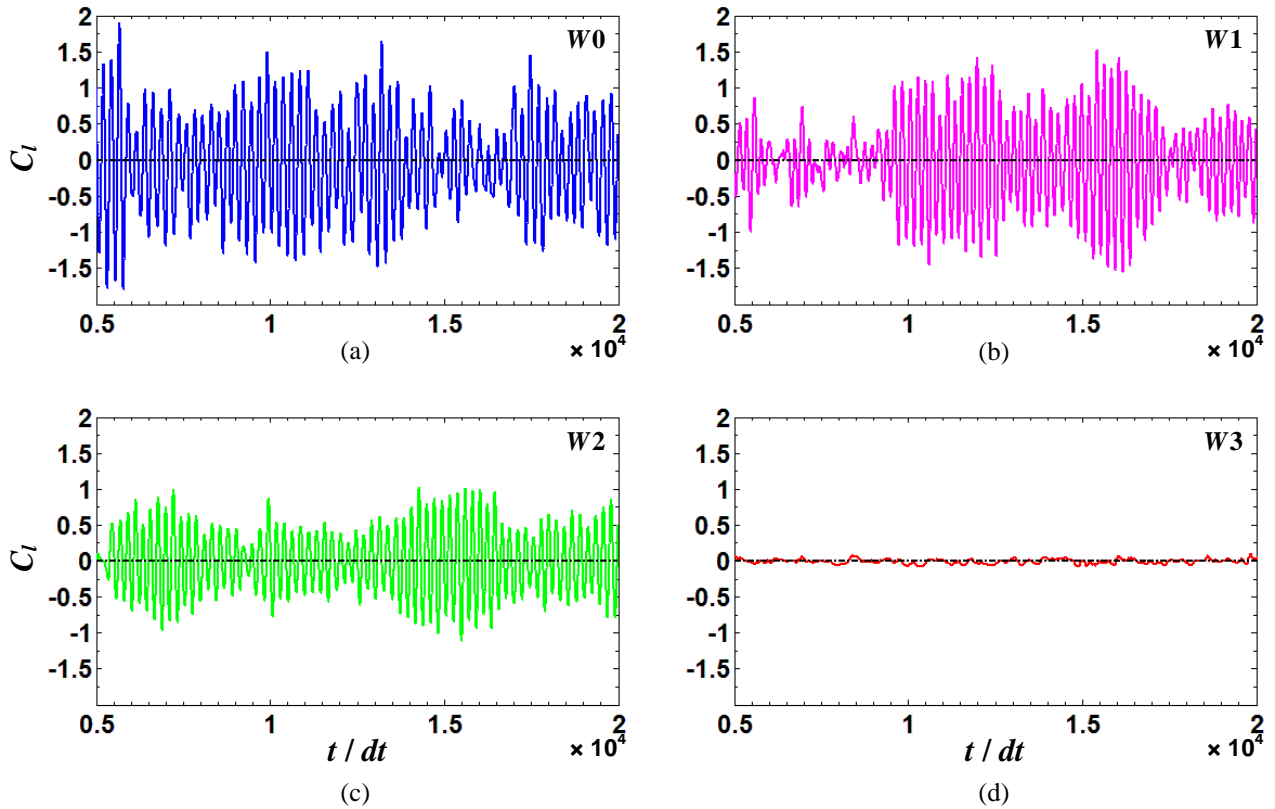


Figure 4.7: Coefficient of lift, C_l , for the plain square cylinder, $W0$ (a, —), and the three SSP geometries, $W1$ (b, —), $W2$ (c, —) and $W3$ (d, —); highlighting the significant reduction in the fluctuations of lift as a result of the SSP with wave steepness, ω/λ , of 0.195 associated with $W3$.

The coefficient of lift, C_l , is plotted for each SSP case in Figure 4.7. As might be expected, large fluctuations of lift about the zero mean value exist for the plain square cylinder. The fluctuations are seen to decrease when an SSP is applied and ω/λ is increased. Figure 4.7(d) portrays the remarkable fact that fluctuations of the lift are negligible in the case of $W3$. The reduction in the fluctuations of lift is about 95%; this clearly demonstrates the practical benefits of applying SSPs to bluff bodies.

The remarkable reduction in the aerodynamic forces, particularly the drag force, is corroborated by the distribution of the time-averaged pressure coefficient, C_p , in Figure 4.8. The distributions are measured on both the upper and lower surfaces of the plain

square cylinder, $W0$, and the SSP cylinder, $W3$, at locations corresponding to the center of the span, and the central peak and valley, respectively. In addition, the numerical results of Yu and Kareem (1998) for a plain square cylinder at $Re = 1 \times 10^5$ is presented for comparison. The mean pressure distribution for the current model, $W0$, displays a local maximum pressure at the leading edge due to the sharp corner of the leading edge, and then follows a flat profile, which is indicative of absent flow reattachment. This is typical for a square cylinder with an aspect ratio below 2.5 (Sohankar 2008), and is in reasonably close agreement with the profile of Yu and Kareem (1998).

The mean pressure distribution for the SSP geometry, $W3$, displays different flow behaviour at the leading edge. Coincident to the valley, a maximum local pressure can be depicted followed by a flat profile (i.e. no pressure recovery similar to a plain leading edge). Likewise, the flow at a peak has absent flow reattachment towards the trailing edge. However, a significant local pressure maximum at the leading edge indicates the presence of a high pressure gradient, and almost stagnant flow as a result of a sharp flow separation. In addition, this high pressure is sustained up to the mid region of the surface of the square cylinder before suddenly decreasing to the value of the free-stream flow. It is to be noted that the minimum x for a peak and valley is taken at the leading edge location.

The pressure distributions given in Figure 4.8 provide a useful insight to the behaviour of the flow field generated by the SSP. It is notable that the pressure distribution that is coincident to a valley of the SSP leading edge resembles a profile similar to that of a plain square cylinder. Nevertheless, the observation at a location of the peak demonstrates the very incoherent nature of the flow field in the spanwise direction, in which a three-dimensional behaviour clearly exists.

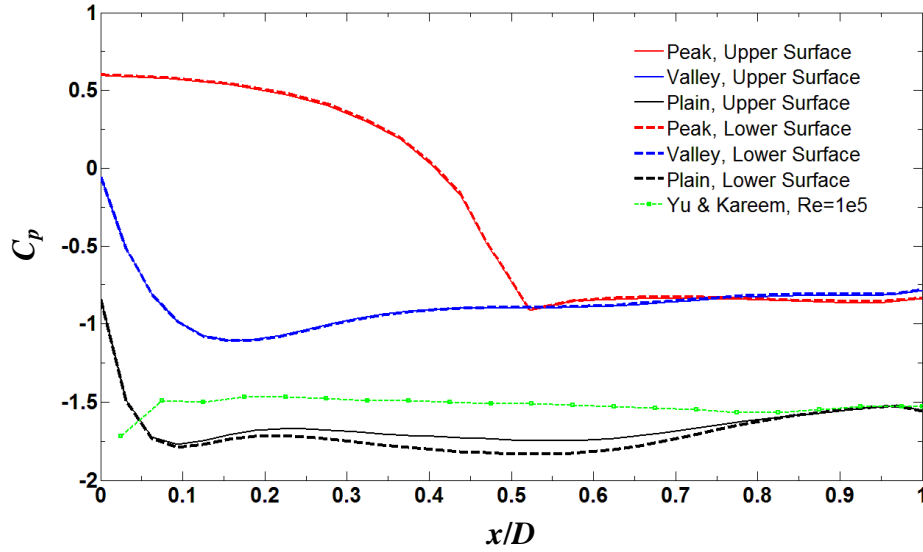


Figure 4.8: Distribution of the time-averaged pressure coefficient, C_p , on the upper and lower surfaces of the plain square cylinder, $W0$, and SSP cylinder, $W3$. Comparison is shown for a plain square cylinder between the current results and the numerical distribution of Yu and Kareem (1998), at $Re = 1 \times 10^5$.

In Figure 4.9, the time-averaged pressure coefficient, C_p , is shown in the wake of both $W0$ and $W3$. The numerical measurements are made behind the center of trailing edge in the streamwise direction along the wake centerline, $y = 0$. For the SSP cylinder, $W3$, the distribution corresponds to the central peak and valley. The numerical results of Sohankar (2006) are also given for a square cylinder at a $Re = 2.2 \times 10^4$; the current numerical results for $W0$ agree reasonably well. The pressure distributions coincident to a valley and a peak of $W3$ both follow the same profile. Hence, the SSP leading edge appears not to adversely affect the pressure distribution in the wake transverse to the direction of the flow; unlike the observations along the cylinder surface. The lower drag force observed with the SSP geometry is corroborated by the higher value of the pressure coefficient in the wake of $W3$. A base pressure closer to the value of the free-stream flow obtains a better pressure recovery. A lower pressure in the wake (or base pressure) results in a higher drag force (Sohankar 2008).

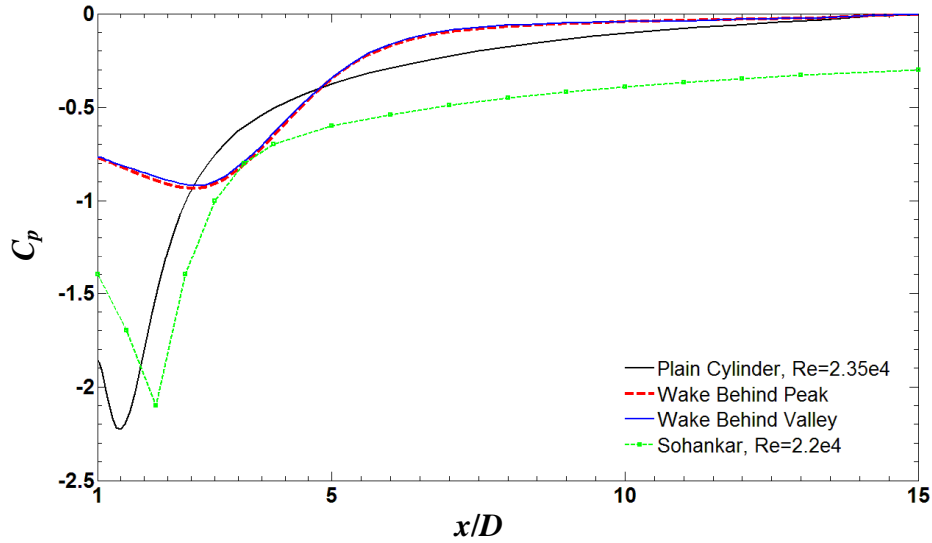


Figure 4.9: Distribution of the time-averaged pressure coefficient, C_p , in the wake of the plain square cylinder, $W0$, and the SSP cylinder, $W3$. Comparison is shown between the current results and the mean pressure distribution of Sohankar (2006), at $Re = 2.2 \times 10^4$.

Figure 4.5 graphically illustrates how the SSP renders the vorticity field substantially incoherent and the vorticity directly downstream of peaks and valleys of an SSP are quite different. Hence, deeper insights of the drag mitigating phenomena and distinct characteristics of the vorticity are obtained by examining the flow in vertical planes coincident with the peaks and valleys of the SSP.

Figure 4.10 portrays perspective views of a square cylinder with and without an SSP; the direction of flow is from left to right. The planes shown for $W0$ correspond to identical planes shown for the SSP geometries. As expected, the vorticity in the wake of a plain square cylinder appears to be quite independent of spanwise location; Kármán vortex shedding occurs along the length of the cylinder in a quite consistent manner in Figure 4.10(a). In contrast, the vorticity downstream of an SSP, namely $W3$ in Figure 4.10(d), is highly dependent on its spanwise location. Downstream of peaks, the sudden

separation of flow from the horizontal surface at the leading edge causes instability within the shear layers and results in the formation of Kelvin-Helmholtz vortices, commonly known as Bloor-Gerrard vortices (Bloor and Gerrard 1966; Sheridan 1992; Khor 2011}. Bloor-Gerrard vortices are characteristic of disturbed boundary layer flows, and are therefore associated with instability in the shear layers (Bloor and Gerrard 1966). These small scale instabilities occur with a frequency of about $3f_{vo}$, where f_{vo} is the vortex shedding frequency of a plain square cylinder of approximately 47 Hz, corresponding to a Strouhal number, St , of 0.14 (Wilcox 1993). This is depicted in the left of Figure 4.10(d). These small scale vortices are also discernable downstream of valleys in the right Figure 4.10(d); however, they appear to be less distinct than those associated with peaks.

In the wakes of $W1$ and $W2$, changes to the flow field resulting from a mildly undulating SSP are not as evident as the changes depicted between $W0$ and $W3$. In the case of $W1$, the shear layers roll-up into Kármán vortices in a similar manner to the wake of $W0$; the wake also appears to be independent of spanwise location and displays a predominantly two-dimensional flow field. The vorticity distribution in the wake of $W2$ appears to portray the topology associated with the plain square cylinder and $W1$. However, upon closer inspection of Figure 4.10(c) it can be seen that coincident to the peak, the roll-up of the shear layer occurs closer to the trailing edge than at the valley. At the valley, the shear layers stretch further downstream before forming Kármán vortices. Hence, the wave steepness, ω/λ , of 0.105 and normalised wavelength, λ/D , of 2.4 generates a flow field that exhibits slight three-dimensionality (i.e. variations in the spanwise direction). Nevertheless, the mild form of the SSP of $W2$ does not affect the flow field as greatly as the SSP of $W3$ with ω/λ of 0.195 and λ/D of 2.4.

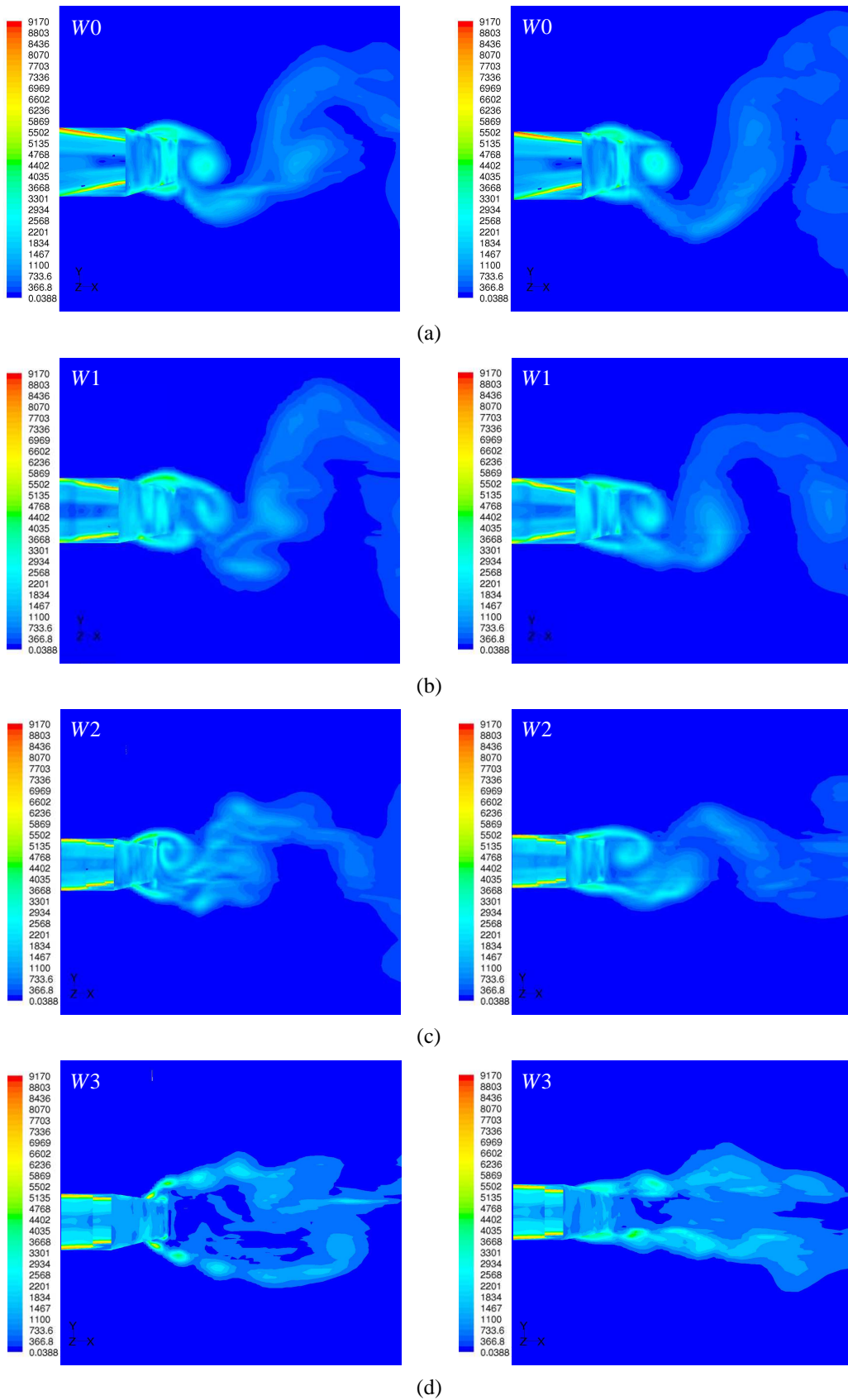


Figure 4.10: Contours of instantaneous vorticity magnitude in the wake of the SSP square cylinders. The flow field is shown in the mid-span vertical x - y plane coincident with a peak (left), and the mid-span vertical x - y plane coincident with a valley (right); (a) W0, (b) W1, (c) W2 and (d) W3.

The vortices downstream of peaks and valleys have largely dissipated at a distance of approximately $4D$ downstream of the SSP cylinder, $W3$. This phenomenon also contrasts with the vortices downstream of a plain cylinder, which retain their coherence for a greater distance. Figure 4.10(d) shows that the shear layers downstream of peaks diverge from a horizontal plane coincident with the centerline of the wake. However, the shear layers downstream of valleys remain relatively parallel to the mean direction of flow. In both cases, the shear layers are symmetrical about the horizontal, but their characteristics are periodic in the spanwise direction. Hence, this is evidence of a vorticity field in the wake of an SSP structure that is associated with the Mode-A type (Meiburg and Lasheras 1988; Williamson 1996).

The observations made regarding the vorticity fields are corroborated by considering the instantaneous flow field around the SSP geometries. Figure 4.11 shows the instantaneous vectors of velocity that approach the leading edge in a horizontal x - z plane coincident to $0.25D$ below the upper surface. The view is normal to the flow that is from left to right. It can be seen that for the case of the plain square cylinder in Figure 4.11(a), the velocity vectors interacting with the leading edge are parallel and streamwise. In contrast, for the SSP geometries, as the wave steepness, ω/λ , increases from 0.026 to 0.195 in Figures 4.11(b), 4.11(c) and 4.11(d), the vectors turn towards the centerline of the peaks and demonstrate a channelling of the flow at these locations. This channelling becomes more evident as the wave steepness of the SSP become large. Hence, the SSP with large wave steepness has the ability to capture and channel the flow. Coincident with valleys, the flow remains streamwise and parallel to the free-stream flow. These phenomena maintain the independent regions of streamwise flow at peaks and valleys. This three-dimensional incoherence in the flow field delays spanwise

interactions at the leading edge and therefore provides substantial control as interactions are established much further downstream; hence, the effectiveness of the SSP.

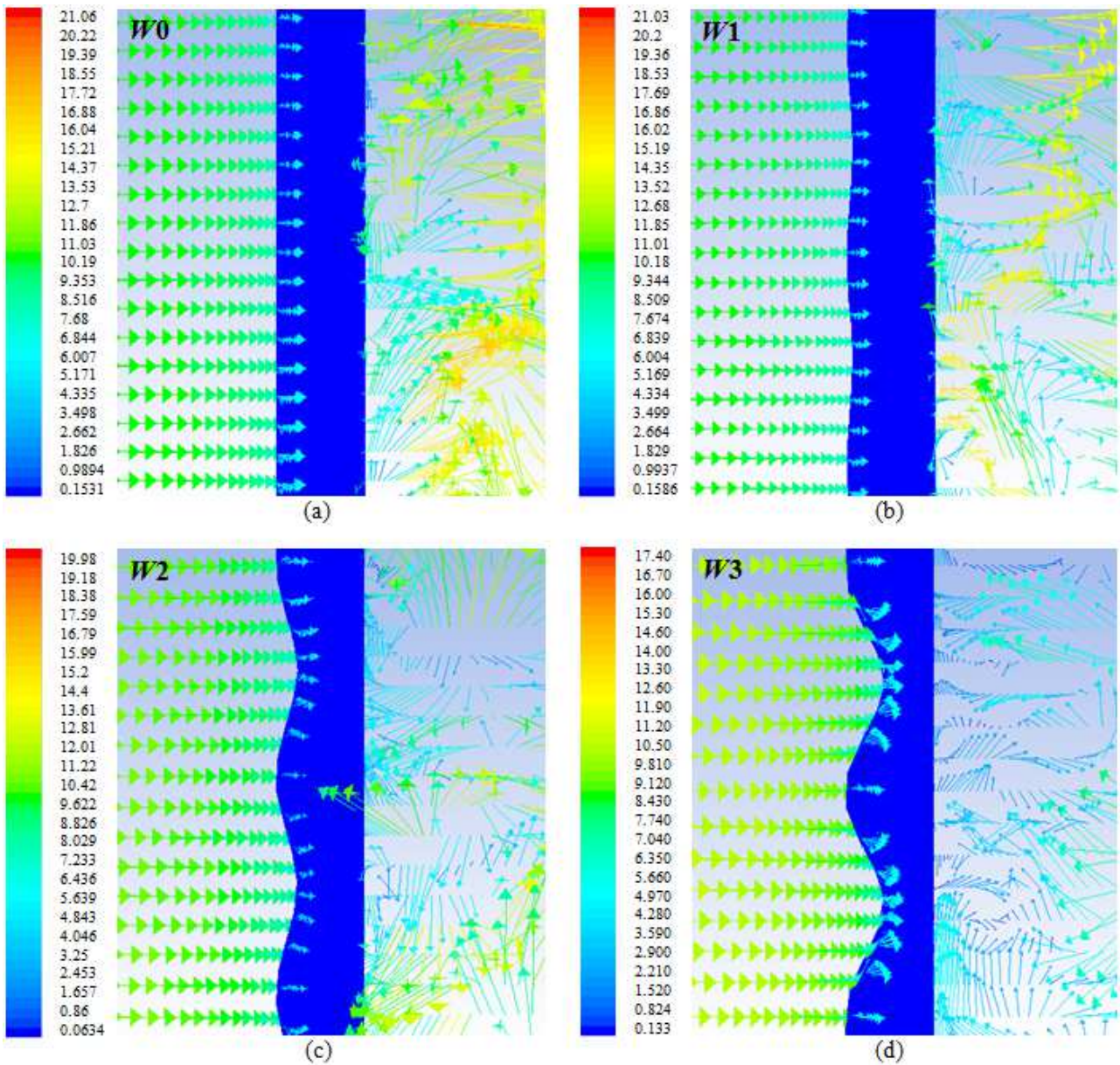


Figure 4.11: Velocity vectors demonstrating the channelling of flow at peaks of the SSP geometry as the wave steepness, ω/λ , increases from (a) ω/λ of 0, W_0 ; (b) ω/λ of 0.026, W_1 ; (c) ω/λ of 0.105, W_2 and (d) ω/λ of 0.195, W_3 . The velocity is shown in a horizontal $x-z$ plane that approaches the leading edge at $0.25D$ below the upper surface.

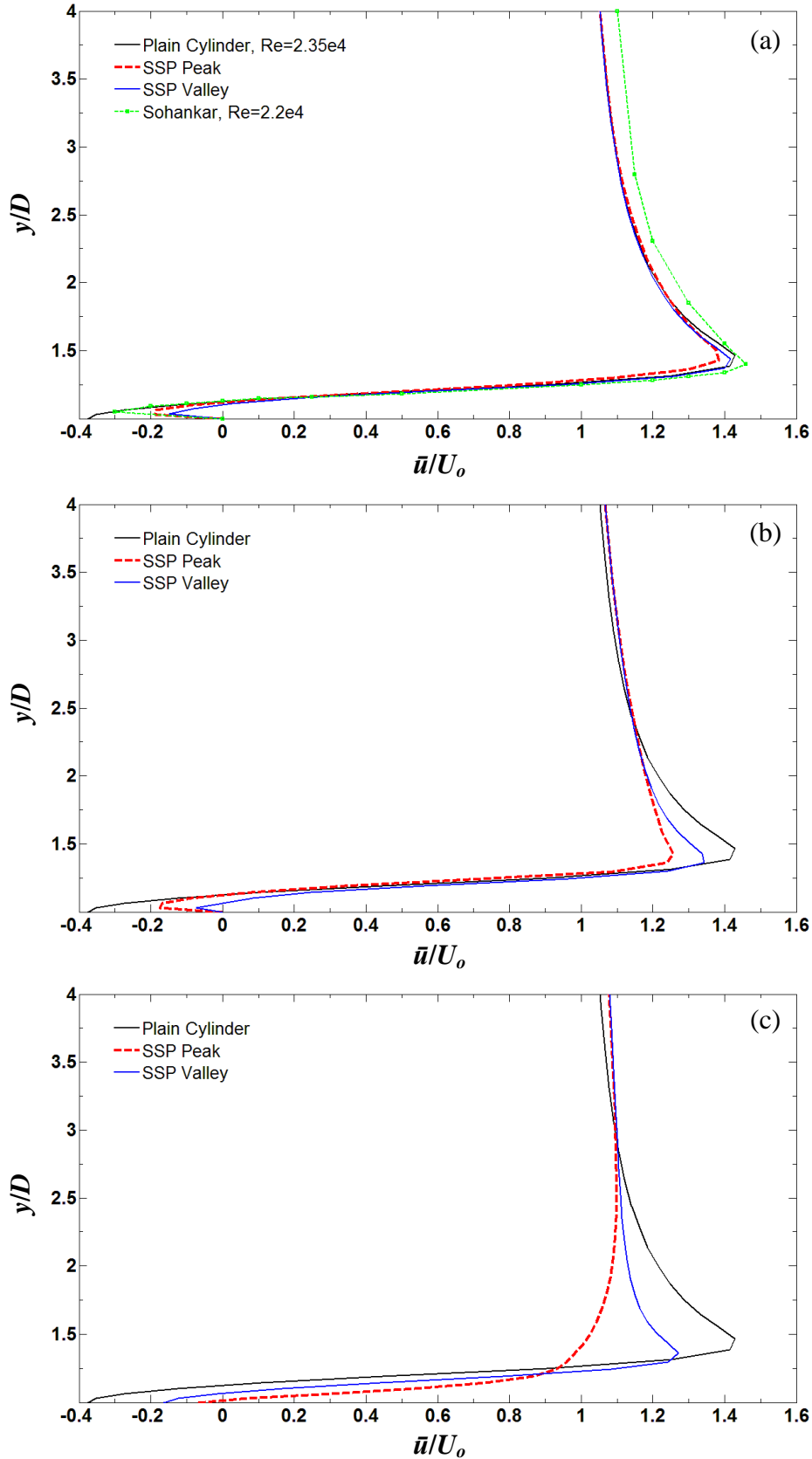


Figure 4.12: Time-averaged streamwise velocity, \bar{u} , profile measured mid-span along the line $x/D = 0.5$, on the upper side of the plain and SSP cylinders, at $Re = 2.35 \times 10^4$, (a) W1, (b) W2 and (c) W3. Comparison is made between the averaged numerical velocity profile of Sohankar (2006), at $Re = 2.2 \times 10^4$.

Figure 4.12 shows the time-averaged streamwise velocity, \bar{u} , profiles on the upper surface of both the plain and SSP cylinders. The measurements are made at the center of the span along the vertical line at $x/D = 0.5$. In the cases of the SSP geometries, the data corresponds to the central peak and valley; whereas in the case of the plain square cylinder the data corresponds to the center of the span. For comparison and verification of the numerical model, the velocity profile for a plain square cylinder is also shown from Sohankar (2006) in Figure 4.12(a). Sohankar (2006) studied the flow around square cylinders at $Re = 2.2 \times 10^4$ using LES. Figures 4.12(a), 4.12(b) and 4.12(c) compare the velocity profiles for $W1$, $W2$ and $W3$, respectively, with the velocity profile of the plain square cylinder, $W0$.

The streamwise velocity profiles for the SSP cylinders show markedly different characteristics. In Figure 4.12(a), the streamwise velocity is unaffected by the presence of the mild perturbation ($\omega/\lambda = 0.026$) on the leading edge of $W1$, as the streamwise velocity coincident to a peak and a valley follows the trend of the plain square cylinder. These profiles also agree well with the numerical velocity profile of Sohankar (2006). When the wave steepness of the SSP is increased to that of $W2$ ($\omega/\lambda = 0.105$), a change in the velocity profiles corresponding to a peak and valley can be seen with respect to $W0$. Although a similar trend can be depicted, there is a shift in the value of streamwise velocity near the upper surface. This is indication of an average SSP slightly affecting the behaviour of the flow field around the bluff body. Hence, the channelling effect of an SSP is beginning to take place.

In Figure 4.12(c), the streamwise velocity profiles for $W3$ show a clear difference, in which the value of the normalised velocity near the upper surface of the SSP geometry is less in a plane coincident to a peak, but higher coincident to a valley.

Furthermore, the magnitude of the velocity is equivalent to the free-stream velocity near the surface at the peak, indicating that flow separation is indeed present from the surface at this location. Therefore, the velocity is slowed to the free-stream velocity near the wall. The flow slows gradually from the surface to the free-stream flow. The use of the large eddy simulation in this research has captured the unique details of the flow field created by the application of the SSP that hitherto been provided, and can lead to a more in depth understanding of the phenomena that is the leading edge comb.

The time-averaged profiles of \bar{u} measured in the wakes of the plain square cylinder, $W0$, and the SSP cylinder, $W3$, are given in Figure 4.13. They demonstrate the highly controlled flow field associated with the sinusoidal perturbations on the leading edge of large wave steepness, ω/λ , of 0.195 aft of the trailing edge. The streamwise velocity is measured at several locations downstream from the trailing edge, corresponding to the central peak and valley for $W3$, and the center of the span for $W0$. In Figure 4.13(a) at $x/D = 0$, noticeable flow reversal of the streamwise velocity exists at the trailing edge coincident to the peak of $W3$. This is due to the separation of the shear layers aft of the leading edge. Coincident to a valley, the velocity profiles resemble that of the plain square cylinder, $W0$, in which flow reversal is absent and the flow appears to remain adjacent to the surface. This discrepancy of the flow between a peak and a valley clearly identifies the independent fluid structures that would affect the downstream evolution of the wake behind an SSP geometry.

In Figure 4.13(b), 4.13(c) and 4.13(d), corresponding to respectively $x/D = 0.5$, 1.5 and 3, the streamwise velocity at the centreline of $W0$ recovers towards the free-stream value. Whereas for $W3$, the streamwise velocity at both the peak and valley experiences flow reversal and tends away from the free-stream value. The initial flow reversal

occurring at the peak at $x/D = 0$ and the existing spanwise three-dimensionality as a result of the SSP, draws the fluid being shed at a valley towards the peak. It is these phenomena that delays the onset of the centreline velocity recovery, and hence attenuates the energy of the flow in the wake of the SSP body. It is not until a downstream distance between $x/D = 4.5$ and 6 that the spanwise flow associated with the peak and valley merges, and the centreline velocity is matched. In addition, the recovery of the streamwise velocity for the wake behind an SSP is delayed until approximately $x/D = 4.5$.

The streamwise velocity profile for the plain square cylinder becomes completely developed into the wake at a downstream distance of $x/D = 6$. This is in contrast to $W3$, in which the velocity profiles continue to develop until a downstream distance of $x/D = 10.5$. This is clear evidence of the lower energy flow produced in the wake of $W3$, as a result of the higher diffusion of vorticity. The wake behind $W0$ broadens rapidly due to the transport of the oppositely apposed vortices shed from the trailing edge, shown in Figure 4.10 (Dutta *et al.* 2008). The entrainment of the fluid in the wake is significantly greater for $W0$ than for $W3$, hence, the reason for the streamwise velocity profiles associated with the SSP cylinder remaining narrow into the wake. At the downstream locations corresponding to the fully developed streamwise flow ($x/D = 6$ and 10.5 for $W0$ and $W3$, respectively), the size of the wake has reached a limiting value as the viscous dissipation diffusion weakens the vorticity.

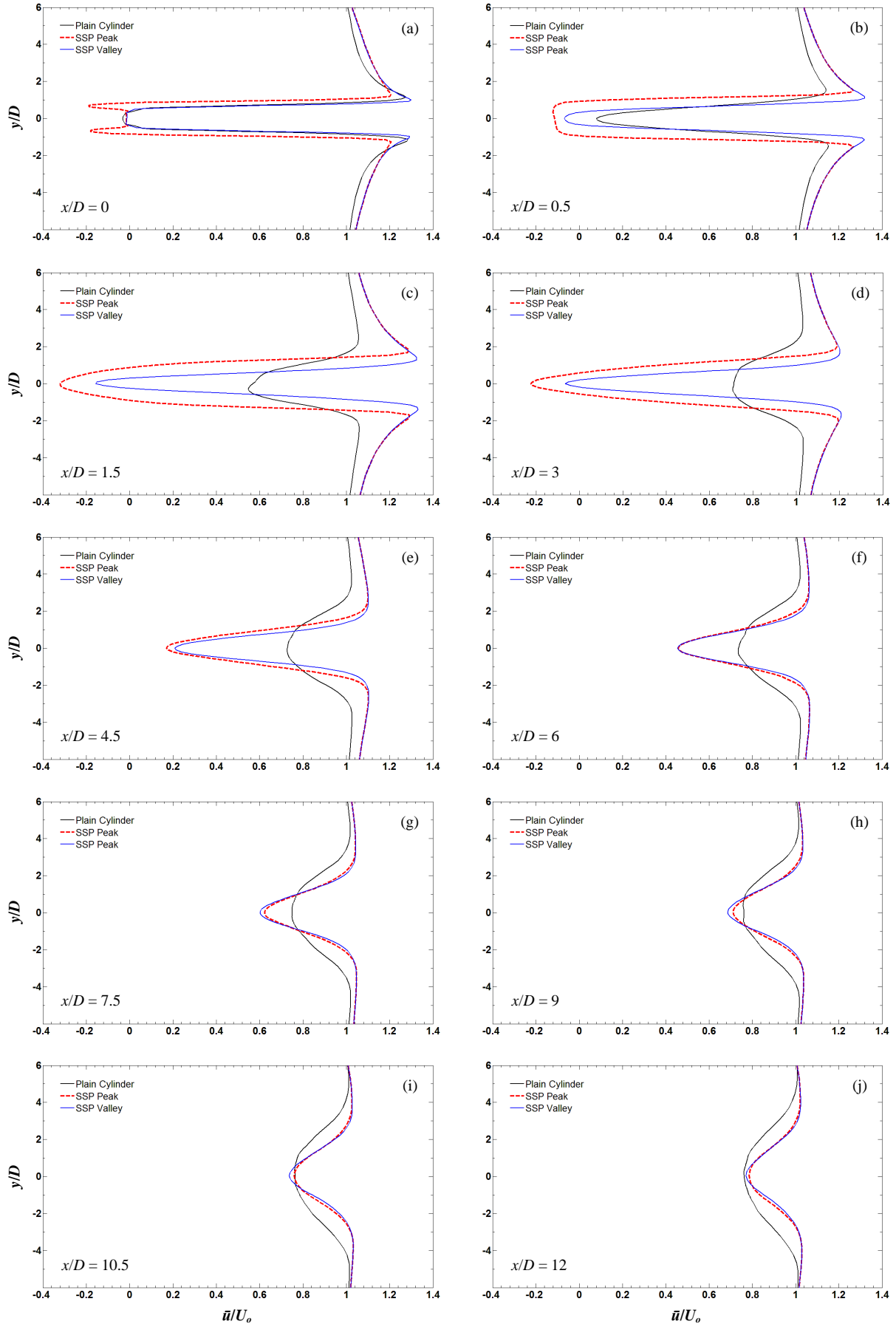


Figure 4.13: Time-averaged streamwise velocity, \bar{u} , profiles measured downstream from the trailing edge along the centerline of the wake of the plain, $W0$, and SSP, $W3$, cylinders, at $Re = 2.35 \times 10^4$; (a) $x/D = 0$, (b) $x/D = 0.5$, (c) $x/D = 1.5$, (d) $x/D = 3$, (e) $x/D = 4.5$, (f) $x/D = 6$, (g) $x/D = 7.5$, (h) $x/D = 9$, (i) $x/D = 10.5$, (j) $x/D = 12$.

The geometry of the SSP is highly dependent on the wavelength, λ , in that its presence in both ω/λ and λ/D affects the selection of the wave height, ω , to obtain the desired steepness. This is especially important in the case of a slender bluff body with a plain trailing edge, as indicated in Equation 4.1.1. Furthermore, the dependence on λ suggests it is likely to be a factor in the effectiveness of controlling the flow. This conjecture is motivated by the non-dimensional pitch (i.e. wavelength) of the leading edge comb observed by Lilley (2009) and described in Equation 2.2.1 of Chapter 2. The flow regimes depicted under laminar flow at $Re = 100$ demonstrate that changes to both ω/λ and λ/D affect the outcome of the flow field. However, under turbulent flow conditions at higher Reynolds number, the flow regimes may be more or less susceptible to any changes in both parameters. Indeed, maintaining the wavelength, λ/D , constant and changing the wave steepness, ω/λ , has been shown in this section to induce the differences in the flow regimes at $Re = 2.35 \times 10^4$.

At this stage of the research, it is believed that under turbulent flow conditions, the wave steepness plays an important role in controlling the flow and mitigating the vortices in the wake. Depending on the choice of the wavelength, λ , and the corresponding selection of the wave height, ω , if the gradient (i.e. ω/λ) of the SSP is mild, the leading edge approaches that of a plain square cylinder. Hence, no significant control of the flow is expected. On the other hand, if the gradient of the SSP is steep, the leading edge is disturbed and controlled effects are expected to take place. Recall that the values of both ω and λ in determining the wave steepness must be sufficient to affect the flow field.

The abovementioned can be illustrated by considering four configurations of an SSP in Figure 4.14; firstly, two geometries at $\lambda/D = 2.4$ and 5.2 , and with identical

steepness of $\omega/\lambda = 0.1$ (Figure 4.14(a)); secondly, two geometries $\lambda/D = 2.4$ and 5.2 , but in this case with $\omega/\lambda = 0.2$ (Figure 4.14(b)). Each of the four cases demonstrates pairs of SSPs that have the same gradient. Recalling the channelling effect that is evident with the SSP cylinder, *W3*, and discussed earlier, it can be seen that the sharper gradient of the pair of SSPs in Figure 4.14(b) is more likely to disturb the flow and localise it at the center of the peaks than for the pair of SSPs in Figure 4.14(a). At a high $Re = 2.35 \times 10^4$, it has been shown that to avoid planarity in the leading edge of the SSP body and to obtain notable control of the flow, the wave steepness, ω/λ , must be substantial to allow the leading edge to capture and modify the flow. This implies that the flow regimes for turbulent flow may be strongly dependent on the wave steepness. The wave steepness in turn is highly dependent on the wavelength, in which the wave height is affected for a bluff body with a plain trailing edge. This is explored in the following sections.

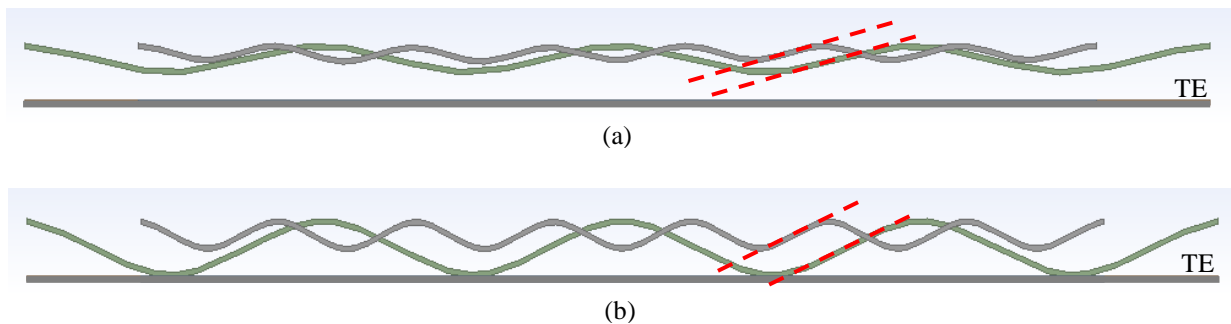


Figure 4.14: A schematic representation of SSP bodies demonstrating similarities in wave steepness (gradient), as indicated by the dashed lines; (a) SSP geometries with identical ω/λ of 0.1 , and λ/D of 2.4 (—) and 5.2 (—); (b) SSP geometries with identical ω/λ of 0.2 , and λ/D of 2.4 (—) and 5.2 (—).

4.3 A Parametric Study of Turbulent Flow Regimes

4.3.1 Performance of Aerodynamic Forces

An objective of this research is to determine whether the flow regimes identified with laminar flow past bluff bodies that have sinusoidally spatial perturbations have any analogues when the flow is turbulent. In this case, bluff bodies with sinusoidally spatial perturbations will be considered, and they are somewhat different to the wavy geometries studied by Darekar and Sherwin (2001b). If there are analogues between laminar and turbulent flows then this rather odd juxtaposition, along with their interactions with basically different geometries might reveal commonalities associated with flows generated by objects that have spatially periodic geometries.

Four measures have been used to determine the effects of wave steepness, ω/λ , and normalised wavelength, λ/D , on the flow regimes, namely the mean drag coefficient, C_d , and the lift coefficient, C_l , and their fluctuations. Results were obtained for three values of the normalised wavelength, λ/D , namely 2.4, 3.2 and 5.2. Values of the wave steepness, ω/λ , shown in Figure 4.1 correspond to Regimes I, II or IIIa of Darekar and Sherwin (2001b), and they do not violate the physically possible because the amplitude of the sinusoidal perturbations are less than the thickness, D , of the bluff body.

The variation of the mean drag coefficient, C_d , with ω/λ for the three values of normalised wavelength is shown in Table 4.1, for $Re = 2.35 \times 10^4$. It can be observed that under the conditions studied that the drag coefficient decreases monotonically as the wave steepness increases, but it appears to be relatively insensitive to the normalised wave length, λ/D . The standard deviation of the drag coefficient also appears to be relatively insensitive to the normalised wavelength, but the standard deviation of the

drag coefficient decreases by a factor in the order of 7 as the wave steepness increases from 0.026 to 0.195.

Table 4.1: The mean drag coefficient, C_d , and the mean absolute lift coefficient, C_l , and their standard deviations for SSPs with a range of ω/λ and λ/D .

ω/λ	λ/D	Mean C_d	C_d Standard Deviation	Absolute C_l	C_l Standard Deviation
0	0	2.407	0.151	2.035	0.413
0.026	2.4	2.273	0.11	1.569	0.366
	3.2	2.238	0.107	1.508	0.289
0.04	5.2	2.244	0.079	1.028	0.23
0.105	2.4	2.023	0.064	1.163	0.256
	3.2	2.041	0.066	1.152	0.294
0.09	5.2	2.042	0.07	0.84	0.188
0.195	2.4	1.599	0.017	0.087	0.019
	3.2	1.548	0.014	0.066	0.013
0.18	5.2	1.488	0.016	0.056	0.012

Table 4.1 presents the dependence of the mean absolute lift coefficient, C_l , on ω/λ and λ/D . It can be observed that the lift coefficient is strongly dependent on the wave steepness, and it decreases from about 1.57 when $\omega/\lambda = 0.026$ and $\lambda/D = 2.4$ to 0.087 when $\omega/\lambda = 0.195$ whilst the normalised wavelength remains unaltered. The lift coefficient appears to decrease somewhat as the normalised wavelength increases. The standard deviation of the lift coefficient is strongly dependent on the geometry of the SSP, and remarkably, a greater than 30-fold reduction from 0.366 when $\lambda/D = 2.4$ and $\omega/\lambda = 0.026$ to 0.012 when $\lambda/D = 5.2$ and $\omega/\lambda = 0.18$ is obtained. In general, the standard

deviation of the variations in the lift coefficient decreases markedly with increasing wave steepness, and there also appears to be a diminution as the normalised wavelength increases from 2.4 to 5.2, although this latter spans a range a little over 2:1.

4.3.2 Topologies of Wakes of Spanwise Sinusoidal Profiles

The results presented above indicate that SSP geometries can give rise to significant reductions in the lift and drag forces on bluff bodies. Insights of the mechanisms associated with the reductions will be achieved by contrasting the topographies of the flow fields generated by bluff bodies that have plain leading edges, and SSP leading edges with different values of ω/λ and λ/D . The degree of coherence of the flows will be quantified by comparing the wakes generated by the bodies. It will be observed that the topographies of the wakes shed by the bluff bodies that have plain and strongly sinusoidal leading edges (i.e. high wave steepness, ω/λ) contrast quite sharply, as compared to other configurations. This study indicates that the flow regimes of bluff bodies immersed in turbulent flows are less sensitive to the normalised wavelength than observed by Darekar and Sherwin (2001b) in cases of laminar flows.

The numerical values of the mean drag and its deviation appear to vary with ω/λ but they are relatively insensitive to the dimensionless wavelength, λ/D . This observation, made when the flow is turbulent, is quite different from the situation that pertains when the flow is laminar. In the latter case, the wavelength appears to be particularly important in controlling flows. In this work investigations are carried out on the effect of maintaining the wave steepness almost constant and doubling the wavelength. The flow fields generated by two SSP geometries, namely $W2$ ($\omega/\lambda = 0.105$, $\lambda/D = 2.4$) and $W2_A$ ($\omega/\lambda = 0.09$, $\lambda/D = 5.2$) are investigated. These geometries are indicated in Figure

4.1. This choice is motivated by the expectation that these geometries will control the flow in a manner that is intermediate between a plain square cylinder, $W0$, and $W3$ ($\omega/\lambda = 0.195$, $\lambda/D = 2.4$). Figure 4.15(a) highlights the vorticity field in a vertical plane that is co-planar with the trailing edge of the two cylinders. It can be seen that in this plane the vorticity fields display vortex loops that are adjacent to the horizontal surfaces downstream of the regions of the peaks. Based on overall magnitude, the vortices generated by $W2$ and $W2_A$ appear to be similar, and the topology of the overall flow field surrounding the two geometries are quite similar as depicted in Figure 4.15(b).

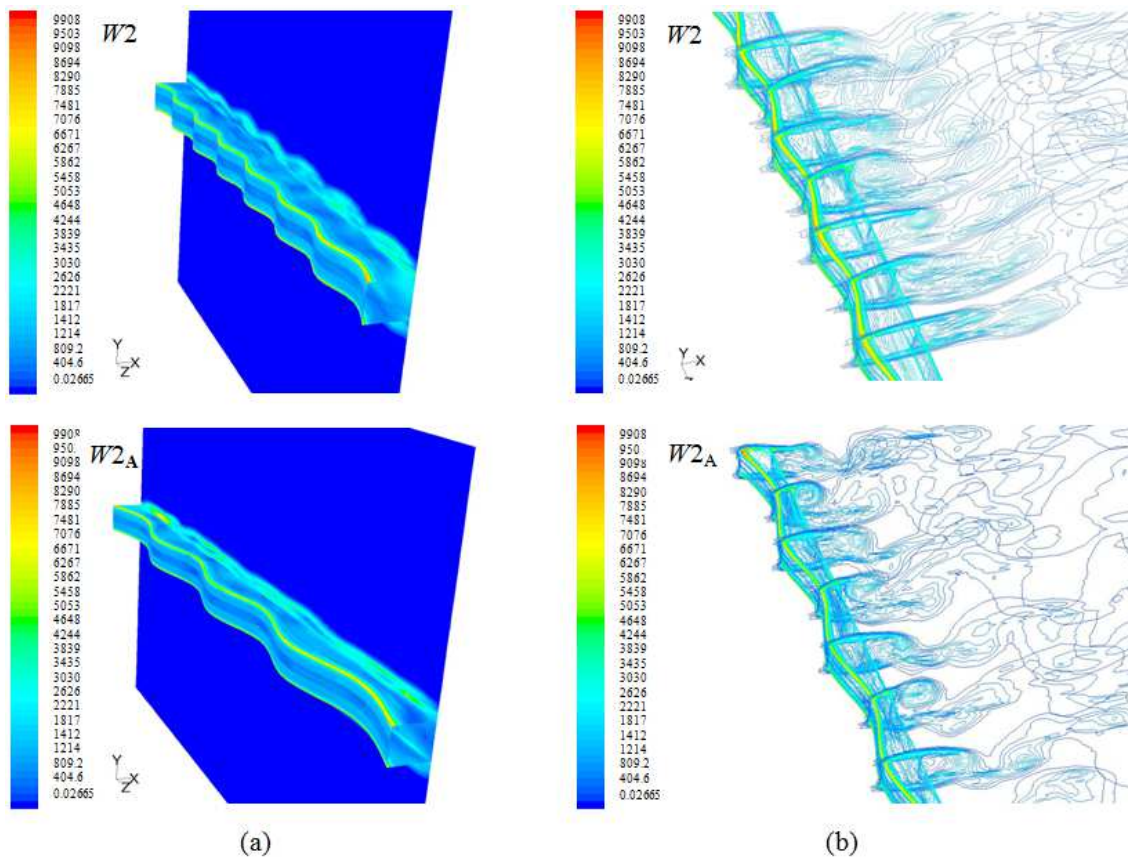


Figure 4.15: Contours of vorticity magnitude for the SSP geometries, (above) $W2$ ($\omega/\lambda = 0.105$ and $\lambda/D = 2.4$) and (below) $W2_A$ ($\omega/\lambda = 0.09$ and $\lambda/D = 5.2$); (a) vertical $y-z$ plane coincident to the trailing edge and (b) spanwise vertical $x-z$ planes coincident to peaks and valleys.

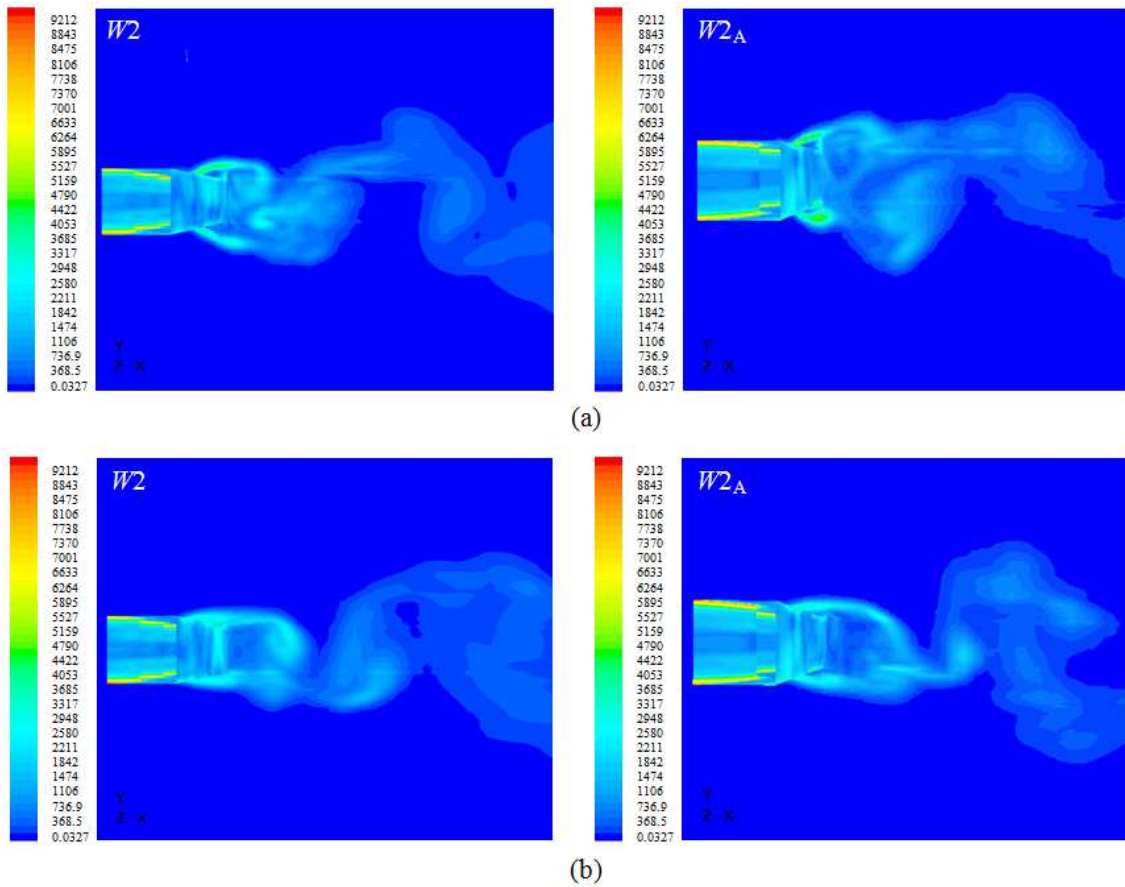


Figure 4.16: Contours of vorticity magnitude for W_2 (left) and W_{2A} (right); (a) vertical x - y planes at peaks and (b) vertical x - y planes at valleys.

The vorticity fields in the wakes of the cylinders W_2 and W_{2A} that are characterised principally by having different wavelengths share several characteristics. These are illustrated in Figure 4.16, as well as in Figure 4.15(b). Firstly, the vorticity fields do not display the same degree of mid-plane symmetry as that observed when considering the strongly sinusoidal leading edge, W_3 . The shear layers coincident with the valleys, Figure 4.16(b), are stretched downstream before they roll up into vortices. This is due to the flow remaining adjacent to the surface of the cylinder at valleys, resulting in a lower pressure gradient. As a consequence, the standard deviations of the drag and lift coefficients are reduced because the temporal disturbances in the shear layers occur at a

distance of about $3D$ downstream from the cylinders. However, the condition downstream of the peaks is somewhat different. In both the $W2$ and $W2_A$ cases, vortices are shed in close proximity to the trailing edge, and this is likely to contribute to temporal fluctuations in the lift and drag forces. Hence, the flow begins to separate from the cylinder surface at peaks. The net effect of the weak interactions near the trailing edge at the valleys, and strong interactions at the peaks would still result in the temporal variations in the drag and lift forces being reduced overall, however the effectiveness of a mild SSP would result in mitigation of aerodynamic forces; this is intermediate between plain cylinders and cylinders with a more marked SSP. This is corroborated by the findings.

A perhaps unexpected difference between the wakes generated by $W2$ and the longer wavelength cylinder, $W2_A$, is evident in the power spectral densities (PSD) of the vertical y -component of velocity portrayed in Figure 4.17. In the case of $W2$, the spectral peak occurs at the full vortex shedding frequency, f_{v0} , of approximately 45 Hz. However, the spectral peak occurs at half this frequency in the wake generated by $W2_A$. Furthermore, the PSD measured at a peak associated with $W2_A$ is less than that observed for $W2$. This is due to the strength of the shear layers in the wake of $W2_A$ especially at peaks and at the measuring point, given the somewhat higher rate of wake decay depicted in Figure 4.16. However, the maximum magnitude of the PSD is about one-third that observed in the case of the plain cylinder which also explains why the standard deviations of the drag and lift coefficients are still reduced in the two SSPs considered.

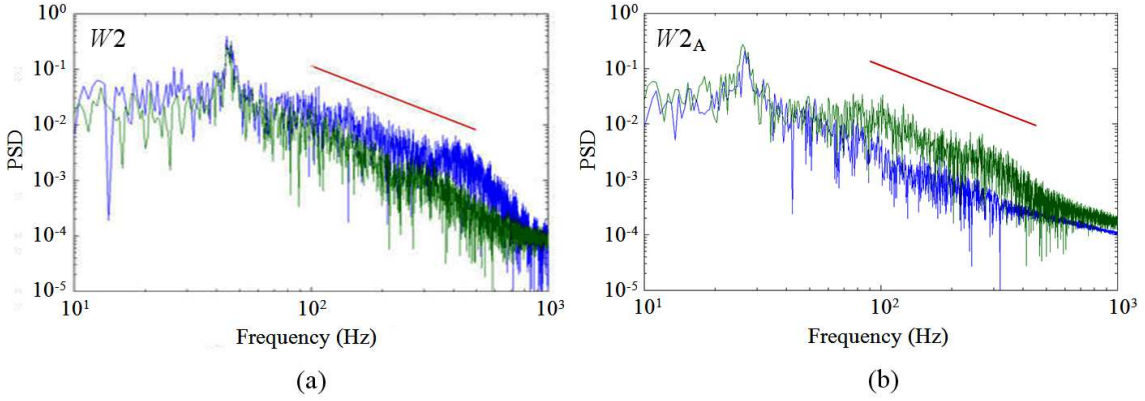


Figure 4.17: PSD of the v -component velocity spectra at peak (—) and valley (—) locations measured at $(x/D, y/D) = (2, 2)$; (a) $W2$ ($\omega/\lambda = 0.105$ and $\lambda/D = 2.4$); (b) $W2_A$ ($\omega/\lambda = 0.09$ and $\lambda/D = 5.2$).

This parametric investigation is continued by maintaining a constant wave steepness, ω/λ , and doubling the normalised wavelength, λ/D ; the two SSP geometries now studied are $W3$ ($\omega/\lambda = 0.195$, $\lambda/D = 2.4$) and $W3_A$ ($\omega/\lambda = 0.18$, $\lambda/D = 5.2$), also indicated in Figure 4.1. These two cases result in physically quite different geometries. The $W3_A$ geometry not only has an SSP with a larger wavelength, but its amplitude is also larger and as a result the dimensionless distance between the peaks and the trailing edge is very small, namely $0.0625D$. To recall, the geometry of $W3_A$ is chosen so as to not violate physical reality. This is likely to have a profound effect on the nature of the wakes produced by the two cylinders. The drag coefficients are nonetheless similar, namely 1.6 and 1.5 in the $W3$ and $W3_A$ cases, respectively, and their standard deviations are almost equal, i.e. 0.017 and 0.016, respectively. However, the mean absolute lift coefficients of the two geometries differ and they assume values of 0.087 and 0.056 in the $W3$ and $W3_A$ cases, respectively. This observation is expected due to the lower surface area of $W3_A$ that results in a lower pressure distribution across the upper and lower surfaces. Nonetheless, the standard deviations of the lift are

proportional to their absolute values being 0.019 and 0.012 respectively for $W3$ and $W3_A$ and they are remarkably over 30 times less than those associated with plain cylinders operating under the same conditions.

The characteristics of the vorticity fields of $W3$ and $W3_A$ are very similar, although at first inspection the vorticity in a plane coincident with the trailing edge of $W3_A$ is qualitatively different from that observed in the case of $W3$, as can be observed in Figure 4.18. This figure shows the vorticity in a plane coplanar with the trailing edge, as well as in vertical planes coplanar to peaks and valleys. In the former case, $W3_A$ loops of vorticity are adjacent to the upper and lower surfaces of the cylinder downstream of the valleys and are less apparent downstream of the peaks. This is in contradistinction to the $W3$ case in which the vortex loops are present and are separated downstream of the peaks. Due to the flow being channelled towards the peaks by the sinusoidal leading edge, there exists an adverse pressure gradient in the streamwise direction, giving the flow a high vertical component of velocity when exiting the peaks regions. This causes the flow to diverge from the horizontal mid-plane quite rapidly, but with relatively low vorticity. As a result of the proximity of the peaks to the trailing edge for $W3_A$, the illusion is given of an opposite spanwise topology emerging between $W3$ and $W3_A$ in the vertical y - z plane. However, the wakes are strikingly similar, as depicted in Figure 4.18(b).

Perspective views of the vorticity field in vertical x - y planes coincident with peaks and valleys are presented in Figure 4.19. In the case of $W3$, the flow downstream of the peaks, as well as valleys contains Bloor-Gerrard (Kelvin-Helmholtz) vortices. These convective small scale instabilities are less evident in the wake of $W3_A$. Nonetheless, both wakes display the upper and lower shear layers at peaks to be divergent about the

horizontal mid-plane due to the abrupt flow separation. The shear layers dissipate at a downstream distance from the cylinder of approximately $3D$. At valleys the flow is attached to the surface and the upper and lower shear layers remain parallel before diverging and dissipating at a downstream distance of $2D$. A likeness to the Mode-A wake instability is present for both wakes of $W3$ and $W3_A$, which is attainable from the highly symmetric upper and lower small scale vortices (Meiburg and Lasheras 1988).

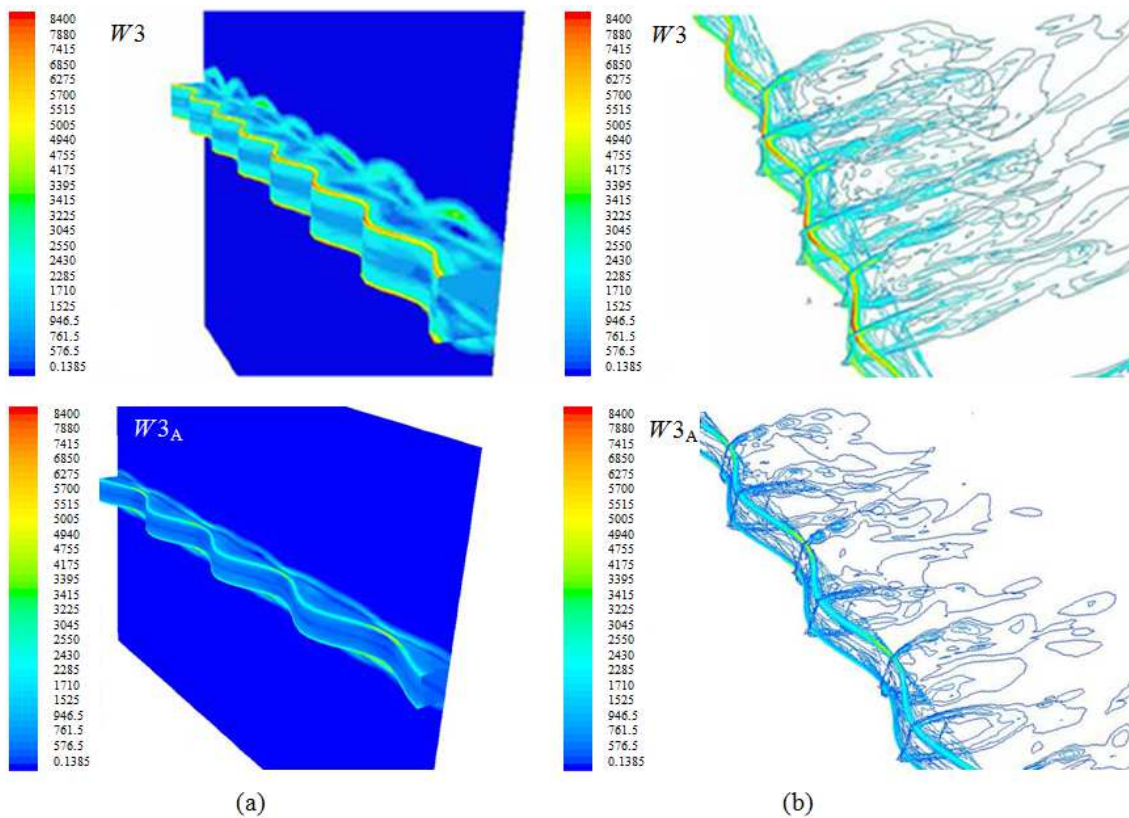


Figure 4.18: Contours of vorticity magnitude for the SSP geometries, (above) $W3$ ($\omega/\lambda = 0.195$ and $\lambda/D = 2.4$) and (below) $W3_A$ ($\omega/\lambda = 0.18$ and $\lambda/D = 5.2$); (a) vertical $y-z$ plane coincident to the trailing edge and (b) spanwise vertical $x-z$ planes coincident to peaks and valleys.

The flow fields of both $W3$ and $W3_A$ have common characteristics. The mitigation of vortex shedding and resulting flow topology is more apparent for $W3_A$, due to the proximity of the leading edge to the trailing edge. However, the observations presented throughout this work confirm the similarity in wake topologies between SSP geometries that have similar wave steepnesses, ω/λ , but not necessarily the same wavelength, λ/D . Hence, it can be stated that the ratio of ω/λ is an important parameter for controlling the flow field when employing the spanwise sinusoidal profile.

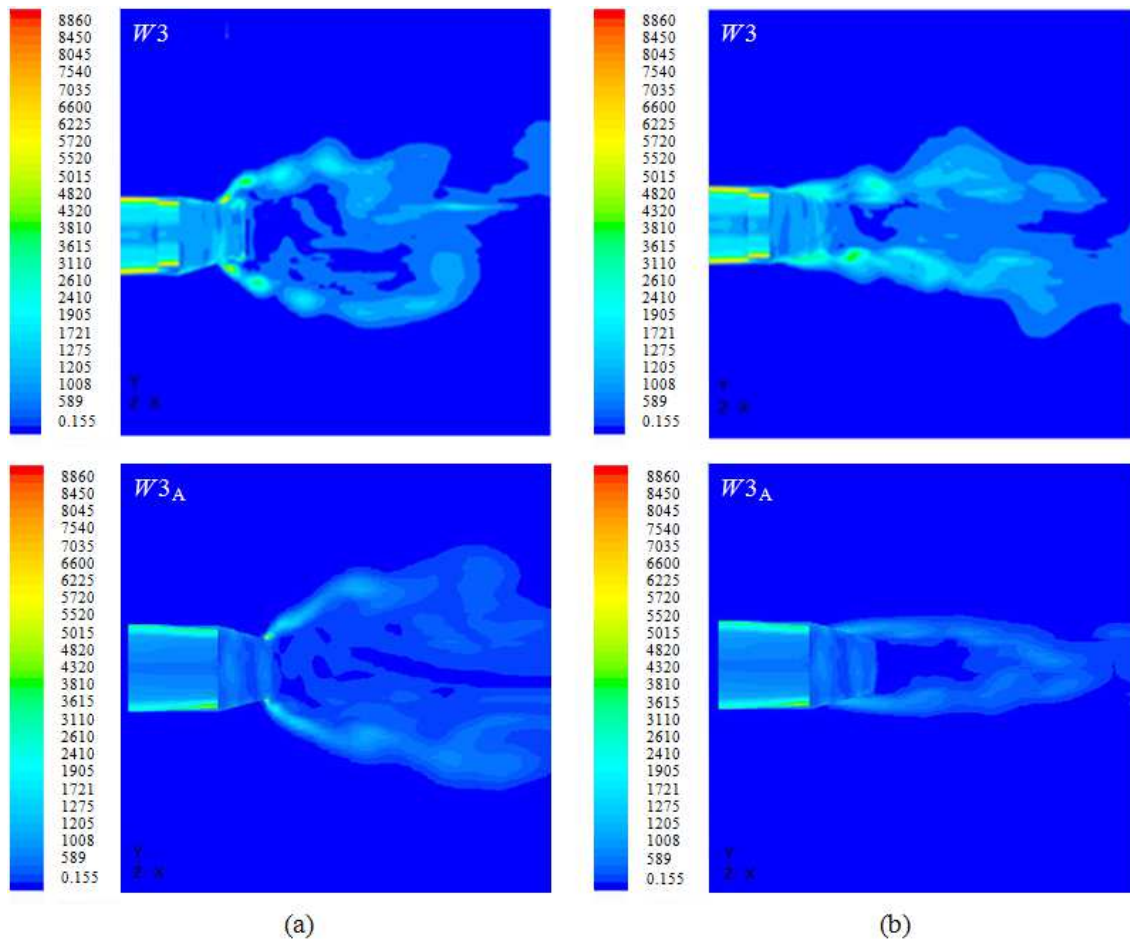


Figure 4.19: Contours of vorticity magnitude for $W3$ and $W3_A$; (a) vertical x - y plane coincident with a peak and (b) vertical x - y plane coincident with a valley.

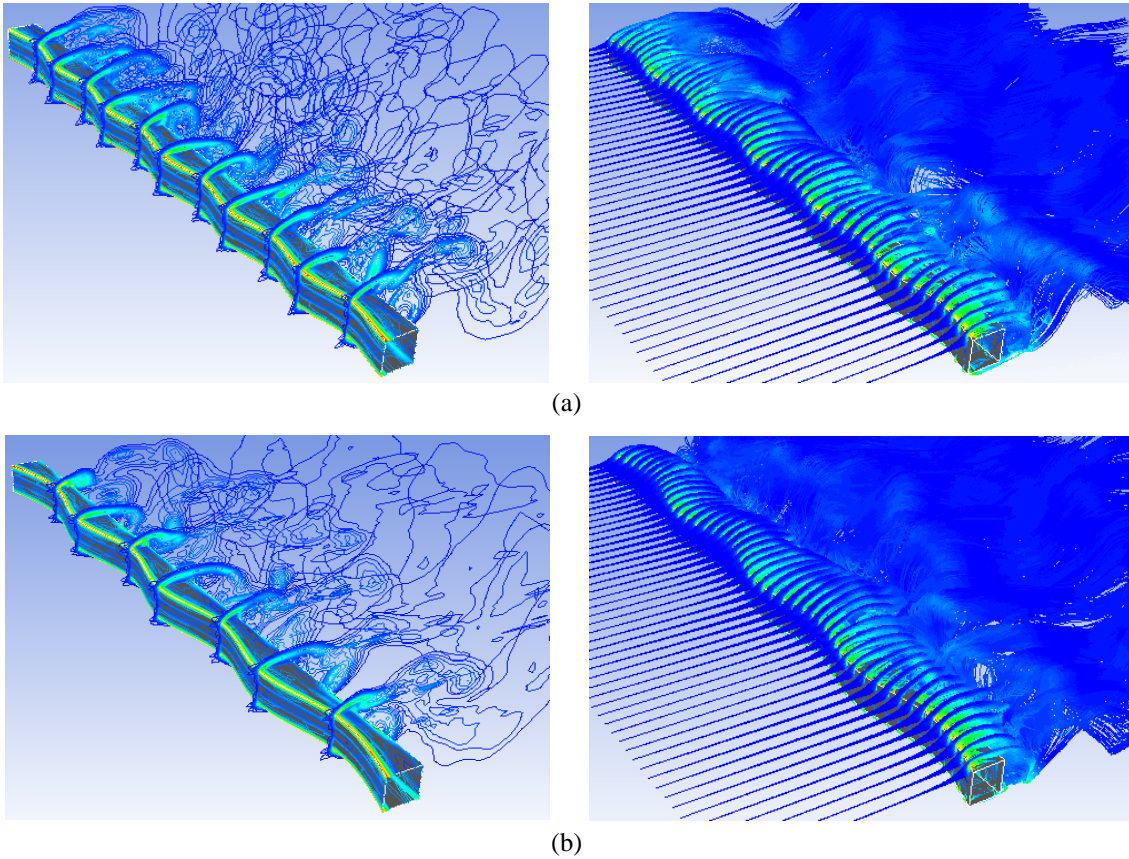


Figure 4.20: Contours of the vorticity fields around SSP square cylinders; (left) vertical x - y planes coincident with peaks and valleys of the SSP, and (right) isometric views of the resulting flow field. (a) SSP with $\omega/\lambda = 0.105$ and $\lambda/D = 3.2$ ($W2_B$), (b) SSP with $\omega/\lambda = 0.09$ and $\lambda/D = 5.2$ ($W2_A$).

To further corroborate the importance of the wave steepness on the control of turbulent flow, the topologies of the flow fields around the SSP configurations are compared. In Figure 4.20, the flow fields are given for the SSP bodies, $W2_A$ ($\omega/\lambda = 0.09$ and $\lambda/D = 5.2$), and an SSP cylinder, $W2_B$ ($\omega/\lambda = 0.105$ and $\lambda/D = 3.2$). Both these geometries have close wave steepness and the flow fields also show resemblance to each other. Clearly, an intermediate wake is present in both cases which is similar to that wake of $W2$ (Figure 4.15). The flow coincident to the valleys experiences stretching of the shear layers aft of the trailing edge; whereas, the flow coincident to the peaks rolls up into vortices near the trailing edge. This was discussed earlier in relation to the

wake of $W2$. Hence, a three-dimensional flow field is present, in which vortex shedding is highly discernable. The SSP cylinders, $W2_A$ and $W2_B$, demonstrate Regime-II type flow.

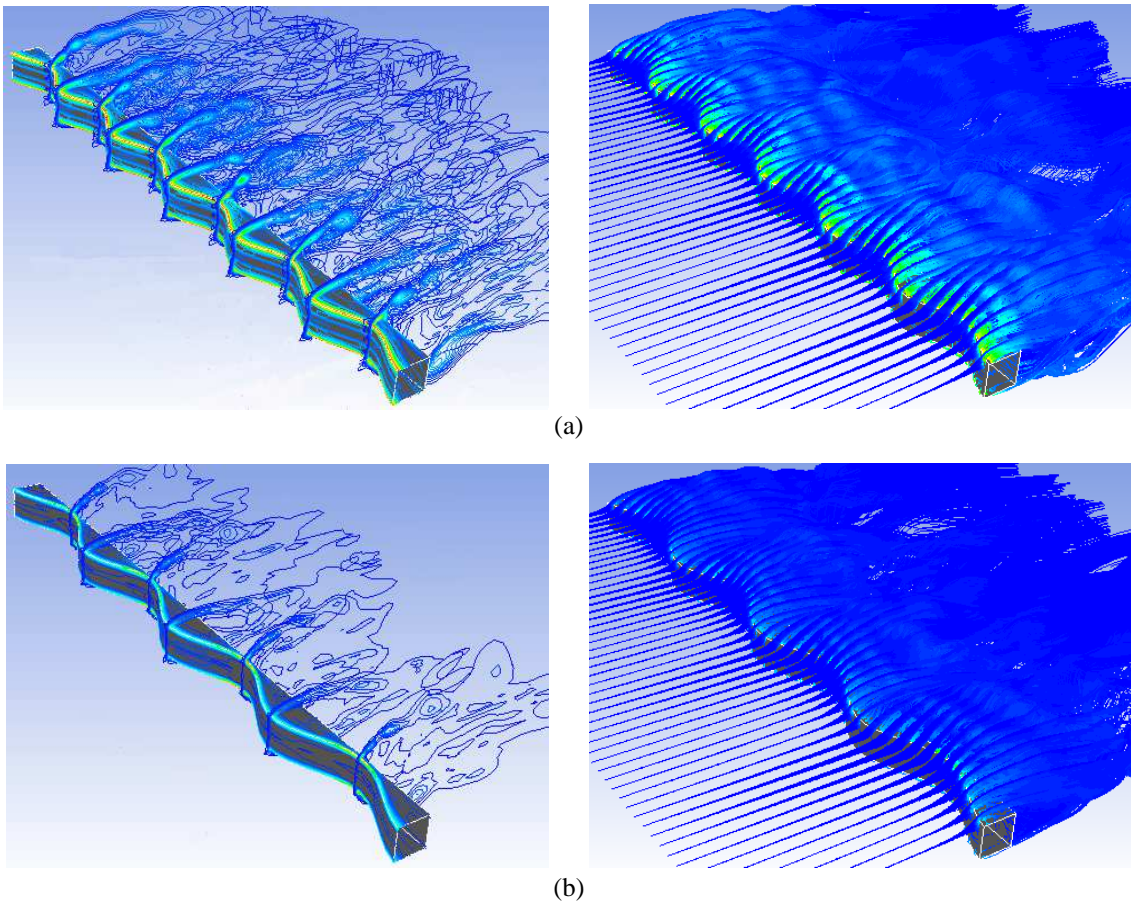


Figure 4.21: Contours of the vorticity fields around SSP square cylinders; (left) vertical x - y planes coincident with peaks and valleys of the SSP, and (right) isometric views of the resulting flow field. (a) SSP with $\omega/\lambda = 0.195$ and $\lambda/D = 3.2$ ($W3_B$), (b) SSP with $\omega/\lambda = 0.18$ and $\lambda/D = 5.2$ ($W3_A$).

In Figure 4.21, the flow fields are shown around $W3_A$ ($\omega/\lambda = 0.18$ and $\lambda/D = 5.2$), and an SSP geometry, $W3_B$ ($\omega/\lambda = 0.195$ and $\lambda/D = 3.2$). Under very similar wave steepness, the flow fields for both geometries clearly demonstrate Regime-III type instability. The flow coincident to the peaks contains Kelvin-Helmholtz instabilities as a result of the flow separation at the leading edge. This is highly discernable in Figure 4.21(b) for $W3_A$ due to the closer proximity between the leading and trailing edges (discussed earlier). At valleys, the flow remains attached to the surface of the cylinders and dissipates shortly after shedding from the trailing edge. The dissimilarities depicted in Figure 4.21 are only the cause of the geometry of the leading edges and the distance of the peaks to the trailing edge. Nevertheless, an incoherent flow field exists similar to that of $W3$. The topologies portrayed in Figures 4.20 and 4.21 support the notions discussed in this chapter that wave steepness governs the topology of the controlled turbulent flow.

4.4 Summary

It has been shown that the mean drag force on square cylinders immersed in turbulent flow can be reduced by about 30% if spanwise sinusoidal profiles (SSPs) are imposed on their leading edges. Furthermore, a validated numerical model indicates that an SSP is able to reduce the magnitude of lift forces by up to 95%. The imposition of an SSP on the leading edge can also reduce the magnitude of the fluctuations of the mean drag and lift by an order of magnitude, and this has potential benefits for reducing fatigue failure of structures exposed to turbulent flows.

Vortices shed along the span of plain square cylinders cause large temporal variations in the lift and drag. However, the wake generated by a square cylinder with

an SSP imposed on the leading edge is found to have a quite different topology. A cylinder with an SSP leading edge with a wave steepness, ω/λ , of 0.195 and a normalised wavelength, λ/D , of 2.4 contains a wake with small-scale Kelvin-Helmholtz instabilities being shed from the cylinder. This is reflected in the power spectral density of the v -component of the velocity that shows a clear vortex shedding frequency in the wake of plain cylinders but not in the case of the SSP geometry. The peaks of the SSP channel the flow and this increases the mass flux at these regions. Vortices shed downstream of valleys are shed predominantly in the direction of the free-stream flow.

Results of the studies indicate that the wavelength of a spanwise sinusoidal profile appears to be of less importance in suppressing the synchronous shedding of vortices in turbulent flow than in laminar flow. Comparisons are made between flow regimes that exist for laminar flow and the wake topologies elucidated for turbulent flows. Numerical simulations suggest that the wave steepness, ω/λ , plays a more important role in suppressing vortex shedding in turbulent flows than in laminar flows.

THE EFFECT OF ASPECT RATIO ON A SPANWISE SINUSOIDAL PROFILE

To date, the research on turbulence generated by bluff bodies has focussed on vortex shedding and flow control around slender bodies such as circular and square cylinders (Griffin and Ramberg 1982; Williamson 1996; Bearman and Owen 1998; Darekar and Sherwin 2001; Catalano *et al.* 2003; Bearman and Brankovic 2004; Dobre *et al.* 2006; Xu *et al.* 2010). On the other hand, many practical applications involve bluff bodies with a large aspect ratio in which the geometries are elongated in the direction of the flow. In contrast to slender bodies, the flow around an elongated bluff body experiences two types of shear layer interactions; flow separation and reattachment. The shear layers are likely to separate aft of the bluff leading edge, then reattach to the surface of the structure some distance downstream, before detaching from the trailing edge after having been shed from the body. Modifying the typical behaviour of the shear layer phenomena may enhance the flow around the elongated bluff body. This can be achieved by applying a spanwise sinusoidal profile (SSP) to the leading edge. However, in addition, the effectiveness of an SSP on the leading edge may be mitigated as a result of the increased distance to the trailing edge.

The research presented in this chapter highlights features of turbulent flow fields around elongated bluff bodies with and without a spanwise sinusoidal profile (SSP) on

their leading edge. The effects of the geometry of the SSP on the coherence of the shear layers and the vorticity field downstream of the structure will be described. Results are interpreted by making use of vorticity magnitude distributions and pathlines, which characterise the topology of the wake. In addition, time-averaged flow properties are provided. Numerical studies indicate that the nature of turbulent flows around elongated SSP geometries differ from that generated by square geometries. The principal findings presented in this chapter are namely,

1) The aerodynamic forces (i.e. drag and lift) and their fluctuations acting on an elongated bluff body can be greatly reduced if an SSP is imposed on the leading edge. The flow field and wake of the elongated SSP body resembles that of a streamlined body, and as a result, a significantly higher base pressure is achieved.

2) The proximity of the SSP leading edge to the trailing edge does not profoundly influence the control of the flow field. The sinusoidal perturbations are capable of largely dissipating the shear layers, and forming a narrow wake behind the elongated body.

5.1 Flow Field around an Elongated SSP Cylinder

In this research, the effectiveness of the SSP has been confirmed and it has been observed that the vortices in the upper and lower shear layers merge in the near to intermediate wake of a square cylinder (slender body) that has an SSP applied to the leading edge. This occurs in the turbulence generated by the body and has been discussed in Chapter 4. However, in many practical applications, cylinders are not square, but they are elongated in the direction of the flow. In other words, they are rectangular and they approach the geometry of flat plates. In this case, it might be

expected that the disturbances in the flow caused by the SSP become attenuated as the cylinder becomes more elongated. As a consequence, the vortical structures downstream of the trailing edge may be anticipated to become less dependent on the geometry of the leading edge.

The square geometries of $W0$ and $W3$ have been elongated in the direction of the flow (i.e. positive x -direction). Hence, two models, namely $W0_E$ and $W3_E$ are presented herein to explore the topology of the flow field around a plain rectangular prism and a rectangular prism with an SSP applied to the leading edge. The computational models are shown in Figure 5.1. Both SSP geometries have aspect ratios D_1/D of 5 (where D_1 is the full width of the elongated cylinders), to examine the behaviour of the flow on the surface of an elongated SSP geometry, and whether or not the detaching-reattaching phenomena can be controlled (modified). Therefore, it is desired to extract details of the flow field that demonstrate the ability of the SSP to passively control the boundary layer developed over a flat surface. In this research, highly effective control of the flow field has been demonstrated to coincide with a largest possible wave steepness, ω/λ , of the spanwise sinusoidal profile. Hence, in the case of $W3_E$, the wave steepness, ω/λ , and normalised wavelength, λ/D , remains identical to that of the square cylinder, $W3$, at values of 0.195 and 2.4, respectively.

As the shear layers reattach to the surface of the elongated SSP geometry, it is expected that this will promote the development of vorticity. Recall that in the wake of a square cylinder, the shear layers coincident to peaks and valleys merge at a downstream distance from the trailing edge of approximately $4D$. In the case of the elongated cylinder, $W3_E$, maintaining the free-stream velocity, U_0 , of 11 ms^{-1} , corresponding to a Reynolds number, Re , equal to 2.35×10^4 can generate the same flow

conditions as that of the square cases, and therefore, the shear layer merging on the surface of the rectangular prism at approximately $4D$. It may be that the merging of the shear layers at a downstream distance of $4D$ allows the re-establishment of Kármán vortices. In fact, the convective Kelvin-Helmholtz instabilities (Bloor-Gerrard vortices) have been characterised to eventually form into Kármán vortices (Sheridan *et al.* 1992). In addition, Dobre (2006) also reported the reoccurrence of vortices within the intermediate wake of a square cylinder at a distance of $9D$ as a result of the shear layers merging at this location. Nevertheless, the energy of the vorticity was reported to be somewhat attenuated due to the passive controller. Whether or not the fluid structures generated on the surface of the elongated body are less dependent on the sinusoidal leading edge as a result of the increased proximity between the leading and trailing edges are to be investigated.

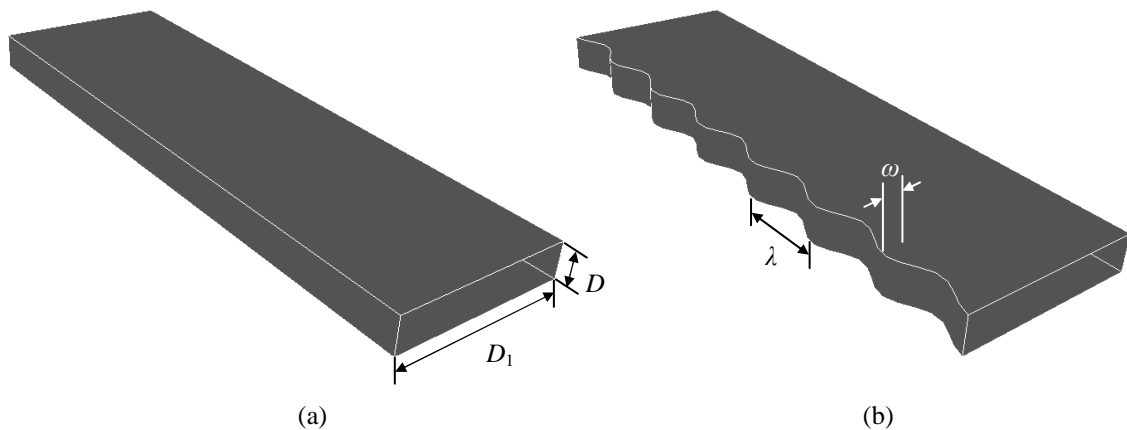


Figure 5.1: Computational models of the plain and SSP elongated cylinders; (a) $W0_E$ and (b) $W3_E$. The wave height (peak-to-peak), ω , and wavelength, λ , of the sinusoidal leading can be depicted.

5.1.1 Performance of Aerodynamic Forces of an Elongated SSP

Achieving control of the flow field as a result of the spanwise sinusoidal profile is associated with a significant reduction of the drag force. In Figure 5.2(a), the coefficient of the mean drag, C_d , is plotted against the non-dimensional time, t/dt , for both $W0_E$ and $W3_E$. The value of the mean drag coefficient for the plain and SSP geometries is respectively 1.17 and 1.06. Hence, it is clear that the elongated SSP geometry experiences up to 10% decrease in mean drag; this in turn corresponds to a significant reduction in the fluctuations of the drag. The reduction in C_d for the elongated SSP geometry is not as large as that of the square geometry, as might be expected priori.

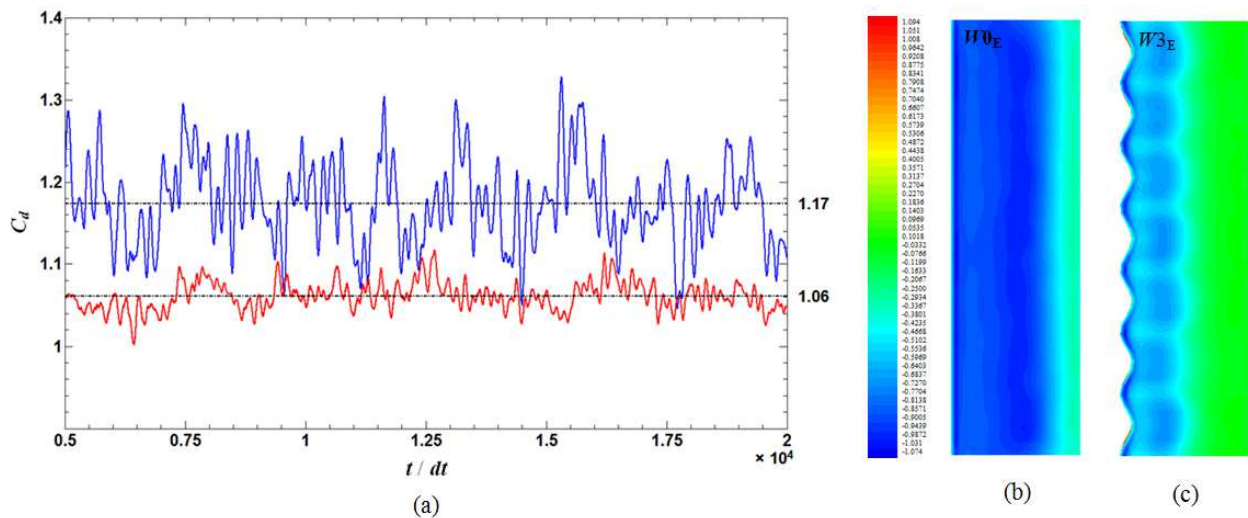


Figure 5.2: (a) Coefficient of drag, C_d , for the plain elongated cylinder, $W0_E$ (blue), and the elongated SSP geometry, $W3_E$ (red), which highlights the reduction of up to 10% in the mean drag and related reduction of the fluctuations as a result of the SSP. This is corroborated by the time-averaged contours of the pressure coefficient, C_p , for (b) $W0_E$ and (c) $W3_E$, taken on the upper horizontal surface of the geometries. $W3_E$ has greater percentage of high pressure across the surface, particularly the highly discernable larger base pressure that is associated with the decrease in mean drag.

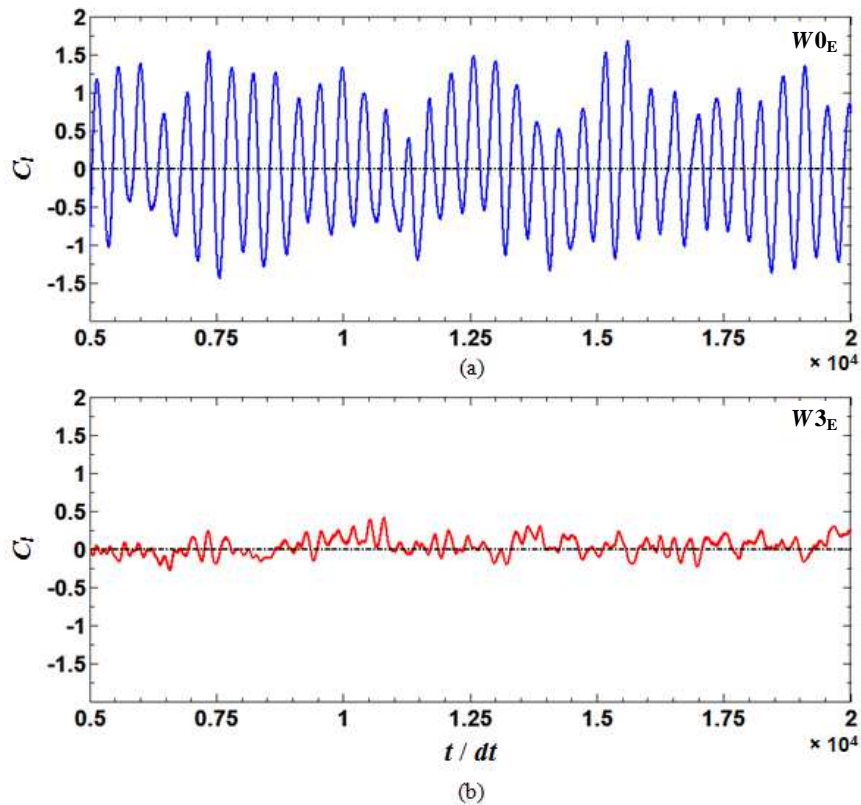


Figure 5.3: Coefficient of lift, C_l , for (a) the plain elongated geometry, $W0_E$, and (b) the elongated SSP geometry, $W3_E$; highlighting the significant reduction in the fluctuations of lift as a result of the SSP.

The reduction in mean drag can be demonstrated by contours of the time-averaged pressure coefficient, C_p , across the upper surfaces of the geometries. In Figure 5.2(b), higher pressure exists across the trailing edge of $W0_E$, while the pressure elsewhere on the surface displays significantly lower values. In stark contrast, higher pressure regions exist across approximately 60% of the surface of $W3_E$, depicted in Figure 5.2(c); this visual representation of C_p helps to corroborate the remarkable difference in mean drag between an uncontrolled ($W0_E$) and controlled ($W3_E$) flow field.

A significant reduction is achieved in the fluctuations of the lift. Figure 5.3 displays the coefficient of lift, C_l , plotted against t/dt . Large fluctuations about the zero mean lift are depicted for $W0_E$. However, these fluctuations become almost negligible for the case of an SSP geometry, $W3_E$, as shown in Figure 5.3(b); this corresponds to an approximately 83% decrease. This ability of the spanwise sinusoidal profile on an elongated geometry to steady the forces acting on the bluff body is indeed a remarkable characteristic.

The significant reduction in the drag force, is corroborated by the distribution of the time-averaged pressure coefficient, C_p , shown in Figure 5.4. The measurements are made on the upper and lower surfaces of both $W0_E$ and $W3_E$, at locations corresponding to the center of the span, and the central peak and valley, respectively. Figure 5.4(a) compares the pressure distribution for the current plain elongated cylinder, and the plain cylinder of Yu *et al.* (2013), which contains an aspect ratio similar to the current case of $D_1/D = 5$, and at $Re = 1 \times 10^5$. A very close agreement exists between the current numerical distribution and the LES distribution of Yu *et al.* (2013), especially the prediction of the pressure recovery approximately mid-way along the surface of the prism. This is due to a concomitant flow reattachment at this region as a result of the streamwise aspect ratio, and both profiles display a similar maximum mean pressure near the trailing edge. In addition, both distributions demonstrate local peak pressures at the leading edge.

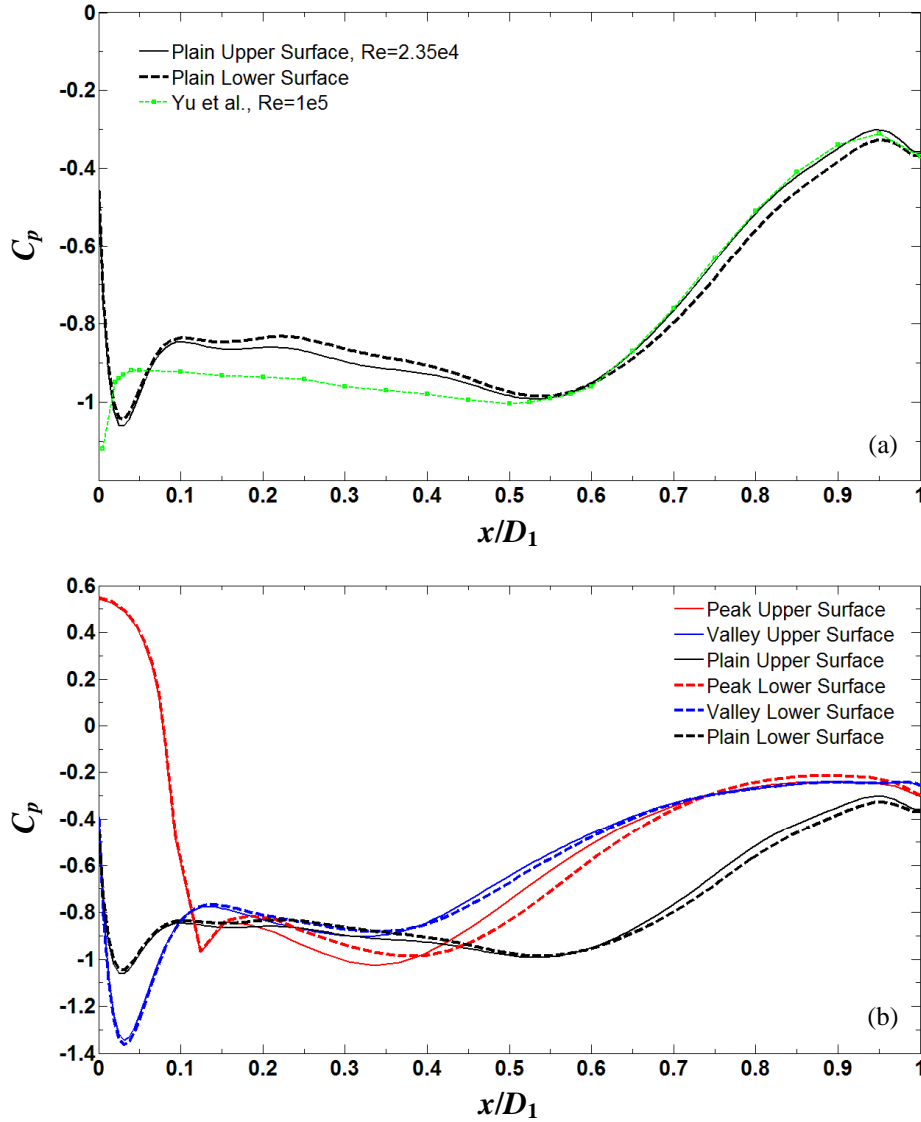


Figure 5.4: Distribution of the time-averaged pressure coefficient, C_p , on the upper and lower surfaces of the plain and SSP elongated cylinders with aspect ratio, D_1/D , of 5. (a) Comparison for a plain elongated cylinder between the current numerical model at $Re = 2.35 \times 10^4$ and that of Yu *et al.* (2013) at $Re = 1 \times 10^5$, and (b) distributions measured at mid-span for the plain elongated cylinder, $W0_E$, and coincident to a peak and valley at the mid-span region for the SSP elongated cylinder, $W3_E$.

Figure 5.4(b) compares the mean pressure distribution for the plain, $W0_E$, and SSP, $W3_E$, elongated cylinders. A high pressure gradient exists at the leading edge coincident to a peak of $W3_E$, as noted by the local maximum pressure above a C_p of 0, indicating a

separated almost stagnant flow. A local maximum mean pressure is also present at the leading edge coincident to a valley of $W3_E$, as well as for $W0_E$, typical when the flow travels around a sharp corner such that of a square cylinder. The mean pressure distributions coincident to a peak and valley display identical flow behaviour after the leading edge (i.e. they follow the same trend). Furthermore, a discernable pressure recovery exists at approximately one quarter the length of the prism aft of the leading edge, which signifies flow reattachment. Hence, not only does an elongated cylinder with a large aspect ratio contain low values of drag force due to flow reattachment; an SSP applied to the leading edge obtains a pressure recovery on the surface much earlier downstream, contributing to an even lower drag force.

In Figure 5.5, the distribution of the time-averaged pressure coefficient, C_p , in the wake of the plain, $W0_E$, and SSP, $W3_E$, elongated cylinders is shown. Similar to the observations for a square cylinder SSP (Figure 4.9), the distributions coincident to a peak and valley of $W3_E$ show close behaviour. As a result of the SSP on the leading edge of the elongated cylinder, the recovery of the pressure to the value of that of the free-stream flow occurs earlier than for $W0_E$. However, the plain and SSP elongated cylinders exhibit similar base pressure at the trailing edge, and the distributions follow closely agreed profiles. This indicates that the aspect ratio of the bluff body affects the characteristics of the flow field downstream of the leading edge. The incoherent three-dimensional flow that is typically generated by an SSP on the leading edge is clearly attenuated towards the trailing edge with a large aspect ratio, in this case $D_1/D = 5$. Nevertheless, a lower drag force exists with $W3_E$ than with $W0_E$ as a combined result of the inherently low drag associated with a large aspect ratio, and the higher base pressure from the application of the SSP.

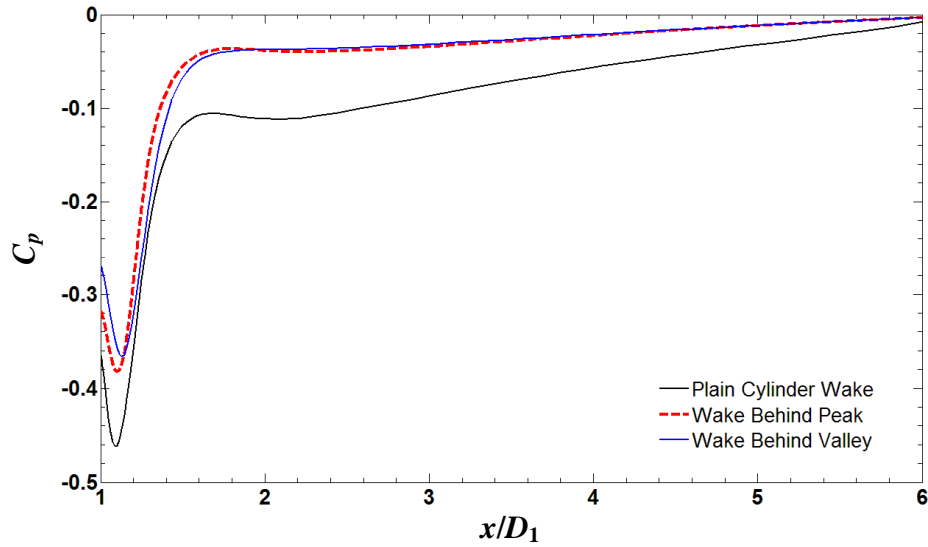


Figure 5.5: Distribution of the time-averaged pressure coefficient, C_p , in the wake of plain elongated cylinder, $W0_E$, and the elongated SSP cylinder, $W3_E$.

The curvature of the separated shear layer adjacent to the trailing edge affects the base pressure and also the pressure recovery into the wake (Sohankar 2008). If the shear layer is forced to remain close to the surface of the cylinder and therefore contains low curvature, such as that observed for $W3_E$, this generates a significant reduction in the drag force (Bearman and Trueman 1972). The instantaneous flow visualisations given in this chapter corroborate these observations.

5.1.2 Topology of the Flow Field around an Elongated SSP

Contrasting evidence of the effectiveness of an SSP on an elongated geometry is demonstrated in Figure 5.6, showing the flow in vertical x - y planes across the span that coincide with peaks and valleys of the sinusoidal leading edge (left of Figure 5.6), and pathlines of the flow representing the magnitude of vorticity (right of Figure 5.6). The Pathlines are approaching the leading edge coincident to a plane $0.25D$ below the upper

surface. This horizontal plane provides strong evidence of the phenomena associated with the flow near the surface of an elongated prism with and without an SSP.

In Figure 5.6(a), the flow around the plain elongated geometry is two-dimensional, passing coherently over the prism and rolling up into vortices at the trailing edge. Recall in this work the definition of a two-dimensional wake is where the flow field experiences changes in only the x - y planes; i.e. there is only slight phase difference in the vortical structures in the spanwise direction. Under idealised conditions the development of the boundary layer on the upper and lower surfaces of the plain elongated prism would indeed be completely two-dimensional. However, in reality the flow field displays some three-dimensional characteristics. Phenomena associated with that of an elongated bluff body (i.e. rectangular prism) are present in Figure 5.6(a), in which the shear layers separate from the horizontal surface aft of the leading edge and reattach to the surface downstream at approximately $3D$ to $4D$. The flow reattaching prior to the trailing edge results in strong circulation of the entrained shear layers to induce vortices. The vortices contain substantial kinetic energy as a result of the high energy mixing of the upper and lower shear layers aft of the trailing edge; i.e. a Kármán vortex street is formed.

Figure 5.6(b) provides a graphic demonstration of the phenomena resulting from an SSP. The fluid-to-structure interaction at the sinusoidally modulated leading edge and the evolving vorticity field aft of the leading edge are clearly evident. The pathlines of iso-vorticity are elevated above the surface of $W3_E$ downstream of the peaks. These regions are associated with a rapid flow separation occurring at the leading edge. Coincident with valleys, the pathlines remain close to the upper and lower surfaces. The spanwise periodic nature depicted in the pathlines is a result of the channelling of the

flow at peaks, as evidenced by the velocity vectors that were evident in the case of the square geometries. It can be seen that the substantial channelling of the flow is localised at the center of the peaks at the leading edge. Hence, the flow at these locations experiences a large pressure gradient and separates abruptly from the surface. The interference of the flow field depicted in Figure 5.6(b) introduced by applying an SSP hinders the development and interaction of the shear layers that would otherwise form a Karman vortex street.

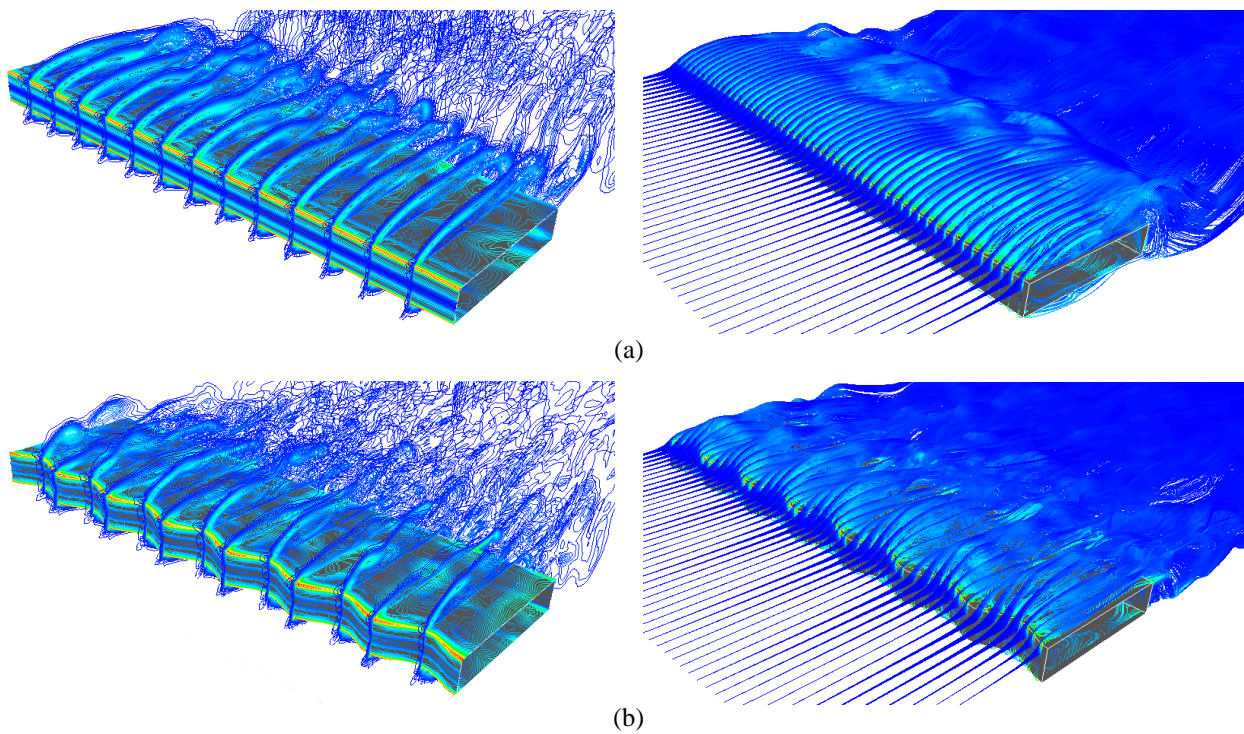


Figure 5.6: Contours of the vorticity fields around (a) $W0_E$ and (b) $W3_E$; (left) vertical x - y planes coincident with peaks and valleys of the SSP, and (right) isometric views of the resulting flow field.

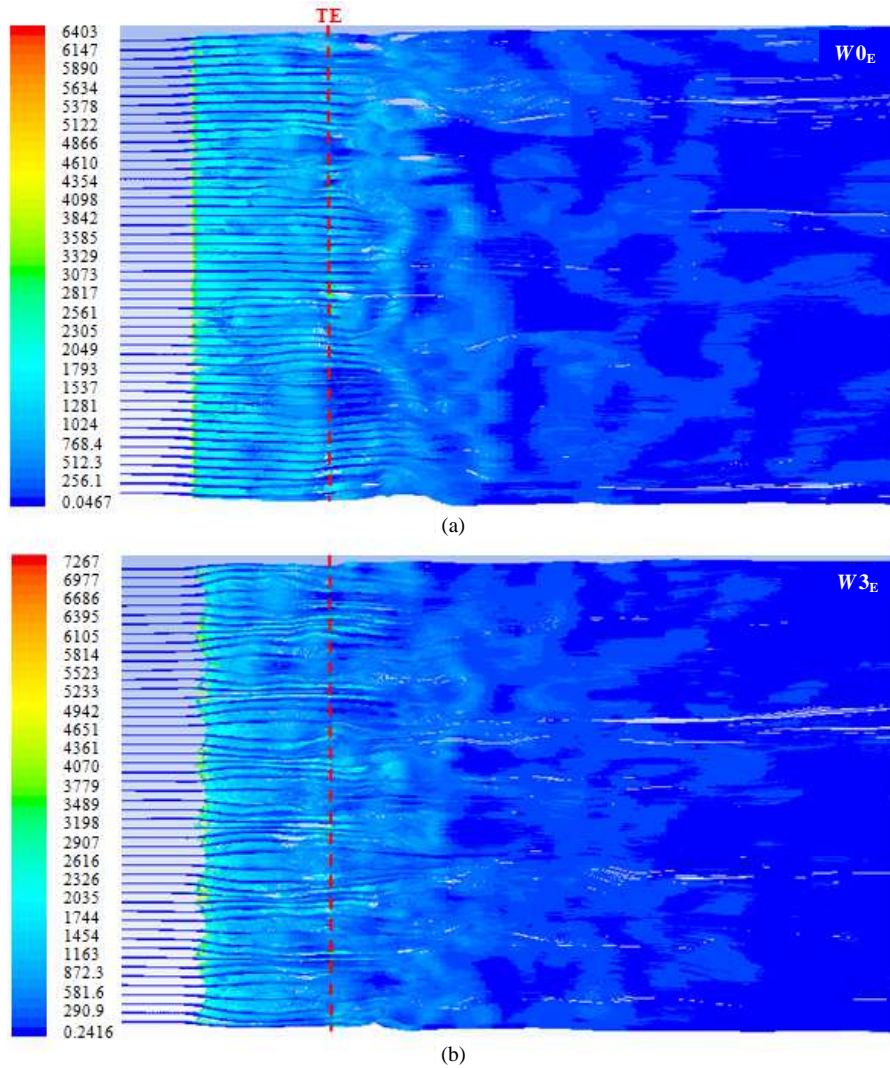


Figure 5.7: Pathlines highlighting the magnitude of vorticity for (a) $W0_E$ and (b) $W3_E$, observed from the top of the horizontal x - z plane coincident with the upper surface of the elongated cylinders.

Observing from the top of the vorticity field of Figure 5.6, the pathlines in Figure 5.7 demonstrate stark evidence of spanwise periodic phenomena. At peaks, the pathlines at a location directly behind the leading edge diverge from a line coincident with the center of the peak. This phenomenon causes the pathlines to converge aft of valleys. This is in contrast to the pathlines shown for a plain elongated geometry in Figure 5.7(a), in which they remain parallel. To explain the flow topology associated with the SSP geometry, $W3_E$, the channelling of the flow and the related increase in pressure

drives the flow to disperse behind the leading edge in reaction to the channelling. This in turn establishes an interaction between the pathlines coincident with both peaks and valleys and causes convergence at valleys. At the trailing edge, the vorticity is dissipated as a result of the lower energy vortical structures. It can be seen that the pathlines converge slightly at the trailing edge to be equally spaced, reflecting the geometry of the leading edge. This three-dimensional behaviour across the span and the streamwise evolution of the pathlines demonstrates significant disturbance to the flow, and it can be seen that the development of the flow field is delayed.

An examination of the vorticity only in planes that are coincident with the peaks and valleys of the SSP provides a clearer idea of the flow phenomena around the elongated prisms. Figure 5.8 shows perspective views of the magnitude of vorticity contours in vertical x - y planes that are coincident with the central peak and valley of the elongated SSP cylinder, $W3_E$. In the case of the plain geometry, $W0_E$, the vorticity is presented in vertical planes coinciding with similar planes to those of $W3_E$. The view is from the side of the prism and the flow direction is from left to right.

The vorticity field around the elongated cylinders display very similar behaviour near the leading edge as that produced by the square SSP cylinder. However, the topology of the wake differs somewhat as a result of the larger aspect ratio. In Figure 5.8(a), it is clear to see the shear layers detach from the surface of $W0_E$ aft of the leading edge. However, the flow appears to remain relatively close to the surface of the cylinder, which allows the flow to reattach immediately upstream to the trailing edge; the entrainment of the fluid forms the roll-up of the shear layers into vortices.

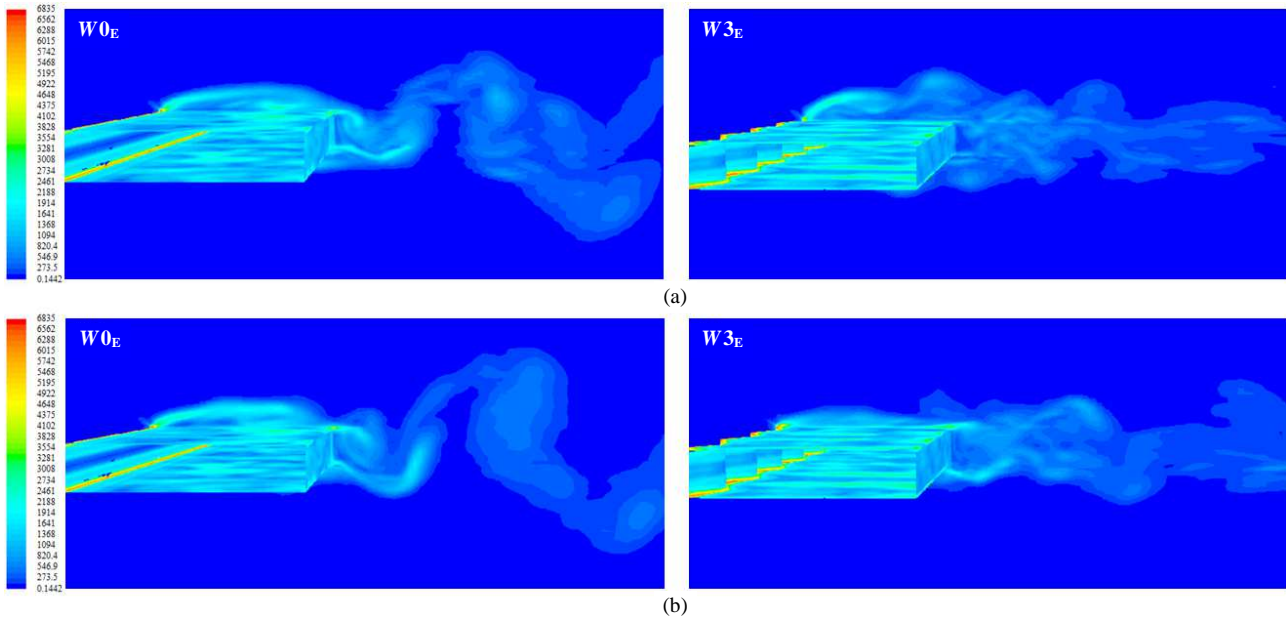


Figure 5.8: Perspective views of the vorticity field around $W0_E$ (left) and $W3_E$ (right); (a) mid-span vertical x - y plane coincident to a peak, and (b) mid-span vertical x - y plane coincident to a valley.

In contrast, the vorticity at peaks of the elongated SSP cylinder, $W3_E$, indicates flow separation directly at the leading edge and this is followed by the roll-up of the free shear layers into what appears to be Kelvin-Helmholtz instabilities (Bloor-Gerrard vortices) in both the upper and lower halves of the prism. These vortices are then shed into the wake, and are shown in Figure 5.8(a). The shedding frequency of the Bloor-Gerrard vortices is about $3f_{v0}$, where f_{v0} is the vortex shedding frequency of the plain square cylinder corresponding to a Strouhal number, St , of 0.14. This is similar to the case of an SSP square cylinder geometry, and is probably a result of employing the same Reynolds number. The SSP interrupts the flow field to cause the small scale vorticity behind a peak of $W3_E$, to be largely dissipated at a downstream distance from the trailing edge of approximately $2D$; whereas the wake behind a plain elongated prism retains its coherence for a greater distance.

In Figure 5.8(b), the same observations as those in Figure 5.8(a) can be made for $W0_E$ regarding the vorticity around the plain elongated geometry. Hence, the vorticity field around $W0_E$ is independent on the spanwise location; this was addressed in earlier observations in Figure 5.6, and is similar to the flow field characteristics around a plain square cylinder. In Figure 5.8(b), in a vertical x - y plane coincident with a valley of the elongated SSP, the flow remains attached to the horizontal surfaces of $W3_E$ up to the trailing edge. In addition, the boundary layer is thin across the upper and lower surfaces. As a consequence, a narrow wake is formed when the flow is shed from the trailing edge and remains parallel to the average flow direction. The energy of the flow in the wake is attenuated at a location of approximately $3D$ downstream from the trailing edge. The loss in energy is a result of the spanwise interaction between the shear layers as the Kelvin-Helmholtz instabilities form coincident with peaks. In contrast to a square cylinder with an SSP, there is an absence of Bloor-Gerrard vortices coincident with a valley for $W3_E$. Nonetheless, it is clear that for an elongated bluff body with the passive controller applied to the leading edge, a periodic structure of the shear layers is generated in the spanwise direction. This is indeed characteristic of a spanwise sinusoidal profile.

The streamwise development of the flow around an elongated SSP cylinder can be explored in great detail by exploring the velocity profiles coincident to the peaks and valleys. Figure 5.9 shows the time-averaged streamwise velocity, \bar{u} , profiles at different streamwise locations on the upper surface of both the plain, $W0_E$, and SSP, $W3_E$, elongated cylinders. The profiles are measured along the center of the span in both cases, in which the streamwise velocity is examined at the central peak and valley of $W3_E$, and the center of $W0_E$. The transition of the flow across the surface with and without the influence of the SSP is demonstrated.

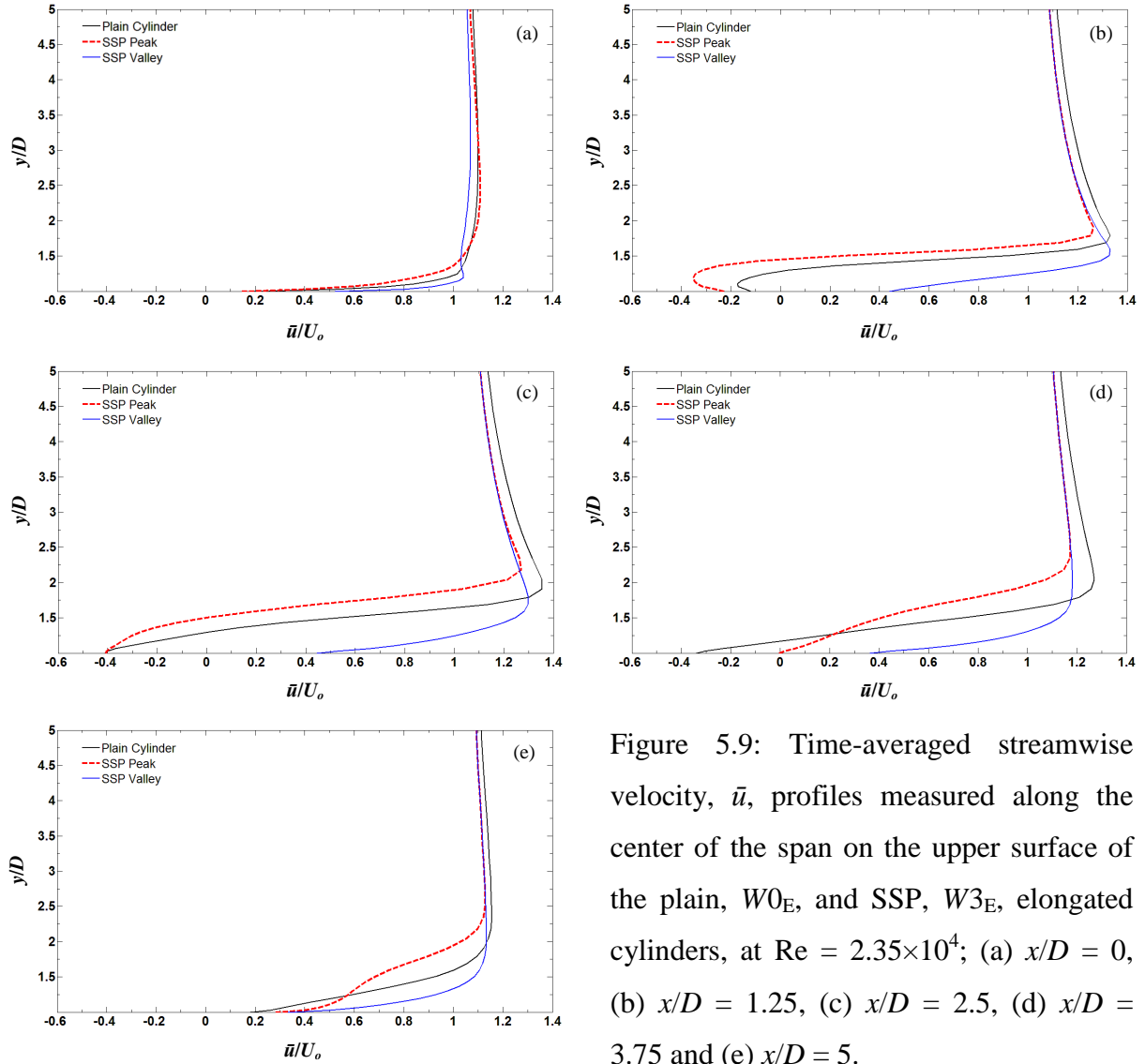


Figure 5.9: Time-averaged streamwise velocity, \bar{u} , profiles measured along the center of the span on the upper surface of the plain, $W0_E$, and SSP, $W3_E$, elongated cylinders, at $Re = 2.35 \times 10^4$; (a) $x/D = 0$, (b) $x/D = 1.25$, (c) $x/D = 2.5$, (d) $x/D = 3.75$ and (e) $x/D = 5$.

At the leading edge, $x/D = 0$ (i.e. location of a valley for $W3_E$), in Figure 5.9(a), typical behaviour of flow separation can be identified as the streamwise velocity of both $W0_E$ and $W3_E$ approach the value of the free-stream velocity quite abruptly near the surface of the leading edge. Furthermore, the velocity profile coincident to the valley of $W3_E$ displays flow reversal close to the surface at approximately $y/D = 1.25$. This may be a repercussion of the channelling phenomena existing at the peak, discussed in Chapter 4 and readdressed in Section 5.1.2. It should be noted that coincident to a peak, the actual leading edge location is $x/D = 0.47$, due to the wave height, ω , of the SSP

equal to 0.015 m. Aft of the leading edge at $x/D = 1.25$ (Figure 5.9(b)), the flow is still detached from the surface at the peak of $W3_E$, and likewise for $W0_E$. There exists a region of flow reversal near the surface due to the entrained fluid in the separated shear layers. At the valley of $W3_E$, the flow is adjacent to the surface as depicted by the higher streamwise velocity, \bar{u} , closer to the surface than for the peak, and also by the absent flow reversal.

It is remarkable that the characteristic of the streamwise velocity at the peak of $W3_E$ follows a similar trend to the velocity profile observed with a plain elongated cylinder, although the flow at a peak experiences larger flow separation. This remains the case for the additional monitored locations downstream from the leading edge along the upper surfaces. However, at $x/D = 3.75$, the velocity profiles shows that the free shear layer identified at the location of the peak reattaches to the surface just before the trailing edge. A boundary layer is formed as a result of the entrained fluid. At the trailing edge, $x/D = 5$, the shedding phenomena can be predicted by the abrupt matching of the streamwise velocity profiles to the value of the free-stream flow. The velocity profiles in Figure 5.9 clearly illustrate quantitatively the continuous attached flow at a valley, and the detaching and reattaching characteristics at a peak, in which a three-dimensional incoherence is generated.

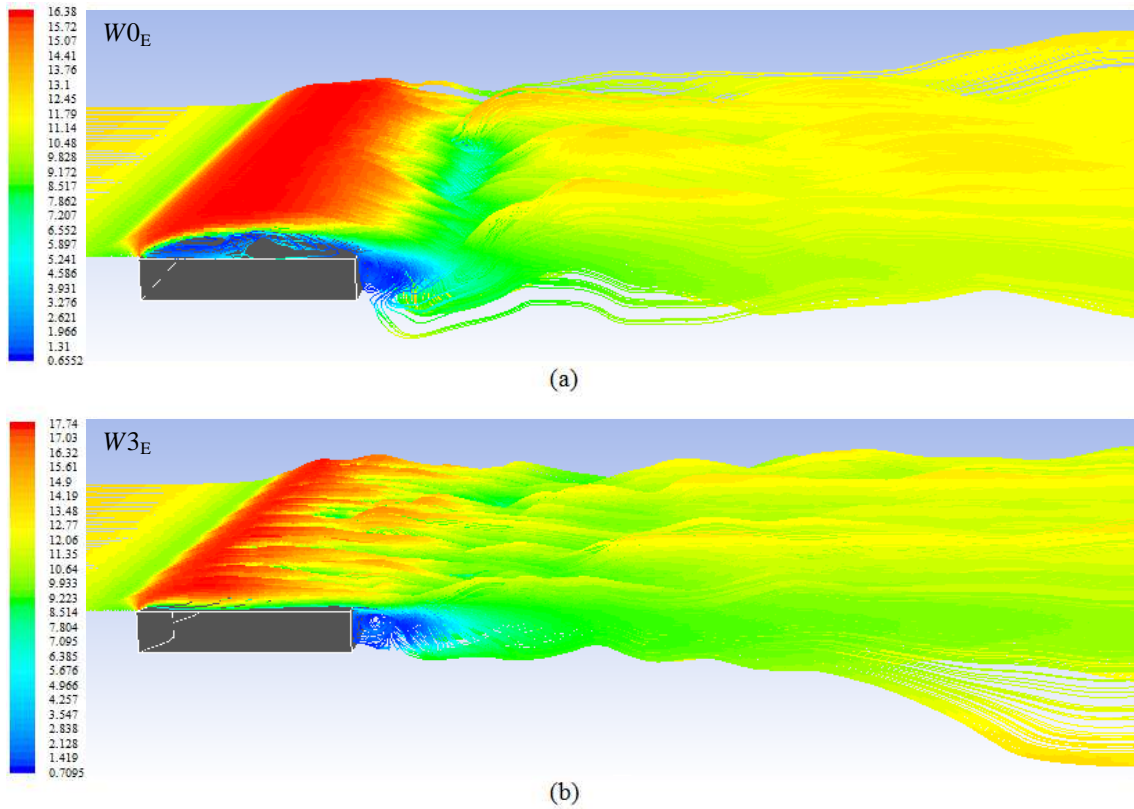


Figure 5.10: Pathlines illustrating the time-averaged velocity field around (a) $W0_E$ and (b) $W3_E$. It can be depicted that an SSP causes the flow field to resemble that of a streamlined geometry.

The wake behind an elongated SSP cylinder is depicted as being quite narrow. It is clear that the application of the SSP to the leading edge of a bluff body causes the flow field to resemble that of a streamlined geometry, such as an airfoil. Indeed, the phenomena of the shear layers are modified to obtain this characteristic. Figure 5.10 demonstrates the phenomenal comparison between the wakes of $W0_E$ and $W3_E$ with the use of pathlines of the time-averaged velocity field, taken in a plane coincident to $0.25D$ below the upper surface. In the case of the plain elongated geometry, the velocity remains high up to the trailing edge as a result of the flow separation at the leading edge and the development of the boundary layers. The circulation of the shear layers at the trailing edge results in the shedding of vortices into the wake. The flow field and hence

the wake associated with $W3_E$ is remarkably streamlined and narrow about the horizontal in much a similar manner as that of a symmetric airfoil. At a streamwise location of approximately half the length of the prism downstream from the leading edge, a decrease in the magnitude of the velocity can be discerned. This indicates a lower energy of the flow field and lower velocity gradients at this location, causing the shear layers to remain close to the surface and form the streamlined wake behind the prism. The SSP is therefore highly effective for application on a practically elongated bluff body.

5.2 Summary

In this chapter, it has been demonstrated that the flow field around elongated bluff bodies is effectively controlled by applying a spanwise sinusoidal profile (SSP) to the leading edge. Namely, the effects of control on rectangular prisms have been researched in detail. The SSP studied on the elongated cylinder has a wave steepness, ω/λ , of 0.195 and a normalised wavelength, λ/D , of 2.4. Significant reductions of up to 10% and 83% in the mean drag and fluctuations of lift are respectively obtained with this geometry. The flow around an elongated SSP cylinder is essentially three-dimensional and this is due to independent regions of the flow in the spanwise direction that are coincident to peaks and valleys.

The aerodynamic properties of the elongated bluff body with an SSP are corroborated by the adumbration of the flow topology, particularly the distribution of high pressure regions. A striking contrast is obtained in which the phenomena of the shear layers render the flow field and wake of the elongated SSP geometry to resemble those of a streamlined geometry. Due to a channelling of the flow at peaks in much a

similar manner to that observed with square cylinders, a spanwise incoherence develops and mitigates spanwise interactions at these locations. This in turn weakens the shear layers and obtains a thin boundary layer across the surface.

The effect of the proximity of the trailing edge to the SSP leading edge does not appear to have a profound influence on the control of the flow. Nevertheless, the flow field at the trailing edge is largely dissipated and as a result, a narrow wake is formed behind the elongated SSP geometry. An SSP proves to be a significant method of controlling the flow field around a practical elongated bluff body and enhances the fluid-to-structure performance of the geometry.

TOPOLOGY OF THE FLOW FIELD AROUND A PARTIAL SPANWISE SINUSOIDAL PROFILE

The flow field around bluff bodies can be effectively controlled by applying a spanwise sinusoidal profile (SSP) to their leading edge. It has been demonstrated that vortex shedding can be suppressed with an SSP with a wave steepness, ω/λ , in excess of 0.1 (Antiohos *et al.* 2010). Achieving a controlled flow field has so far been established with an SSP applied across the entire span of the geometry (i.e. a leading edge that is entirely sinusoidal). In some practical cases however, a continuous SSP across the leading edge may not be an appropriate choice. This can be due to deleterious effects from the surrounding flow field existing only at local regions along the span of the structure, therefore rendering a full span SSP unnecessary. Examples of such cases could encompass the flow around the tower of wind turbines and communication towers. In these cases, the flow field has a strong influence on the aerodynamic performance and structural integrity at only one or two locations along the span; this could be at the distal region of the towers. Furthermore, recall the leading edge comb is located on only the primary feathers of the wing. In this chapter, bluff bodies with spanwise sinusoidal profiles applied to sections of the leading edges are researched to elucidate the topology of the flow field at the boundary of sinusoidal and plain leading edges. This study has revealed phenomena that were hitherto unobserved.

6.1 Effectiveness of a Partial Spanwise Sinusoidal Profile

It has been shown that a full-span sinusoidal profile has the ability to control the flow and prevent vortex shedding and their associated deleterious effects. However, the question remains as to whether or not effective control can still be achieved using a partially applied SSP. For example, might there be some spanwise interactions between the flow over the plain and SSP regions? Hence, the topology of the flow associated with three different configurations of a partial SSP is researched. These configurations include a partial SSP applied in only the central region of the span; a partial SSP applied to the two end regions of the span (i.e. the center of the span is plain); and a partial SSP that continually occupies half the span. These can be seen in Figure 6.1 and are denoted as $PSSP_1$, $PSSP_2$ and $PSSP_3$. The choice of $PSSP_1$ is to explore the effectiveness of a partial SSP that is adjacent to a coherent uncontrolled flow field on both sides. In a similar manner, the choice of $PSSP_2$ is to explore the effectiveness of partial SSPs if placed on both sides of the coherent flow field. The geometry of $PSSP_3$ is to elucidate the likelihood of a partial SSP being able to control the flow when applied to approximately half the span; in this case both coherent and incoherent flow fields are of equivalent strength across the span.

In previous chapters, it has been demonstrated that highly effective control of the flow field is achieved with a wave steepness, ω/λ , of the SSP in excess of 0.1 (Dobre *et al.* 2006; Antiohos *et al.* 2010). The three partial SSP geometries each contain a wave steepness equal to 0.195, which is identical to that of the full SSP geometry, $W3$. Hence, the wavelength, λ , and wave height, ω , across the partial spans are respectively 76.8 mm and 15 mm.

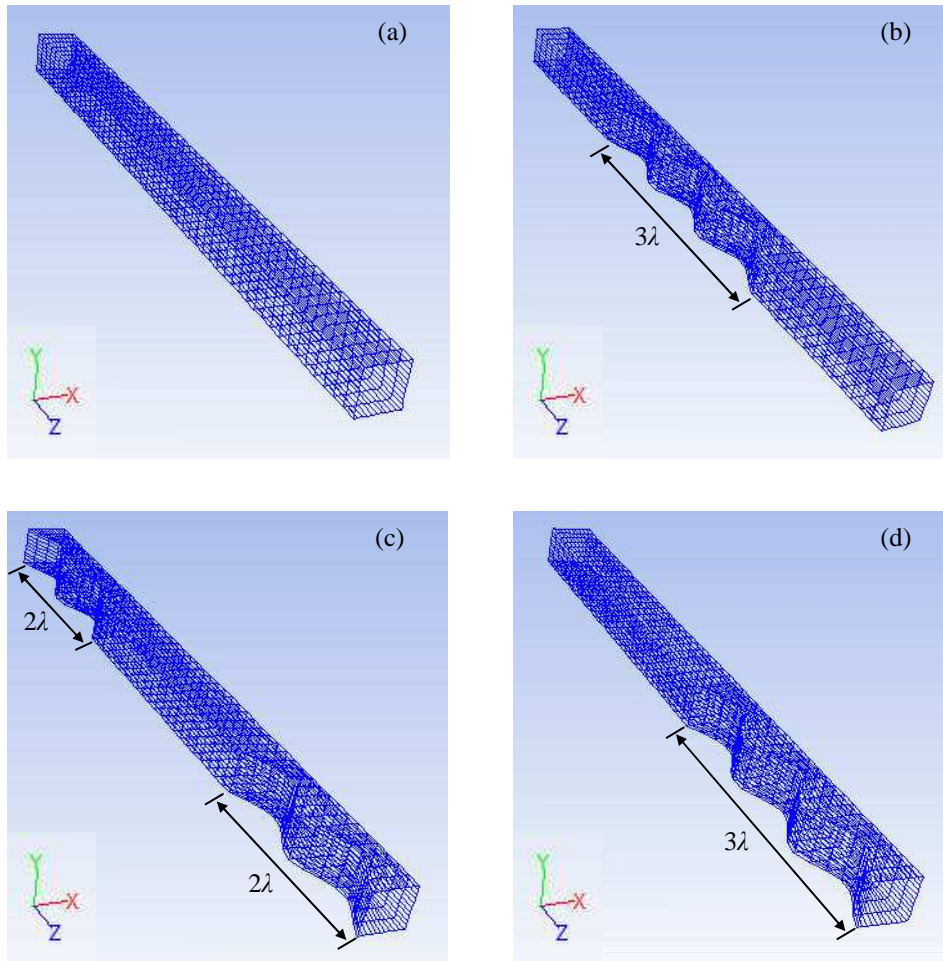


Figure 6.1: Schematic of the partial SSP geometries; (a) plain geometry, (b) $PSSP_1$, (c) $PSSP_2$ and (d) $PSSP_3$.

6.1.1 Performance of Aerodynamic Forces of a Partial SSP

The principal motivation for applying SSPs is to reduce the absolute and fluctuating components of drag force, and the fluctuating components of the lift force. It has been shown that SSPs result in technologically highly significant reductions in these forces. However, it is essential that we consider the situation when an SSP is imposed only on a section of the leading edge of a bluff body.

Figure 6.2 shows the coefficient of mean drag, C_d , plotted against normalised time, t/dt , where dt is the time step. The plots of C_d are presented for a bluff body with a plain leading edge and for the three partial SSP geometries, $PSSP_1$, $PSSP_2$ and $PSSP_3$. The values of mean drag, C_d , are 2.35, 1.95, 1.81 and 1.98 respectively for $W0$, $PSSP_1$, $PSSP_2$ and $PSSP_3$. It is discernable that significant reductions are achieved with the partial application and the largest decrease observed for $PSSP_2$, as expected, as a higher ratio of the partial SSP on the leading edge exists for this geometry. The highest drag coefficients of 1.95 and 1.98 associated with $PSSP_1$ and $PSSP_3$ respectively is also expected, as these configurations contain a larger ratio of uninterrupted plain span in comparison to $PSSP_2$; a more organised coherent flow structure would be present.

As noted in Chapter 4, the coefficient of mean drag varies on two distinct time scales. The high frequency variations are associated with the vortex shedding frequency, and the lower frequency appears to arise from some cyclic disturbance in the flow field. However, in the case of the partial SSPs, the low frequency disturbances appear to be more regular than in the corresponding case where the SSP extends across the entire surface of the leading edge. This suggests a spanwise interaction between coherent and incoherent flows of respectively plain and SSP regions. Without performing Fourier analysis on the histories of the force coefficients it is difficult to pinpoint the exact frequencies. By inspection, the histories of C_d display an irregular fluctuation about the mean value; this is more evident for the cases of $PSSP_1$ and $PSSP_2$. Where the drag coefficient associated with a base pressure has alternatively low and high values that occur at irregular intervals throughout the sequence, this corresponds to abrupt interactions between two different flow patterns (Ohya 1994; Sohankar 2008). In the cases of partially applied SSPs, it is believed that the phenomena of the two time scales associated with the fluctuations of C_d have not been previously observed so starkly.

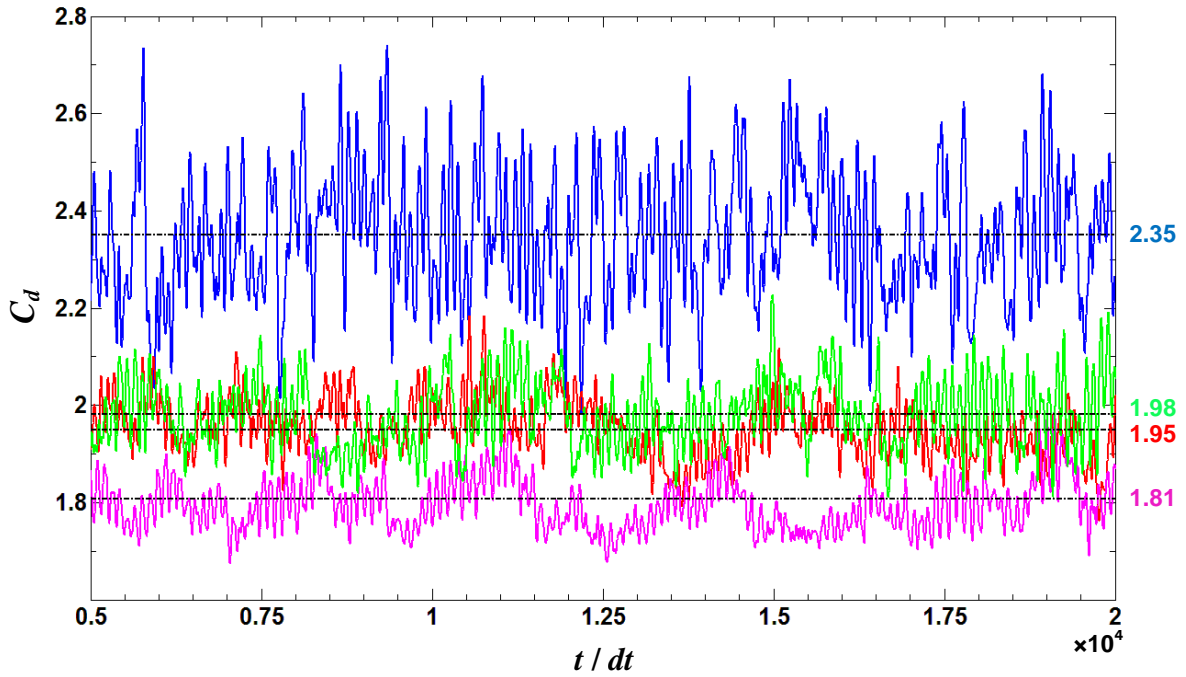


Figure 6.2: Coefficient of drag, C_d , for the plain square cylinder, W_0 (—), and the three partial SSP geometries, $PSSP_1$ (—), $PSSP_2$ (—) and $PSSP_3$ (—); highlighting the significant reduction in the mean drag and related reduction of the fluctuations as a result of the partial SSP with wave steepness, ω/λ , of 0.195 associated with W_3 .

In Figure 6.3, the coefficients of lift, C_l , are plotted for all three partial SSP geometries. It is clear that large fluctuations in lift exist for a plain geometry. However, once applying a partial spanwise sinusoidal profile to the leading edge of the plain geometry, a significant decrease in the fluctuations is achieved. The magnitude of the fluctuations is quite similar in Figures 6.3(b) and 6.3(d) for $PSSP_1$ and $PSSP_3$, respectively. This may be due to the similar ratio of partial SSP across the span for the two cases. A higher reduction in lift fluctuation can be seen in Figure 6.3(c) which is associated with $PSSP_2$. This quantitatively corroborates the effectiveness of a partial SSP with a higher partial ratio, and the observations of Figure 6.3 demonstrate that obtaining a controlled flow field is independent of the spanwise location and ratio to the plain span.

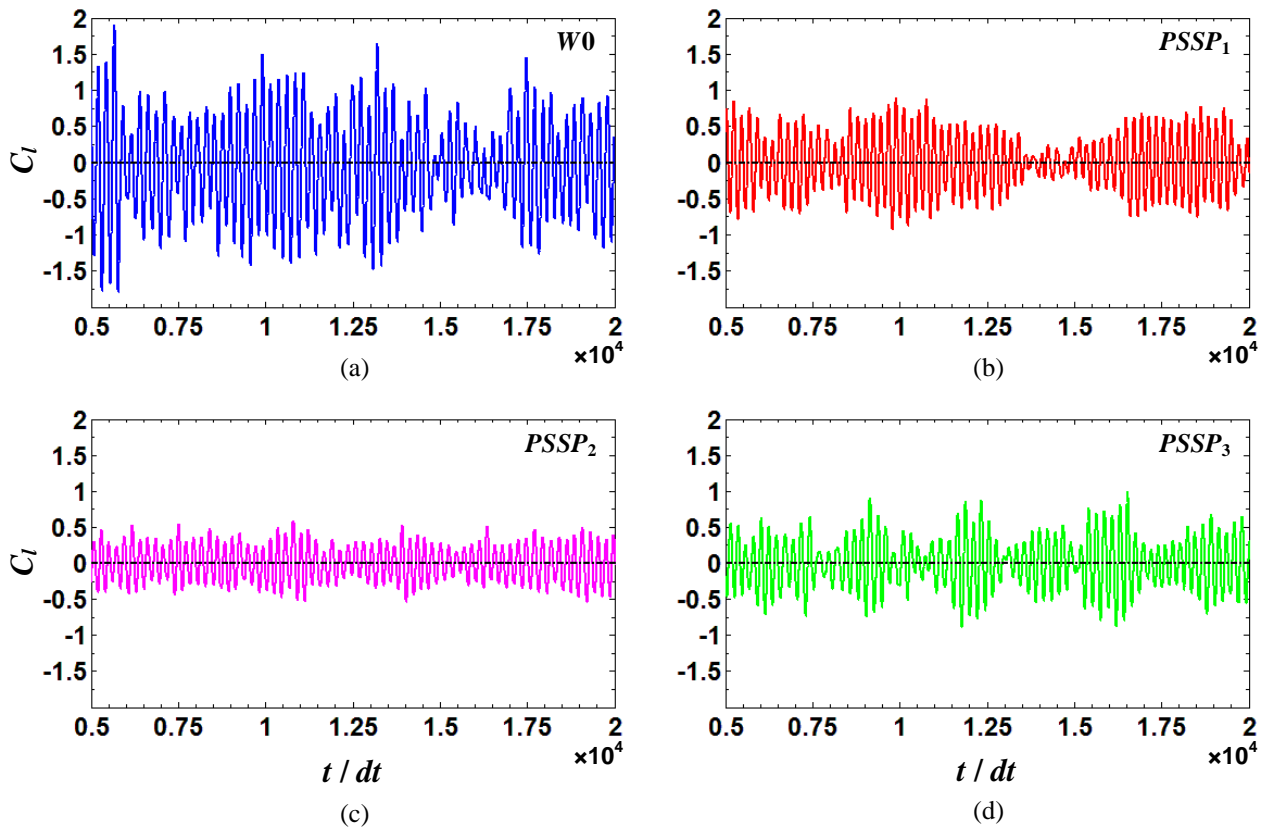


Figure 6.3: Coefficient of lift, C_l , for the plain square cylinder, $W0$ (a, —), and the three partial SSP geometries, $PSSP_1$ (b, —), $PSSP_2$ (c, —) and $PSSP_3$ (d, —); highlighting the significant reduction in the fluctuations of lift as a result of the partial SSP with wave steepness, ω/λ , of 0.195 associated with $W3$.

A remarkable observation is made in Figure 6.3, in which beats exist in the C_l history. These beats are superimposed on the high frequency fluctuations, and this is clearly evident in Figure 6.3(d), which corresponds to $PSSP_3$. This may have a profound effect on the engineering of the structure with a partial SSP. Reasoning behind the highly discernable beat phenomenon with $PSSP_3$ can be due to the planform area, in which the plain and SSP regions both occupy approximately half the span. In this case, the phenomena (vortex shedding and Kelvin-Helmholtz instabilities) associated with these regions interact more strongly. The alternative partial SSP geometries studied,

$PSSP_1$ and $PSSP_2$, have discontinued (interrupted) regions along the span; hence, these geometries have a less developed flow field in the spanwise direction.

6.1.2 Topological Study by Means of Flow Visualisations

The phenomena that give rise to the effectiveness of an SSP partially applied to the leading edge of a bluff body can be elucidated by visualising the topology of the flow. The images on the left of Figure 6.4 display contours of vorticity in a vertical y - z plane coincident with the trailing edge of the geometries, as well as the vorticity along the front, upper and lower surfaces. To the right hand side of Figure 6.4, the vorticity field is presented in evenly distributed vertical x - y planes along the span that are coincident with the peaks and valleys of a full span SSP under the same parameters for the wave height and wave steepness.

Vorticity is chosen for the exploration herein rather than velocity, as vorticity is associated with the curl of the velocity vector, and hence the phenomena associated with vortex shedding are more apparent within a vorticity field (White 2003). In Figure 6.4, the colour scale represents the magnitude of the vorticity, with the largest magnitude in red being located along the upper and lower corners of the leading edge (i.e. the connecting edges between the leading edge and horizontal surfaces).

The vorticity in Figure 6.4 displays phenomena that are associated typically with both plain and SSP geometries. This is to be expected. However, the topology of the flow field provides useful insights into the phenomena. At the boundaries of the plain spans and partial SSPs, the coherent flow may transfer over into the region of the partial SSP, and eventually become rendered incoherent towards the center of the SSP (i.e. the partial SSP will only be effective at its center). It is the incoherence of the SSP that is

transferred into the coherent region. Instead, of there being a sharp distinction of the SSP / plain boundary, there is a transitional region in between.

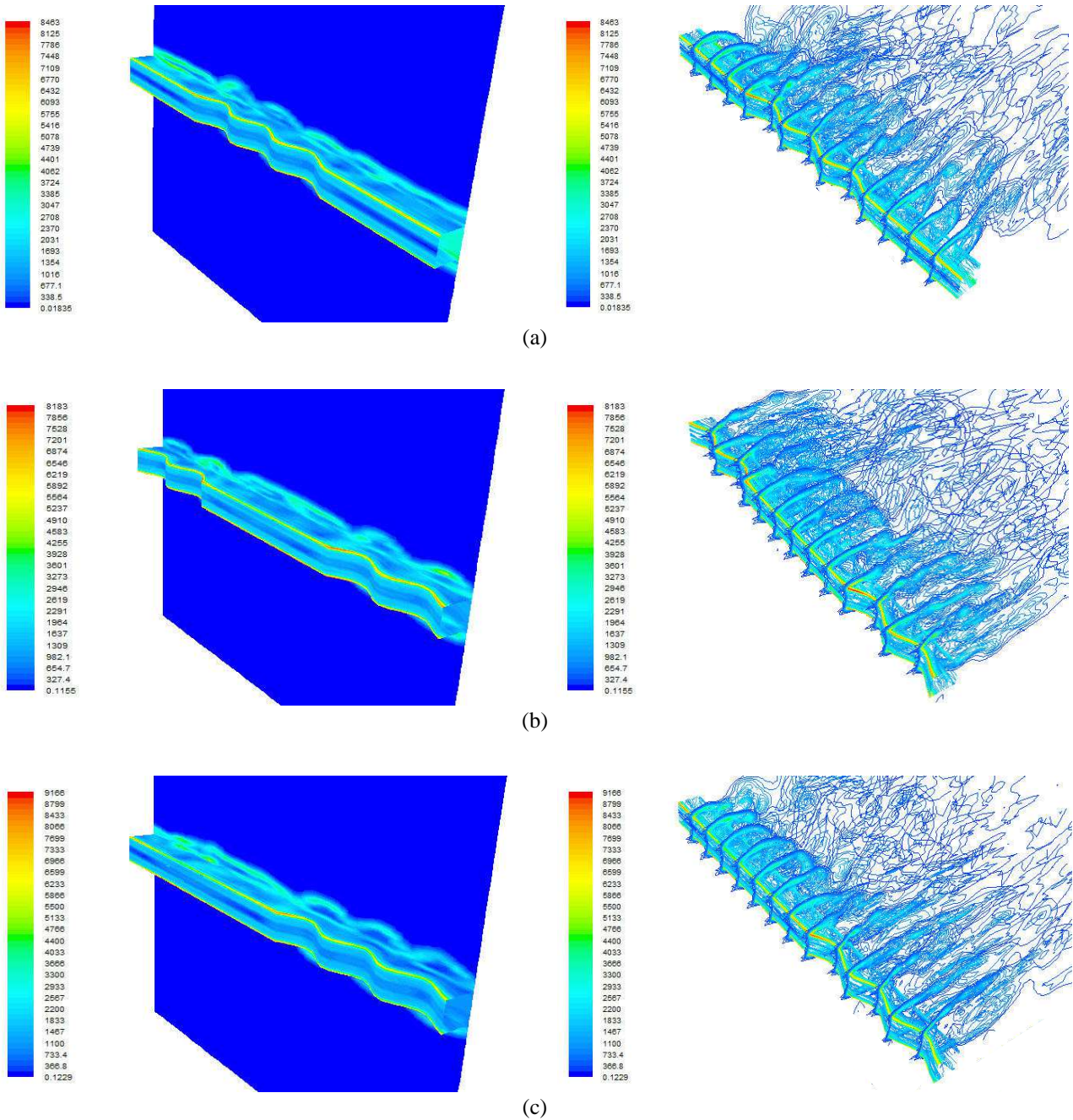


Figure 6.4: Contours of vorticity magnitude for the TE plane (left) and spanwise peak and valley planes (right); (a) $PSSP_1$, (b) $PSSP_2$ and (c) $PSSP_3$.

At the locations of the partial SSPs, the contours of vorticity that are present in the vertical y - z plane of Figure 6.4 coincident with the trailing edge resemble the sinusoidal pattern of the SSP. Therefore, in the case of the three geometries, this pattern emerges at the center of the span, two outer ends of the span, and across half the span, respectively for $PSSP_1$, $PSSP_2$ and $PSSP_3$. Elsewhere along the spans is indication of the flow field that is associated with a plain leading edge. In the vertical x - y planes that are coincident with peaks of the partial SSP, the flow is detached directly aft of the leading edge, and at valleys the flow is attached. Furthermore, at the boundary of the plain and partial SSP, the vorticity in the vertical y - z plane contains significantly less energy, as indicated by the absence in vorticity magnitude. There appears to be a cut-off region between the interaction of the coherent and incoherent flow fields along the span. Observing the flow field in the vertical x - y planes, the flow coincident to the boundary of the plain and SSP spans displays characteristics that are associated with an intermittent flow; hence, a Regime II-type pattern. Therefore, it would seem that the two partial spans (plain and SSP) contain independent flow fields that are adjoin by an interacting flow at the boundary.

It is evident that the flow field around the partial SSP geometries contains regions of flow structures that are independent in the spanwise direction. The three-dimensional flow field associated with the spanwise incoherence as a result of the partial SSP can only be depicted at the partial regions. At the regions of the plain leading edge, the flow exhibits coherence and therefore vortex shedding. Hence, the characteristics of both uncontrolled and controlled flow fields are present; however, it can be seen in the topology of the overall flow field that the two individual structures of the flow are quite independent. At the vertical x - y plane intersecting the span of the plain leading edge and partial SSP, and also including the adjacent vertical x - y planes, it can be seen in Figure

6.4 that negligible interaction seems to exist between the coherent and incoherent flow fields. Hence, from this observation alone, it is suggested that there is no evident transfer or blending of the flow structures other than intermittency detected at the boundary. The intermittency is the same as Regime II, discussed in Chapter 4. These phenomena may suggest an effective control of the local flow field can be achieved with a partial SSP.

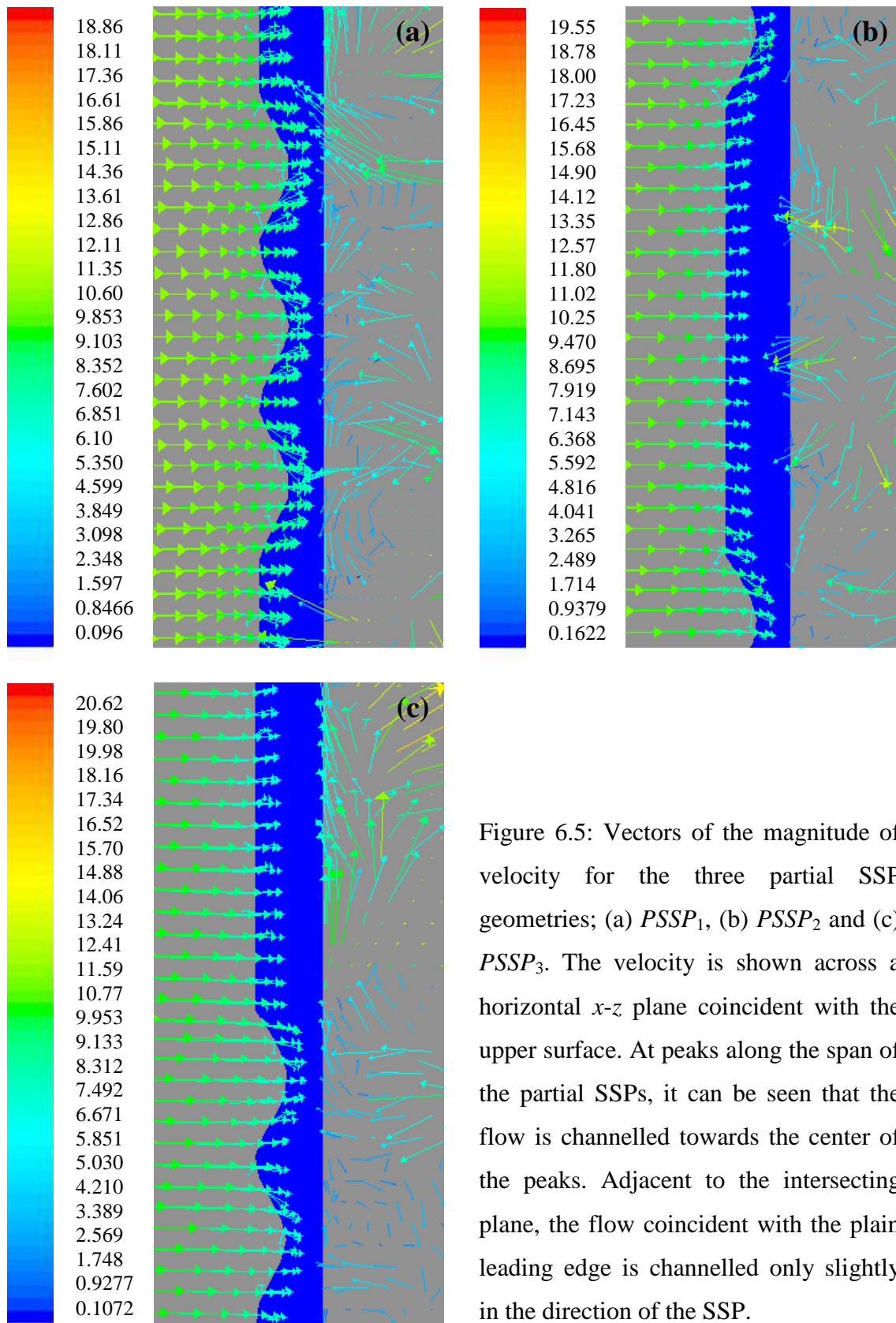


Figure 6.5: Vectors of the magnitude of velocity for the three partial SSP geometries; (a) $PSSP_1$, (b) $PSSP_2$ and (c) $PSSP_3$. The velocity is shown across a horizontal x - z plane coincident with the upper surface. At peaks along the span of the partial SSPs, it can be seen that the flow is channelled towards the center of the peaks. Adjacent to the intersecting plane, the flow coincident with the plain leading edge is channelled only slightly in the direction of the SSP.

In Figure 6.5, the instantaneous vectors of velocity magnitude are displayed for the three partial SSP geometries. The vectors are approaching the leading edge in a horizontal x - z plane coincident to the upper surface of the geometries; the view is from the top and the flow is from left to right. Across the spans with the plain leading edges, the velocity vectors are parallel to the streamwise direction. Coincident to valleys, the vectors are also parallel to the streamwise direction. It is only at the intersecting region between the plain and SSP spans that the vectors change direction and become channelled towards the center of the adjoining peak of the partial SSP. Likewise, the flow is channelled at the remaining peaks. It is evident that in a similar manner to the full span SSP geometry with large wave steepness ($\omega/\lambda > 0.1$), a partial SSP under the same parameter has the ability to capture the flow across its span and mitigate a coherent flow field from occurring. It should be noted that as it has been discussed in previous chapters, the effect of channelling of the flow will only occur when the wave steepness, ω/λ , is significant (i.e. $\omega/\lambda > 0.1$). It is a stark observation that both the coherent (uncontrolled) and incoherent (controlled) flow fields co-exist independently across the span containing a partial spanwise sinusoidal profile.

Pathlines representing the vorticity field in a horizontal plane approaching the leading edge coincident with the upper surface of the three geometries of the partial SSP are displayed in Figure 6.6. It is desired to observe the fluid-to-structure interactions within the vorticity field and the impact of the partial leading edges on the flow. The vorticity in this plane provides significant details of the flow topology associated with a partial SSP near the surface of the geometry. Across the spans of the plain leading edge of $PSSP_1$ in Figure 6.6(a), the development of the boundary layers and mixing of the shear layers induces vortex shedding into the wake. However, contrast to prior observations for a plain geometry in which vortices are shed uniformly along the span,

the instantaneous shedding of vortices on either side of the partial SSP occurs oppositely. For example, it can be seen in Figure 6.6(a) that to one side of the partial SSP, vortices are shed from the upper surface; whereas, to the other side they are being shed from the lower surface. A partial SSP located mid-way along a plain leading edge is shown to disrupt the uniformity of the coherent shedding process, or at least prevent a spanwise communication of the coherent structures.

In the case of placing two partial spans of the SSP along the geometry, the flow field coincident with the plain span of $PSSP_2$ in Figure 6.6 does not appear to hold any adverse effect. The shear layers roll-up into vortices uniformly across the uncontrolled region. Along the spans of the partial SSP, the sinusoidal pattern emerges in the flow field. The separation of the flow from the upper surface of the geometry being coincident to peaks and the flow attachment at valleys is clearly discernable. As a result of the flow being channelled at the regions of peaks, this concentration of flow causes a high pressure gradient at this location and hence flow separation at the leading edge. The dispersion of flow concentration in line with the location of the valleys results in a decrease in the pressure gradients and allows the flow at these regions to remain fixed to the surface of the geometry. In Figure 6.6(c), the placement of a partial SSP across half the span of the geometry has no direct impact on the flow field associated with the plain half of the span. The two halves of the geometry exhibit the coherent and incoherent flow fields associated with the plain and SSP spans, respectively.

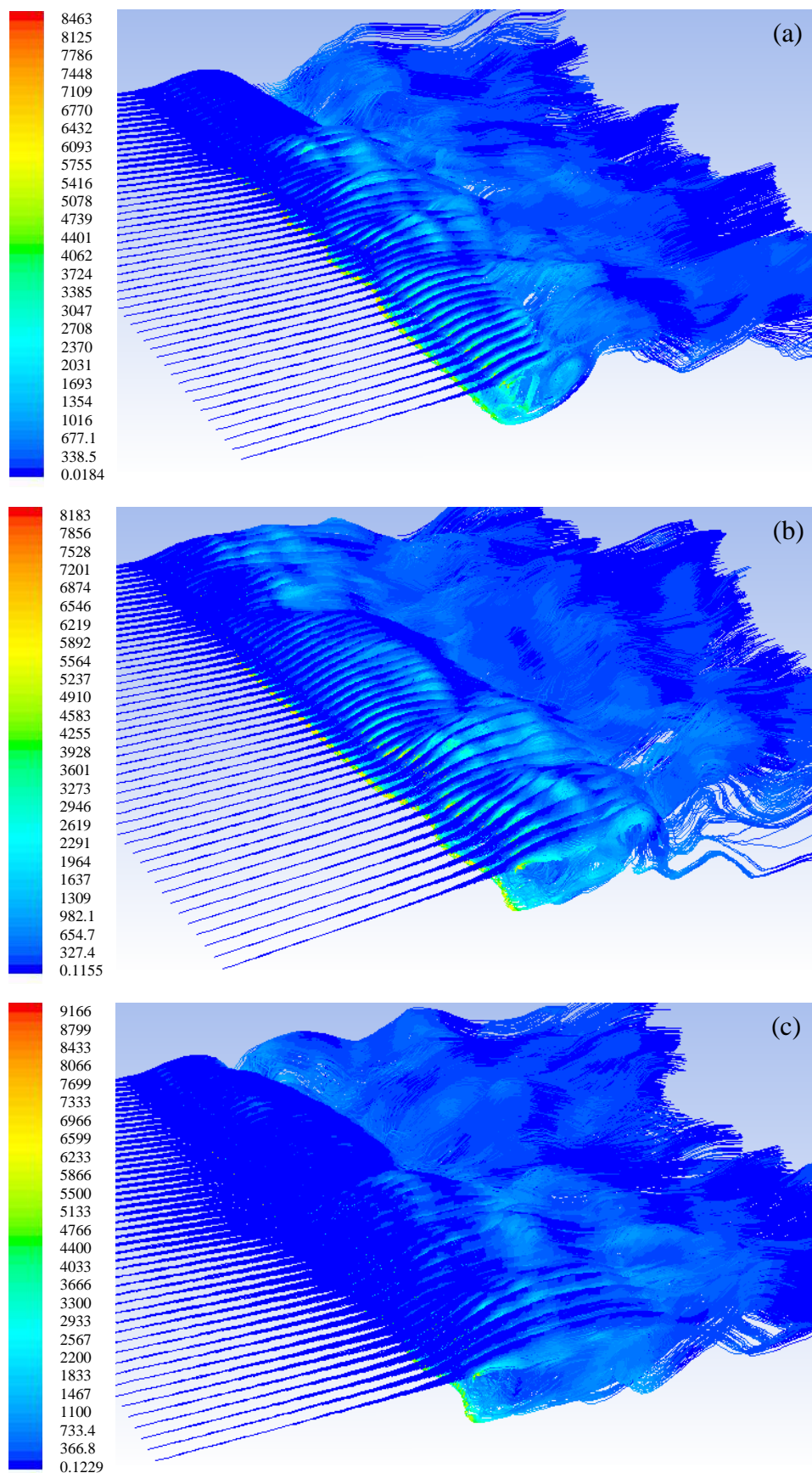


Figure 6.6: Pathlines highlighting the vorticity field approaching the leading edge of the three partial SSP geometries in a horizontal x - z plane coincident with the upper surface; (a) $PSSP_1$, (b) $PSSP_2$ and (c) $PSSP_3$.

Another insight of the topology of the flow field around the partial SSP geometries is taken from the above view. As the vorticity pathlines are a lot clearer to visualise in this perspective. In Figure 6.7, the vorticity field is shown in the same horizontal plane coincident with the upper surface of the geometries. At the spans associated with the plain leading edge, the pathlines of vorticity remain parallel and streamwise (this is expected and demonstrated with the velocity vectors). The channelling of the flow at peaks of the partial SSP that ultimately results in an adverse pressure gradient at the leading edge is seen to cause a reaction in the flow field in the form of flow convergence in line with the valleys. At the regions where the plain and partial SSP spans intersect, the pathlines coincident to the adjoining valley of the SSP merge with the streamwise pathlines that are coincident to the plain leading edge. This establishes somewhat of a void in the flow field, in the wake and directly in-line with the intersecting point. The one case that demonstrates this void the largest is for $PSSP_3$; the streamlines are quite divergent from this location about the spanwise direction. The pathlines in Figure 6.7 indicate the independent structures of both the uncontrolled and controlled flow fields; not only across the bluff geometry, but especially in the wake.

In order to corroborate the above observations, the vorticity field is presented in vertical x - y planes that are coincident with both a peak and a valley across the span of the partial SSP, a vertical x - y plane coincident along the span of the plain leading edge, and a vertical x - y plane at the intersection between these two spans. This is primarily to demonstrate the independent flow structures, as well as the spanwise transition of the flow field more clearly.

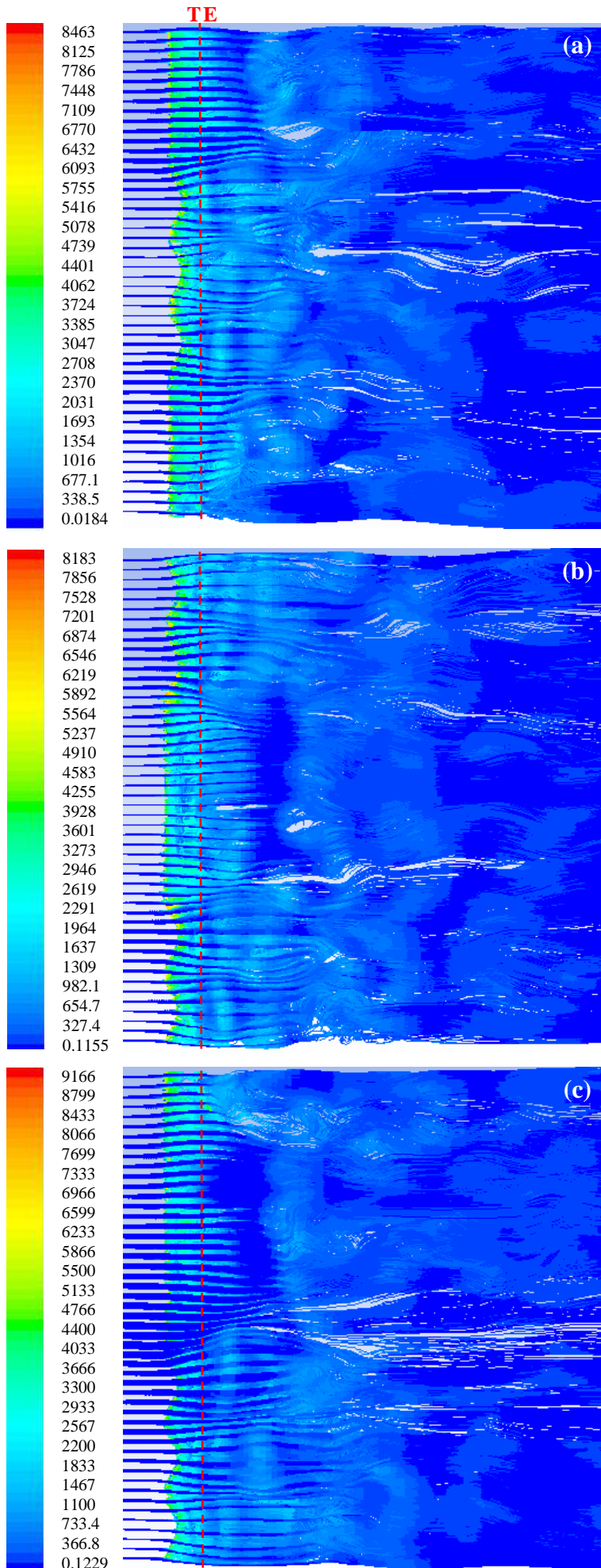


Figure 6.7: Above view of the three partial SSP geometries showing the pathlines of the vorticity field approaching the leading edge in a horizontal $x-z$ plane coincident with the upper surface; (a) $PSSP_1$, (b) $PSSP_2$ and (c) $PSSP_3$.

The contours of vorticity are presented in Figure 6.8 for $PSSP_1$. In Figure 6.8(a), vortex shedding is evident in a plane that is coincident with a plain leading edge. Hence, the partial SSP does not have an impact at this region. The vorticity depicted in Figure 6.8(c) coincident with a peak indicates the separation of the boundary layer at the leading edge and shear layer instabilities in the form of Bloor-Gerrard vortices, or otherwise known Kelvin-Helmholtz instabilities (Bloor and Gerrard 1968). The frequency of these small scale vortices is in the order of approximately $3f_{vo}$, where f_{vo} is the vortex shedding frequency for a plain square section. The wake at this plane remains divergent about the mid-horizontal plane behind the cylinder. In Figure 6.8(d), the vorticity clearly shows attached boundary layers to the upper and lower horizontal surfaces of the geometry; this is depicted in the vertical x - y plane coincident with a valley. The wake in this case remains relatively parallel about the horizontal and shows only very slight indication of shear layer instability in the wake at this plane.

At the vertical x - y plane that is coincident with the intersection between the plain leading edge and partial SSP in Figure 6.8(b), signs of an intermittent structure are more evident. Both upper and lower boundary layers remain attached to the surface of the geometry; however, there is absent stretching of the shear layers in the streamwise direction, which in turn prevents the roll-up of vortices into the wake, and results in a high rate of dissipation. Nevertheless, intermittently the shear layers tend to stretch and form vortex like structures into the wake. Hence, the partial SSP does not have a complete influence on the flow at this spanwise location, but begins to change the coherent fluid properties at this spanwise point.

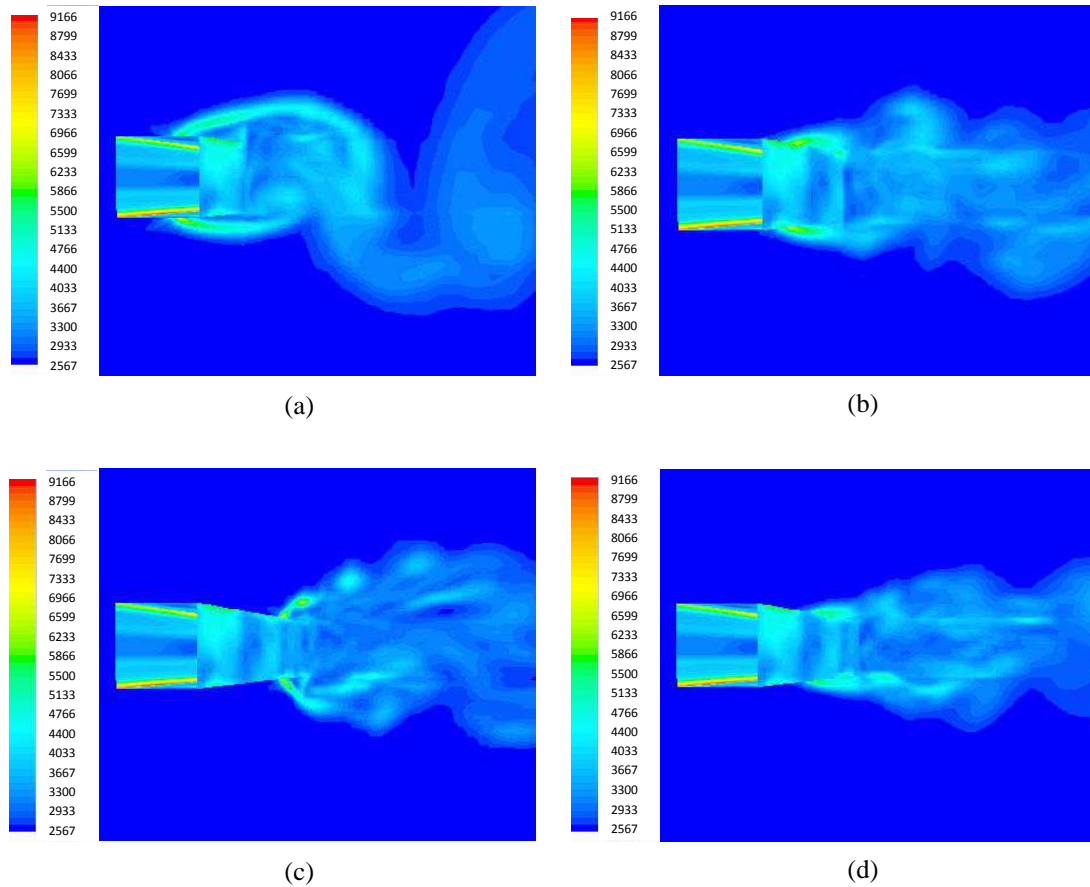


Figure 6.8: Contours of vorticity magnitude for $PSSP_1$ showing the spanwise flow transition in vertical x - y planes coincident to (a) the plain leading edge, (b) the intersecting plane, (c) a peak of the partial SSP, and (d) a valley of the partial SSP.

The observations gathered from the visualisations of the flow field appear to suggest that the passive control is independent of spanwise location. Hence, applying a partial SSP at any location along the span of the geometry will result in achieving control of the flow at the local position and mitigating the shedding of vortices across the entire partial SSP span. The presence of the uncontrolled coherent flow adjacent to the partial SSP does not appear to adversely affect the outcome of the application.

6.2 Summary

The work in this chapter demonstrates that a spanwise sinusoidal profile (SSP) embodied only partially to the leading edges of square cylinders is an effective, and more importantly, a practical adaptation. The partial SSPs have a wave steepness, ω/λ , of 0.195 and a normalised wavelength, λ/D , of 2.4. It is shown that a three-dimensional flow field occurs around the bluff bodies at local regions where the SSP is present. Elsewhere, a two-dimensional flow field exists which is associated with the plain leading edges. Remarkably, at the boundary between the plain and SSP spans, the flow exhibits an intermediate characteristic similar to the Regime-II type instability, which was introduced in Chapter 4. Hence, there are independent regions of controlled and uncontrolled flow that are adjoined by a small region at the boundaries, in which the flows interact.

Reductions are obtained in the mean drag and the fluctuations of lift force of up to 23% and 71%, respectively. This is attributed by the independent regions of three-dimensional flow coincident to the spans of the partial SSP. The aerodynamic properties are corroborated by visualisations of the flow topology. The shear layers around the partial SSP bodies clearly demonstrate the presence of both the two-dimensional and three-dimensional flow fields corresponding to plain and SSP spans, respectively. The channelling of the flow at the peaks of the SSP is responsible for the interaction between the two independent flow regions, as the field reacts in a divergent manner from the convergence at peaks. Overall, an SSP proves to be an outstanding mechanism for reducing the deleterious effects and modifying the flow field at the local regions where the sinusoid exists.

CONCLUSIONS AND FUTURE WORK

7.1 Contributions of the Thesis

In this thesis, investigations are made into the control of turbulent flow around bluff bodies by means of bio-inspired spanwise sinusoidal profiles (SSPs) on the leading edges. This is achieved by numerically modelling the transport phenomena using large eddy simulation (LES). The numerical analysis contributes to the existing understanding of the three-dimensional flow around bluff bodies; in particular, the phenomena associated with a controlled flow field. The contributions of this research are summarised as follows.

- It has been shown that the mean drag force on square cylinders immersed in turbulent flows can be reduced by about 30% if spanwise sinusoidal profiles (SSPs) are embodied on their leading edges.
- The validated numerical model indicates that an SSP is able to reduce the lift force fluctuations by up to 95%. This has potential benefits for reducing fatigue failure of structures exposed to turbulent flows.
- Vortices shed along the span of plain square cylinders cause large temporal variations in the lift and drag. A cylinder with an SSP leading edge with a wave steepness, ω/λ , of 0.195 and a normalised wavelength, λ/D , of 2.4 contains a wake

with small-scale Kelvin-Helmholtz (Bloor-Gerrard) instabilities being shed from the cylinder.

- The peaks of the SSP channel the flow and this increases the mass flux at these regions. Vortices shed downstream of valleys are shed predominantly in the direction of the free-stream flow.
- A parametric study indicates that the wave steepness of a spanwise sinusoidal profile appears to be of greater importance in suppressing the synchronous shedding of vortices in turbulent flow than in laminar flow.
- A spanwise sinusoidal profile (SSP) not only controls the flow field around square cylinders, but it effectively renders the flow field around elongated bluff bodies to resemble that of a streamlined geometry. This is demonstrated in Chapter 5.
- The SSP studied on the elongated cylinder has a wave steepness, ω/λ , of 0.195 and a normalised wavelength, λ/D , of 2.4. Reductions of up to 10% and 83% in the mean drag and fluctuations of lift are respectively obtained with this SSP geometry.
- The flow around an elongated SSP cylinder is three-dimensional due to a channelling of the flow at peaks in a similar manner to that observed in the case of square cylinders. A spanwise incoherence develops, and this in turn weakens the shear layers and results in a thin boundary layer adjacent to the surface. As a result, a narrow wake is formed behind the elongated SSP geometry.
- The effect of the proximity of the trailing edge to the SSP leading edge does not profoundly influence the control of the flow field around elongated bluff bodies.

- When an SSP is embodied only partially to the leading edges of square cylinders, a three-dimensional flow field occurs around the bluff bodies at local regions where the SSP is present. Elsewhere, a two-dimensional flow field exists which is associated with the plain leading edges.
- At the boundary between spans with plain and SSP leading edges, there are independent regions of controlled (three-dimensional) and uncontrolled (two-dimensional) flow that are adjoined by a small region where the two flow regimes interact.
- In a specific case considered, the mean drag and the fluctuations of the lift force are reduced by up to 23% and 71%, respectively, for a partial SSP.
- The channelling of the flow at the peaks of the SSP region triggers the interaction at the boundaries between plain and SSP regions. This is because flows in the latter region are three-dimensional.
- Overall, an SSP demonstrates to be an outstanding practical mechanism for reducing the deleterious effects produced by turbulent flows around bluff bodies.

7.2 Suggestions for Future Work

The research presented in this thesis has demonstrated the effectiveness and practicality of bio-inspired spanwise sinusoidal profiles (SSPs) in reducing the fluctuating forces on bluff bodies. This study has revealed avenues of further research that would be important from both fundamental and practical points of view.

The bluff bodies in this work were maintained at a zero angle of attack to the approaching fluid, i.e. the leading edge of the bodies is normal to the upstream flow at all times. It is suggested that investigations be carried out on bluff bodies fitted with SSPs that have a range of angles of attack – possibly ranging from 0° as at present to 180° . It is possible that SSPs are effective to some degree at all angles of attack, but this is of course speculative. This would also align the research with flow over an owl's wing, and the effect of angle of attack would be particularly useful in dealing with practical cases associated with elongated bluff bodies. In addition, it is most important to increase the range of Reynolds numbers studied, as this could reveal as yet unsuspected phenomena.

This research has considered only an idealised form of the leading edge comb. However, the potential of the trailing edge fringe as a flow control mechanism has been discussed in Chapter 2, where its ability to suppress trailing edge noise is highlighted. This prompts a further study in which a trailing edge fringe is attached to square and elongated bluff bodies; the trailing edge fringe could be idealised as a porous medium that absorbs the turbulent flow structures and mitigates the aerodynamic noise. Furthermore, the trailing edge fringe and spanwise sinusoidal profile can be implemented simultaneously to elucidate their combined effectiveness in controlling the turbulent flow field and aerodynamic forces. Additionally, the SSP can be modified to take a different geometric form such as a sawtooth or square tooth pattern. Rather than a porous medium, the trailing edge can be castellated, in which both the leading and trailing edges have identical or different geometries.

Preliminary studies on these suggestions for future work can be carried out numerically. However, it is essential that the effectiveness of the leading and trailing

edge passive controls are integrated with practical ‘real-life’ models, such as towers, buildings, bridges, and so on. Furthermore, the research can be extended to hydrodynamic problems, such as water currents around marine risers, oil rig platforms, off-shore wind turbine towers, weather stations and the keels of ships and boats.

REFERENCES

- Anderson, EA & Szewczyk, AA 1997, 'Effects of a splitter plate on the near wake of a circular cylinder in 2 and 3-dimensional flow configurations', *Experiments in Fluids*, vol. 23, pp. 161 – 174.
- ANSYS FLUENT 12.0: *Theory Guide, Section 4.11 Large Eddy Simulation (LES) Model* 2009, Release 12.0, ANSYS Inc., Canonsburg, PA, pp. 61 – 71.
- ANSYS FLUENT 12.0: *UDF Manual* 2009, Release 12.0, ANSYS Inc., Canonsburg, PA.
- Antiohos, AA, Semercigil SE & Turan OF 2009, 'CFD Design of a Generic Controller for Vortex-Induced Resonance', in *Proc. 7th International Conference on CFD in the Minerals and Process Industries*, CSIRO, Melbourne, Australia, 9 – 11 December.
- Antiohos AA, Semercigil SE & Turan OF 2010, 'LES of a Passive Control for Vortex Shedding from Bluff Bodies', in *Proc. 17th Australasian Fluid Mechanics Conference*, Auckland, New Zealand, 5 – 9 December.
- Bachmann, T, Klän, S, Baumgartner, W, Klaas, M, Schröder, W & Wagner, H 2007, 'Morphometric characterisation of wing feathers of the barn owl *Tyto alba pratincola* and the pigeon *Columba livia*', *Frontiers in Zoology*, vol. 4, no. 23, pp.1 – 15.
- Bar-Cohen, Y 2006, *Biomimetics: biologically inspired technologies*, CRC, Boca Ranton.
- Bearman, P & Brankovic, M 2004, 'Experimental studies of passive control of vortex-induced vibration', *European Journal of Mechanics B/Fluids*, vol. 23, pp. 9 – 15.
- Bearman, PW & Owen, JC 1998, 'Reduction of bluff-body drag and suppression of vortex shedding by the introduction of wavy separation lines', *Journal of Fluids and Structures*, vol. 12, pp. 123 – 130.

- Benyus, JM 1997, *Biomimicry*, Harper Collins, New York.
- Blackburn, HM & Karniadakis, GE 1993, 'Two- and three-dimensional simulations of vortex-induced vibration of a circular cylinder', *proceedings of the 3rd International Offshore and Polar Engineering Conference*, Singapore, pp. 715 – 720.
- Blevins, RD 1990, *Flow-Induced Vibration*, 2nd edn, Van Nostrand Reinhold, New York.
- Blevins, RD 2009, 'Vibration of structures induced by fluid flow', in AG Piersol & TL Paez (ed.), *Harris' Shock and Vibration Handbook*, 6th edn, McGraw-Hill Professional, New York, pp. 1 – 20.
- Bloor, MS 1963, 'The transition to turbulence in the wake of a circular cylinder', *Journal of Fluid Mechanics*, vol. 19, pp. 290 – 304.
- Bloor, MS & Gerrard, JH 1966, 'Measurements on turbulent vortices in a cylinder wake', *proceedings of the Royal Society of London: Series A, Mathematical and Physical Sciences*, vol. 294, pp. 319 – 342.
- Breuer, M 1998, 'Numerical and modelling influences on large eddy simulations for the flow past a circular cylinder', *International Journal of Heat and Fluid Flow*, vol. 19, pp. 512 – 521.
- Bushnell, DM & Moore, KJ 1991, 'Drag reduction in nature', *Annual Review of Fluid Mechanics*, vol. 23, pp. 65 – 79.
- Bushnell, DM 1994 'Viscous Drag Reduction in Aeronautics' in *Proc. 19th Congress of the International Council of the Aeronautical Sciences*, vol. 1, no. ICAS-94-0.1, American Institute of Aeronautics and Astronautics, Washington, D.C., pp. 34 – 56.
- Catalano, P, Wang, M, Iaccarino, G & Moin, P 2003, 'Numerical simulation of the flow around a circular cylinder at high Reynolds numbers', *International Journal of Heat and Fluid Flow*, vol. 24, pp. 463 – 469.

- Curren, KC, Bose, N & Lien, J 1994, 'Swimming kinematics of a harbor porpoise (*Phocoena phocoena*) and an Atlantic white-sided dolphin (*Lagenorhynchus acutus*)', *Marine Mammal Science*, vol. 10, pp. 485 – 492.
- Custodio, D 2007, *The effect of Humpback Whale-like leading edge protuberances on hydrofoil performance*, M.Sc. Thesis, Worcester Polytechnic Institute, Massachusetts.
- Darekar, RM & Sherwin, SJ 2000, 'Flow past a square section cylinder with a wavy stagnation face', *Journal of Fluid Mechanics*, pp. 1 – 33.
- Darekar, RM & Sherwin, SJ 2001, 'Flow past a bluff body with a wavy stagnation face', *Journal of Fluids and Structures*, vol. 15, pp. 587 – 596.
- Dassen, T, Parchen, R, Bruggeman, J & Hagg, F 1996, 'Results of a wind tunnel study on the reduction of airfoil self-noise by the application of serrated blade trailing edges', *proceedings of the European Union Wind Energy Conference and Exhibition*, Gothenburg, Sweden, 20 – 24 May.
- Deardorff, JW 1970, 'A numerical study of three-dimensional turbulent channel flow at large Reynolds numbers', *Journal of Fluid Mechanics*, vol. 41, pp. 453 – 480.
- Dimarogonas, AD & Haddad, S 1992, *Vibration for Engineers*, 2nd edn, Prentice-Hall Inc., New Jersey.
- Dobre, A & Hangan, H 2004, 'Investigation of the three-dimensional intermediate wake topology for a square cylinder at high Reynolds number', *Experiments in Fluids*, vol. 37, pp. 518 – 530.
- Dobre, A, Hangan, H & Vickery, B 2006, 'Wake control based on spanwise sinusoidal perturbations', *AIAA*, vol. 44, no. 3, pp. 485 – 492.
- Dutta, S, Panigrahi, PK & Muralidhar, K 2008, 'Experimental investigation of flow past a square cylinder at an angle of incidence', *Journal of Engineering Mechanics*, vol. 134, no. 9, pp. 788 – 803.

- El-Gammal, M, Hangan, H & King, P 2007, 'Control of vortex shedding-induced effects in a sectional bridge model by spanwise perturbation method', *Journal of Wind Engineering and Industrial Aerodynamics*, vol. 95, pp. 663 – 678.
- Evans, K, Kemper, C & Hill, M 2001, 'First records of the spectacled porpoise (*Phocoena dioptrica*) in continental Australian waters', *Marine Mammal Science*, vol. 17, pp. 161 – 170.
- Fish, FE, Howle, LE & Murray, MM 2008, 'Hydrodynamic flow control in marine mammals', *Integrative and Comparative Biology*, vol. 48, no. 6, pp. 788 – 800.
- Fish, FE, Weber, PW, Murray, MM & Howle, LE 2011, 'The tubercles on humpback whales' flippers: application of bio-inspired technology', *Integrative and Comparative Biology*, vol. 51, pp. 203 – 213.
- Gerrard, JH 1966, 'The mechanics of the formation region of vortices behind bluff bodies', *Journal of Fluid Mechanics*, vol. 25, no. 2, pp. 401 – 413.
- Graham, RN 1934, 'The Silent Flight of Owls', *Journal of the Royal Aeronautical Society*, vol. 38, pp. 837 – 843.
- Griffin, OM & Ramberg, SE 1982, 'Some recent studies of vortex shedding with application to marine Tubulars and Risers', *Journal of Energy Resources Technology*, vol. 104, pp. 2 – 13.
- Herr, M 2006, 'Experimental study on noise reduction through trailing edge brushes', *New Results in Numerical and Experimental Fluid Mechanics V*, vol. 92, pp. 365 – 372.
- Hover, FS, Miller, SN & Triantafyllou, MS 1997, 'Vortex-induced vibration of marine cables: Experiments using force feedback', *Journal of Fluids and Structures*, vol. 11, pp. 307 – 326.
- Jaworski, J & Peake, N 2012, 'Poroelastic trailing edge noise and the silent flight of the owl', *65th Annual Meeting of the APS DFD*, vol. 57, San Diego.
- Jordan, SA & Ragab, SA 1998, 'A large eddy simulation of the near wake of a circular cylinder', *Journal of Fluids Engineering, ASME*, vol. 120, pp. 243 – 252.

- Kato, C & Ikegawa, M 1991, 'Large eddy simulation of unsteady turbulent wake of a circular cylinder using the finite element method', *Advances in Numerical Simulation of Turbulent Flows*, ASME, vol. 117, pp. 49 – 58.
- Khor, M, Sheridan, J & Hourigan, K 2011, 'Power-spectral density estimate of the Bloor-Gerrard instability in flows around circular cylinders', *Experimental Fluids*, vol. 50, pp. 527 – 534.
- Kohut, M 2007, *What do Owls and Think-Pads have in common?*, Lenovo Blog, Lenovo Pty Ltd, viewed 25 June 2008, <<http://www.lenovoblogs.com/insidethebox/2007/05/what-do-owls-and-thinkpads-have-in-common/>>.
- Krajnovic, S & Davidson, L 2002, 'Large-eddy simulation of the flow around a bluff body', *AIAA*, vol. 40, no. 5, pp. 927 – 936.
- Kravchenko, AG & Moin, P 2000, 'Numerical studies of flow over a circular cylinder at $Re_D = 3900$ ', *Physics of Fluids*, vol. 12, pp. 403 – 417.
- Kroeger, RA, Grushka, HD & Helvey, TC 1972, 'Low speed aerodynamics for ultra-quiet flight', *AFFDL, TR-71-75*, pp. 1 – 155.
- Kumar, RA, Sohn, CH & Gowda, BHL 2008, 'Passive control of vortex-induced vibrations: An overview', *Recent Patents on Mechanical Engineering*, vol. 1, pp. 1 – 11.
- Lam, K & Lin, YF 2008, 'Large eddy simulation of flow around wavy cylinders at a subcritical Reynolds number', *International Journal of Heat and Fluid Flow*, vol. 29, pp. 1071 – 1088.
- Lam, K & Lin, YF 2009, 'Effects of wavelength and amplitude of a wavy cylinder in cross-flow at low Reynolds numbers', *Journal of Fluid Mechanics*, vol. 620, pp. 195 – 220.
- Landahl, MT & Mollo-Christensen, E 1992, *Turbulence and random processes in fluid mechanics*, 2nd edn, Cambridge University Press, Cambridge.

- Liang, C & Papadakis, G 2007, 'Large eddy simulation of pulsating flow over a circular cylinder at subcritical Reynolds number', *Computers and Fluids*, vol. 36, pp. 299 – 312.
- Liang, G, Wang, J, Chen, Y, Zhou, C, Liang, J & Ren, L 2010, 'The study of Owl's silent flight and noise reduction on fan vane with bionic structure', *Advances in Natural Science*, vol. 3, no. 2, pp. 192 – 198.
- Lilley, GM 1998, 'A study of the silent flight of the Owl', *AIAA*, pp. 1 – 6.
- Lilley, GM 2009, 'The silent flight of the Owl: with applications of Owl technology to the design of future quiet commercial aircraft', *Lecture at Department of Building Services Engineering, Hong Kong Polytechnic University*, 2nd December.
- Lu, XY, Dalton, C & Zhang, J 1997a, 'Application of large eddy simulation to an oscillating flow past a circular cylinder', *Journal of Fluids Engineering*, ASME, vol. 119, pp. 519 – 525.
- Lu, XY, Dalton, C & Zhang, J 1997b, 'Application of large eddy simulation to flow past a circular cylinder', *Journal of Offshore Mechanics and Arctic Engineering*, ASME, vol. 119, pp. 219 – 225.
- Lu, S & Turan, O 2000, 'Numerical prediction of flow fields around circular cylinders: Forced motion and dynamic response cases', *Journal of Fluids Engineering*, vol. 122, pp. 703 – 714.
- Meiburg, E & Lasheras, JC 1988, 'Experimental and numerical investigation of the three-dimensional transition in plane wakes', *Journal of Fluid Mechanics*, vol. 190, pp. 1 – 37.
- Modeling and Meshing Guide* 2009, Release 12.0, ANSYS Inc., Canonsburg, PA.
- Moin, P 2002, 'Advances in large eddy simulation methodology for complex flows', *International Journal of Heat and Fluid Flow*, vol. 23, pp. 710 – 720.
- Mueller, T 2008, *Biomimetics: design by nature*, National Geographic Society, pp. 68 – 91.

- Oerlemans, S, Schepers, JG, Guidati, G & Wagner, S 2001, 'Experimental demonstration of wind turbine noise reduction through optimized airfoil shape and trailing-edge serrations', in *Proc. European Wind Energy Conference and Exhibition*, Copenhagen, 2 – 6 July.
- Ohya, H 1994, 'Note on a discontinuous change in wake pattern for a rectangular cylinder', *Journal of Fluids and Structures*, vol. 8, pp. 325 – 330.
- Okajima, A 1982, 'Strouhal numbers of rectangular cylinders', *Journal of Fluid Mechanics*, vol. 123, pp. 379 – 398.
- Owen, JC, Bearman, PW & Szewczyk, AA 2001, 'Passive control of VIV with drag reduction', *Journal of Fluids and Structures*, vol. 15, pp. 597 – 605.
- Pavlov, VV 2006, 'Dolphin skin as a natural anisotropic compliant wall', *Bioinspiration and Biomimetics*, vol. 1, pp. 31 – 40.
- Roach, J 2004, 'Owls' silent flight may inspire quiet aircraft technology', *National Geographic News*, viewed 17 April 2008, <<http://news.nationalgeographic.com/news/pf/9501079.html>>.
- Roache, PJ 1990, 'Need for control of numerical accuracy', *Journal of Spacecraft and Rockets*, vol. 27, no. 2, pp. 98 – 102.
- Saha, AK, Biswas, G & Muralidhar, K 2003, 'Three-dimensional study of flow past a square cylinder at low Reynolds numbers', *International Journal of Heat and Fluid Flow*, vol. 24, pp. 54 – 66.
- Shah, KB & Ferziger, JH 1997, 'A fluid mechanics view of wind engineering: Large eddy simulation of flow past a cubic obstacle', *Journal of Wind Engineering and Industrial Aerodynamics*, vol. 67 – 68, pp. 211 – 224.
- Shan, H, Jiang, L, Liu, C, Love, M & Maines, B 2008, 'Numerical study of passive and active flow separation control over a NACA0012 airfoil', *Computers and Fluids*, vol.37, pp. 975 – 992.
- Sheridan, J, Soria, W, Jie, W & Welsh, MC 1992, 'The kelvin-helmholtz instability of the separated shear layer from a circular cylinder', in: Eckelmann, H, Graham, JM,

- Huerre, P, Monkewitz, PA (Eds.), *Bluff Body Wakes, Dynamics and Instabilities, Proceedings of IUTAM Symposium*, Goettingen, Germany, Springer-Verlag, Berlin, p. 115.
- Sieradzki, A 2008, *Comb edge of Owl feather*, photograph, The Owl Pages, viewed 25 June 2008, <<http://www.owlpages.com/image.php?image=articles-Owl+Physiology-Feathers-2>>.
- Slagter, W 2011, 'A collaborative approach to solving engineering problems with CFD: How leading researchers benefit', *ANSYS White Paper*, ANSYS Inc., Canonsburg, Pennsylvania.
- Sohankar, A, Davidson, L & Norberg, C 2000, 'Large eddy simulation of flow past a square cylinder: Comparison of different subgrid scale models', *Journal of Fluids Engineering*, vol. 122, pp. 39 – 47.
- Sohankar, A 2006, 'Flow over a bluff body from moderate to high Reynolds numbers using large eddy simulation', *Computers and Fluids*, vol. 35, pp. 1154 – 1168.
- Sohankar, A 2008, 'Large eddy simulation of flow past rectangular-section cylinders: Side ratio effects', *Journal of Wind Engineering and Industrial Aerodynamics*, vol. 96, pp. 640 – 655.
- Szewczyk, AA, Owen, JC & Bearman, PW 2003, 'Method and apparatus for reducing drag and suppressing vortex-induced vibration', *United States Patent*, No. US 6619887B1, September 16.
- Tanner, M 1972, 'A method of reducing the base drag of wings with blunt trailing edges', *Aeronautical Quarterly*, vol. 23, no. 1, pp. 15 – 23.
- Tinoco, H, Lindqvist, H & Frid, W 2010, 'Numerical simulation of industrial flows', in Prof. L Angermann (ed.), *Numerical simulations – Examples and applications in computational fluid dynamics*, InTech, Croatia, pp. 231 – 262.
- Tombazis, N & Bearman, PW 1997, 'A study of three-dimensional aspects of vortex shedding from a bluff body with a mild geometric disturbances', *Journal of Fluid Mechanics*, vol. 330, pp. 85 – 112.

- Tutar, M & Holdo, AE 2000, 'Large eddy simulation of a smooth circular cylinder oscillating normal to a uniform flow', *Journal of Fluids Engineering*, vol. 122, pp. 694 – 702.
- Van den Abeele, F, Vande Voorde, J & Goes, P 2008, 'Numerical modelling of vortex induced vibrations in submarine pipelines', *excerpt from the proceedings of the COMSOL Conference*, Hannover.
- Versteeg, H & Malalasekera, W 2007, *An Introduction to Computational Fluid Dynamics: The Finite Volume Method*, 2nd edn, Prentice Hall, UK.
- Watts, P & Fish, FE 2001, 'The influence of passive, leading edge tubercles on wing performance', *proceedings of the Twelfth International Symposium on Unmanned Untethered Submersible Technology*, Autonomous Undersea Systems Institute, Durham New Hampshire.
- White, FM 2003, *Fluid Mechanics*, 5th edn, McGraw Hill, New York.
- Wilcox, DC 1993, *Turbulence Modelling for CFD*, 3rd edn, DCW Industries Inc., New York.
- Williamson, CHK 1996, 'Vortex dynamics in the cylinder wake', *Annual Review of Fluid Mechanics*, vol. 28, pp. 477 – 539.
- Williamson, CHK & Govardhan, R 2004, 'Vortex-induced vibrations', *Annual Review of Fluid Mechanics*, vol. 36, pp. 413 – 455.
- Winn, HE & Reichley, NE 1985, 'Humpback whale (*Megaptera novaeangliae*): The Sirenians and Baleen Whales', in SH Ridgway & R Harrison (eds.), *Handbook of Marine Mammals*, vol. 3, Academic Press, London, pp. 241 – 273.
- Wolfgang, MJ, Anderson, JM, Grosenbaugh, MA, Yue, DKP & Triantafyllou, MS 1999, 'Near-body flow dynamics in swimming fish', *Journal of Experimental Biology*, vol. 202, pp. 2303 – 2327.
- Xiyun, L & Guocan, L 2002, 'A Large Eddy Simulation of the near wake of a circular cylinder', *Journal of the Chinese Society of Theoretical and Applied Mechanics*, vol. 18, no. 1, pp. 18 – 30.

- Xu, CY, Chen, LW & Lu, XY 2010, 'Large-eddy simulation of the compressible flow past a wavy cylinder', *Journal of Fluid Mechanics*, vol. 665, pp. 238 – 273.
- Yu, D & Kareem, A 1998, 'Parametric study of flow around rectangular prisms using LES', *Journal of Wind Engineering and Industrial Aerodynamics*, vol. 78, pp. 653 – 662.
- Yu, D, Butler, K, Kareem, A, Glimm, J & Sun, J 2013, 'Simulation of the influence of aspect ratio on the aerodynamics of rectangular prisms', *Journal of Engineering Mechanics*, vol. 139, pp. 429 – 438.

CORRELATION ANALYSIS OF THE BOUNDARY LAYERS AROUND SSP BLUFF BODIES

A.1 Boundary Layer Topology Analysis of a Square SSP

Additional research of the flow topology was conducted by analysing the near wall flow features at the leading and trailing edge of each corresponding peak and valley plane for both $W0$ and $W3$. Hence, a comparative analysis is presented herein between the natural undisturbed flow topology and best controlled flow topology, respectively. The topology analysis in this section is performed through a cross-correlation of data at the near wall. This discussion will aim to demonstrate of the features and structures that are present within the flow while applying the passive control.

Both velocity and pressure histories have been measured. The data has shown similar trends are observed at each peak and valley plane. Therefore for brevity, only the two central peak locations and the two central valley locations are discussed. As a comparison to $W3$, four corresponding points located at the center of $W0$ have also been selected. The points for both $W0$ and $W3$ are indicated as 1 through to 4 in Figure A.1. The locations of the leading edge points correspond to the first grid cell above and in front of the leading edge, while the locations of the trailing edge points correspond to the first grid cell directly above the trailing edge. Hence, the measuring points are located 1×10^{-3} m away from the cylinder surface.

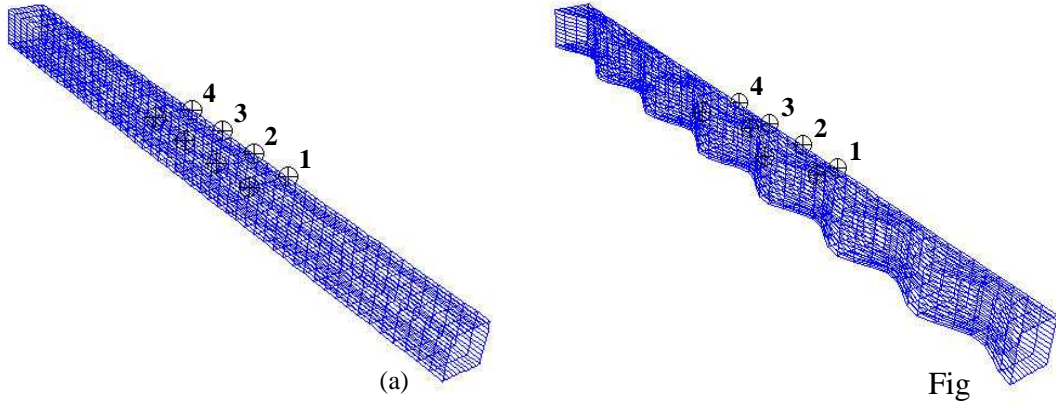


Figure A.1: Data points for the boundary layer topology analysis; (a) W0; (b) W3.

The process of correlation analysis allows specific coherent structures within the flow to be identified between particular physical quantities. In this case, the analysis focuses on the relationship between streamwise u -velocity and pressure. The correlation function filters the many spectral components that exist within the data due to non-stationary structures in the flow. Only the dominant frequencies corresponding to the coherent structures are presented, allowing a relationship to be formulated. The standard cross-correlation sequence is defined as

$$R_{u \cdot P}(m) = \sum_{i=1}^N u(t_i) \cdot P(t_i + m) \quad (\text{A.1.1})$$

where m is a predefined lead or lag, τ_i , equal to the time step size, $t_{i+1} - t_i$. In order to achieve a more accurate estimate of the cross-correlation, a normalised cross-correlation is obtained as

$$R_{u \cdot P, unbiased}(m) = \frac{1}{N - |m|} R_{u \cdot P}(m) \quad (\text{A.1.2})$$

This normalisation prevents any bias from occurring, as well as preventing any gradient within the sequence due to bias normalisation. The velocity-pressure histories and resulting unbiased cross-correlation function are given next for both W0 and W3 at

points 1 to 4. The following section will firstly discuss each of the four points in succession at the leading edge. The details at each trailing edge location will then follow with a similar approach.

A.1.1 Correlations at the Leading Edge of the Square Cylinder

In Figure A.2(a), u -velocity and pressure are plotted against time for both $W0$ and $W3$ at the leading edge at point 1, which corresponds to a peak plane. It should be noted herein that the history plots in this section show only 1 s of the complete data set, in order to clearly demonstrate the contrast between the compared histories. However, the analysis is still conducted with the full range of the data. The blue curve represents the velocity data, while the green curve represents the pressure data. The unbiased cross-correlation sequence, $R_{u-P,unbiased}$, between the streamwise u -velocity and pressure is presented in Figure A.2(b). Similar to the time histories, the correlations are plotted for 1 s of the data set with leading time, $t_i + \tau_i$. Therefore, the time axis represents lead, and zero time represents the initial cross-correlation at neither lead nor lag.

The history in Figure A.2(a) for $W0$ clearly shows the presence of an organised periodic structure between the velocity-pressure coupling, as a constant half cycle phase difference exists. A periodic structure is not as clear within the data history for $W3$, as few distinct frequencies occur. Both u -velocity and pressure do not acquire the exact phase difference which exists for $W0$. This behaviour for $W3$ indicates interference to the coherent flow structure. The magnitude of the overall data confirms this flow disturbance, as the average maximum velocity magnitude between $W0$ and $W3$ is approximately 1.5 ms^{-1} and 0.3 ms^{-1} , respectively. The average maximum magnitude for pressure between the two comparisons is approximately 70 Pa and 8 Pa, respectively. Therefore, a decrease is obtained for the streamwise velocity and pressure of approximately 80 percent and 88 percent, respectively. This is a significant contribution to the mitigation of the original coherent structures. It should be noted here that the values of average maximums are taken for the complete data sets from the simulations.

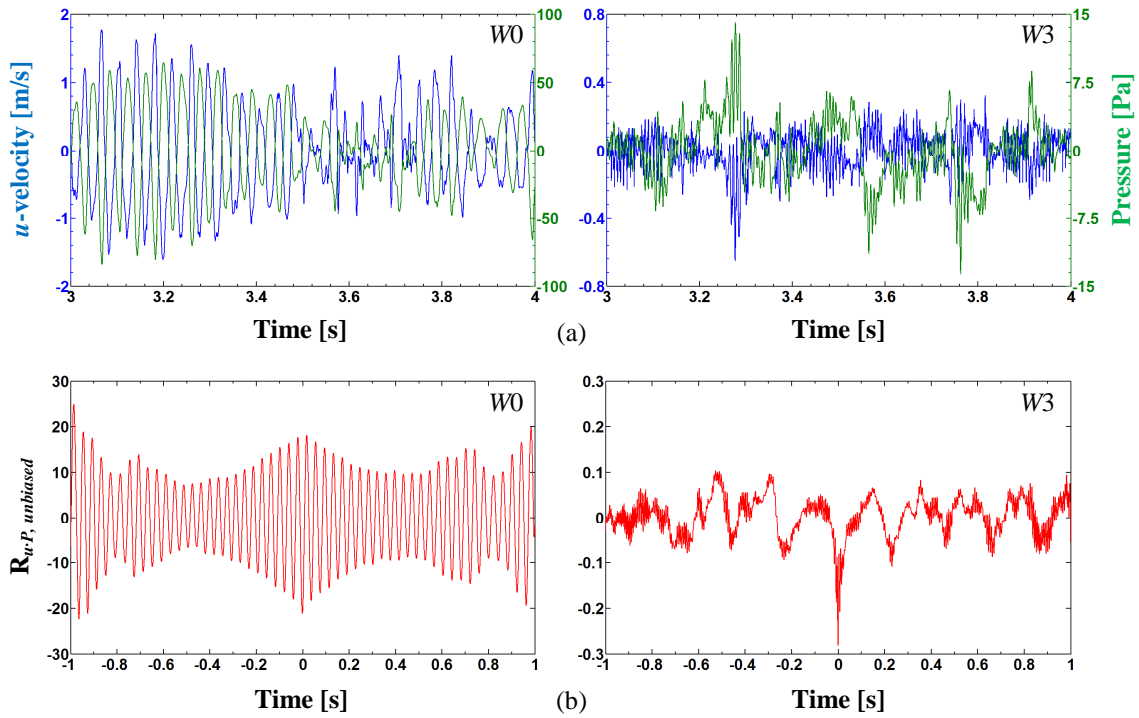


Figure A.2: Cross-correlation between u -velocity (—) and pressure (—) at the leading edge of point 1 for $W0$ (left) and $W3$ (right); (a) data history and (b) unbiased cross-correlation sequence.

The cross-correlation function in Figure A.2(b) shows a strong correlation between the u -velocity and pressure for $W0$ occurring at zero time delay. This strong correlation is further supported by the comparably high correlation magnitude throughout the time delay sequence. A clear periodic structure exists with a clear single frequency existing between the interactions of the two data sets. For $W3$, the strength of the correlation between the data can be considered negligible in comparison to that of $W0$. The correlation function of $W3$ reveals a periodic structure with a high frequency density. Although the largest correlation occurs at zero time delay for $W3$, the overall magnitude is approximately less than one percent of the magnitude for $W0$.

Power spectral density (PSD) calculations are performed for the data, in order to determine the specific coherent structures that are present within the flow between $W0$ and $W3$. Hence, conducting a Fourier transform verifies the degree of correlation existing for both cases. The PSD of u -velocity, pressure, and unbiased cross-correlation function at point 1 are given in Figures A.3(a), A.3(b) and A.3(c) for $W0$, and Figures

A.3(d), A.3(e) and A.3(f) for $W3$. The horizontal axis of these plots has a frequency range up to approximately $7f_{vo}$.

For $W0$, the dominant structures in both the velocity and pressure data occur at approximately $0.5f_{vo}$ in Figures A.3(a) and A.3(b). In Figure A.3(c), correlation clearly exists between these two flow variables at only $0.5f_{vo}$. For $W3$, spectral peaks occur at approximately $0.2f_{vo}$, $2.5f_{vo}$ and $3f_{vo}$. This is shown in Figures A.3(d) and A.3(e) for both u -velocity and pressure. However, the spectral density in Figure A.3(f) shows only spectral peaks at approximately $0.2f_{vo}$, $2.5f_{vo}$ and $3f_{vo}$. The presence of a fundamental peak occurring at $0.2f_{vo}$ indicates the shift in frequency content of the typically dominant coherent structures. The spectral peaks at approximately $2.5f_{vo}$ and $3f_{vo}$ correspond to the shear layer instabilities in the form of Bloor-Gerrard vortices.

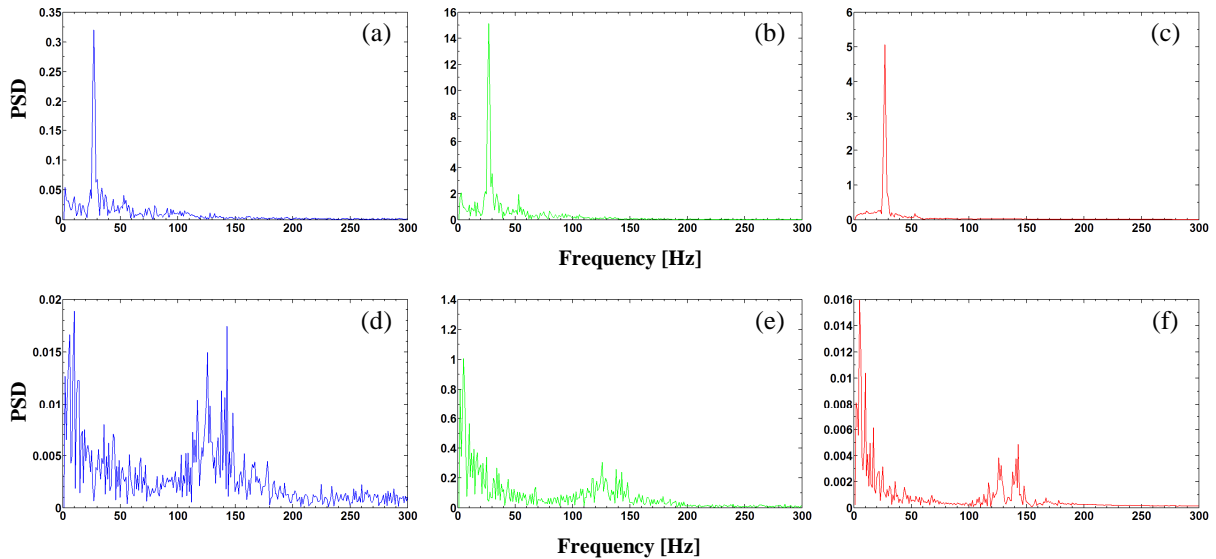


Figure A.3: PSD of u -velocity (—), pressure (—) and unbiased cross-correlation function (—) at the leading edge of point 1 for (a, b, c) $W0$ and (d, e, f) $W3$.

The time histories of u -velocity and pressure at point 2 of the leading edge of both $W0$ and $W3$ are provided in Figure A.4(a). This point corresponds to a valley plane for the controlled cylinder, $W3$. As expected during the analysis, a similar periodic structure within the data as to that at point 1 emerges for $W0$. This is clearly the result of maintaining an undisturbed leading edge. The maximum average magnitudes for the streamwise velocity and pressure throughout the simulations also remain the same at approximately 1.5 ms^{-1} and 70 Pa , respectively.

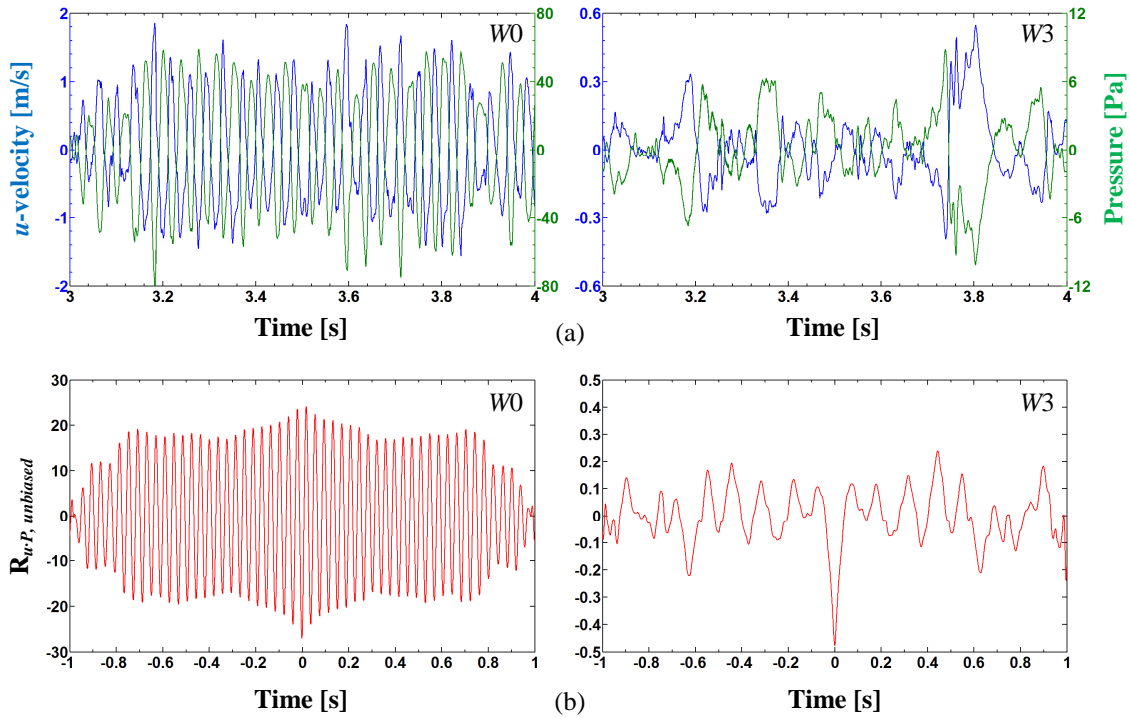


Figure A.4: Cross-correlation between u -velocity (—) and pressure (—) at the leading edge of point 2 for W0 (left) and W3 (right); (a) data history and (b) unbiased cross-correlation sequence.

For W3, the data in Figure A.4(a) contains a dissimilar structure to that at point 1 in Figure A.2(a). The histories are much clearer, allowing the identification of two or three frequencies within the content more apparent. This is evident of the boundary layer three-dimensionality along the span, as structures between peak and valley planes differ periodically. The overall magnitudes remain relatively similar to the peak plane, in this case. The maximum average streamwise velocity and pressure are approximately 0.35 ms^{-1} and 7 Pa , respectively. Therefore, the reductions in velocity and pressure fluctuations achieved at the leading edge of a valley plane are approximately 76 percent and 90 percent, respectively.

The cross-correlation sequence for the leading edge of W0 at point 2 shows high correlation between the streamwise u -velocity and pressure in Figure A.4(b). Larger correlation than that of the peak location exists throughout the sequence, with the presence of a clear single frequency. For W3, the cross-correlation sequence in Figure A.4(b) is slightly larger than that of point 1, and the magnitude at the largest correlation

at zero time delay is approximately two percent that of $W0$. Therefore, the correlation magnitude indicates an interruption to the coherent flow at a valley. It is clear that the velocity-pressure coupling for $W3$ is correlated at one or two distinct frequencies at the leading edge at the valley.

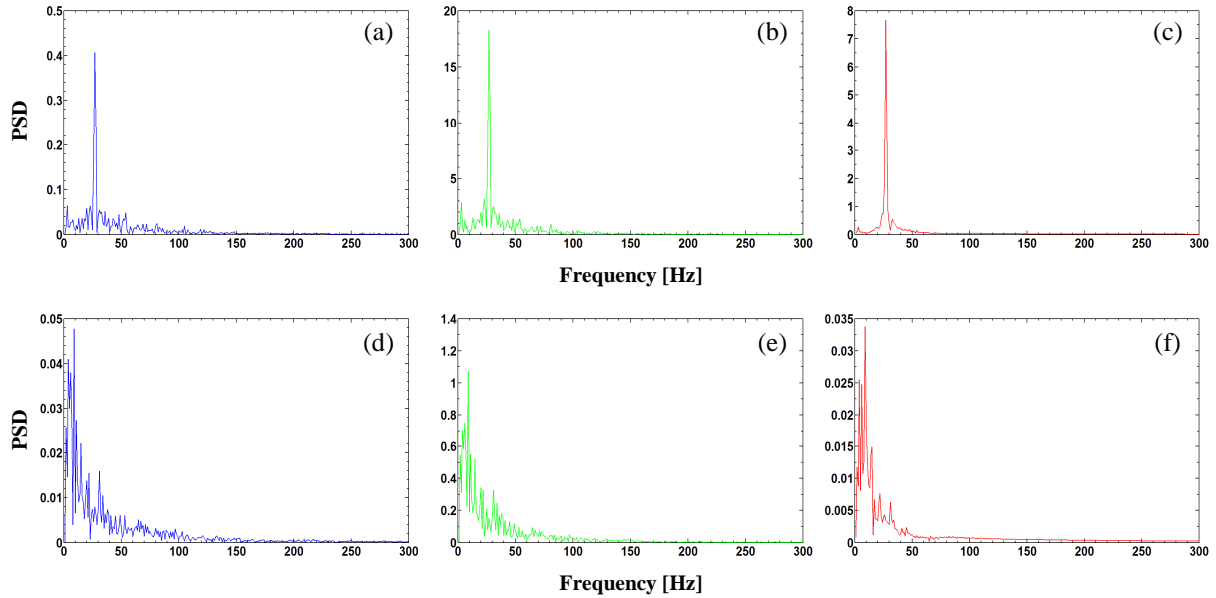


Figure A.5: PSD of u -velocity (—), pressure (—) and unbiased cross-correlation function (—) at the leading edge of point 2 for (a, b, c) $W0$ and (d, e, f) $W3$.

Obtaining the power spectral densities for u -velocity, pressure and the cross-correlation function of both $W0$ and $W3$ produces the plots shown in Figure A.5. For $W0$, a clear spectral peak appears again at a frequency equal to approximately $0.5f_{v0}$. This is shown in Figures A.5(a), A.5(b) and A.5(c). For the PSD of $W3$ at point 2, the velocity-pressure coupling is correlated only at a frequency of approximately $0.2f_{v0}$. This is shown in Figures A.5(d), A.5(e) and A.5(f). This frequency shift observation is indicative of the vortex-shedding mitigation achieved, and the observed structure at only $0.2f_{v0}$ is characteristic to the attached boundary layer at a valley plane. Hence, there is no obvious additional shear layer instabilities present at a valley.

Continuing along the span of the square cylinders to the leading edge at point 3, corresponding to another peak plane for the controlled cylinder, $W3$, it is expected to observe quite similar behaviour as to that established at point 1. The time histories for the streamwise velocity and pressure in Figure A.6(a), confirm this. Average maximum

magnitudes for velocity and pressure remain relatively similar to the values at point 1 at approximately 1.5 ms^{-1} and 70 Pa , respectively. For $W3$, the magnitude for the time history also remains consistent between the two peak locations, at approximately 0.35 ms^{-1} and 7 Pa for velocity and pressure, respectively. Therefore, reductions are approximately 76 percent for velocity and 90 percent for pressure.

Considering the plots for the cross-correlation function, Figure A.6(b) demonstrates a high correlation between u -velocity and pressure at zero time delay, and a comparable magnitude throughout the sequence for $W0$. Few distinct frequencies are clearly being correlated between the data for $W3$. The observations from the cross-correlation sequence suggest the same frequencies occur at the leading edge for both points 1 and 3. Similar correlation magnitude is obtained, which also demonstrates the consistency between the two points, and accuracy of the numerical model.

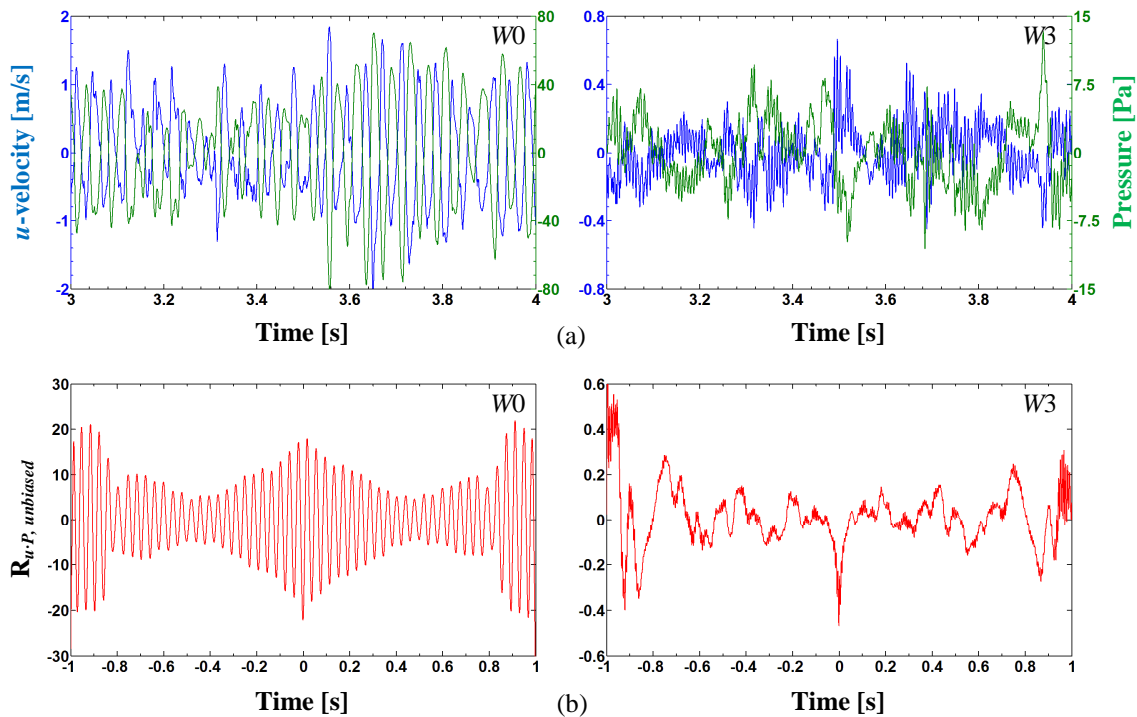


Figure A.6: Cross-correlation between u -velocity (—) and pressure (—) at the leading edge of point 3 for $W0$ (left) and $W3$ (right); (a) data history and (b) unbiased cross-correlation sequence.

The PSD plots in Figure A.7(a), A.7(b) and A.7(c) for $W0$ at point 3 indicate the coherent structures occurring at approximately $0.5f_{vo}$. For $W3$, spectral peaks appear at approximately $0.2f_{vo}$ and $2.5f_{vo}$ to $3f_{vo}$. It should be noted that within Figure A.7(f), the streamwise u -velocity and pressure are only correlated at $0.2f_{vo}$, as negligible spectral content surrounds $3f_{vo}$. Hence, the significant difference between the two peak planes discussed for points 1 and 3 is observed in the strength of the spectral content at $3f_{vo}$. As coherent structures exist dominantly at $0.2f_{vo}$ for both u -velocity and pressure at both peak leading edge locations, it is quantitatively corroborated that similar coherent structures occur along peak planes. The presence of the small scale Bloor-Gerrard vortices occurring at approximately $3f_{vo}$ do not appear to influence the correlation at the leading edge.

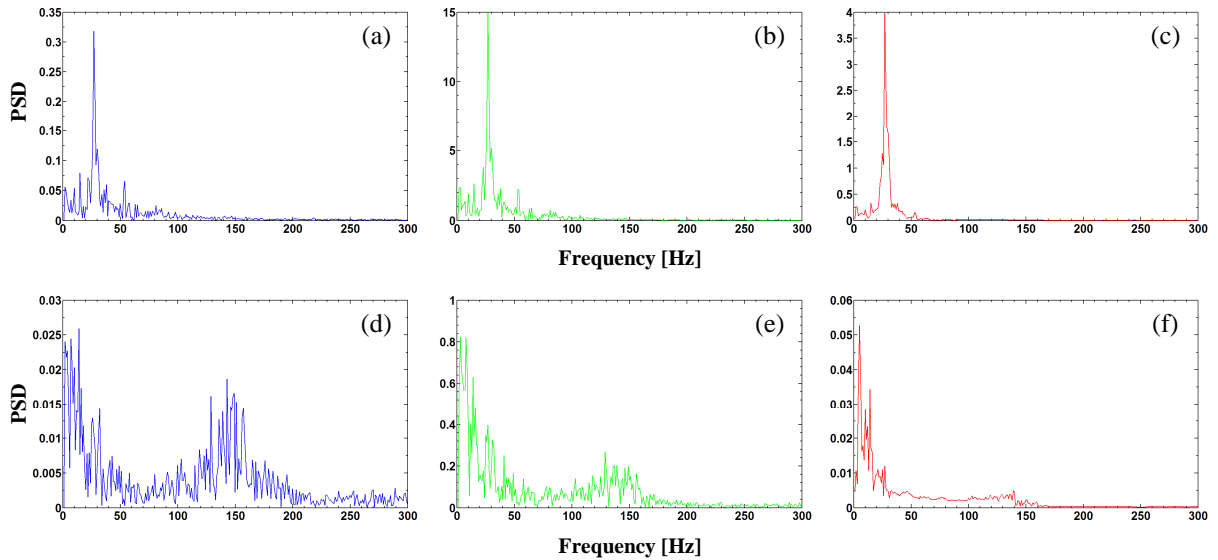


Figure A.7: PSD of u -velocity (—blue—), pressure (—green—) and unbiased cross-correlation function (—red—) at the leading edge of point 3 for (a, b, c) $W0$ and (d, e, f) $W3$.

At the leading edge at point 4, the trends for $W0$ show the constant half cycle phase lead and average maximum velocity and pressure magnitudes of approximately 1.5 ms^{-1} and 60 Pa , respectively. For the controlled square cylinder, $W3$, a similar trend in the time history exists at the leading edge between the valley plane at point 2 and that of point 4. The average maximum magnitudes for streamwise velocity and pressure are approximately 0.35 ms^{-1} and 7 Pa , respectively. Therefore, the reductions in fluctuations achieved for both velocity and pressure are approximately 76 percent and 88 percent,

respectively. The cross-correlation sequence in Figure A.8(b) for $W0$ at point 4 indicates the high correlation usually observed between the streamwise velocity and pressure for this configuration. The trend throughout the time sequence is also similar between each leading edge point. For $W3$, the magnitude of the correlation function is comparable to that of the valley plane at point 2, with similar frequency content observed.

The spectral distribution at point 4 for $W0$ shows the correlation at a frequency of approximately $0.5f_{vo}$. This can be seen in Figures A.9(a), A.9(b) and A.9(c). The frequency distribution for $W3$ shows the correlation occurring at $0.2f_{vo}$. This observation is identical to that made at point 2 for the corresponding valley plane, and is shown in Figures A.9(d), A.9(e) and A.9(f).

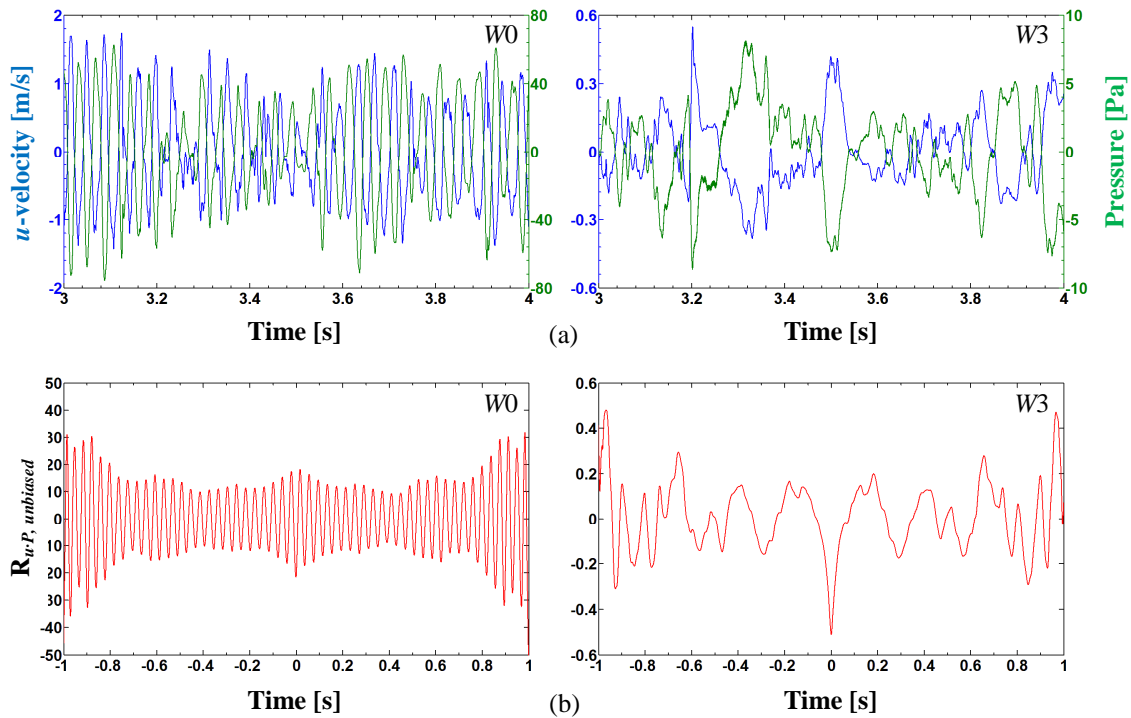


Figure A.8: Cross-correlation between u -velocity (—) and pressure (—) at the leading edge of point 4 for $W0$ (left) and $W3$ (right); (a) data history and (b) unbiased cross-correlation sequence.

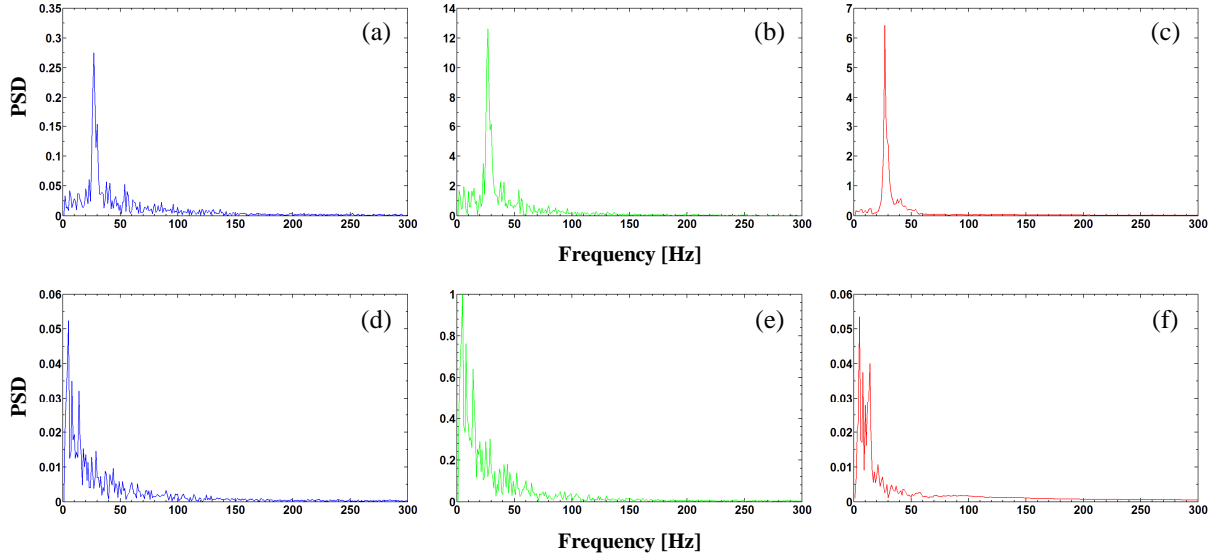


Figure A.9: PSD of u -velocity (—), pressure (—) and unbiased cross-correlation function (—) at the leading edge of point 4 for (a, b, c) $W0$ and (d, e, f) $W3$.

Table A.1: Summary of observations for the spanwise boundary layer topology analysis.

LE Point	W0			W3				
	u -velocity [ms ⁻¹]	Pressure [Pa]	Correlated Frequency [Hz]	u -velocity [ms ⁻¹]	Pressure [Pa]	Correlated Frequency [Hz]	Velocity reduction [%]	Pressure reduction [%]
1	1.5	70	$0.5f_{vo}$	0.3	8	$0.2f_{vo}, 3f_{vo}$	80	88
2	1.5	70	$0.5f_{vo}$	0.35	7	$0.2f_{vo}$	76	90
3	1.5	70	$0.5f_{vo}$	0.35	7	$0.2f_{vo}, 3f_{vo}$	76	90
4	1.5	60	$0.5f_{vo}$	0.35	7	$0.2f_{vo}$	76	88

Table A.1 provides a summary of the observations discussed in this section. Similar reductions in the velocity and pressure fluctuations are obtained throughout all the leading edge points 1 to 4. As the histories of the velocity-pressure coupling are random time-dependent data sets, it is expected that some slight differences in overall percent reductions are obtained. Nevertheless, it is important that the reductions compare well. It can be observed that the key difference across the four points is the shift in frequency

content between the uncontrolled and controlled cases. This is a clear quantitative representation of the mitigation of the coherent bluff body flow.

A.1.2 Correlations at the Trailing Edge of the Square Cylinder

In Figure A.10(a), u -velocity and pressure are plotted against time for both $W0$ and $W3$ at the trailing edge at point 1 from Figure A.1. This point corresponds to a peak plane. The history in Figure A.10(a) for $W0$ clearly shows the presence of an organised periodic structure between the velocity-pressure coupling. However, when inspecting a period of 0.5 s for the data, instead of the histories remaining at a constant half cycle phase difference, the data appears to be almost in phase.

A periodic structure is not as clear within the data history for $W3$ at the trailing edge, as few distinct frequencies are clearly present. The velocity-pressure coupling appears to contain similar features and coherent structures to that of point 1 at the leading edge. Observing only 0.5 s of the history in Figure A.10(a), it is revealed that the velocity-pressure coupling is almost completely in phase for $W3$. There is however, slight indication that the fundamental frequency is out of phase. The average maximum velocity magnitude for $W0$ and $W3$ in Figure A.10(a) is approximately 8 ms^{-1} and 2.5 ms^{-1} , respectively. These average magnitudes are taken across the whole simulated data range. The average maximum magnitude for pressure between the two comparisons is approximately 80 Pa and 16 Pa, respectively. Therefore, a decrease is obtained for the streamwise velocity and pressure of approximately 69 percent and 80 percent, respectively.

The cross-correlation function in Figure A.10(b) shows a strong correlation between the u -velocity and pressure for $W0$ occurring at zero time delay. Correlation diminishes slightly for larger lead time; however there remains a comparably high correlation magnitude throughout the correlation sequence. It is clear that correlation for $W0$ between u -velocity and pressure exists at two distinct frequencies. For $W3$, the strength of the correlation is highly mitigated and approximately three percent that of $W0$. The correlation function of $W3$ reveals an unclear periodic structure with a high frequency density, which is a somewhat similar observation to that made at the leading edge.

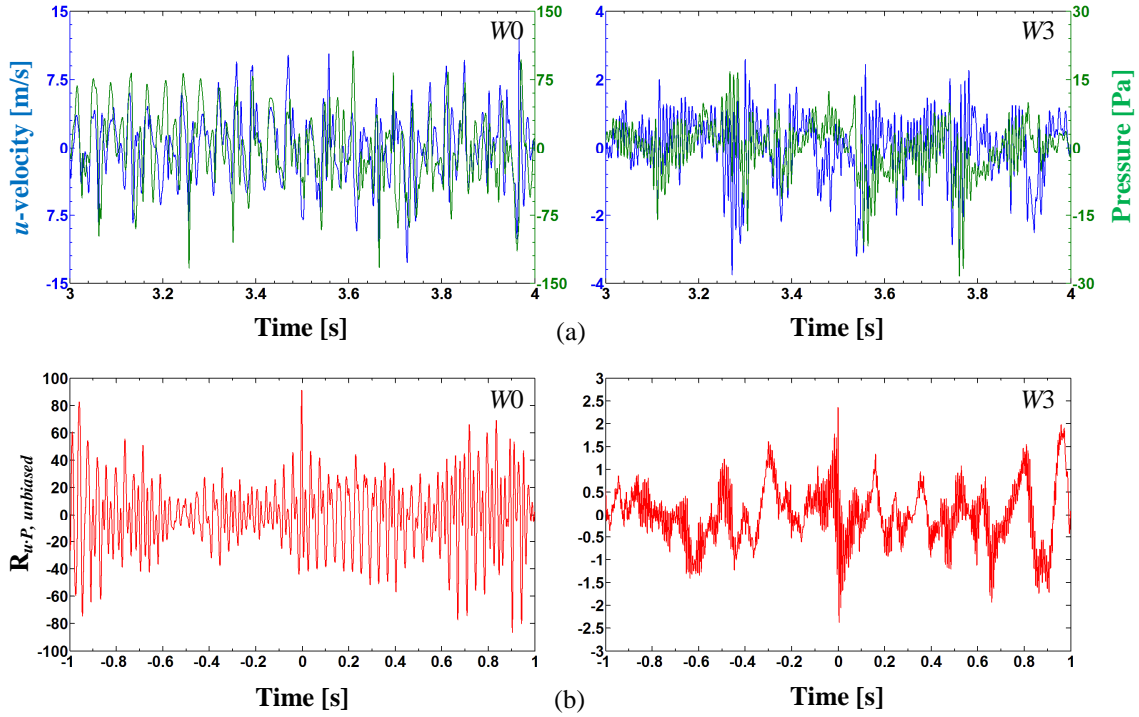


Figure A.10: Cross-correlation between u -velocity (—) and pressure (—) at the trailing edge of point 1 for W0 (left) and W3 (right); (a) data history and (b) unbiased cross-correlation sequence.

Power spectral density (PSD) calculations at the trailing edge at point 1 are given in Figures A.11(a), A.11(b) and A.11(c) for W0, and Figures A.11(d), A.11(e) and A.11(f) for W3. The horizontal axis of these plots has a frequency range up to approximately $6f_{vo}$. The dominant structures in both the velocity and pressure data of W0 are equally present at approximately $0.5f_{vo}$ and f_{vo} . This is indicated in Figures A.11(a) and A.11(b). At the trailing edge, the effects of the Strouhal number, St , for the square section geometry are clearly apparent, due to the full presence of the vortex-shedding structures caused by some development of the boundary flow. In Figure A.11(c), correlation also exists at $0.5f_{vo}$ and f_{vo} . For W3, correlation occurs at the frequency of approximately $0.2f_{vo}$, $2.5f_{vo}$ and $3f_{vo}$. This is shown in Figures A.11(d), A.11(e) and A.11(f), respectively. The spectral peaks at approximately $2.5f_{vo}$ and $3f_{vo}$ correspond to the Bloor-Gerrard shear layer instabilities.

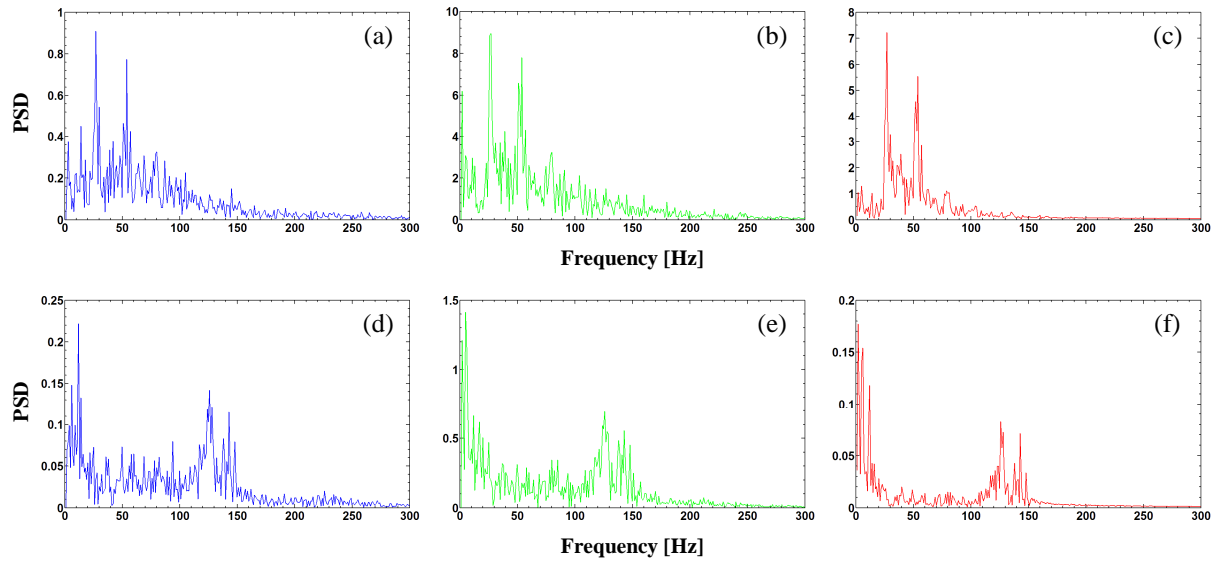


Figure A.11: PSD of u -velocity (—), pressure (—) and unbiased cross-correlation function (—) at the trailing edge of point 1 for (a, b, c) W0 and (d, e, f) W3.

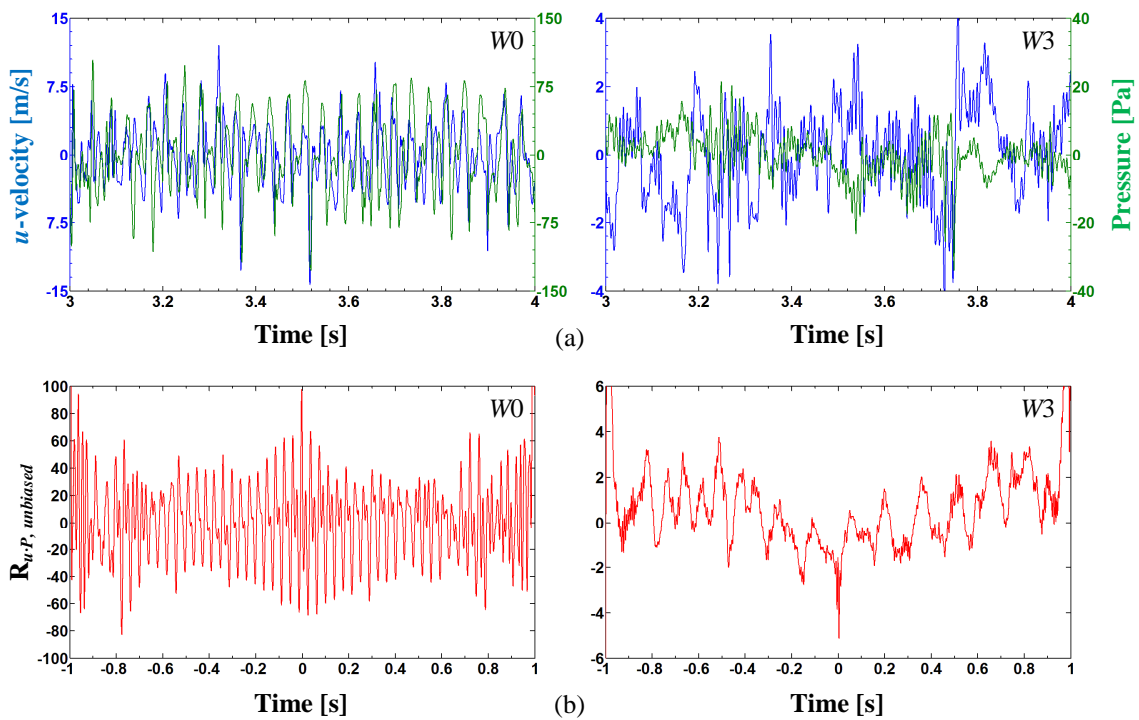


Figure A.12: Cross-correlation between u -velocity (—) and pressure (—) at the trailing edge of point 2 for W0 (left) and W3 (right); (a) data history and (b) unbiased cross-correlation sequence.

The time histories of u -velocity and pressure at point 2 at the trailing edge are provided in Figure A.12(a). This point corresponds to a valley plane for the controlled cylinder, $W3$. Similar history to that at point 1 for $W0$ is shown, with maximum average magnitudes of u -velocity and pressure at approximately 8 ms^{-1} and 80 Pa , respectively. For $W3$, the data in Figure A.12(a) shows the maximum average streamwise velocity and pressure are approximately 3 ms^{-1} and 18 Pa , respectively. Therefore, the reductions in velocity and pressure fluctuations achieved at the trailing edge of a valley plane are approximately 62 percent and 78 percent, respectively.

In Figure A.13, the PSD at point 2 reveals dominant flow structures occurring at approximately $0.5f_{vo}$ and f_{vo} for $W0$ within both velocity and pressure data. This is shown in Figures A.13(a) and A.13(b). Hence, correlation also occurs at these two frequencies in Figure A.13(c). For $W3$, the coherent structures primarily exist at approximately $0.2f_{vo}$ for both u -velocity and pressure in Figures A.13(d) and A.13(e). Correlation of the velocity-pressure coupling exists at only $0.2f_{vo}$ in Figure A.13(f).

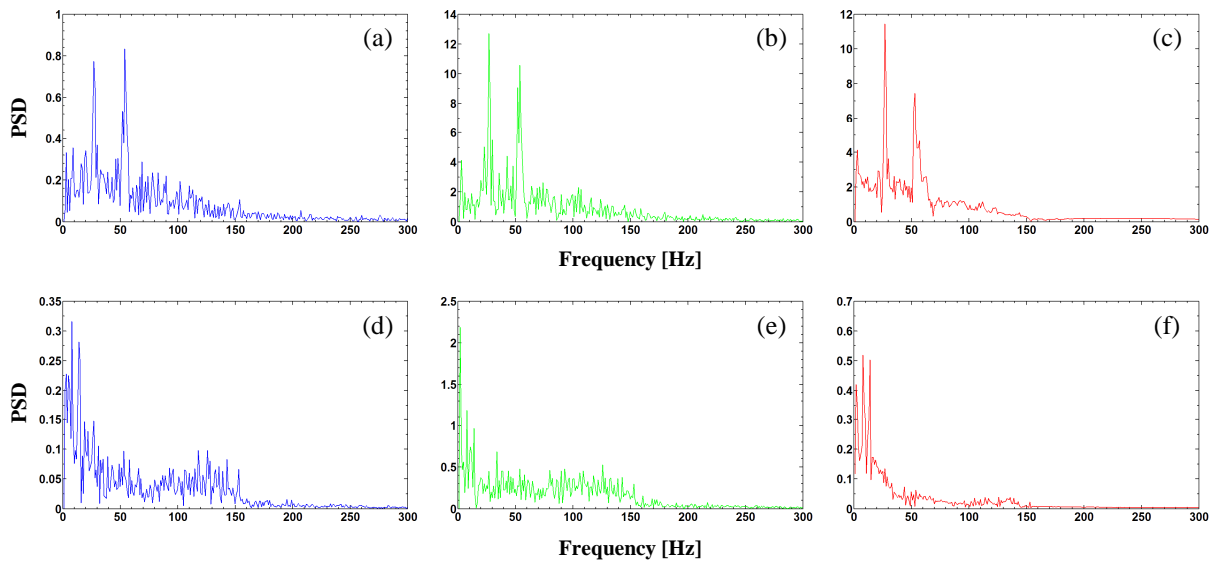


Figure A.13: PSD of u -velocity (—), pressure (—) and unbiased cross-correlation function (—) at the trailing edge of point 2 for (a, b, c) $W0$ and (d, e, f) $W3$.

At the trailing edge at point 3, corresponding to a peak plane for the SSP cylinder, $W3$, the histories for the streamwise velocity and pressure in Figure A.14(a) show average maximum magnitudes for velocity and pressure remain relatively similar to the

values at point 1 at approximately 2 ms^{-1} and 15 Pa , respectively. For $W0$, the same consistent behaviour to that at previous points along the trailing edge is observed. The average maximum magnitudes are 8 ms^{-1} and 80 Pa for velocity and pressure, respectively. Hence, reductions are achieved at approximately 75 percent for velocity and 81 percent for pressure.

The PSD plots in Figure A.15(a), A.15(b) and A.15(c) for $W0$ at point 3 indicate the dominant structures and correlation occurring at approximately $0.5f_{vo}$ and f_{vo} . For $W3$, the dominant flow structures are present at $0.2f_{vo}$. As point 3 corresponds to a peak plane, it is expected that evidence of the shear layer instabilities caused by the leading edge flow separation will exist in the data. The significant difference between the frequency distribution for the trailing edge at both peak locations is the strength of the coherent structures corresponding to the shear layer instabilities.

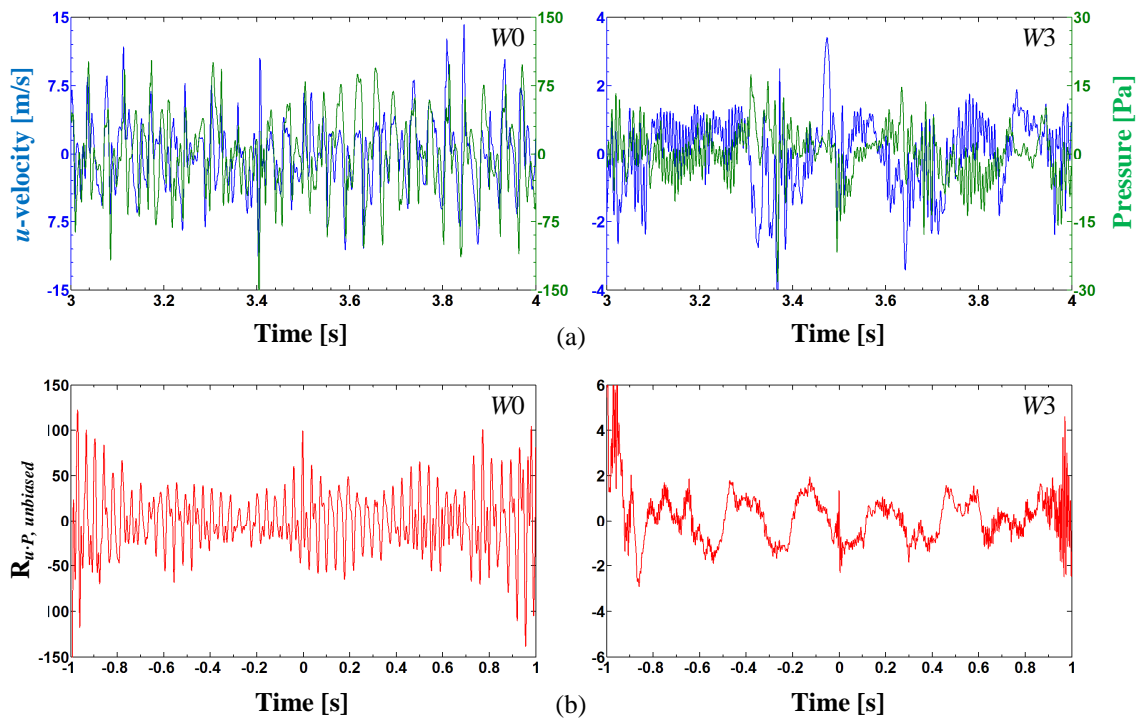


Figure A.14: Cross-correlation between u -velocity (—) and pressure (—) at the trailing edge of point 3 for $W0$ (left) and $W3$ (right); (a) data history and (b) unbiased cross-correlation sequence.

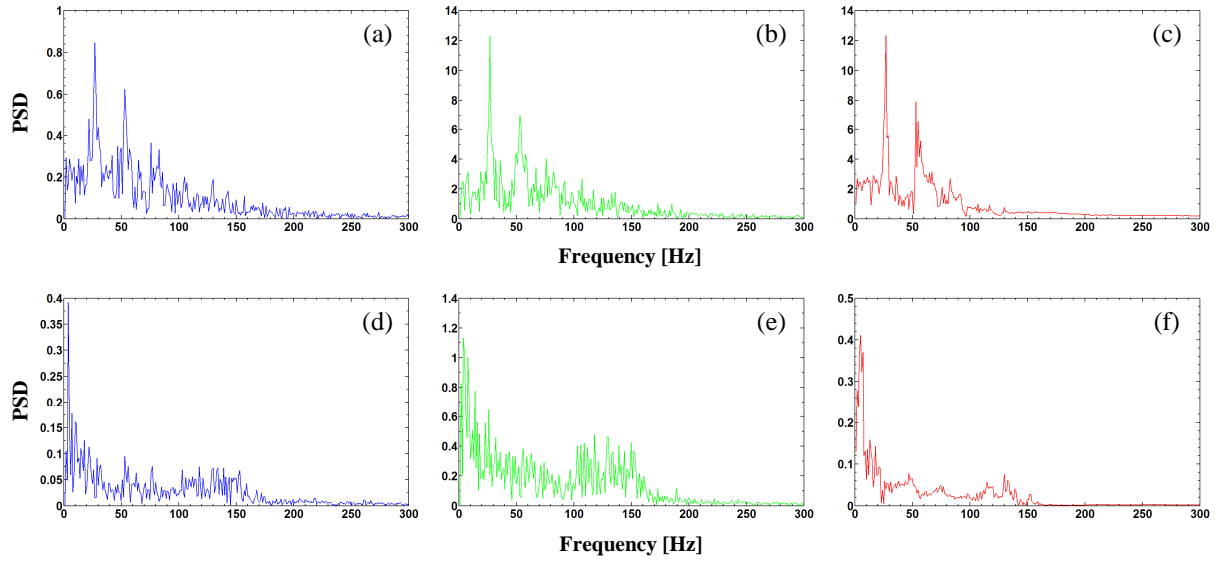


Figure A.15: PSD of u -velocity (—), pressure (—) and unbiased cross-correlation function (—) at the trailing edge of point 3 for (a, b, c) W0 and (d, e, f) W3.

At point 4, the expected trend in the histories for the plain square cylinder, W0, which are present for all previous trailing edge points are apparent. This is shown in Figure A.16(a). These trends are the phase similarities in the velocity-pressure coupling, and average maximum velocity and pressure magnitudes of approximately 8 ms^{-1} and 80 Pa, respectively. For the controlled square cylinder, W3, a similar trend in the time history exists at the trailing edge between the valley plane at point 2 and that of point 4. The fundamental frequency is clearly out of phase, while the higher frequencies appear to be in phase. The average maximum magnitudes for the streamwise velocity and pressure are approximately 3 ms^{-1} and 15 Pa, respectively. Reductions in fluctuations achieved for both velocity and pressure are therefore, approximately 62 percent and 81 percent, respectively. The cross-correlation sequence in Figure A.16(b) indicates approximately 97 percent decrease in the correlation strength between the data sets is observed at point 4, and similar frequency content to that at point 2.

The power spectral density at point 4 indicates correlation occurring for W0 at both approximately $0.5f_{v0}$ and f_{v0} . This can be seen in Figures A.17(a), A.17(b) and A.17(c). The frequency distribution for W3 shows the correlation occurring at $0.2f_{v0}$. Slight indication of spectral content within the frequency distribution is present between

approximately $2f_{vo}$ to $3f_{vo}$. As mentioned for point 2, the occurrence of content at this frequency range is due to the shear layer instabilities occurring at the trailing edge of valley planes. The measuring point is located directly above the trailing edge of the square cylinder; hence, the boundary layer separates at this location, due to the influence of shedding flow.

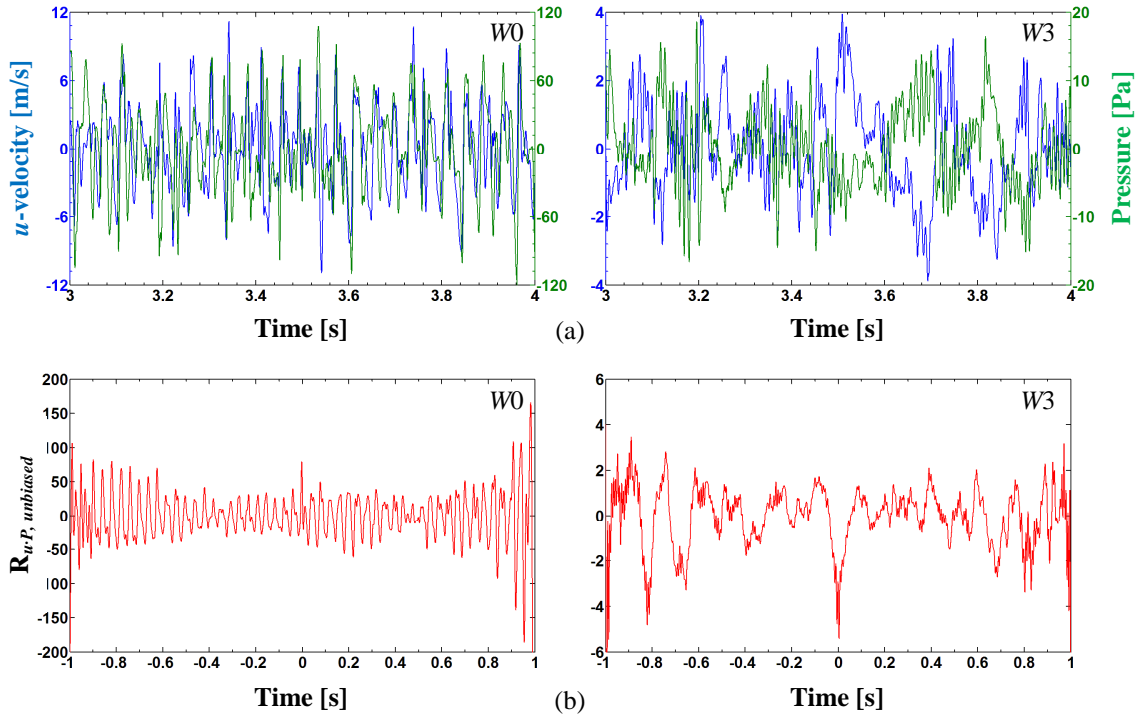


Figure A.16: Cross-correlation between u -velocity (—) and pressure (—) at the trailing edge of point 4 for W0 (left) and W3 (right); (a) data history and (b) unbiased cross-correlation sequence.

Table A.2 below provides a summary of the observations discussed in this section. Similar reductions in the velocity and pressure fluctuations are obtained throughout all the trailing edge points 1 to 4. This is a clear quantitative representation of the mitigation of the coherent and incoherent bluff body flow. Correlation at point 3 does occur at approximately $3f_{vo}$, however, the presence at this frequency is considered negligible in comparison to that of point 1. This is due to the weak spectral content at $3f_{vo}$ within the velocity PSD. Nevertheless, the observations show the same overall coherent structures appearing between valley planes and peak planes.

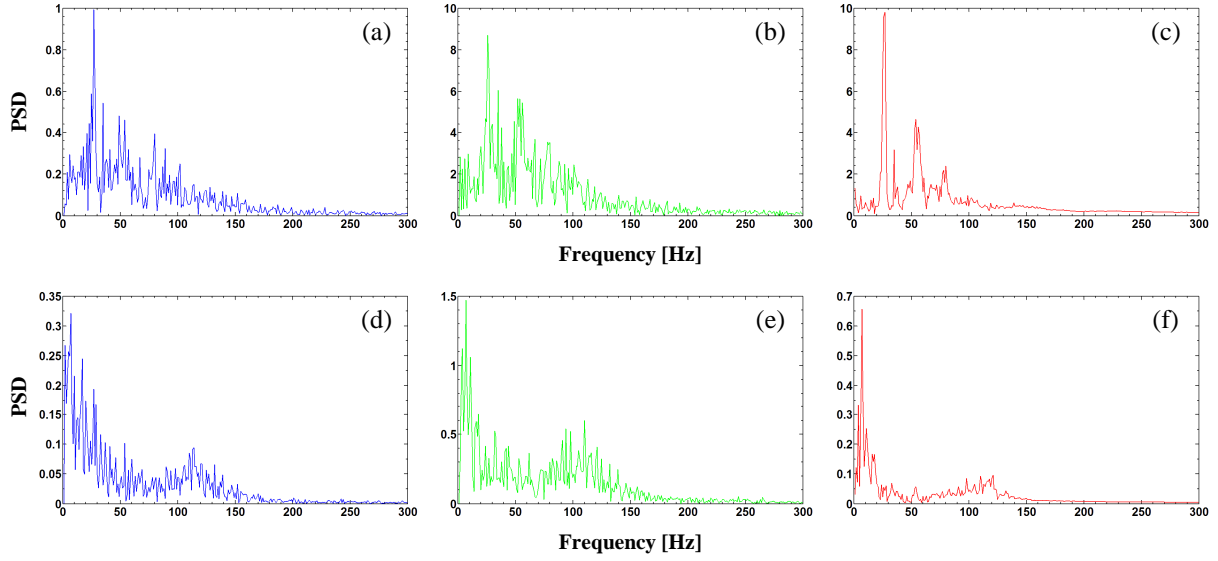


Figure A.17: PSD of u -velocity (—), pressure (—) and unbiased cross-correlation function (—) at the trailing edge of point 4 for (a, b, c) W0 and (d, e, f) W3.

Table A.2: Summary of observations for the spanwise boundary layer topology analysis.

LE Point	W0			W3				
	u -velocity [ms ⁻¹]	Pressure [Pa]	Correlated Frequency [Hz]	u -velocity [ms ⁻¹]	Pressure [Pa]	Correlated Frequency [Hz]	Velocity reduction [%]	Pressure reduction [%]
1	8	80	$0.5f_{vo}, f_{vo}$	2.5	16	$0.2f_{vo}, 3f_{vo}$	69	80
2	8	80	$0.5f_{vo}, f_{vo}$	3	18	$0.2f_{vo}$	62	78
3	8	80	$0.5f_{vo}, f_{vo}$	2	15	$0.2f_{vo}$	75	81
4	8	80	$0.5f_{vo}, f_{vo}$	3	15	$0.2f_{vo}$	62	81

CORRELATION ANALYSIS OF THE BOUNDARY LAYER AROUND AN ELONGATED SSP

B.1 Boundary Layer Topology Analysis of an Elongated SSP

Additional investigation of the flow topology is conducted by analysing the near wall flow features at the leading and trailing edges of the rectangular prisms. Histories of u -velocity and pressure are obtained at leading and trailing edge spanwise points corresponding to peak and valley planes for the elongated SSP cylinder, $W3_E$, as well as the plain elongated cylinder, $W0_E$. Cross-correlation analysis is performed between the velocity and pressure data at each individual point, in order to determine the fluid structures that are present within the boundary layers of the prisms. For brevity, only five spanwise points are discussed for both $W0_E$ and $W3_E$. The purpose for selecting such points is to demonstrate the symmetry of flow structures within the boundary layer about the mid-span location. The points discussed herein are indicated for the elongated cylinders in Figure B.1.

The monitor points along the leading edge of both prisms correspond to the first grid cell above and in front of the leading edge, while the monitor points along the trailing edge correspond to the first grid cell directly above the trailing edge. Therefore, the measurement locations are placed at a distance of 1×10^{-3} m from the cylinder wall. The cross-correlation observations in the following section will firstly discuss the leading edge locations for $W0_E$ and $W3_E$. The details at the trailing edge locations will then follow with a similar approach, in order to demonstrate the flow structures concisely.

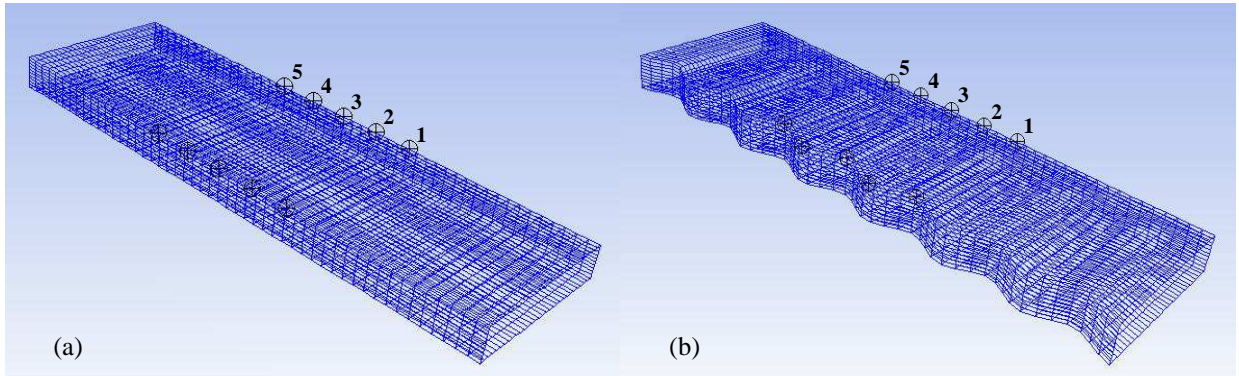


Figure B.1: Data points for the boundary layer and wake topology analysis; (a) $W0_E$; (b) $W3_E$.

B.1.1 Correlations at the Leading Edge of the Elongated Cylinder

Histories for u -velocity and pressure fluctuations are plotted against time for $W0_E$ and $W3_E$ at the leading edge points in Figures B.2 and B.5, respectively. The history plots in this section show one complete second of the data set, in order to clearly demonstrate the topology variation between each location. It should be noted however, that the analysis is still conducted with the full range of the simulated data of 4 s. The blue curve in the time histories represents the u -velocity data, while the green curve represents the pressure data.

The unbiased cross-correlation sequence, $R_{u,P,unbiased}$, between the streamwise u -velocity and pressure for both prisms at the leading edge points are presented in Figures B.3 and B.6. Similar to the time histories, the correlations are plotted for 1 s of leading and lagging time, $t_i + \tau_i$ and $t_i - \tau_i$, respectively. The positive time in the correlation plots representing lead, and the negative time representing lag. The initial cross-correlation at neither lead nor lag is at zero time delay.

The time histories for $W0_E$ are presented in Figure B.2 below. Each plot represents points 1 through to 5 of Figure B.1. It can be clearly seen that the flow exhibits a consistent structure of the velocity-pressure coupling along the span, as well as a constant half cycle phase difference and one clear distinct frequency dominating the fluctuation at each point. It can also be seen that beats exist within the periodic

structures. The maximum magnitudes of both u -velocity and pressure fluctuations are approximately between 0.25 to 0.5 ms^{-1} and 7 to 16 Pa , respectively.

The plots for unbiased cross-correlation between u -velocity and pressure at the leading edge points 1 to 5 for $W0_E$ present high correlation existing only at zero time delay. The velocity-pressure coupling does not acquire a consistently constant correlation magnitude. The expected observations however, indicate a singular correlated frequency between u -velocity and pressure of approximately f_{vo} .

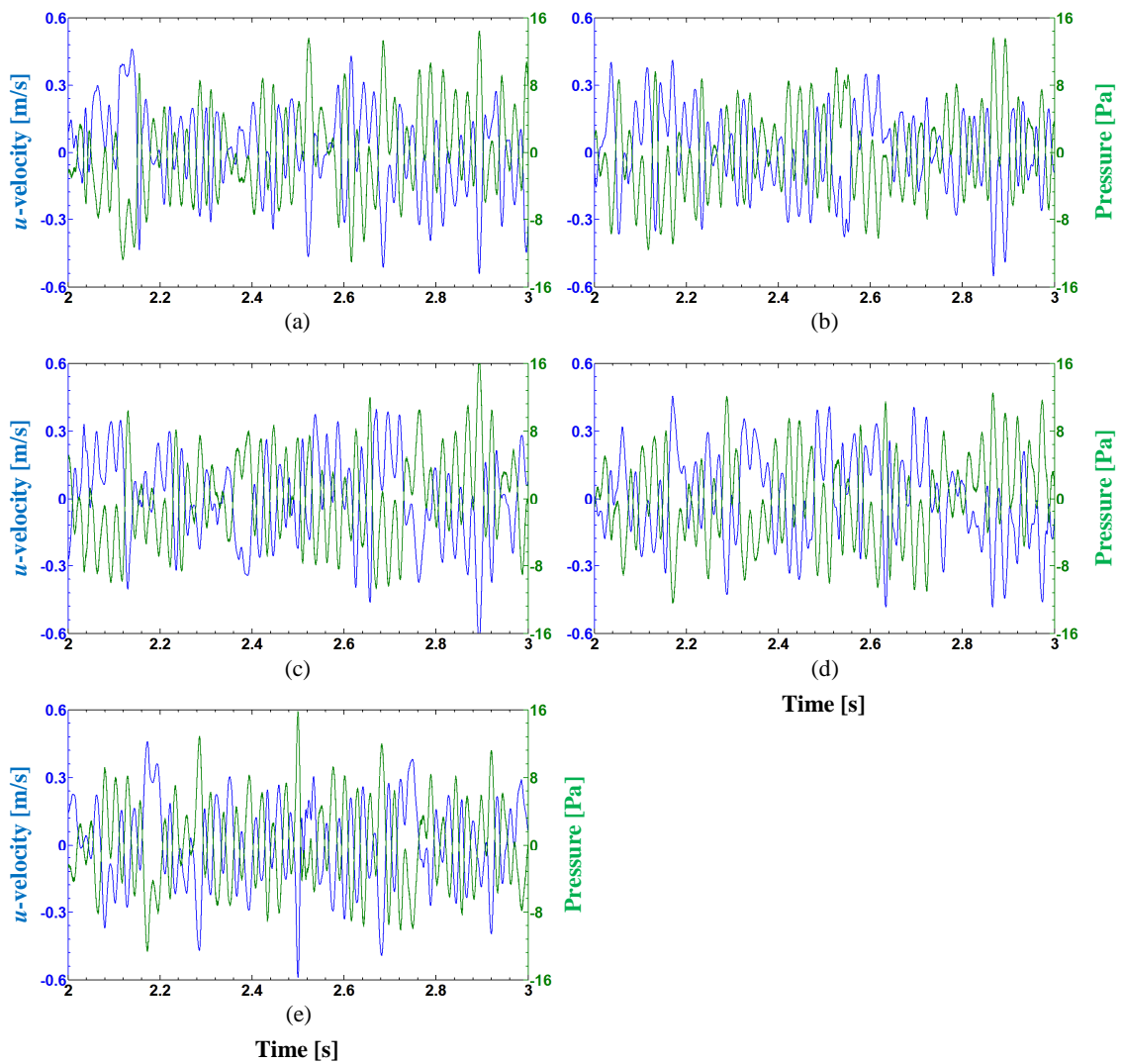


Figure B.2: Histories of u -velocity (—) and pressure (—) at the leading edge locations of $W0_E$; (a) point 1; (b) point 2; (c) point 3; (d) point 4; (e) point 5.

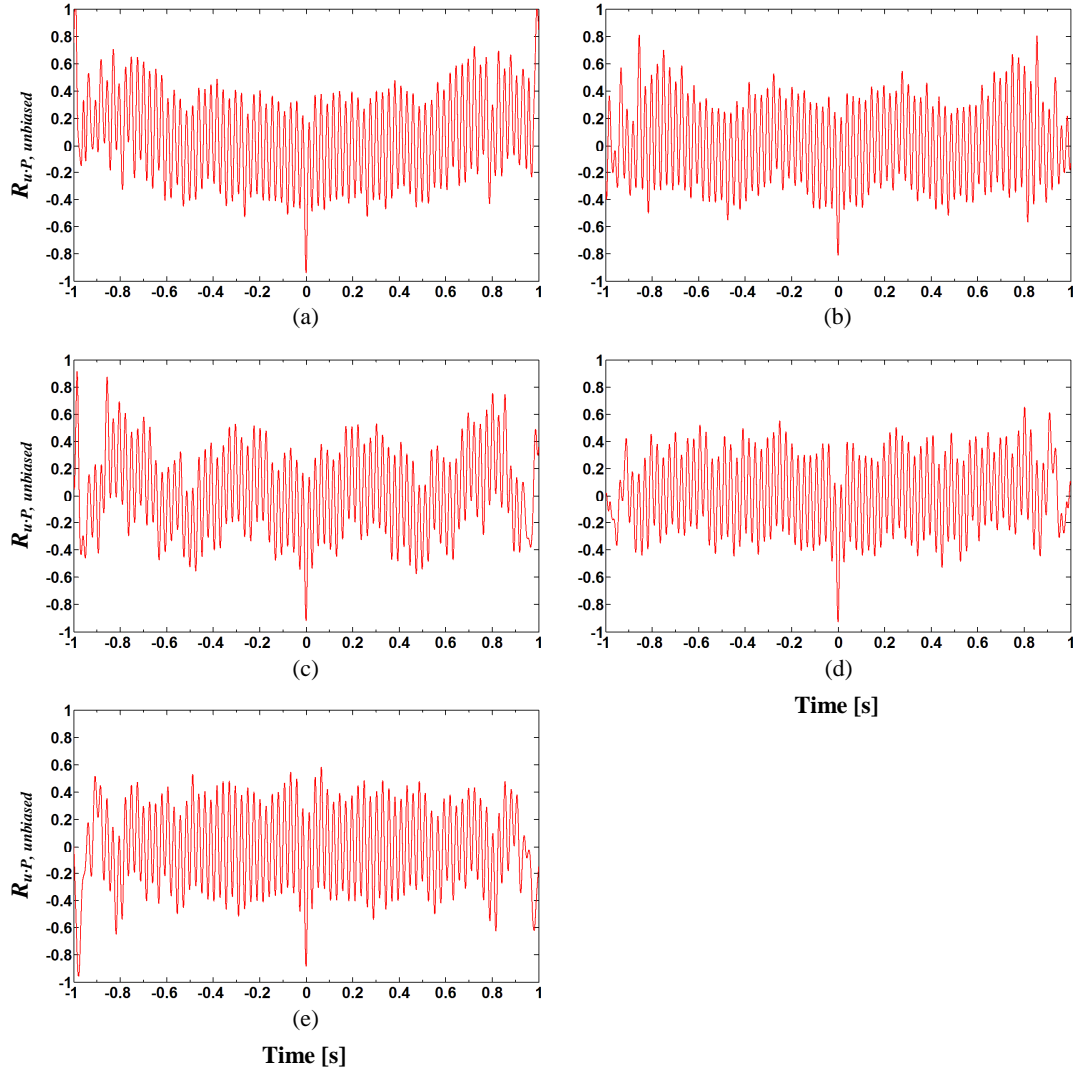


Figure B.3: Unbiased cross-correlation between u -velocity and pressure at the leading edge locations of $W0_E$; (a) point 1; (b) point 2; (c) point 3; (d) point 4; (e) point 5.

The power spectral densities (PSD) for u -velocity, pressure and unbiased cross-correlation function, reveal in Figure B.4, frequency content at approximately f_{v0} . Presence of additional spectral content within the frequency distributions also surrounds f_{v0} , with comparable spectral peaks occurring at $0.2f_{v0}$ for points 2 and 3 of $W0_E$. This is shown in Figures B.4(b) and B.4(c), respectively.

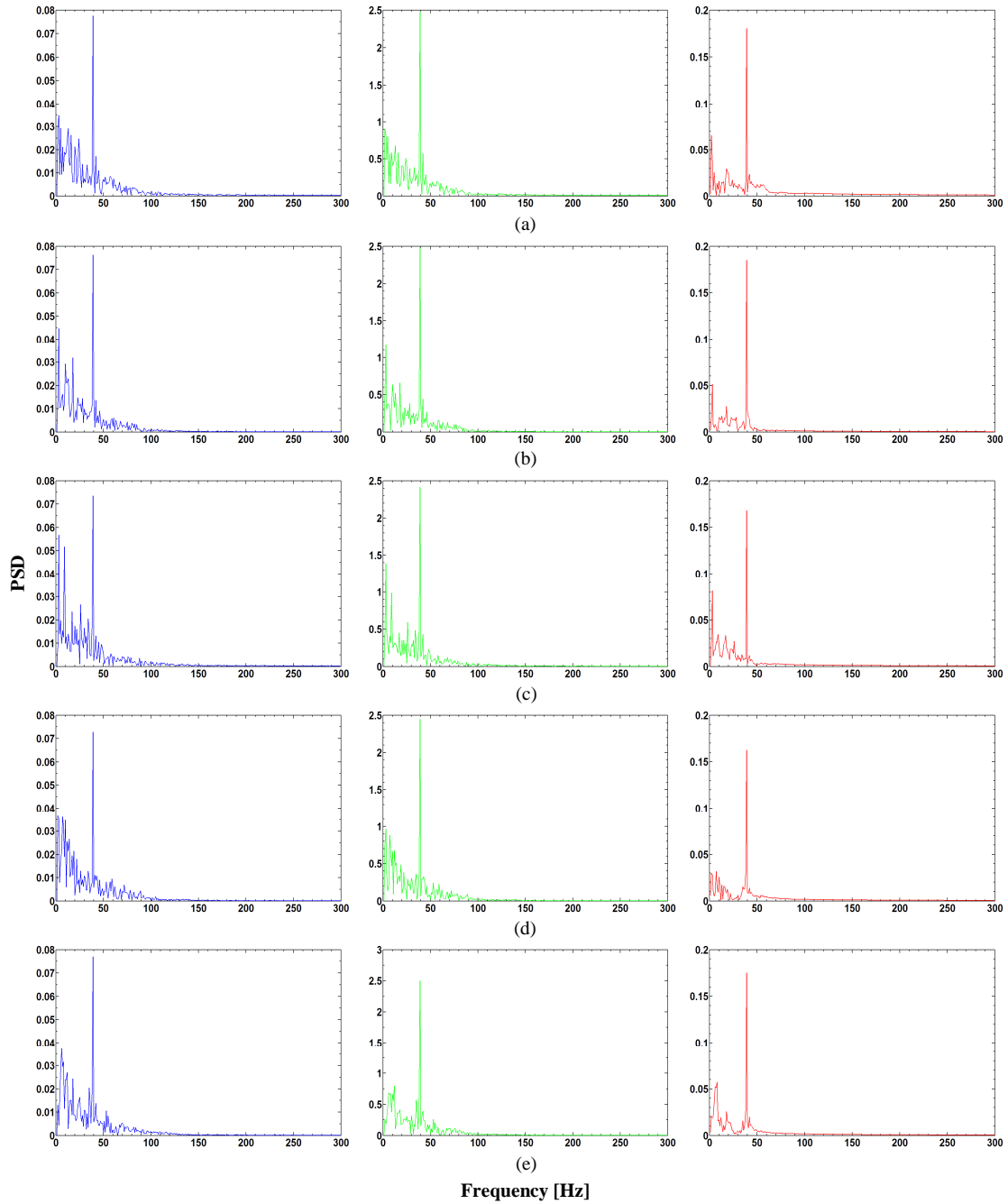


Figure B.4: PSD of u -velocity (—), pressure (—) and unbiased cross-correlation function (—) at the leading edge of $W0_E$; (a) point 1; (b) point 2; (c) point 3; (d) point 4; (e) point 5.

In Figure B.5, the time histories of u -velocity and pressure are presented at the leading edge points 1 to 5 for $W3_E$. Points 1, 3 and 5 correspond to monitor points at peak locations, while points 2 and 4 correspond to monitor points at valley locations. At all peak monitors in Figures B.5(a), B.5(c) and B.5(e), the velocity-pressure history

contains a periodic structure with a dominant low frequency and presence of higher frequency components. The maximum fluctuating magnitudes for both velocity and pressure are approximately between 0.2 to 0.6 ms^{-1} and 5 to 17 Pa, respectively. These magnitudes compare well with those for $W0_E$. Therefore, the reduction in fluctuations for u -velocity and pressure between $W0_E$ and $W3_E$ are only approximately 20 percent and 29 percent, respectively.

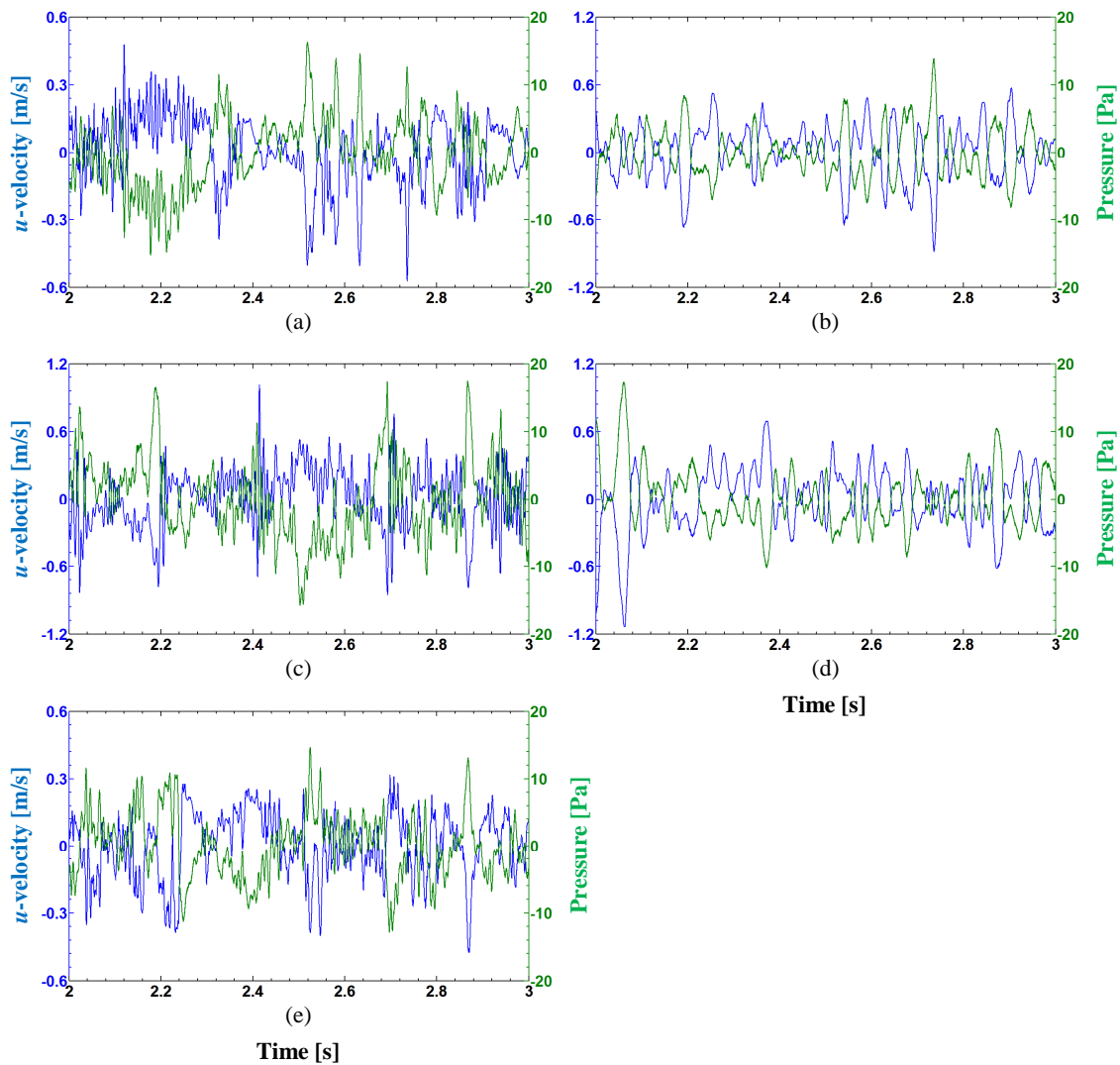


Figure B.5: Histories of u -velocity (—) and pressure (—) at the leading edge locations of $W3_E$; (a) point 1; (b) point 2; (c) point 3; (d) point 4; (e) point 5.

At both the valley monitors in Figures B.5(b) and B.5(d), the data contains a periodic structure with a predominantly low frequency distribution. The maximums of the fluctuations for the velocity-pressure coupling are approximately between 0.15 to 0.8 ms^{-1} and 2.5 to 14 Pa , respectively. Hence, reductions in fluctuations exist between $W0_E$ and $W3_E$ for u -velocity and pressure up to approximately 40 percent and 12 to 43 percent, respectively. The overall maximum magnitudes at both peak and valley locations are less than those for the plain elongated cylinder. This observation and also the presence of high frequency content demonstrate the mitigation of the coherent flow.

Observing the unbiased cross-correlation between u -velocity and pressure for $W3_E$, at peak locations 1, 3 and 5, strong correlation exists at zero time delay with much lower correlation occurring throughout the remaining correlation sequence. This is shown in Figures B.6(a), B.6(c) and B.6(e). In comparison to the correlations for $W0_E$, the magnitudes are much less, and the few distinct frequencies are apparent with a dominant lower frequency. In Figures B.6(b) and B.6(d), corresponding to valley monitor locations, the velocity-pressure coupling is highly correlated at zero time delay and less correlated in the remaining time delay sequence. Similar to the peak locations, the magnitude of correlation function at the valleys is much less than that for $W0_E$. The correlation between u -velocity and pressure primarily occurs at a low frequency with only minor frequency content present in the higher range.

Plots for the PSD at each leading edge location of $W3_E$ are presented in Figure B.7. Consecutive plots correspond to the monitor points 1 through to 5. In Figures B.7(a), B.7(c) and B.7(e), the PSD at peak locations contains a frequency distribution with spectral content between $0.2f_{vo}$ to $3f_{vo}$. The dominant structures and correlation occur at approximately $0.2f_{vo}$. Spectral peaks are also present between approximately $2f_{vo}$ and $2.5f_{vo}$. This occurrence is more apparent at point 3, in Figure B.7(c). It is associated with the vortices present within the separated boundary layers at peak planes, due to shear layer instability.

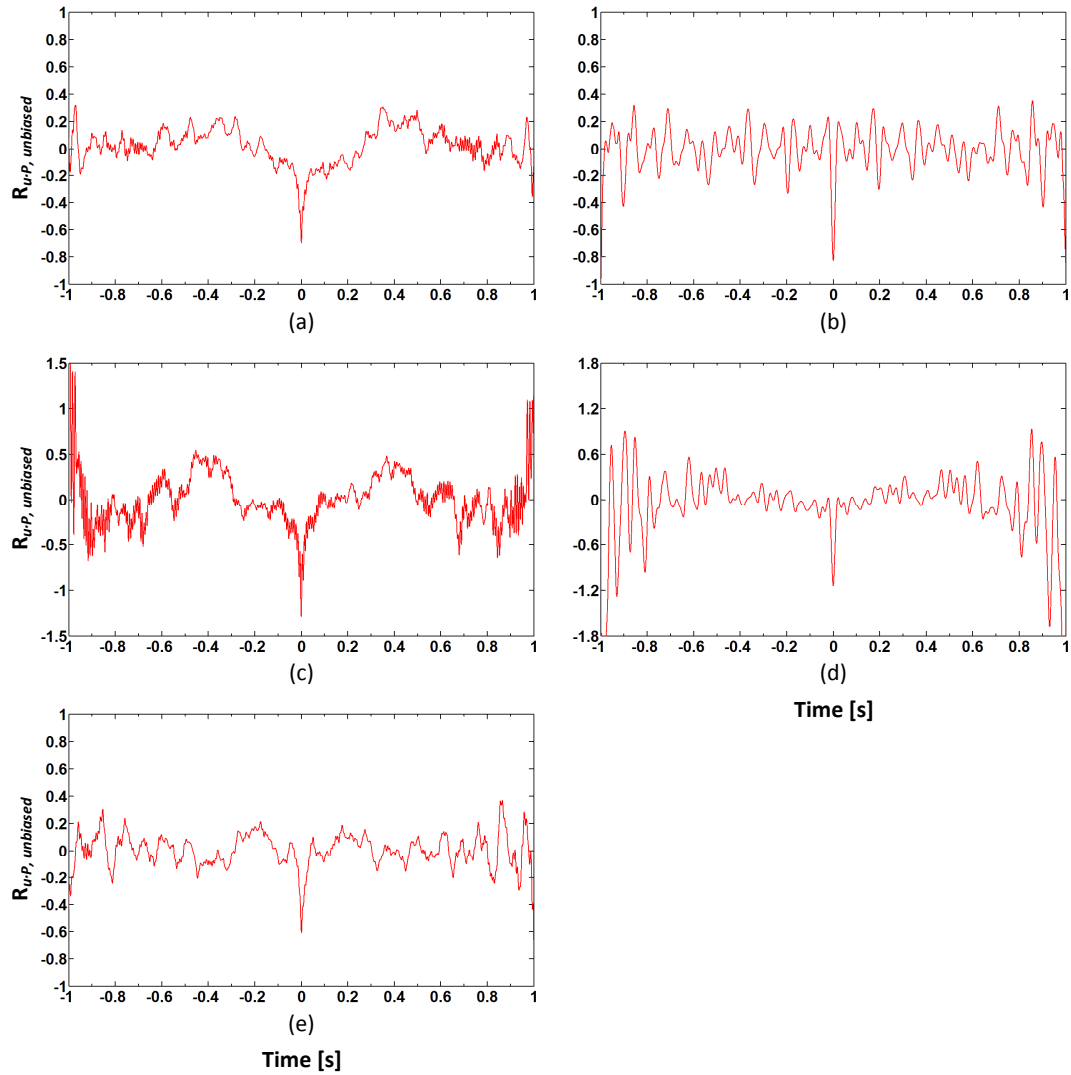


Figure B.6: Unbiased cross-correlation between u -velocity and pressure at the leading edge of $W3_E$; (a) point 1; (b) point 2; (c) point 3; (d) point 4; (e) point 5.

The PSD at valley locations displays a frequency distribution between $0.2f_{vo}$ and f_{vo} . This is shown in Figures B.7(b) and B.7(d). Unlike the peak locations, the dominant flow structures within the velocity and pressure data exist at approximately $0.4f_{vo}$ to $0.5f_{vo}$. Correlation between u -velocity and pressure occurs at approximately $0.4f_{vo}$.

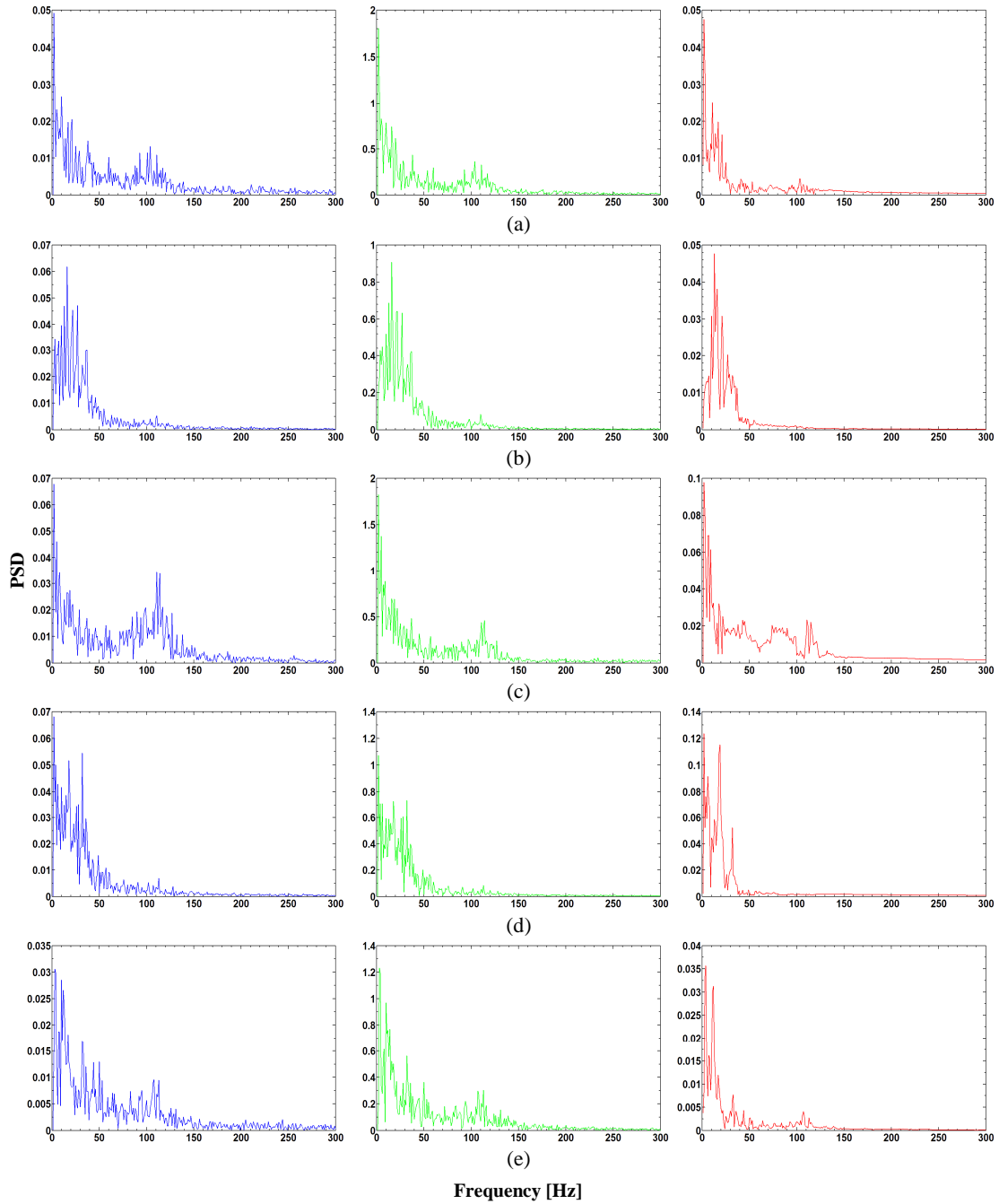


Figure B.7: PSD of u -velocity (—), pressure (—) and unbiased cross-correlation function (—) at the leading edge of $W3_E$; (a) point 1; (b) point 2; (c) point 3; (d) point 4; (e) point 5.

A summary of the observations presented herein for the leading edge of $W3_P$ is provided in Table B.1. It should be noted that the values of maximums for both u -velocity and pressure are taken as average values across the whole data range. Higher reductions are obtained at valley planes as a result of the attached boundary layer. The

presence of vortices within the shear layers at peak planes results in only minor reductions occurring between the plain square prism and controlled prism.

Table B.1: Summary of leading edge correlation observations for $W0_E$ and $W3_E$.

LE Point	$W0_E$			$W3_E$				
	u -velocity [ms ⁻¹]	Pressure [Pa]	Correlated Frequency [Hz]	u -velocity [ms ⁻¹]	Pressure [Pa]	Correlated Frequency [Hz]	Velocity reduction [%]	Pressure reduction [%]
1	0.25 – 0.5	7 - 16	f_{vo}	0.25 – 0.9	6 - 17	$0.2f_{vo}$	20 ± 4	29 ± 4
2	0.25 – 0.5	7 - 16	f_{vo}	0.3 – 0.8	4 - 14	$0.4f_{vo}$	40 ± 4	43 ± 4
3	0.25 – 0.5	7 - 16	f_{vo}	0.25 – 0.9	6 - 17	$0.2f_{vo}$	20 ± 4	29 ± 4
4	0.25 – 0.5	7 - 16	f_{vo}	0.3 – 0.8	4 - 14	$0.4f_{vo}$	40 ± 4	43 ± 4
5	0.25 – 0.5	7 - 16	f_{vo}	0.25 – 0.9	6 - 17	$0.2f_{vo}$	20 ± 4	29 ± 4

B.1.2 Correlations at the Trailing Edge of the Elongated Cylinder

Histories for u -velocity and pressure are plotted against time for $W0_E$ and $W3_E$ at the trailing edge points in Figures B.8 and B.11, respectively. The blue curve represents the velocity data, while the green curve represents the pressure data. The unbiased cross-correlation sequence, $R_{u,P,unbiased}$, between the streamwise u -velocity and pressure at the trailing edge for the uncontrolled square prism and the controlled square prism are presented in Figures B.9 and B.12, respectively.

The time histories of u -velocity and pressure for $W0_E$ along the trailing edge are presented in Figure B.8. Each plot displays identical features, indicating an undisturbed flow field around $W0_E$. The phase difference between the velocity and pressure appears to remain at mostly a half cycle, and the maximums of the fluctuations range from between approximately 4 to 8 ms⁻¹ and 20 to 50 Pa for u -velocity and pressure, respectively.

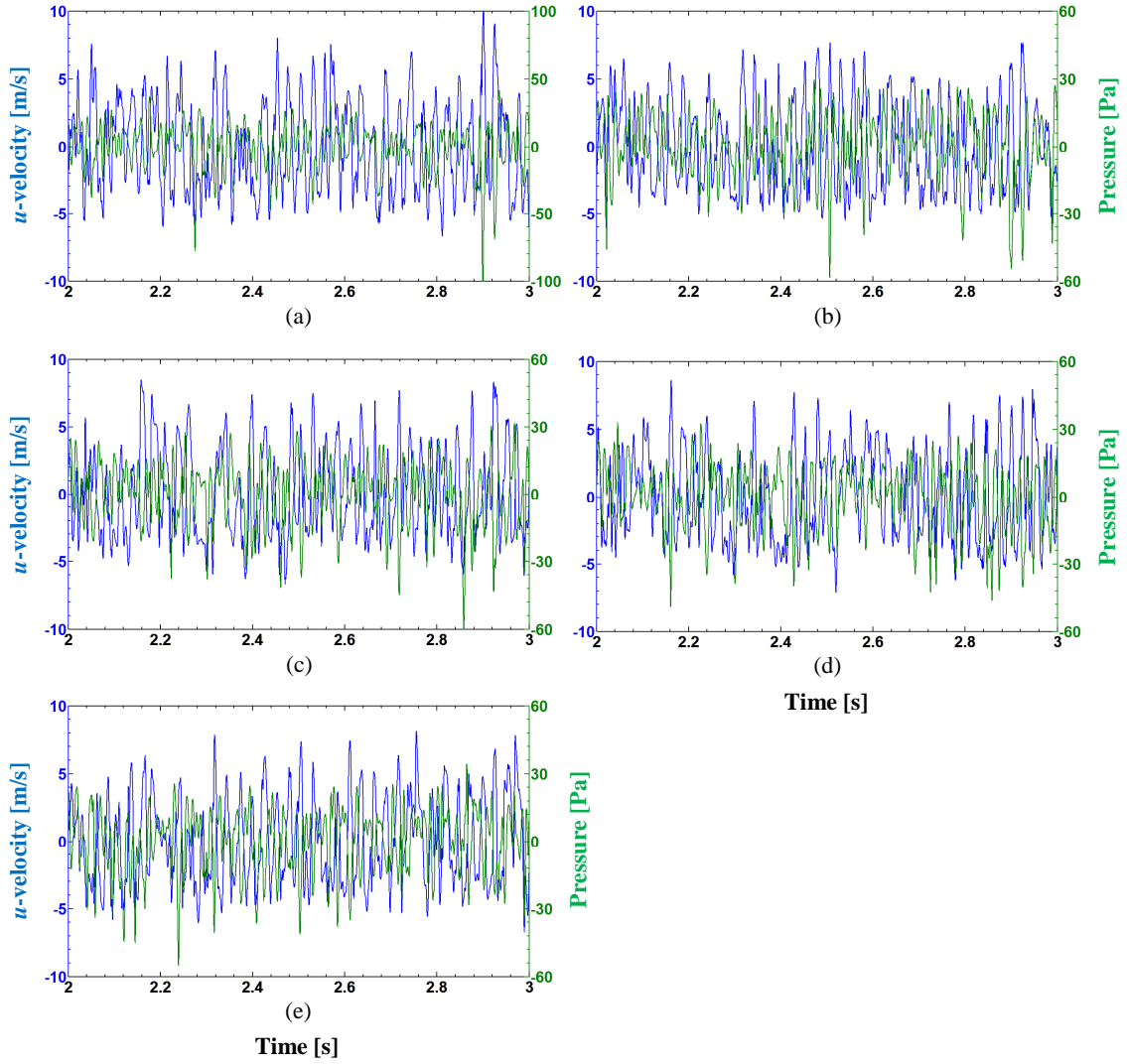


Figure B.8: Histories of u -velocity (—) and pressure (—) at the trailing edge locations of $W0_E$; (a) point 1; (b) point 2; (c) point 3; (d) point 4; (e) point 5.

The unbiased cross-correlation function at points 1 through to 5 at the trailing edge of $W0_E$ is presented in Figure B.9. The velocity-pressure coupling is highly correlated at a constant magnitude through the time delay sequence. Each point clearly contains a single correlated frequency between the velocity and pressure at approximately f_{vo} . In comparison to the leading edge observations for $W0_E$, the flow structure at the trailing edge is clearly developed and organised, as the interactions between u -velocity and pressure are well correlated.

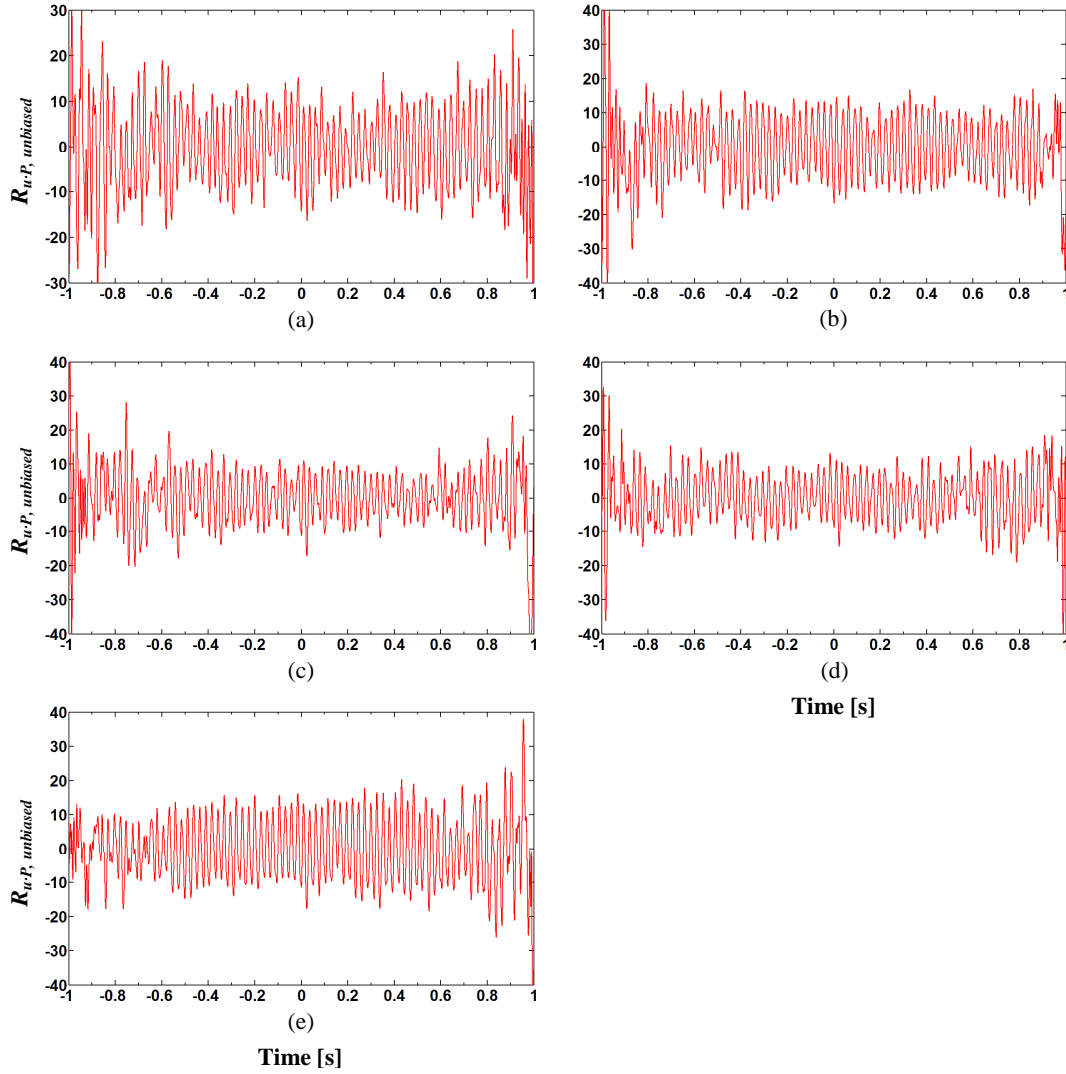


Figure B.9: Histories of u -velocity (—) and pressure (—) at the trailing edge locations of $W0_E$; (a) point 1; (b) point 2; (c) point 3; (d) point 4; (e) point 5.

The power spectral densities at the trailing edge for $W0_E$ are presented in Figure B.10, and show clear structures existing at approximately f_{vo} at each point 1 to 5. The plots for u -velocity show this behaviour existing quite dominantly. However, the PSD of pressure contains a frequency distribution with high spectral content adjacent to the peak at f_{vo} . This observation is present between approximately f_{vo} to $2f_{vo}$. The presence of additional, but smaller spectral content within the frequency distribution of the pressure data is a result of the boundary layer separation occurring just before the trailing edge. Hence, the shear layer instabilities cause the high fluctuations in the air pressure at this instance, and are reflected in the trailing edge analysis.

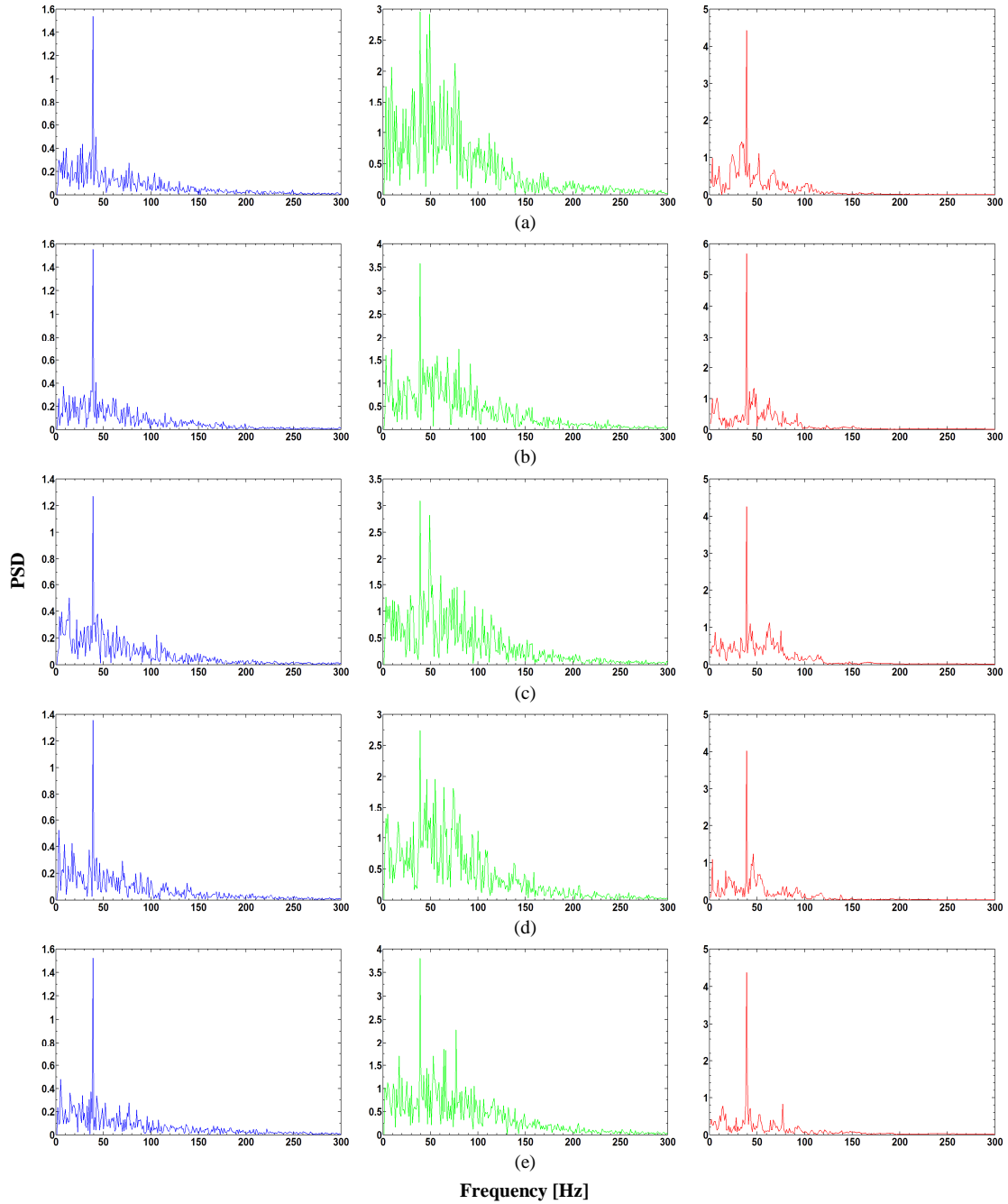


Figure B.10: PSD of u -velocity (—), pressure (—) and unbiased cross-correlation function (—) at the trailing edge of $W0_E$; (a) point 1; (b) point 2; (c) point 3; (d) point 4; (e) point 5.

The time histories of the u -velocity and pressure data at the trailing edge for $W3_E$ are presented in Figure B.11. Strong mitigation of the flow parameters is achieved at each point 1, 3 and 5, corresponding to peak monitor points. This can be seen in Figures B.11(a), B.11(c) and B.11(e), respectively. The range of maximum fluctuations for u -

velocity and pressure are approximately 1.5 to 6 ms^{-1} and 7 to 15 Pa , respectively. Therefore, reductions are approximately obtained between 25 to 63 percent and $65 - 70$ percent for u -velocity and pressure, respectively.

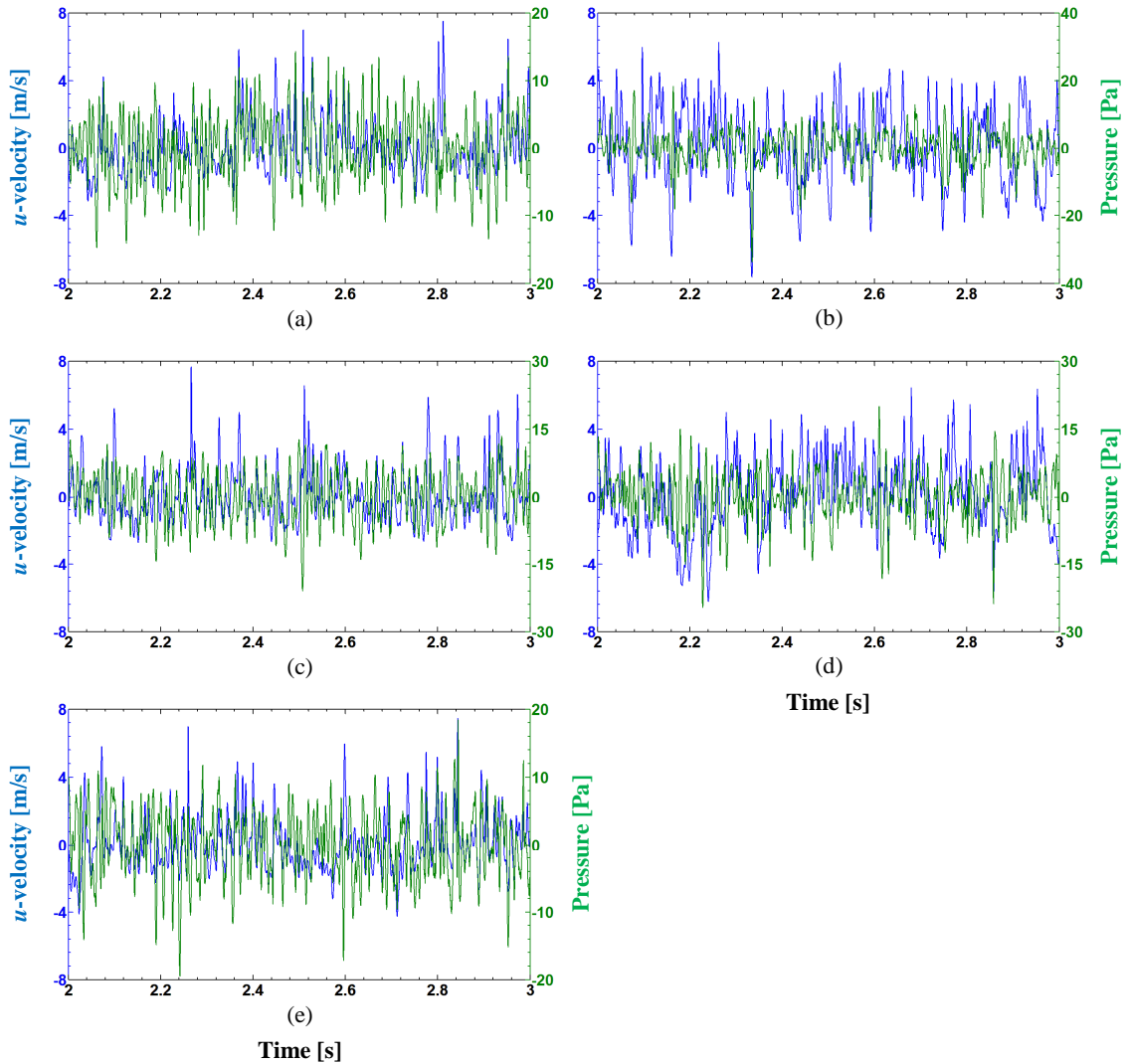


Figure B.11: Histories of u -velocity (—) and pressure (—) at the trailing edge locations of $W3_E$; (a) point 1; (b) point 2; (c) point 3; (d) point 4; (e) point 5.

At valley monitors, points 2 and 4, similar observations to a peak plane can be made in Figures B.11(b) and B.11(d), respectively. The frequency content and the range of magnitudes for both velocity and pressure are identical. However, the overall fluctuations for the velocity are higher than at a peak plane, as they occur predominantly

at a higher scale. This is unexpected, due to the attached boundary layer determined at valleys. Nevertheless, due to the placement of the trailing edge monitors at the valleys, the scale for velocity is larger. The maximum fluctuations for the velocity-pressure coupling at the valley locations of the trailing edge are approximately between 2 to 6 ms^{-1} and 5 to 20 Pa. Hence, the obtained reductions for u -velocity and pressure are approximately 25 to 50 percent and 60 to 75 percent, respectively.

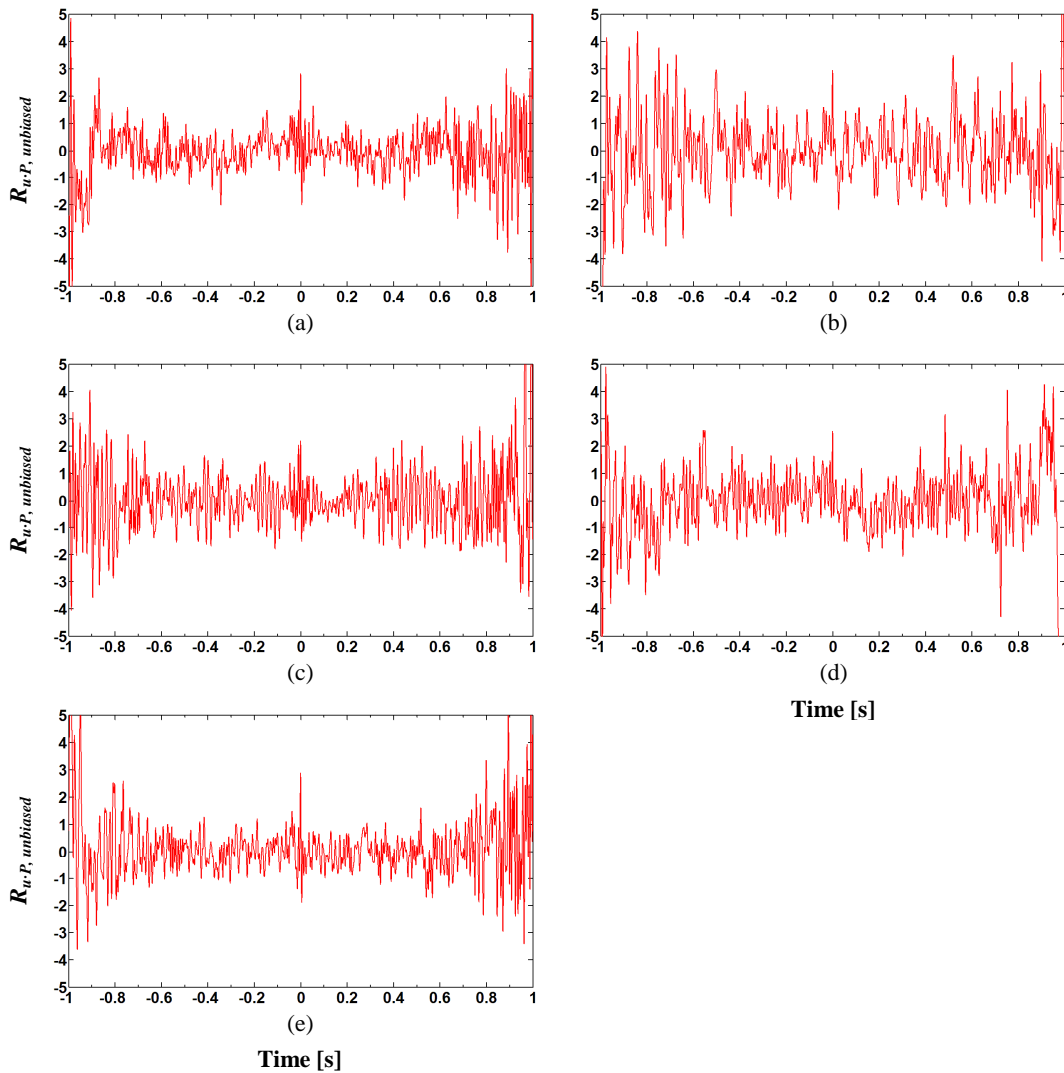


Figure B.12: Unbiased cross-correlation between u -velocity and pressure at the trailing edge locations of $W3_E$; (a) point 1; (b) point 2; (c) point 3; (d) point 4; (e) point 5.

For each trailing edge point 1 to 5, the unbiased cross-correlation sequences appear quite similar, unlike the observations made at the leading edge. The sequences are presented in Figure B.12. Correlation between u -velocity and pressure is somewhat higher at the trailing edge, and the dominant frequency of the periodic structure that is present between the interactions also contains additional higher frequencies. These observations are the same between peak and valley locations. Therefore, it is important to address the fluid structures present within the flow through a frequency analysis.

The PSD of the u -velocity, pressure and unbiased cross-correlation function are presented in Figure B.13. The frequency distributions of both peak and valley locations are identical. The u -velocity and pressure contain high spectral content between $0.2f_{vo}$ to $2.5f_{vo}$. However, at peak locations in Figures B.13(a), B.13(c) and B.13(e), the frequency distributions contain dominant structures at approximately $0.2f_{vo}$ and $0.5f_{vo}$, and also between $2f_{vo}$ and $2.5f_{vo}$. This observation is similar to that at the leading edge; however it is more prominent in this case. The observation is also only present for the velocity PSD. For pressure, the dominant structures exist at approximately f_{vo} and $2f_{vo}$ to $2.5f_{vo}$. The occurrence at higher frequencies is due to the presence of the shear layer instabilities. Correlation exists between the velocity-pressure coupling at f_{vo} and $2.5f_{vo}$ for peak monitors.

For the valley monitor points, Figures B.13(b) and B.13(d) contain frequency distributions with dominant spectral content at and around approximately $0.2f_{vo}$ for velocity. Spectral content exists at a frequency equivalent to $0.5f_{vo}$ and between f_{vo} to $2f_{vo}$ for pressure. The presence of high frequencies is evident of the interference within the flow, as a result of the passive control. In the case of point 4, the velocity and pressure are correlated at approximately $0.5f_{vo}$ and f_{vo} at point 2, and $0.5f_{vo}$ and $1.5f_{vo}$. This is shown in Figures B.13(b) and B.13(d), respectively.

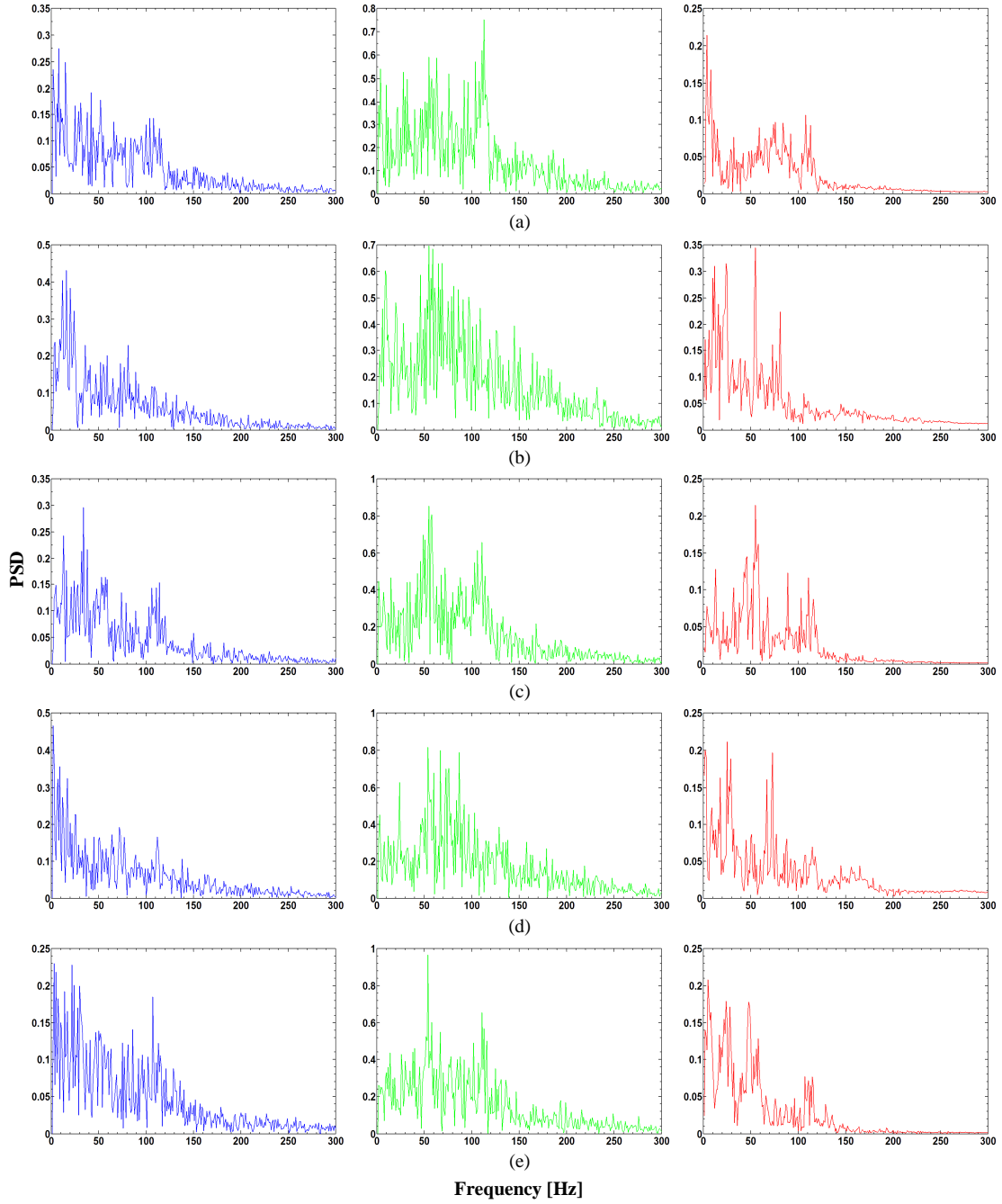


Figure B.13: PSD of u -velocity (—), pressure (—) and unbiased cross-correlation function (—) at the trailing edge locations of $W3_E$; (a) point 1; (b) point 2; (c) point 3; (d) point 4; (e) point 5.

A summary of the observations presented herein for the trailing edge of both $W0_E$ and $W3_E$ is provided in Table B.2. It should be noted that the values of maximums for both u -velocity and pressure are taken as average values across the whole data range. It

is observed that slightly fewer reductions are obtained at valleys. Nevertheless, the overall reductions obtained between peak and valley planes agree well, and for this reason it is clear to see the effectiveness of the spanwise sinusoidal profile (SSP) on an elongated cylinder. The frequency of the fluid structures is shifted to comparable lower frequencies due to the SSP. The turbulent properties are expected to be dominant at the trailing edge, especially for rectangular prisms such as $W0_E$ and $W3_E$, and interaction between the planes is also expected. The resulting reductions and close frequency content demonstrate this observation to be the case.

Table B.2: Summary of trailing edge correlation observations for $W0_E$ and $W3_E$.

LE Point	$W0_E$			$W3_E$				
	u -velocity [ms ⁻¹]	Pressure [Pa]	Correlated Frequency [Hz]	u -velocity [ms ⁻¹]	Pressure [Pa]	Correlated Frequency [Hz]	Velocity reduction [%]	Pressure reduction [%]
1	4 – 8	20 – 50	$\approx f_{vo}$	1.5 – 6	7 – 15	$0.2f_{vo}$	25 – 63	65 – 70
2	4 – 8	20 – 50	$\approx f_{vo}$	2 – 6	5 – 20	$0.4f_{vo}$	25 – 50	60 – 75
3	4 – 8	20 – 50	$\approx f_{vo}$	1.5 – 6	7 – 15	$0.2f_{vo}$	25 – 63	65 – 70
4	4 – 8	20 – 50	$\approx f_{vo}$	2 – 6	5 – 20	$0.4f_{vo}$	25 – 50	60 – 75
5	4 – 8	20 – 50	$\approx f_{vo}$	1.5 – 6	7 – 15	$0.2f_{vo}$	25 – 63	65 – 70

CORRELATION ANALYSIS OF THE BOUNDARY LAYER AROUND A PARTIAL SSP

C.1 Boundary Layer Topology Analysis of a Partial SSP

Investigation of the flow topology around the partial SSP geometries from Chapter 6 was conducted by analysing the near wall flow features at the leading and trailing edge of corresponding peaks and valleys. Histories of u -velocity and pressure are obtained, in order to perform the cross-correlation analysis, and for brevity, only seven spanwise points are discussed for $PSSP_1$ and $PSSP_2$, and only five spanwise points are discussed for $PSSP_3$. The purpose for selecting such points is to demonstrate the symmetry of flow structures within the boundary layer about the mid-span location. Emphasis is made on the similarities between each peak and valley of the partial SSP regions, and the consistent topology for the uncontrolled (plain) spanwise regions. Detail is also focussed on the structures that are present at the boundaries between the SSP and plain regions. The points discussed in this Appendix are indicated for each partial SSP configuration in Figure C.1.

The locations of the leading edge measuring points correspond to the first grid cell above and in front of the leading edge, while the locations of the trailing edge points correspond to the first grid cell directly above the trailing edge. This corresponds to measurement locations at a distance of 1×10^{-3} m from the cylinder wall. In order to discuss the work in a concise manner, the topology of flow structures that exist along the span of the partially controlled square cylinders are addressed firstly at the leading edge locations for $PSSP_1$, $PSSP_2$ and $PSSP_3$. The details at the trailing edge locations will then follow with a similar discussion.

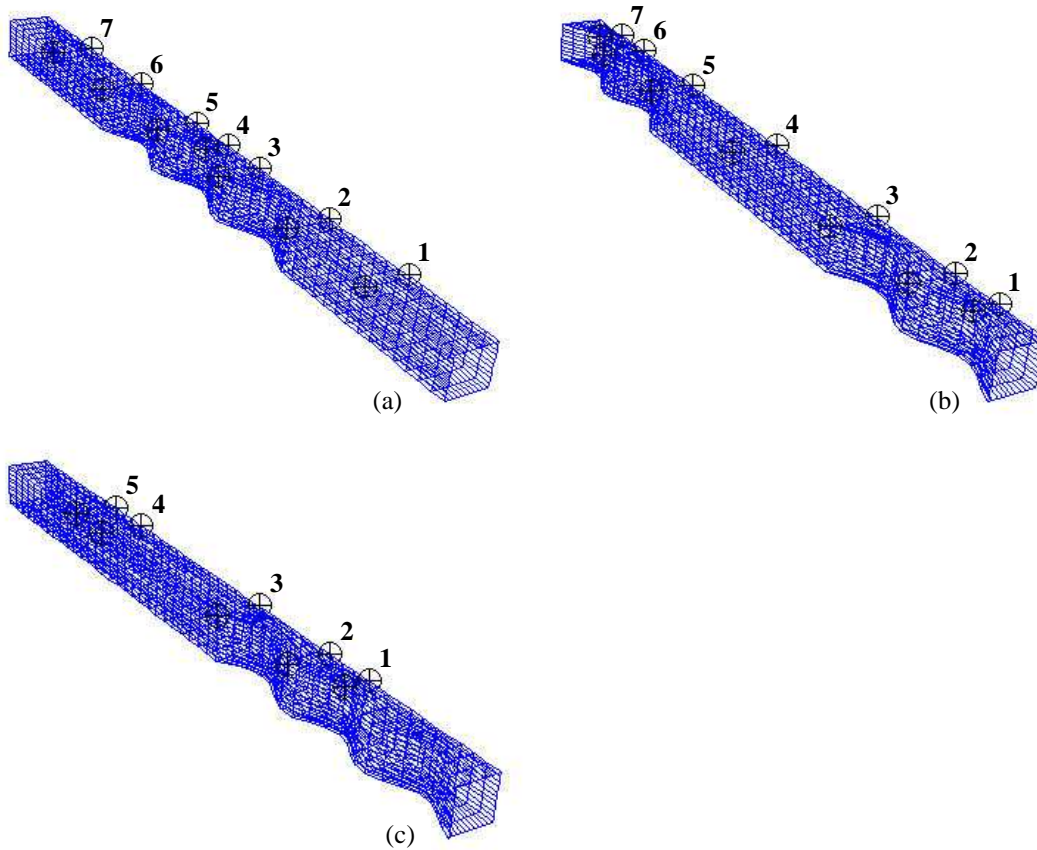


Figure C.1: Data points for the boundary layer and wake topology analysis; (a) $PSSP_1$; (b) $PSSP_2$; (c) $PSSP_3$.

C.1.1 Correlations at the Leading Edge of the Partial SSP Cylinder

Histories for u -velocity and pressure fluctuations are plotted against time for $PSSP_1$, $PSSP_2$ and $PSSP_3$ at the leading edge points in Figures C.2, C.5 and C.8, respectively. It should be noted herein that the history plots in this section show 1 s of the data set, in order to clearly demonstrate the topology variation between each location. However, the analysis is still conducted with the full range of the data. The blue curve represents the velocity data, and the green curve represents the pressure data.

The unbiased cross-correlation sequence, $R_{u-P,unbiased}$, between the streamwise u -velocity and pressure for all three partial control configurations at the leading edge points are presented in Figures C.3, C.6 and C.9. The correlations are plotted for 1 s of

the data with leading and lagging time, $t_i + \tau_i$ and $t_i - \tau_i$, respectively. Therefore, positive time representing lead and negative time representing lag, with zero representing the initial cross-correlation at neither lead nor lag.

The time histories for $PSSP_1$ are presented in Figure C.2. Each plot corresponds to each consecutive point along the span at the leading edge, as indicated in Figure C.1(a). At points 1 and 7 the velocity-pressure coupling has a constant half cycle phase difference. This behaviour is an expected characteristic of what has been observed for a plain square cylinder and can be seen in Figures C.2(a) and C.2(g). The maximum magnitudes for velocity and pressure are approximately between 1 to 1.7 ms^{-1} and 25 to 40 Pa, respectively.

The histories at the junction points 2 and 6 for $PSSP_1$ also contain a periodic structure. The presence of periodicity in Figures C.2(b) and C.2(f) is not as clear and organised as that of the uncontrolled span of the square cylinder, and therefore indicates interference of the coherent structure exists at these locations. From close observation of the time histories at the boundaries, the presence of both uncontrolled and controlled frequency content that has typically been observed in the previous appendices is observed again here. It demonstrates that the direct effectiveness of the passive control to interrupt the coherent flow structure at the intersection of the partial SSP and plain regions.

In Figures C.2(c) and C.2(e), the characteristics that are typical at a valley plane can be observed. The magnitudes of both u -velocity and pressure between each leading edge observation point within the controlled span in Figure C.2 are somewhat similar. The maximum magnitude for u -velocity remains between approximately 0.75 and 1.5 ms^{-1} for both peak and valley locations. The maximum magnitude for pressure remain between approximately 15 and 25 Pa. Overall magnitudes between each monitor location demonstrate slight decrease at valley and peak locations, as compared to the uncontrolled regions. This slight variation begins at the boundary locations. Decreases in velocity and pressure fluctuations are obtained between approximately 11 to 25 percent and 37 to 40 percent, respectively.

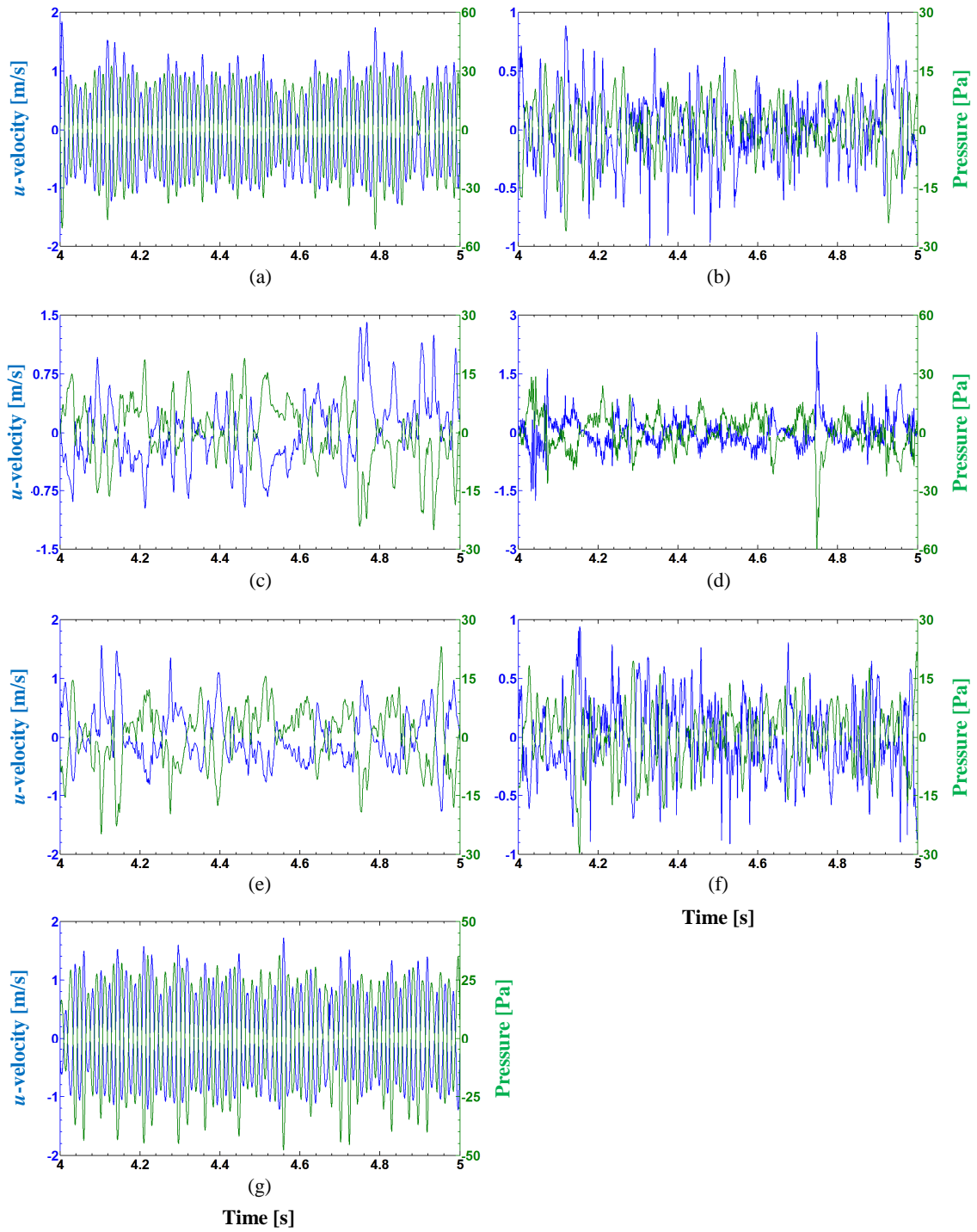


Figure C.2: Histories of u -velocity (—) and pressure (—) at the leading edge locations of $PSSP_1$; (a) point 1; (b) point 2; (c) point 3; (d) point 4; (e) point 5; (f) point 6; (g) point 7.

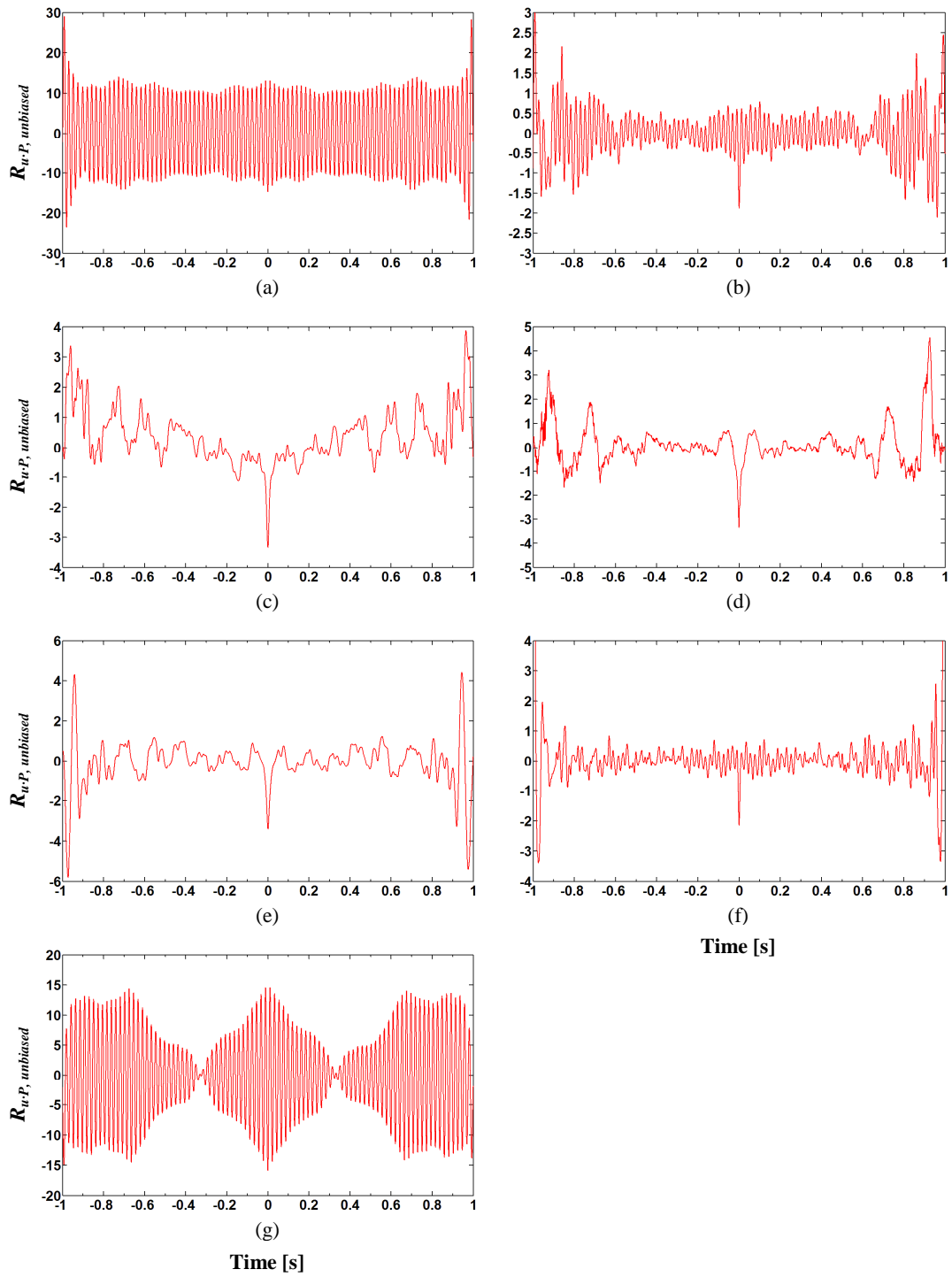


Figure C.3: Unbiased cross-correlation between u -velocity and pressure at the leading edge of $PSSP_1$; (a) point 1; (b) point 2; (c) point 3; (d) point 4; (e) point 5; (f) point 6; (g) point 7.

The unbiased cross-correlation function between u -velocity and pressure is presented for the leading edge points of $PSSP_1$ in Figure C.3. A consistently high correlation exists between the velocity and pressure along the plain span of $PSSP_1$ at point 1. This is indicated throughout the time delay sequence in Figure C.3(a). A clear periodic relationship is observed between the velocity-pressure interactions at a single frequency. Similar observations are shown in Figure C.3(g) at point 7. However, negligible correlation occurs at approximately 0.3 s lead and lag, causing a beat phenomenon to appear within the correlation sequence. The reason for this is not completely understood. Nevertheless, inspection of the time history plot of Figure C.2(g) indicates large magnitudes occurring for the minima of the pressure history. Therefore, this asymmetry about the zero mean data may account for this anomaly.

A clear frequency can be observed in Figures C.3(b) and C.3(f) corresponding to the boundary locations. However, the magnitude of correlation between the data sets at these locations is significantly less than that of the uncontrolled span, and although the frequency content appears similar to Figures C.3(a) and C.3(g), the periodicity is not clear. This corroborates the effectiveness of the configuration for the passive control application, as the correlation between u -velocity and pressure contains interference directly at the border of the partial SSP. At peak and valley locations for $PSSP_1$, high correlation only occurs at zero time delay. This is indicated in Figures C.3(c), C.3(d) and C.3(e). The magnitude of correlation at zero time delay for the uncontrolled span is orders of magnitude larger than the zero time delay for the controlled span. A non-periodic correlation exists at the controlled span with the suggestion of two or three clearly distinct frequencies. These observations are not as evident within the time histories.

Power spectral density (PSD) calculations are performed, in order to determine exactly, the specific fluid structures that are present within the flow for the plain (uncontrolled) span of the partial SSP configurations, and whether or not these same structures are also present for the controlled span. The PSD of u -velocity, pressure and unbiased cross-correlation function at the leading edge locations are given in Figures C.4, C.7 and C.10, respectively. The horizontal axis of these plots has a frequency range up to approximately $6f_{vo}$. For the plain span of $PSSP_1$, a spectral peak occurs at approximately f_{vo} in Figures C.4(a) and C.4(g), for both u -velocity and pressure. The

magnitude of the spectral peak is representative of the corresponding magnitudes for the velocity and pressure histories.

In Figures C.4(b) and C.4(f), a dominant spectral peak is also present at a frequency of approximately f_{vo} for the boundary points. The dominant correlated flow structures at the junctions of the partial control are associated with the plain span. However, the magnitude of the spectral peak at f_{vo} is significantly smaller than that for the plain span, and the occurrence of the surrounding spectra within the PSD of the cross-correlation function indicates disturbance to the coherent flow. The appearance of comparable spectra between $0.2f_{vo}$ and f_{vo} in Figure C.4(f) is evidence that the boundaries of the partial SSP cylinder contain flow characteristics from both the uncontrolled and controlled frequency distributions.

At the leading edge points corresponding to valleys for $PSSP_1$, the dominant frequency content occurs at approximately $0.2f_{vo}$. This is shown in Figures C.4(c) and C.4(e). The frequency distribution also contains spectral content at frequencies between $0.2f_{vo}$ and f_{vo} . However, there is an absence of any identifiable spectral peaks. At the peaks correlation occurs at $0.2f_{vo}$. The shift in frequency content from f_{vo} at the uncontrolled span to $0.2f_{vo}$ at the controlled span demonstrates the effectiveness of embodying a partial SSP. As for the spanwise symmetry that occurs, it suggests that the flow characteristics for both uncontrolled and controlled spans exist independently and only interact at the boundaries. The correlation analysis at the leading edge for the remaining two partial control configurations, $PSSP_2$ and $PSSP_3$ are discussed below to confirm this observation.

The time histories for streamwise u -velocity and pressure at the leading edge of $PSSP_2$ are presented in Figure C.5. In Figure C.5(d), corresponding to point 4, the velocity-pressure coupling has a constant half cycle phase difference. The maximum magnitudes for u -velocity and pressure are approximately between 1.5 to 2.5 ms^{-1} and 40 to 70 Pa , respectively. At the valley locations of points 2 and 6 for $PSSP_2$, two to three distinct frequencies can be observed in the time histories of Figures C.5(b) and C.5(f). The maximum magnitudes at the peaks and valleys are approximately between 0.75 to 1.5 ms^{-1} and 15 to 20 Pa for velocity and pressure, respectively. Therefore, reductions in velocity and pressure fluctuations are obtained between 40 to 50 percent and 63 to 71 percent, respectively.

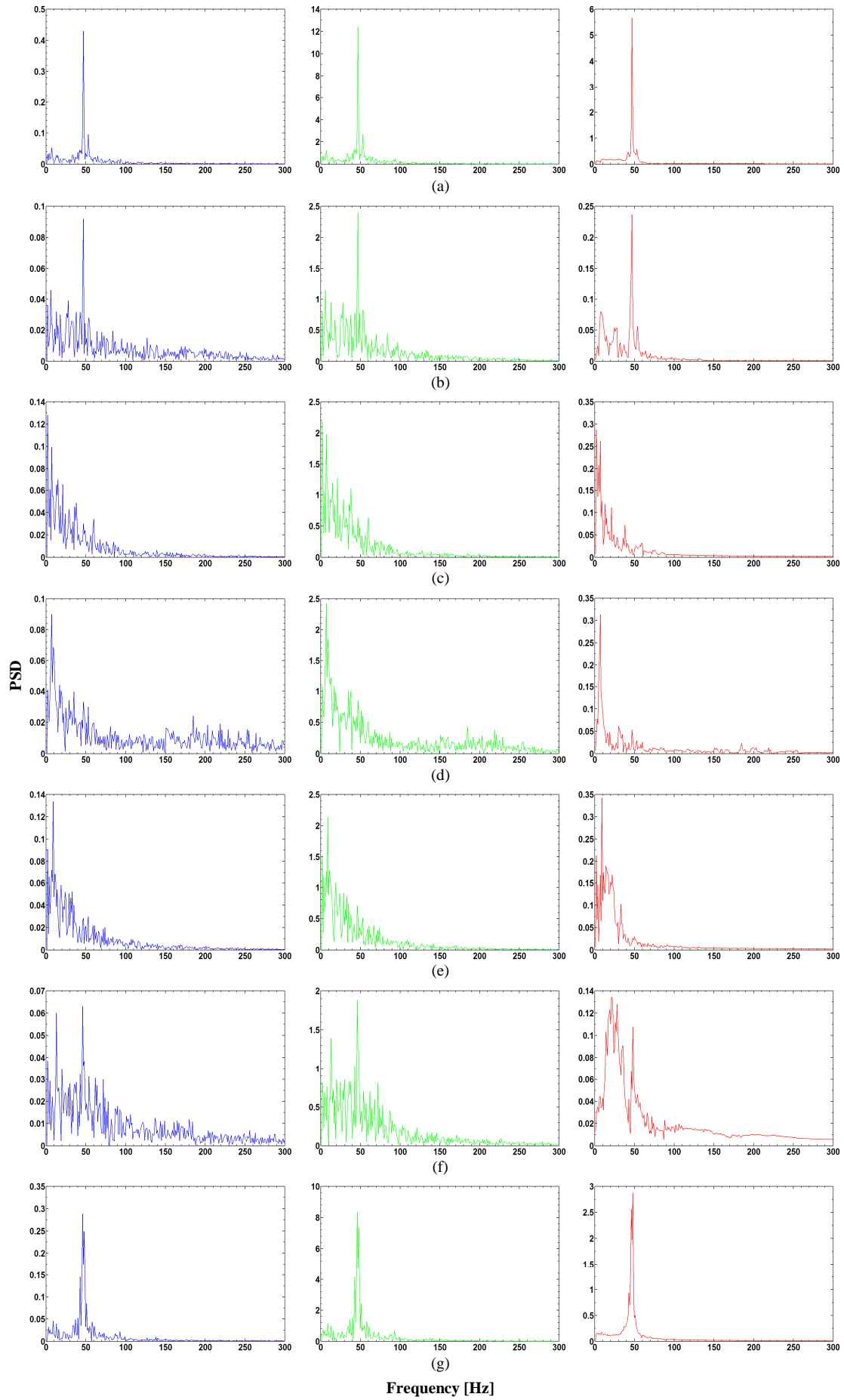


Figure C.4: PSD of u -velocity (—), pressure (—) and unbiased cross-correlation function (—) at the leading edge of $PSSP_1$; (a) point 1; (b) point 2; (c) point 3; (d) point 4; (e) point 5; (f) point 6; (g) point 7.

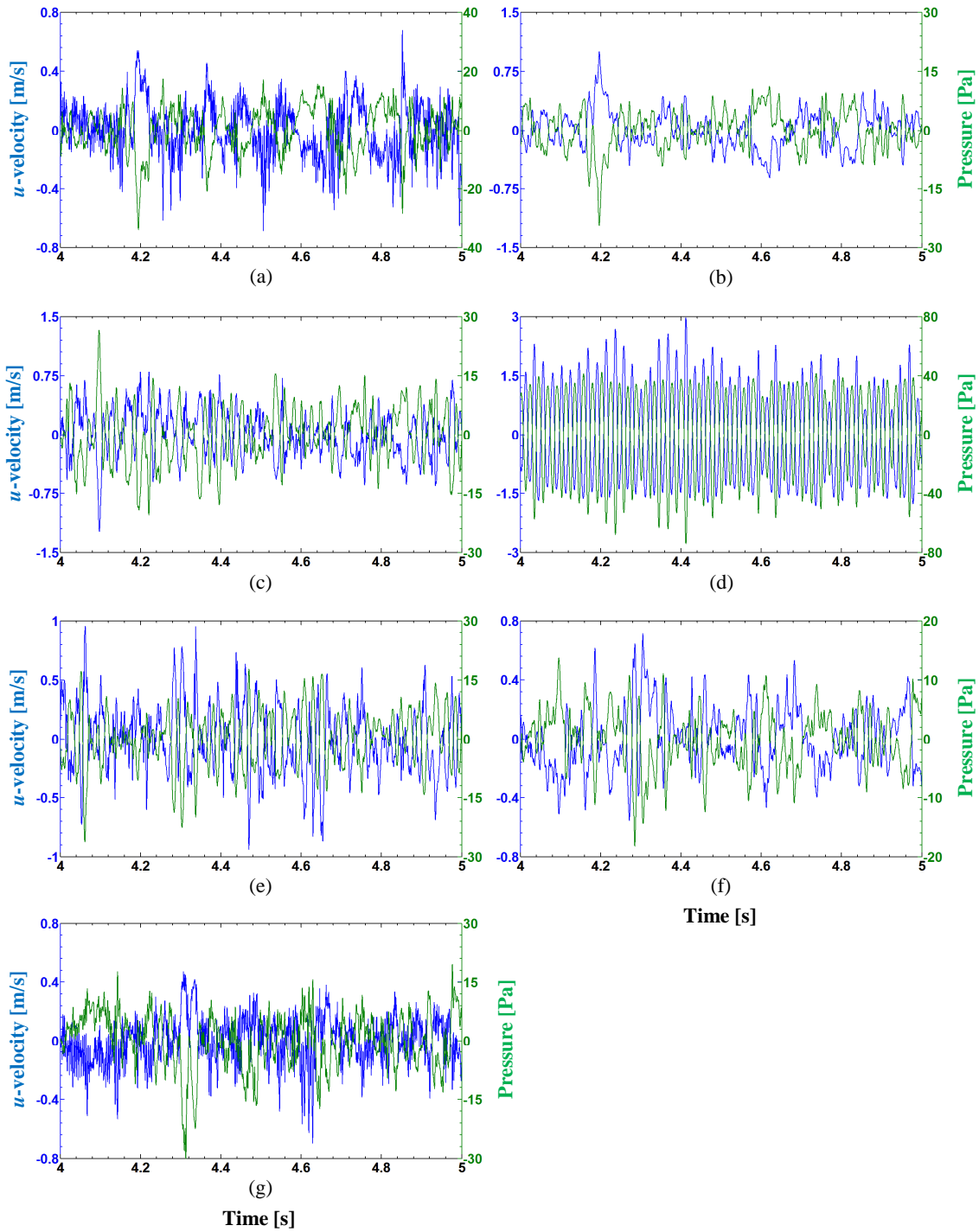


Figure C.5: Histories of u -velocity (—) and pressure (—) at the leading edge locations of $PSSP_2$; (a) point 1; (b) point 2; (c) point 3; (d) point 4; (e) point 5; (f) point 6; (g) point 7.

At the boundaries, points 3 and 5, of $PSSP_2$, the maximum magnitudes for the velocity-pressure coupling are approximately 0.5 to 0.75 ms^{-1} and 10 to 20 Pa , respectively. This detail is noted for Figures C.5(c) and C.5(e). It is very interesting at this stage to observe a complete mitigation of the coherent flow through the application of a partial SSP, regardless to the position of the passive control along the span. It appears that overall flow control is slightly greater for $PSSP_2$ than for $PSSP_1$. Nevertheless, both configurations show starkly similar behaviour, and flow structures that co-exist independently across the span.

A high correlation exists between u -velocity and pressure for $PSSP_2$ along the uncontrolled span. This is shown in Figure C.6(d) for the leading edge monitor point 4, as the magnitude remains relatively constant throughout the cross-correlation sequence. The velocity and pressure are clearly correlated at a single frequency. Equally high correlations exist at zero time delay between the velocity-pressure coupling at both peaks and valleys, with negligible correlation throughout the remaining cross-correlation sequence. The details are shown in Figures C.6(a) and C.6(g), and C.6(b) and C.6(f). This is important not only due to magnitude; however due to similar structures appearing between each point 1, 2, 6 and 7. At the boundaries, points 3 and 5, in Figures C.6(c) and C.6(e), the periodic structure is clear with the presence of one distinct frequency similar to that of the plain span of $PSSP_2$.

In Figure C.7(d), a distinctly clear correlation is present at f_{vo} at point 4 within the uncontrolled span. At the boundaries, points 3 and 5, there is presence of a spectral peak at f_{vo} . This is presented in Figures C.7(c) and C.7(e). Correlation also exists for frequencies between $0.2f_{vo}$ and f_{vo} at the boundaries of the partial SSP and plain spans. In Figures C.7(a) and C.7(g), correlation of the dominant flow structures occur at approximately $0.2f_{vo}$, with a secondary peak occurring at f_{vo} for the peak monitor points 1 and 7 of $PSSP_2$. Smaller spectral content is also present throughout the frequency range, and for both u -velocity and pressure, slightly larger content is present at approximately $4f_{vo}$. At the valley locations 2 and 6, the dominant correlation occurs at approximately $0.2f_{vo}$, with much smaller spectral content existing at f_{vo} . The detail that cannot be observed within the cross-correlation sequence plots of Figure C.6 is the absence of spectral content beyond $2f_{vo}$ at valley planes. There is no harmonic of f_{vo} occurring at $4f_{vo}$ for the valley locations, as is observed for the peak locations.

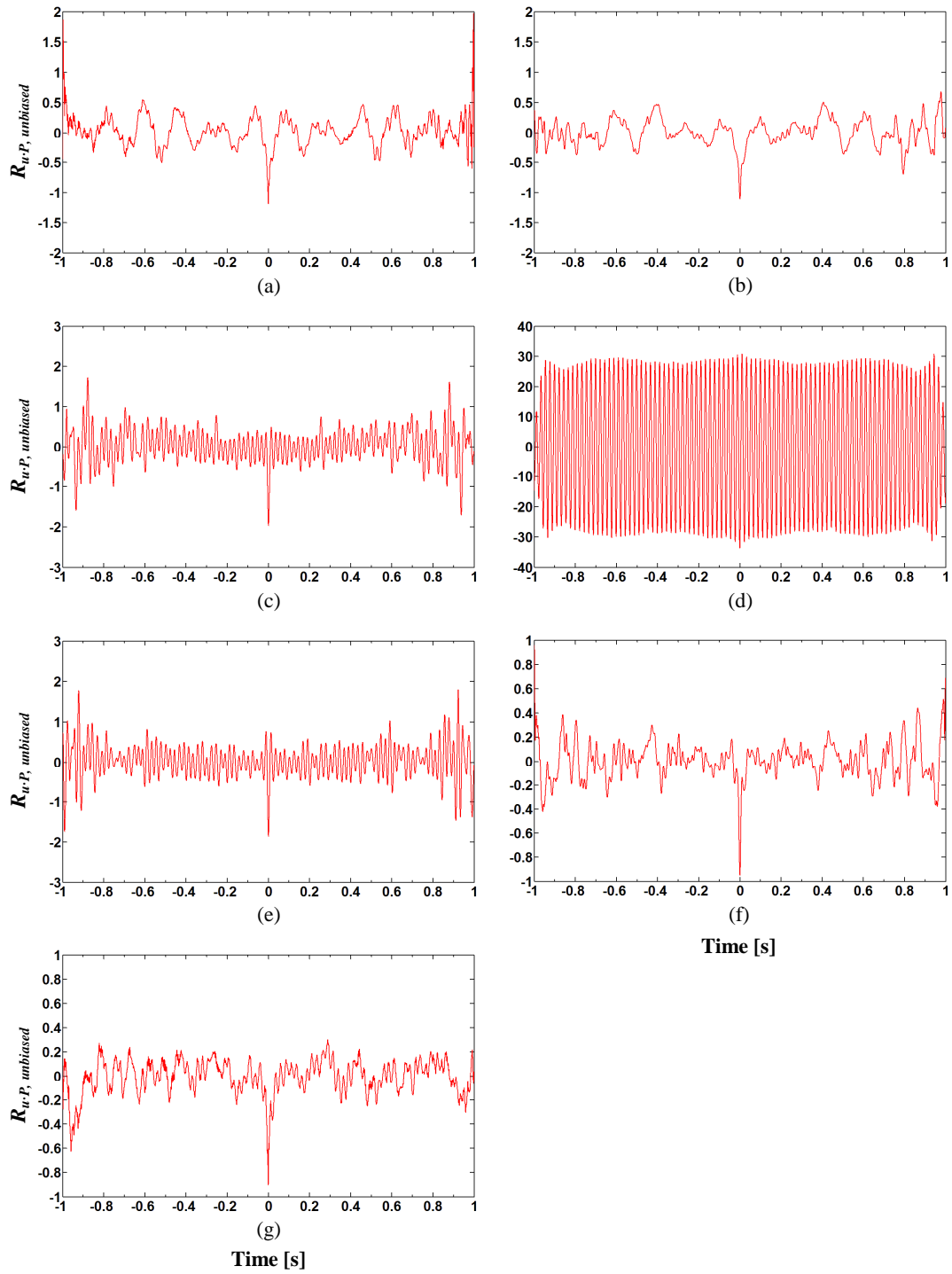


Figure C.6: Unbiased cross-correlation between u -velocity and pressure at the leading edge of $PSSP_2$; (a) point 1; (b) point 2; (c) point 3; (d) point 4; (e) point 5; (f) point 6; (g) point 7.

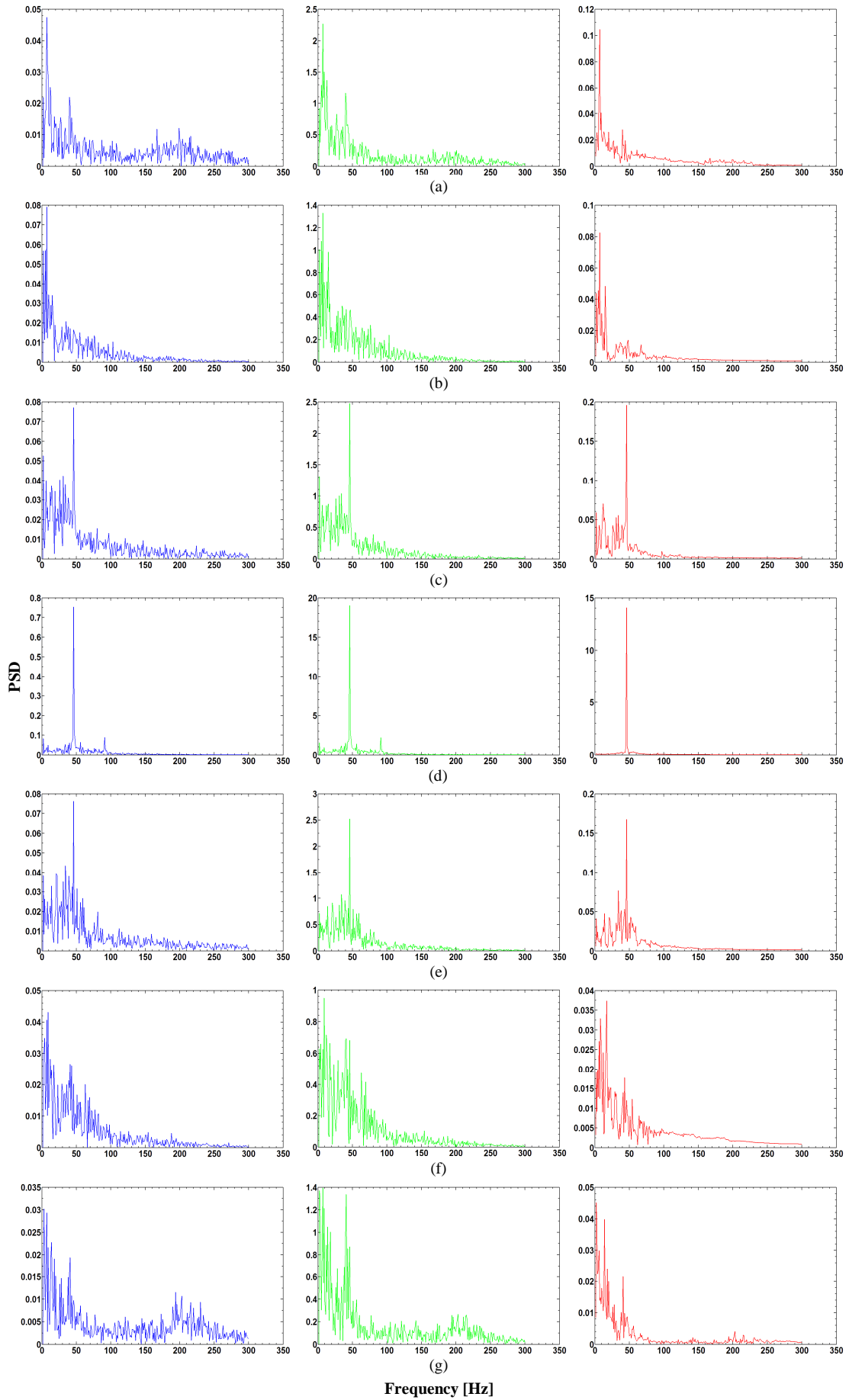


Figure C.7: PSD of u -velocity (—), pressure (—) and unbiased cross-correlation function (—) at the leading edge of $PSSP_2$; (a) point 1; (b) point 2; (c) point 3; (d) point 4; (e) point 5; (f) point 6; (g) point 7.

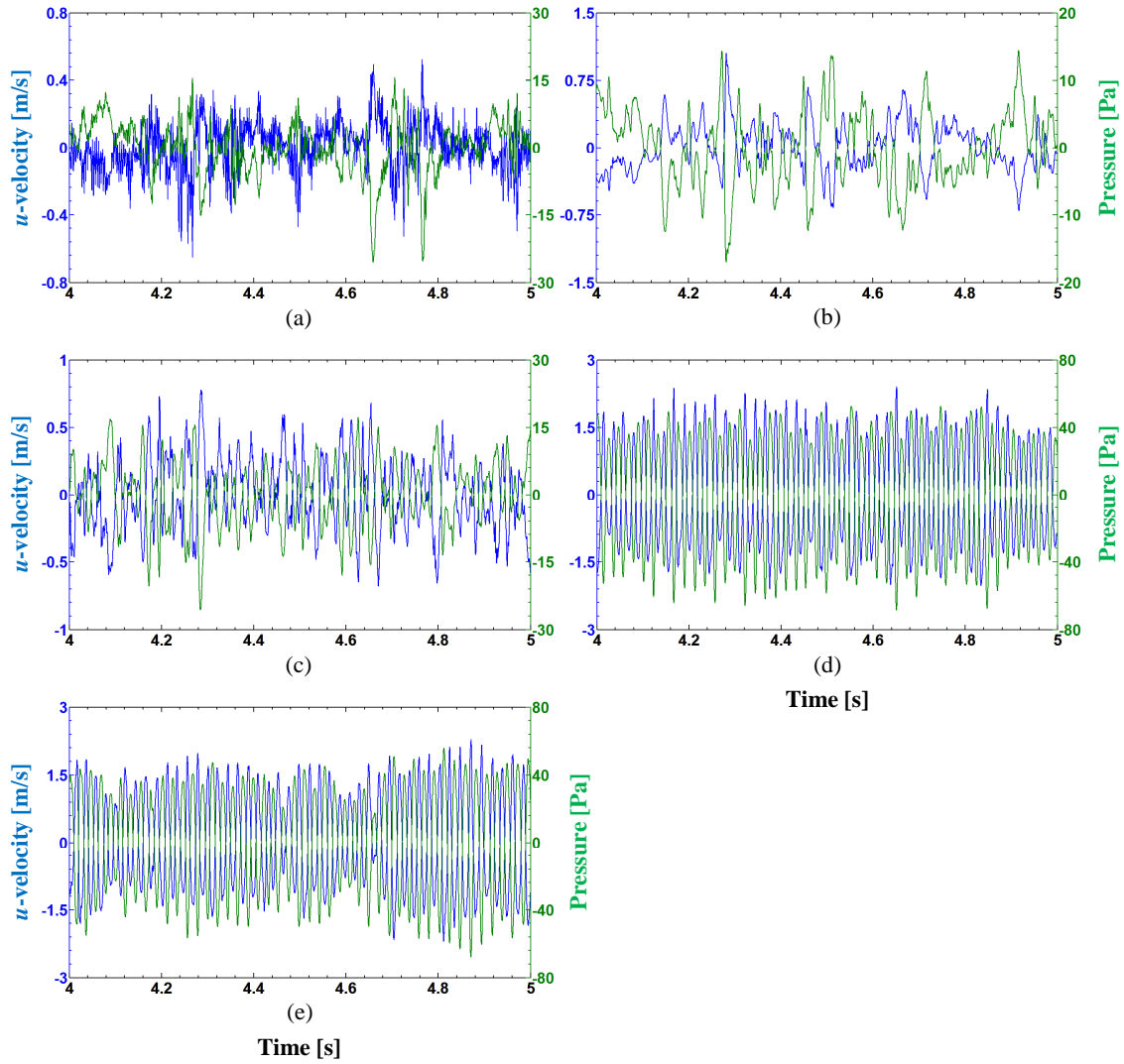


Figure C.8: Histories of u -velocity (—) and pressure (—) at the leading edge locations of $PSSP_3$; (a) point 1; (b) point 2; (c) point 3; (d) point 4; (e) point 5.

The time histories for u -velocity and pressure at the leading edge of $PSSP_3$ are presented in Figure C.8. It is to be noted that this configuration only contains five monitor points, as shown in Figure C.1. Hence, there are two monitors within both the plain (uncontrolled) and SSP (controlled) regions, and one monitor at the intersection of the half spans. At points 4 and 5 shown in Figures C.8(d) and C.8(e) the maximums for u -velocity and pressure are between 1.5 to 2 ms^{-1} and 40 to 60 Pa, respectively. For the monitor point 1, corresponding to a peak, the maximum magnitudes for the velocity-pressure coupling at this location are approximately between 0.3 to 0.6 ms^{-1} and 10 to 20 Pa, respectively. At a valley, Figure C.8(b) includes a somewhat periodic structure

containing two to three apparent distinct frequencies. The maximums for the velocity and pressure at the monitor point 2 are approximately 0.4 to 0.8 ms^{-1} and 5 to 15 Pa , respectively. Reductions in fluctuations for u -velocity and pressure are obtained between 70 to 80 percent and 67 to 75 percent at a peak location, respectively. The reductions at a valley location are between 60 to 73 percent and 75 to 87 percent for u -velocity and pressure, respectively. In Figure C.8(c), a periodic structure similar to that of the plain span is present for the velocity-pressure coupling of $PSSP_3$. The presence of additional frequencies can be observed within the time history plot at point 3, indicating the presence of both uncontrolled and controlled flow structures. The maximum magnitudes for u -velocity and pressure are as previously observed between approximately 0.4 to 0.75 ms^{-1} and 10 to 25 Pa , respectively.

The cross-correlation sequences for u -velocity and pressure are presented in Figure C.9 for $PSSP_3$. High correlation exists between the velocity-pressure coupling along the uncontrolled span at points 4 and 5. This is also similar to the observations for the previous two partial SSP configurations. This correlation is observed to also occur at the vortex-shedding frequency, f_{vo} and the details are provided in Figures C.9(d) and C.9(e). At the boundary, point 3, in Figure C.9(c), the periodicity of the natural structure is correlated, as well as few additional frequencies that cause the variable correlation magnitude throughout the cross-correlation sequence.

At the monitor points 1 and 2 corresponding to a peak and valley, a slightly higher correlation is present between the velocity and pressure at zero time delay for a point 2. However, both plots in Figures C.9(a) and C.9(b) show the presence of similar frequency content and negligible correlation throughout the time delay sequence. The cross-correlation plot for point 1 shows the presence of at least one additional frequency.

Observing the PSD for u -velocity, pressure and the cross-correlation function for $PSSP_3$, the plots of Figure C.10 consecutively demonstrate the transition from the controlled incoherent flow structures through to the uncontrolled coherent structures. In Figure C.10(a), the dominant structures for both velocity and pressure occur at approximately $0.2f_{vo}$, with a mitigated flow structure at f_{vo} . However, correlation is only present at $0.2f_{vo}$ for the peak location, as a much smaller, negligible spectral peak is present at f_{vo} . At the given valley location, there is no clear indication of dominant flow

structures for the PSD of both velocity and pressure in Figure C.10(b). The PSD of the cross-correlation sequence however, shows only a clear dominant flow structure at $0.2f_{vo}$.

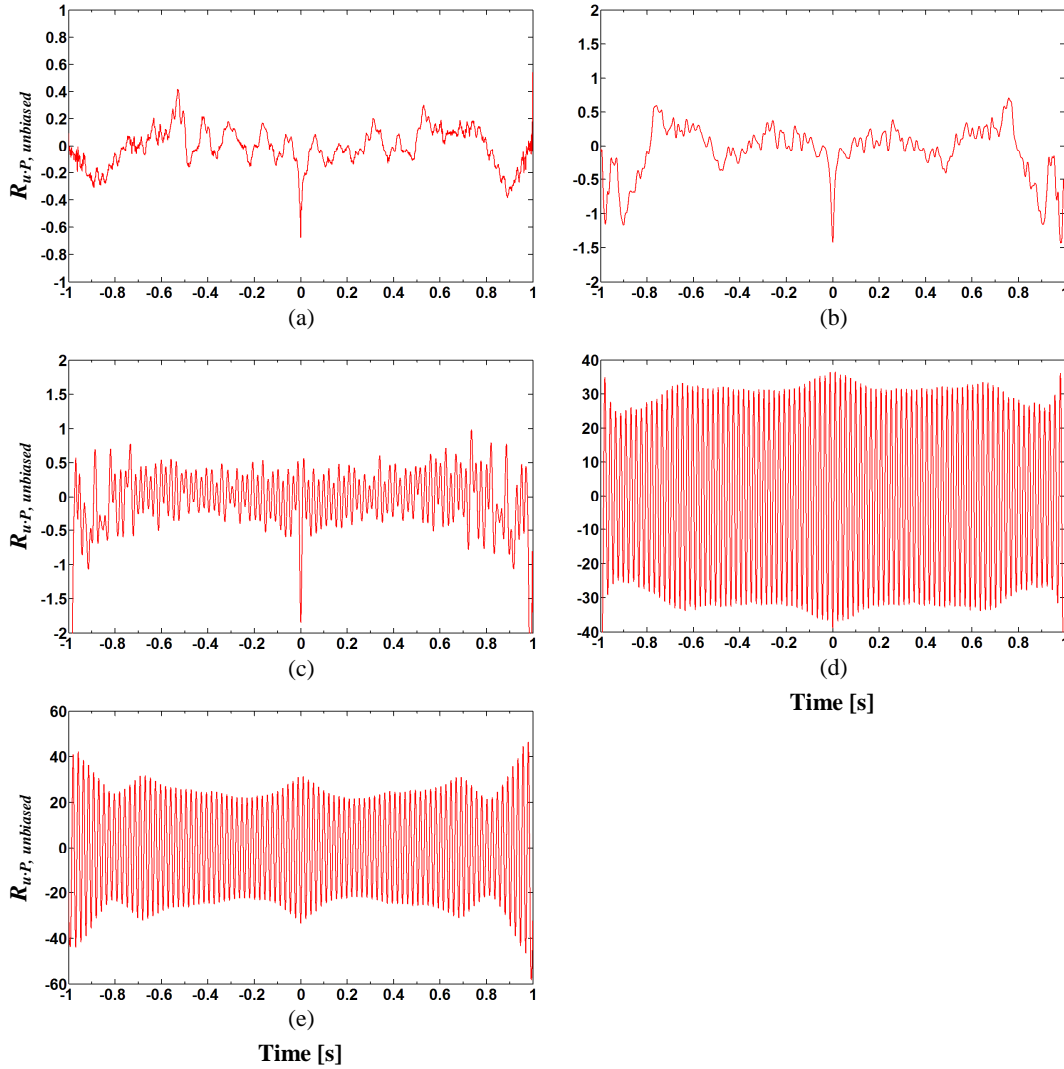


Figure C.9: Unbiased cross-correlation between u -velocity and pressure at the leading edge of $PSSP_3$; (a) point 1; (b) point 2; (c) point 3; (d) point 4; (e) point 5.

In Figure C.10(c), the presence of a spectral peak exists at approximately f_{vo} for the boundary location. Additional smaller spectral content is also present surrounding $0.5f_{vo}$. Correlation exists dominantly at this location at f_{vo} , while also containing a structure at approximately $0.2f_{vo}$, as well as $0.5f_{vo}$. The observations for this particular boundary point herein contain the strongest evidence of co-existing structures between plain and SSP characteristics. At the monitor points 4 and 5 within the plain span of the cylinder,

a very clear spectral peak is obtained at f_{vo} . Minor spectral content is also present at approximately $2f_{vo}$ for both the u -velocity and pressure PSD. Nonetheless, correlation is only present at f_{vo} in Figures C.10(d) and C.10(e). Table C.1 provides a summary of the leading edge observations.

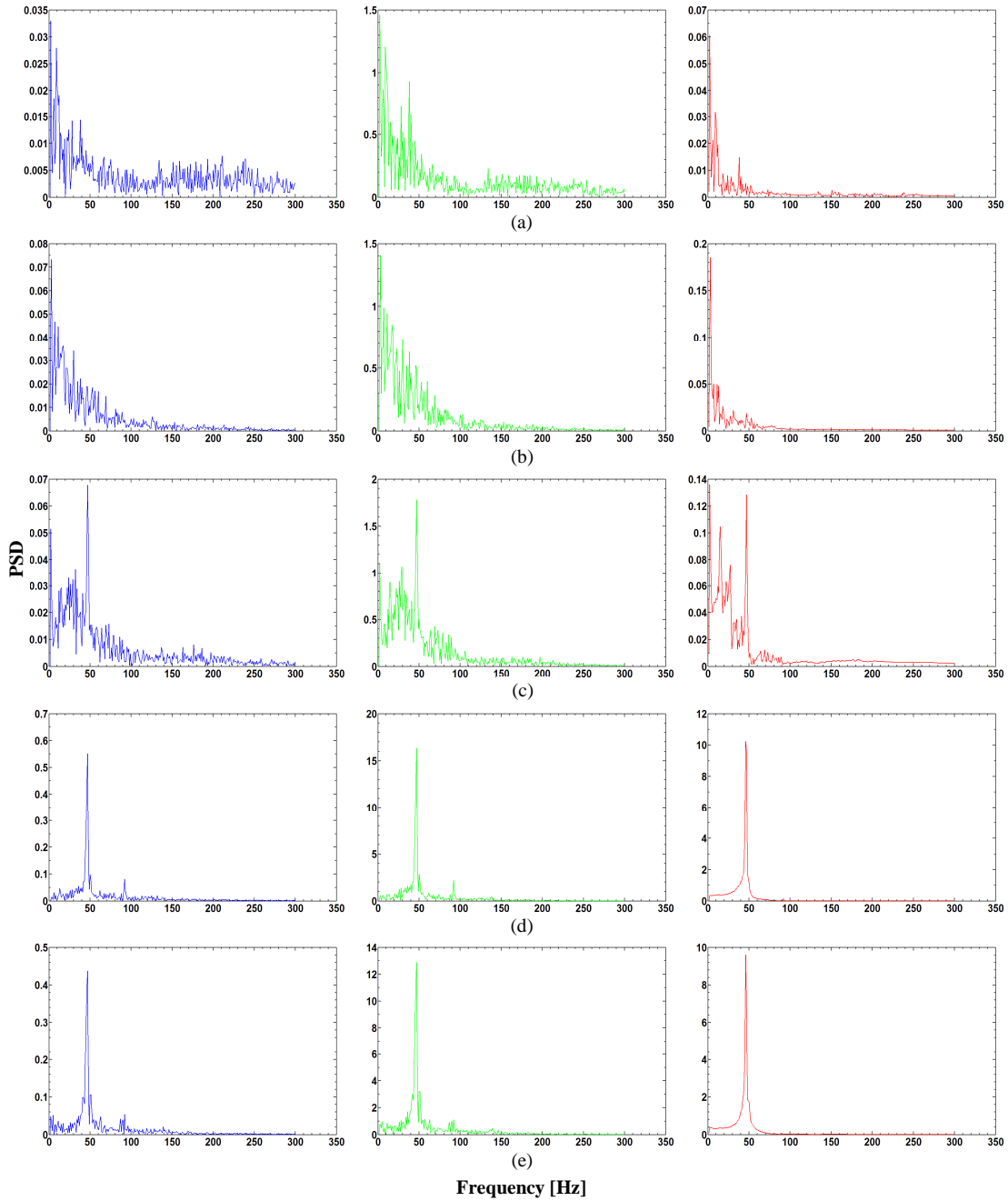


Figure C.10: PSD of u -velocity (—), pressure (—) and unbiased cross-correlation function (—) at the leading edge of $PSSP_3$; (a) point 1; (b) point 2; (c) point 3; (d) point 4; (e) point 5.

Table C.1: Summary of leading edge correlation observations for the partial SSPs.

LE Points	Uncontrolled Span			Controlled Span				
	u -velocity [ms ⁻¹]	Pressure [Pa]	Correlated Frequency [Hz]	u -velocity [ms ⁻¹]	Pressure [Pa]	Correlated Frequency [Hz]	Velocity reduction [%]	Pressure reduction [%]
$PSSP_1$	1 - 1.7	25 - 40	f_{vo}	0.75 - 1.5	15 - 25	$0.2f_{vo}$	11 - 25	37 - 40
$PSSP_2$	1.5 - 2.5	40 - 70	f_{vo}	0.75 - 1.5	15 - 20	$0.2f_{vo}$	40 - 50	63 - 71
$PSSP_3$	1.5 - 2	40 - 60	f_{vo}	0.3 - 0.8	5 - 20	$0.2f_{vo}$	60 - 80	67 - 87

C.1.2 Correlations at the Trailing Edge of the Partial SSP Cylinder

Histories for u -velocity and pressure are plotted against time for $PSSP_1$, $PSSP_2$ and $PSSP_3$ at the trailing edge points in Figures C.11, C.14 and C.17, respectively. The unbiased cross-correlation sequence, $R_{u,P,unbiased}$, between the streamwise u -velocity and pressure at the trailing edge for all three partial SSP configurations are presented in Figures C.12, C.15 and C.18. The time histories at each point along the trailing edge of $PSSP_1$ are presented in Figure C.11. The presence of a periodic structure is apparent and the histories appear to be in phase. These details of the flow structure are shown at points 1 and 7 in Figures C.11(a) and C.11(g). The maximum magnitudes for the velocity and pressure are approximately between 5 to 10 ms⁻¹ and 40 to 60 Pa, respectively.

The histories at the junction points 2 and 6 for $PSSP_1$ contain a periodic structure. However, this periodicity in Figures C.11(b) and C.11(f) is not as apparent due to the presence of high frequency content and interference of the natural structure at these locations. Close observation of the time histories at the boundaries between the plain and partial SSP spans reveals the data continually in and out of phase. This indicates the possibility that two flow structures are still effectively present at the trailing edge coincident to the boundaries.

From Figures C.11(c) and C.11(e), the velocity-pressure coupling appears to contain a consistent half cycle phase difference, which is similar to the structure at the leading edge. The maximums for u -velocity and pressure are approximately between 0.5 to 1.5 ms⁻¹ and 10 to 25 Pa, respectively. Therefore, the reductions in fluctuations

obtained at the trailing edge of a valley location for $PSSP_1$ are between approximately 85 to 90 percent and 58 to 75 percent for velocity and pressure, respectively.

At the trailing edge location at point 4, corresponding to a peak of the partial SSP, the velocity-pressure histories also appear to be consistently in and out of phase, instead of remaining out of phase, such as the observations at the leading edge. The magnitude appears mitigated as compared to that at a valley location. The maximum magnitudes at the peaks are on average between approximately 2 to 6 ms^{-1} and 25 to 60 Pa for the velocity and pressure, respectively. Hence, at the trailing edge of the peak location, the fluctuations are reduced by approximately 40 to 60 percent and 17 to 38 percent for u -velocity and pressure, respectively.

An examination of the unbiased cross-correlation function between u -velocity and pressure is presented for the trailing edge points of $PSSP_1$ in Figure C.12. A consistently high correlation similar to the leading edge exists between the velocity-pressure coupling along the uncontrolled span at point 1. This is indicated in Figure C.12(a). A periodic correlation is observed between the velocity and pressure at what appears to be f_{vo} . Similar observations can be made for Figure C.12(g) at point 7. However, there is the presence of almost negligible correlation occurring at approximately 0.3 s lead and lag. It appears that the structures existing at the leading edge also translate to the trailing edge of $PSSP_1$.

At the boundaries, large correlation also exists between the velocity and pressure data at zero time delay. However, similar frequency content can be observed between these locations and the peak. Hence, Figures C.12(b), C.12(d) and C.12(f) display identical correlation at points 2, 4 and 6. The only difference being the clearer appearance of a periodic structure and much lower correlation magnitude at the location of the peak. At the valleys of $PSSP_1$, high correlation only occurs at zero time delay. This is indicated in Figures C.12(c) and C.12(e). Both peaks and valleys experience large mitigation of correlation between the velocity-pressure coupling.

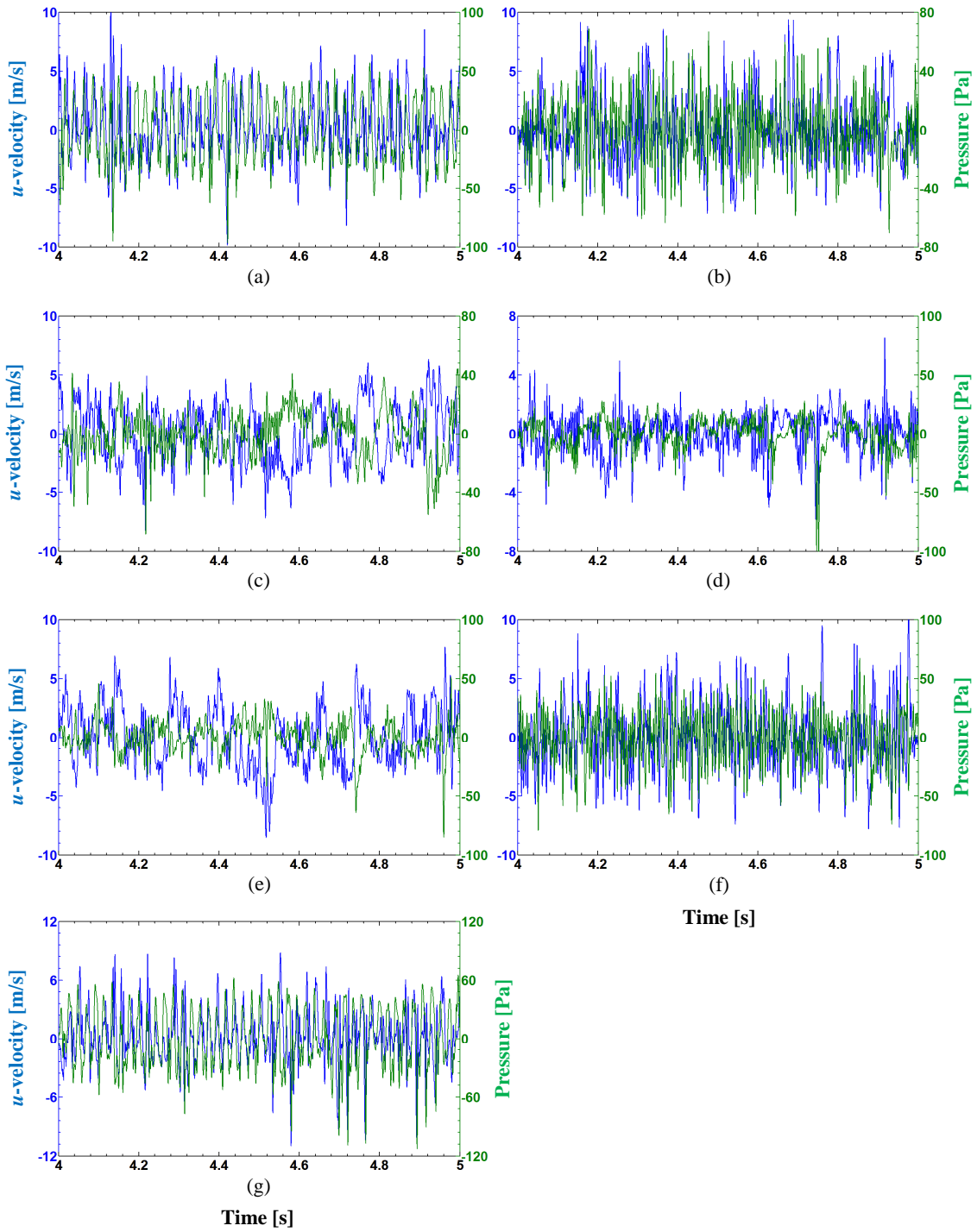


Figure C.11: Histories of u -velocity (—) and pressure (—) at the trailing edge locations of $PSSP_1$; (a) point 1; (b) point 2; (c) point 3; (d) point 4; (e) point 5; (f) point 6; (g) point 7.

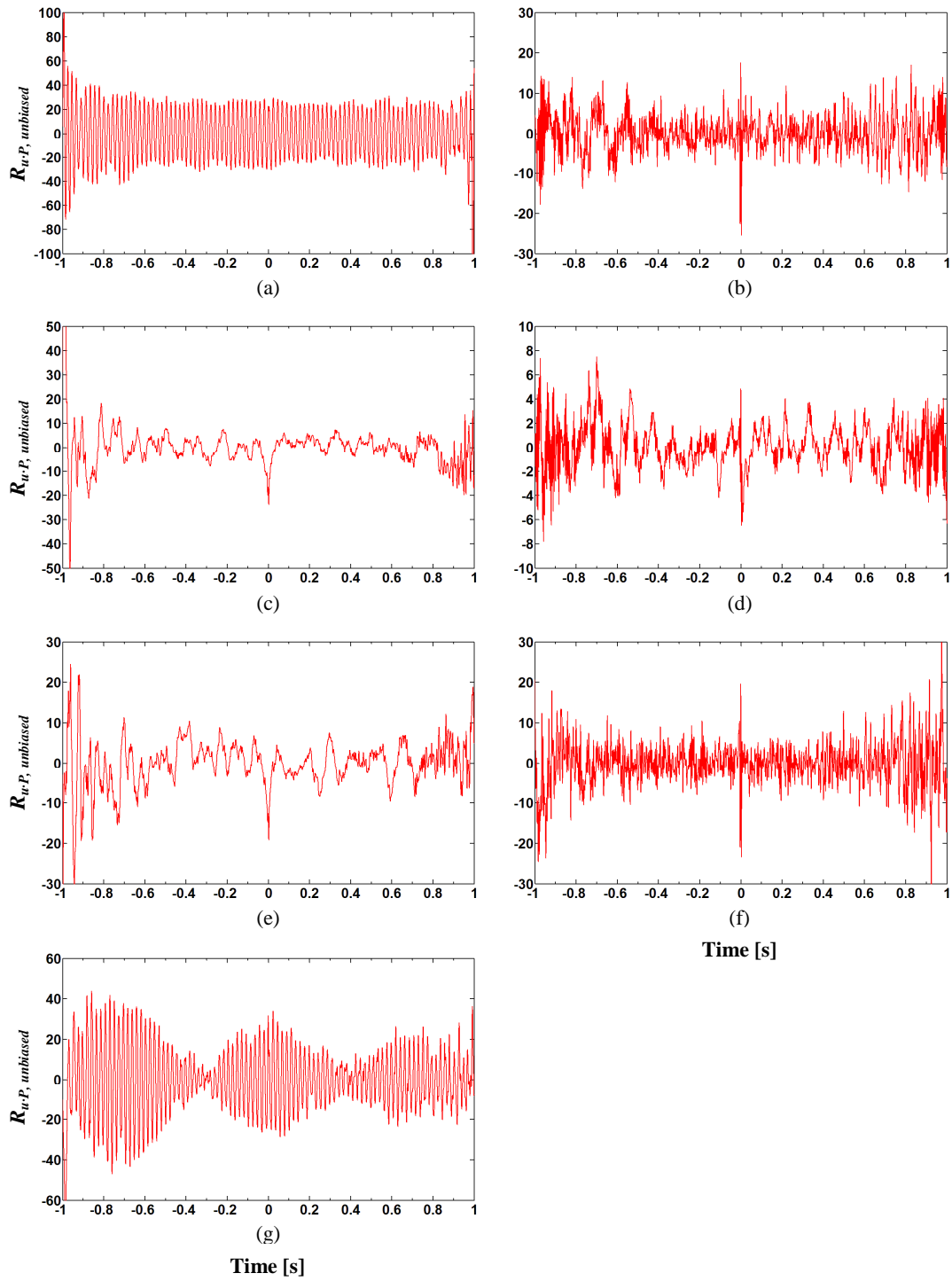


Figure C.12: Unbiased cross-correlation between u -velocity and pressure at the trailing edge of $PSSP_1$; (a) point 1; (b) point 2; (c) point 3; (d) point 4; (e) point 5; (f) point 6; (g) point 7.

The power spectral densities of u -velocity, pressure and unbiased cross-correlation function at the trailing edge locations of the three partial SSP configurations are given in Figures C.13, C.16 and C.19. The horizontal axis of these plots has a frequency range up to approximately $6f_{vo}$. For the plain span of $PSSP_1$, a spectral peak is clearly present at approximately f_{vo} in both Figures C.13(a) and C.13(g), for both u -velocity and pressure. The magnitude of the spectral peaks is representative of the corresponding magnitudes for the velocity and pressure histories. In Figure C.13(g), small spectral peaks are present at approximately $2f_{vo}$ and $3f_{vo}$ within the pressure PSD. The slight appearance of these harmonics of f_{vo} is indicative of the harmonic structure that is correlated between the data at point 7 in Figure C.12(g).

In Figure C.13(b), corresponding to point 2, very large spectral density is present and dominant structures within the velocity-pressure coupling are not apparent. The frequency content is broadband, however only slight indication is given to structures occurring at approximately $0.2f_{vo}$ and f_{vo} within the u -velocity PSD. Correlation between the velocity and pressure is therefore apparent at $0.2f_{vo}$. At point 6 in Figure C.13(f), the frequency content is broadband. However, observations indicate a correlation at approximately f_{vo} for u -velocity and $3.5f_{vo}$ for pressure. Therefore, these observations indicate that the location of the boundaries situated at the trailing edge is affected by the flow generated by the partial SSP span. At the trailing edge points corresponding to valleys the dominant frequency content for both u -velocity and pressure occur at approximately $0.2f_{vo}$. This is shown in Figures C.13(c) and C.13(e). The frequency distribution also contains additional content that is broadband. However, there is an absence of any identifiable spectral peaks, and large spectral magnitudes occur at and adjacent to $0.5f_{vo}$. At the peaks, both velocity and pressure contain spectral content throughout the frequency distribution. This is shown in Figure C.13(d). However, dominant structures occur at $0.2f_{vo}$ with frequency scatter up to f_{vo} . Within the PSD for u -velocity, large spectral content is also present at approximately $3f_{vo}$ to $4f_{vo}$. Correlation occurs at $0.2f_{vo}$ with negligible correlated content at surrounding frequencies. The shift in frequency content from f_{vo} at the plain span to $0.2f_{vo}$ at the SSP span demonstrates the interruption to the flow.

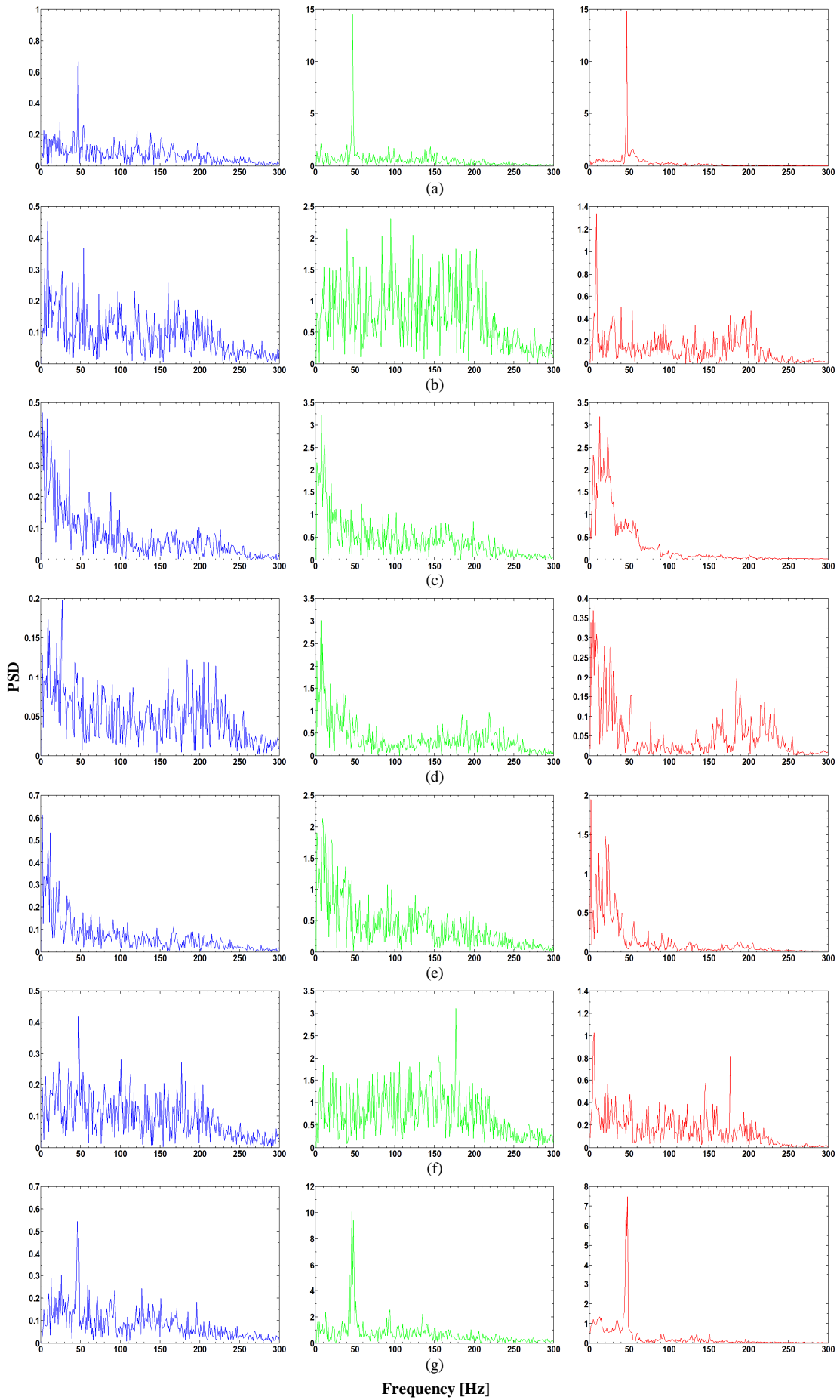


Figure C.13: PSD of u -velocity (—), pressure (—) and unbiased cross-correlation function (—) at the trailing edge of $PSSP_1$; (a) point 1; (b) point 2; (c) point 3; (d) point 4; (e) point 5; (f) point 6; (g) point 7.

The time histories for streamwise u -velocity and pressure at the trailing edge of $PSSP_2$ are presented in Figure C.14. In Figure C.14(d), a clear periodic structure is present for the monitor point 4, located within the plain span at the center of the square cylinder. The velocity-pressure coupling appears to be consistently in phase. The maximum magnitudes for u -velocity and pressure are approximately between 5 to 10 ms^{-1} and 50 to 110 Pa, respectively. At the peaks, the maximum magnitudes for the velocity and pressure fluctuations are between approximately 3 to 5 ms^{-1} and 20 to 50 Pa, respectively.

At the valleys, points 2 and 6, of $PSSP_2$, a periodic structure is slightly more evident containing few distinct frequencies. This can be observed in the time histories of Figures C.14(b) and C.14(f). The maximum magnitudes at the valleys are approximately between 3 to 7.5 ms^{-1} and 20 to 50 Pa for velocity and pressure, respectively. Therefore, reductions in velocity and pressure fluctuations at the trailing edge for both peak and valley locations are similarly obtained between 25 to 50 percent and 40 to 55 percent, respectively. At the boundaries, points 3 and 5, of $PSSP_2$, the velocity-pressure coupling is continually in and out of phase. Hence, the occurrence of two distinct flow structures is evident. The maximum magnitudes for the velocity-pressure coupling are approximately 4 to 8 ms^{-1} and 30 to 60 Pa, respectively. This detail is observed in Figures C.14(c) and C.14(e).

A high correlation exists between u -velocity and pressure for $PSSP_2$ along the plain span, and this is shown in Figure C.15(d) at the trailing edge for point 4. High correlation exists at zero time delay between the velocity-pressure coupling at the valleys, points 2 and 6, and negligible correlation throughout the remaining cross-correlation sequence. It should be noted herein that high correlation exists in Figures C.15(b) and C.15(f). However, this is only due to less averaging occurring between the final values in the data sets towards the ends of the sequences. Therefore, only the cross-correlation at zero time delay and the adjacent sequence information are true observations of the interactions. The cross-correlation at the peaks is shown in Figures C.15(a) and C.15(g). Negligible correlation exists between u -velocity and pressure throughout the cross-correlation sequence. However, few distinct frequencies can be observed at points 1 and 7. At the boundaries, points 3 and 5, shown in Figures C.15(c)

and C.15(e), a periodic structure can be observed with a similar frequency distribution to both the peaks and valleys.

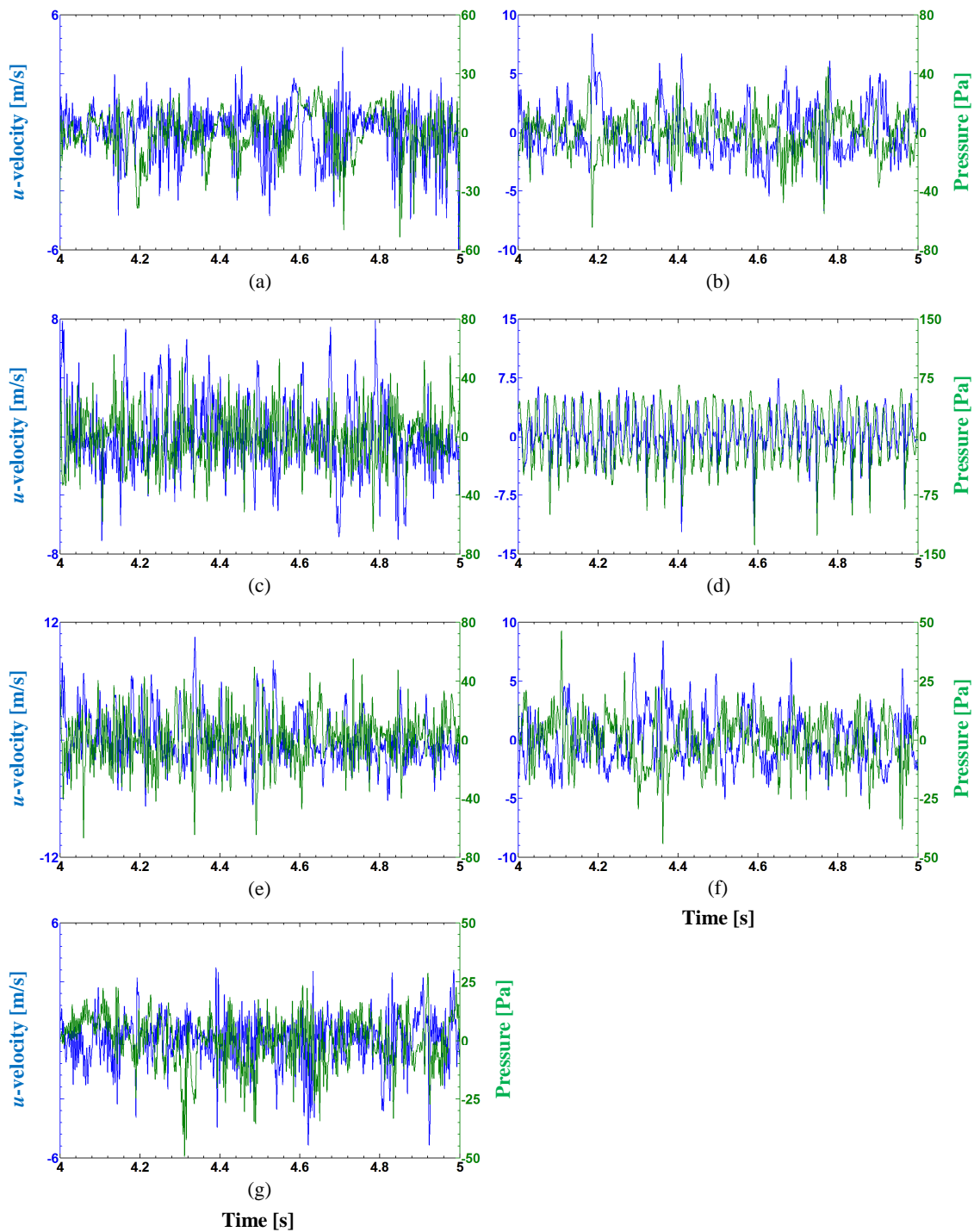


Figure C.14: Histories of u -velocity (—) and pressure (—) at the trailing edge locations of $PSSP_2$; (a) point 1; (b) point 2; (c) point 3; (d) point 4; (e) point 5; (f) point 6; (g) point 7.

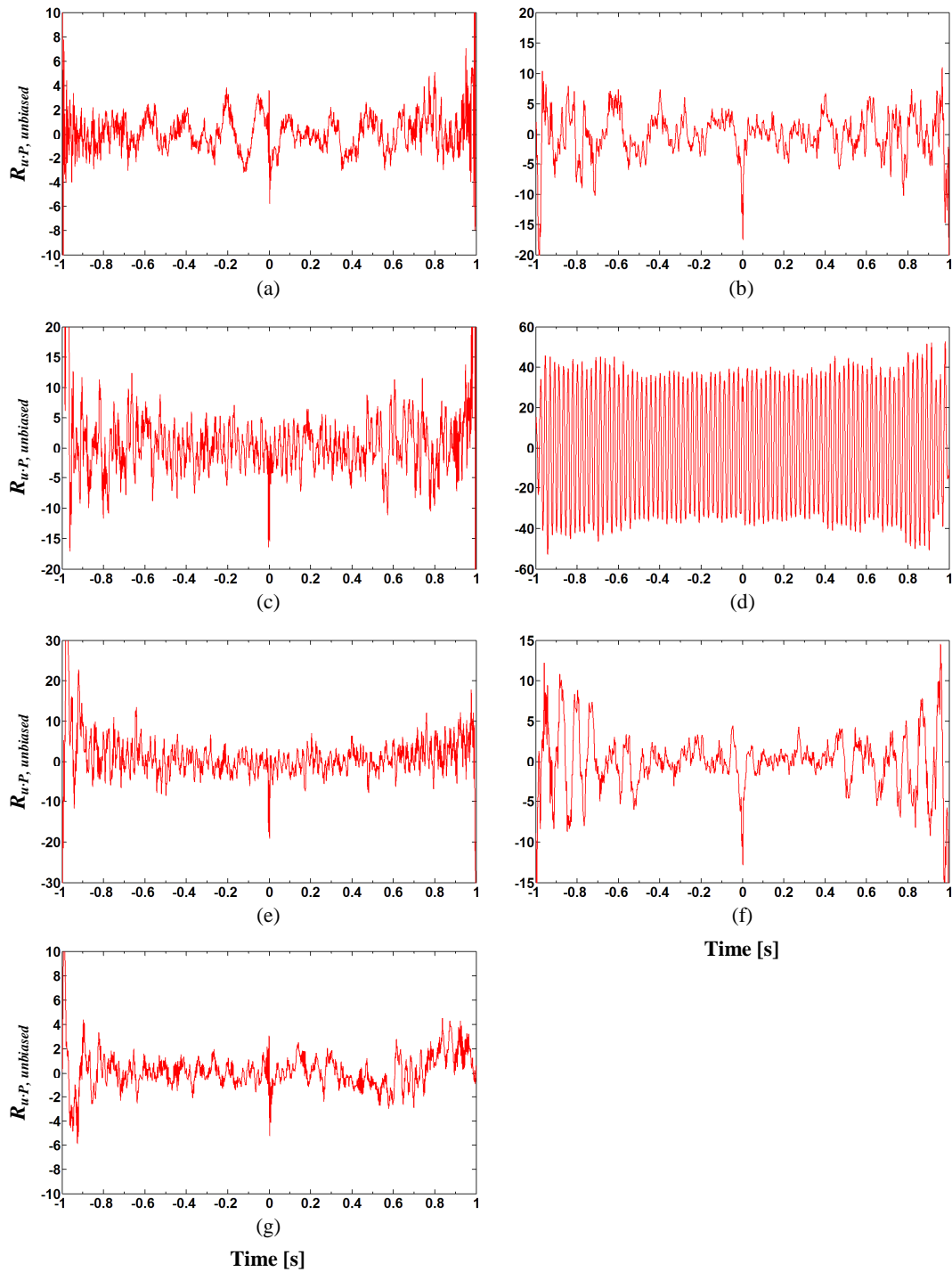


Figure C.15: Unbiased cross-correlation between u -velocity and pressure at the trailing edge of $PSSP_2$; (a) point 1; (b) point 2; (c) point 3; (d) point 4; (e) point 5; (f) point 6; (g) point 7.

The frequency distributions of the power spectral densities for $PSSP_2$ are presented in Figure C.16. A spectral peak is clearly observed at approximately f_{vo} in Figure

C.16(d), at the plain span. Harmonics of f_{vo} are also present at approximately $2f_{vo}$ and $3f_{vo}$ for u -velocity and only $3f_{vo}$ for pressure. However, strong correlation only exists at f_{vo} . In Figures C.16(b) and C.16(f), both boundaries, points 3 and 5, display spectral peaks at frequencies f_{vo} for u -velocity and pressure. However, the frequency distribution of the pressure data also contains spectral content between $3f_{vo}$ and $4f_{vo}$. The PSD for pressure is also accompanied with spectral content at approximately $0.2f_{vo}$. Correlation between the velocity-pressure coupling exists primarily at f_{vo} , with interactions also occurring at $0.2f_{vo}$. Hence, it appears that for $PSSP_2$, the structures that exist at the trailing edge at the boundaries are dominated by the coherent flow.

For Figures C.16(b) and C.16(f), corresponding to points 2 and 6, respectively, the spectral density is broadband for both u -velocity and pressure at valleys. The dominant structures within the velocity-pressure coupling occur at approximately $0.2f_{vo}$, although the frequency distribution shows content between $0.2f_{vo}$ to f_{vo} . At the peaks, points 1 and 7, large spectral distribution exists for the velocity fluctuations throughout the frequency domain and the pressure fluctuations are also broadband. However, clear structures exist at $0.2f_{vo}$, as well as f_{vo} within the pressure PSD. The characteristics of the spectral distributions in Figure C.16 indicate the apparent effectiveness of the partially applied SSP. Similarly for $PSSP_1$, the shift in the frequency distribution of the structures for $PSSP_2$ demonstrates the mitigation of the coherent structures. In addition, the symmetry that can be achieved about the central span location corroborates the independent flow structures, and the accuracy of the numerical model.

The time histories for u -velocity and pressure along the trailing edge of $PSSP_3$ are presented in Figure C.17. At the plain spans, points 4 and 5 in Figures C.17(d) and C.17(e) there is a phase difference within the velocity-pressure coupling. The maximums for u -velocity and pressure fluctuations are approximately between 5 to 10 ms^{-1} and 60 to 115 Pa, respectively. At point 1, corresponding to a peak, there is a slight phase difference between the velocity and pressure histories; however a close match in phase exists. The maximum magnitudes for the velocity-pressure coupling at this location are approximately between 1.5 to 5 ms^{-1} and 15 to 40 Pa, respectively. The reductions in turbulent fluctuations achieved for velocity and pressure at this location are between approximately 50 to 70 percent and 65 to 75 percent, respectively.

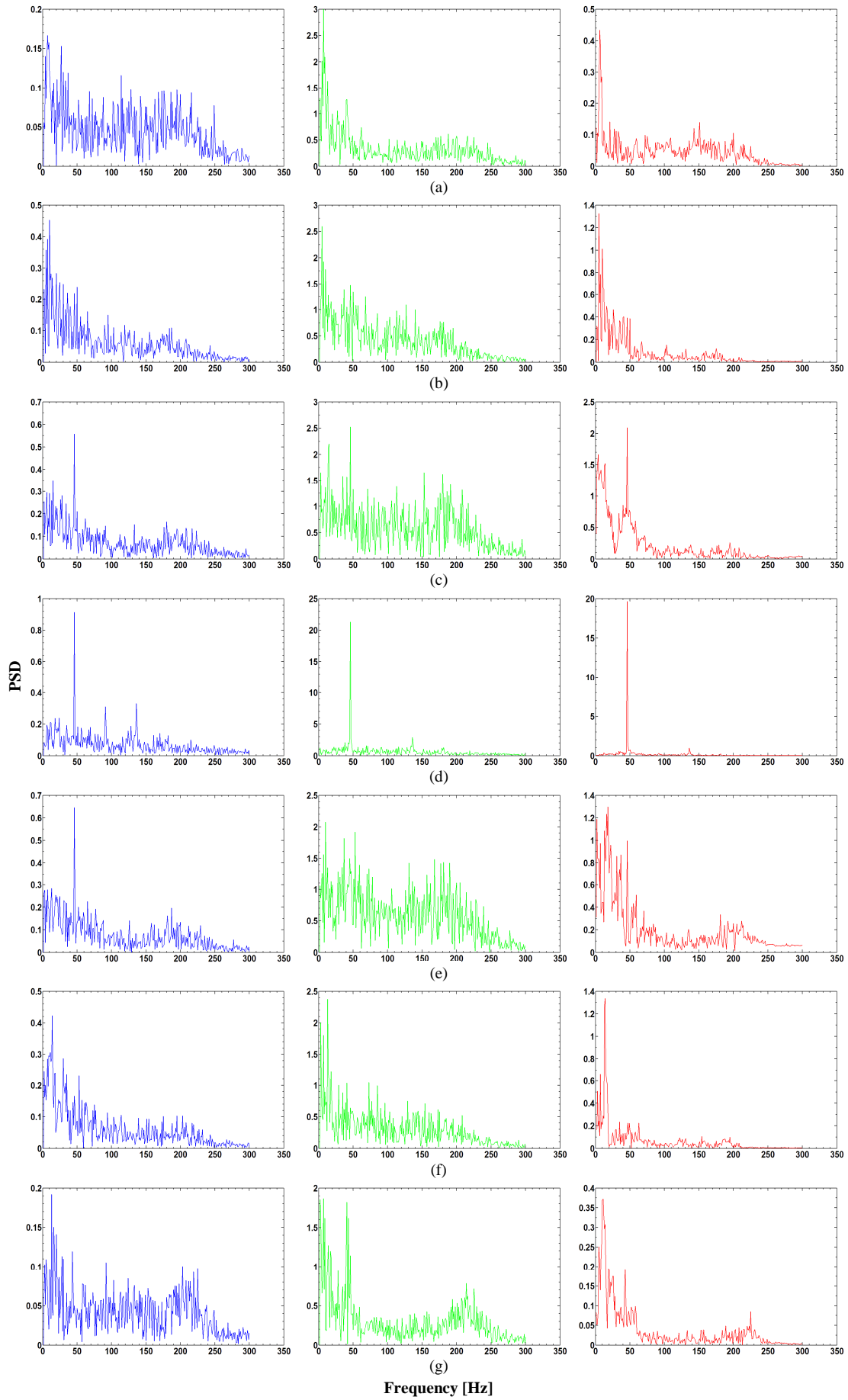


Figure C.16: PSD of u -velocity (—), pressure (—) and unbiased cross-correlation function (—) at the trailing edge of $PSSP_2$; (a) point 1; (b) point 2; (c) point 3; (d) point 4; (e) point 5; (f) point 6; (g) point 7.

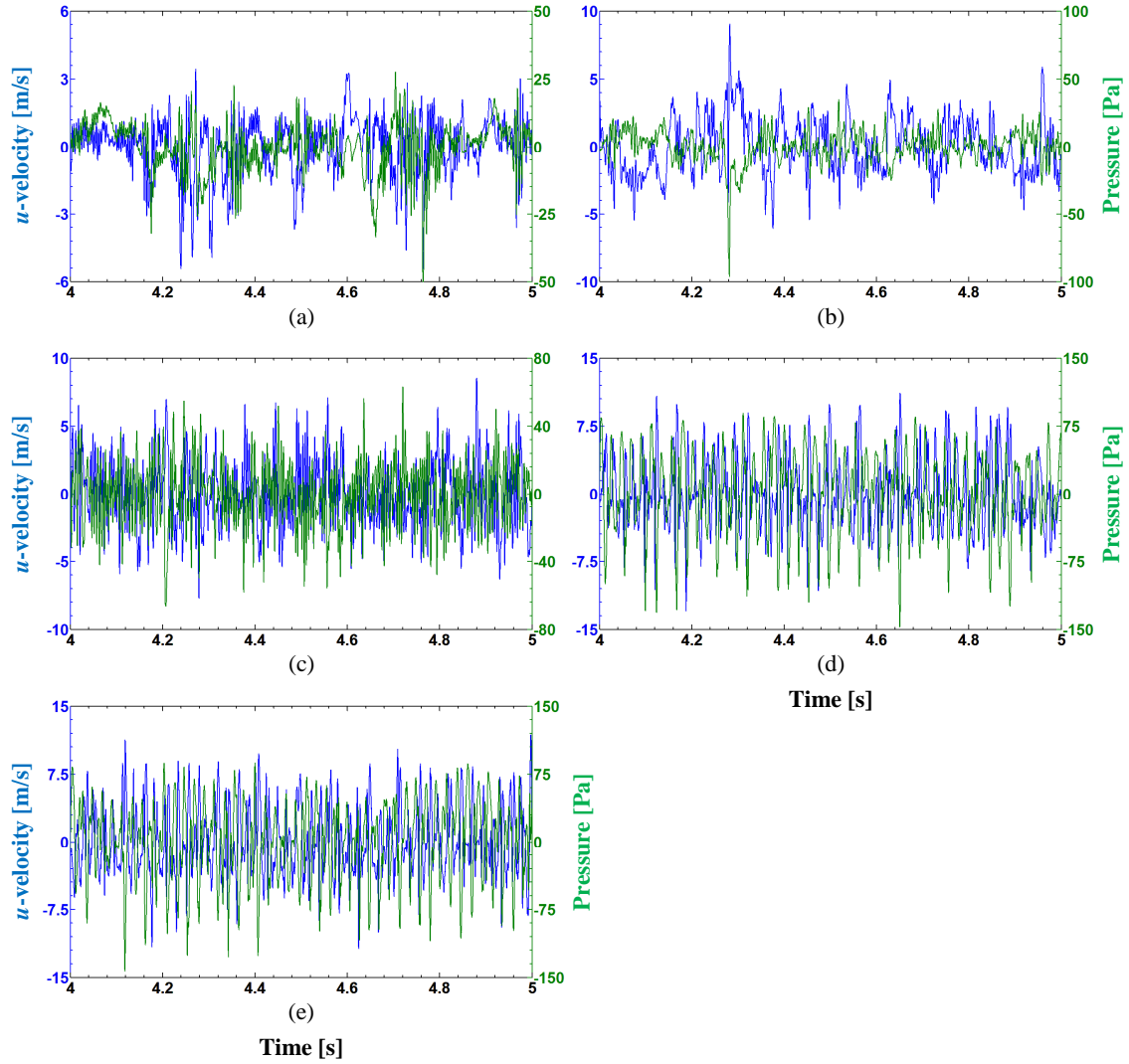


Figure C.17: Histories of u -velocity (—) and pressure (—) at the trailing edge locations of $PSSP_3$; (a) point 1; (b) point 2; (c) point 3; (d) point 4; (e) point 5.

At a valley, in Figure C.17(b), the phase between u -velocity and pressure at point 2 is at a half cycle phase difference. The maximums for the velocity and pressure at this location are approximately 2.5 to 7.5 ms^{-1} and 25 to 80 Pa, respectively. The reductions are between 25 to 50 percent and 30 to 58 percent for u -velocity and pressure, respectively. Higher reductions are obtained at the peak, point 1. At the boundary, point 3, Figure C.17(c) contains a periodic structure similar to that of the plain span at points 4 and 5. The presence of additional frequencies similar to the content for peaks and valleys can also be observed. The maximum magnitudes for u -velocity and pressure are as previously observed between approximately 4 to 8 ms^{-1} and 30 to 60 Pa, respectively.

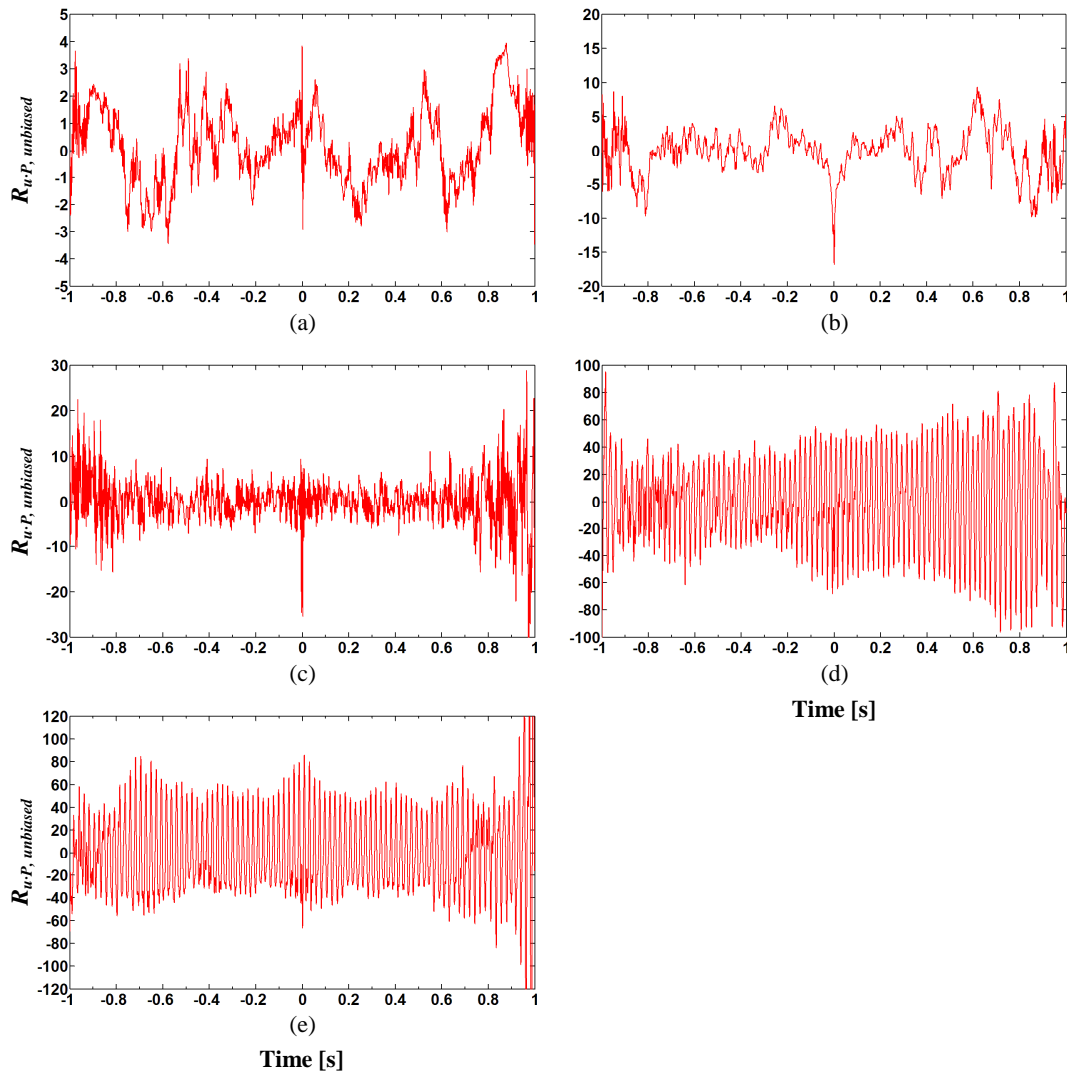


Figure C.18: Unbiased cross-correlation between u -velocity and pressure at the trailing edge location of $PSSP_3$; (a) point 1; (b) point 2; (c) point 3; (d) point 4; (e) point 5.

The cross-correlation sequences for the velocity and pressure data are presented in Figure C.18 for $PSSP_3$. High correlation exists between the velocity-pressure coupling along the plain span at points 4 and 5. The correlation magnitude increases with time lead, causing asymmetry about the zero time delay. This can be seen in Figure C.18(d). At the peak, point 1 of $PSSP_3$, a periodic structure is clearly evident containing few distinct frequencies. The magnitude of cross-correlation is significantly less than that for the uncontrolled span. This observation is given for Figure C.18(a). At the valley, point 2, there is high correlation at zero time delay between u -velocity and pressure. The magnitude throughout the remaining correlation sequence is similar to that at a point 1.

At the boundary, point 3, in Figure C.18(c), the periodicity of the coherent structure is correlated with the structures of the SSP span. This causes high correlation at zero time delay, and similar correlation magnitude to points 1 and 2 elsewhere throughout the sequence.

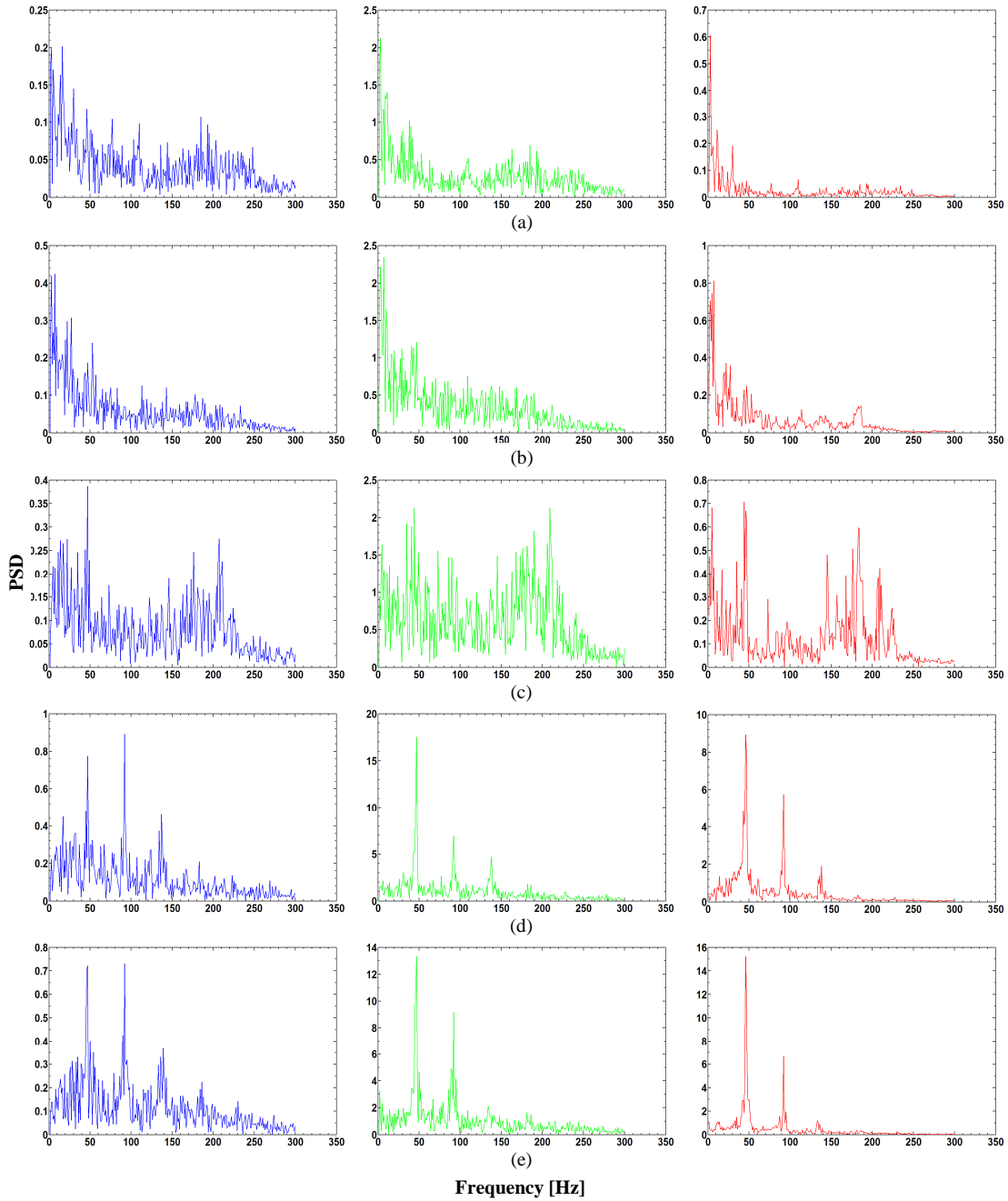


Figure C.19: PSD of u -velocity (—), pressure (—) and unbiased cross-correlation function (—) at the trailing edge of $PSSP_3$; (a) point 1; (b) point 2; (c) point 3; (d) point 4; (e) point 5.

The PSD for u -velocity, pressure and the cross-correlation function for $PSSP_3$ demonstrate the transition from the SSP (controlled) incoherent flow structures through to the plain (uncontrolled) coherent structures in Figure C.19. In Figure C.19(a), the dominant structures for both velocity and pressure occur at approximately $0.2f_{vo}$, with a broadband frequency distribution. However, correlation is present at approximately $0.2f_{vo}$ and $0.5f_{vo}$ at the peak.

At the valley, point 2, there is presence of spectral peaks at approximately $0.2f_{vo}$, $0.5f_{vo}$ and f_{vo} for the u -velocity, and approximately $0.2f_{vo}$ and f_{vo} for pressure. This is shown in Figure C.19(b). The correlation occurs at the peaks at $0.2f_{vo}$, $0.5f_{vo}$ and f_{vo} . In Figure C.19(c), the boundary, point 3, contains a frequency distribution with spectral peaks occurring at approximately f_{vo} , as well as between $3f_{vo}$ and $4f_{vo}$. This is indicated for both u -velocity and pressure. In both Figures C.19(d) and C.19(e), the spectral content within the plain span of $PSSP_3$ contains peaks at approximately f_{vo} and its harmonics $2f_{vo}$, $3f_{vo}$ and $4f_{vo}$ for u -velocity. Whereas, frequency content occurs at f_{vo} , $2f_{vo}$ and $3f_{vo}$ for pressure. Correlation exists between the velocity-pressure coupling at f_{vo} and $2f_{vo}$. The summary of the trailing edge observations for the partial SSPs is given in Table C.2.

Table C.2: Summary of trailing edge correlation observations for the partial SSPs.

LE Points	Uncontrolled Span			Controlled Span				
	u -velocity [ms ⁻¹]	Pressure [Pa]	Correlated Frequency [Hz]	u -velocity [ms ⁻¹]	Pressure [Pa]	Correlated Frequency [Hz]	Velocity reduction [%]	Pressure reduction [%]
$PSSP_1$	5 - 10	40 - 60	f_{vo}	0.5 - 6	10 - 60	$0.2f_{vo}$	40 - 90	17 - 75
$PSSP_2$	5 - 10	50 - 110	f_{vo}	3 - 7.5	20 - 50	$0.2f_{vo}, f_{vo}$	25 - 50	40 - 55
$PSSP_3$	5 - 10	60 - 115	$f_{vo}, 2f_{vo}, 3f_{vo}$	1.5 - 7.5	15 - 80	$0.2f_{vo}, 0.5f_{vo}, f_{vo}$	25 - 70	30 - 75

EXPLORATION OF A SEMI-ACTIVE CONTROL METHOD FOR VORTEX-INDUCED RESONANCE

As flow passes over a resonant structure, such as a marine riser used for off-shore drilling, the vortices that are shed as a result of obstructing the flow, may induce significantly large levels of vibration. This vibration is caused by the force exerted on each side of the structure, as vortices are shed alternatively from each side, giving rise to oscillatory motion. When the vortex shedding frequency approaches the natural frequency of the structure, the structural oscillations grow and start establishing a strong interaction with the shedding mechanism in the flow (Blevins 2009). Allowing such structural resonance to occur is detrimental for safety. Therefore, it is important to develop concepts for controlling fluid-structure interactions.

Hover *et al.* (1997) implement a hybrid analysis through numerically controlled oscillations of elastically mounted circular cylinders and marine cables in cross-flow. The numerical model simulates the structural resonance using input data of real time load-cell measurements from the experimental setup. This approach establishes the fluid-structure interactions through a closed-loop feedback system that can identify distinct wake details experimentally through a numerical control principle. The hybrid technique of Hover *et al.* (1997) obtains accurate details of frequency and response amplitude of an oscillating structure in cross-flow. This work provides insights for using numerical methods to obtain a design procedure for a generic control of vortex-induced resonance.

The objective of this appendix is to present observations of numerical predictions for a proposed control technique, designed to prevent the formation of organised vortex-

induced resonance. The proposed technique is a semi-active parameter control, which results in a variable natural frequency through a variable structural stiffness. Its design advantage is pre-determining the timing and magnitude of actuation, in order to remove the need for sensing and computing. This study was conducted in parallel to the work of this thesis. It was intended to apply a spanwise sinusoidal profile (SSP) to the separation lines of circular and square cylinders, in order to compare active and passive control methods. Hence, the combined application of an SSP and a semi-active control is recommended as a future work.

D.1 Model Description

The model of the circular cylinder for the two-dimensional flow simulations is shown in Figure D.1. The cylinder is assigned a mass (m), stiffness (k) and a viscous damping coefficient (c). The model represents the dynamics of a simple structure at one vibration mode, possibly the fundamental one. This single degree of freedom (SDOF) system is allowed to oscillate in the y -direction in Figure D.1, perpendicular to the flow which travels from left to right. The model is fixed in the flow direction.

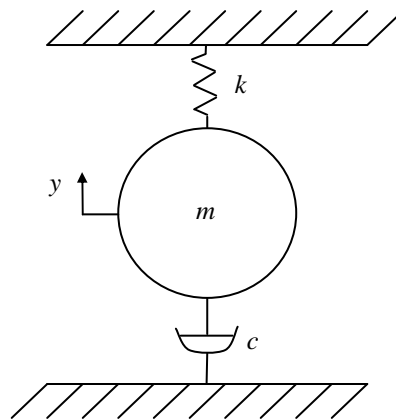


Figure D.1: Schematic representation of the elastically mounted circular cylinder in cross-flow.

The spring constant and mass were chosen such that the structural resonance frequency corresponds to the vortex shedding frequency at a Reynolds number, Re of 1000. The definition for the Reynolds number regarding the circular cylinder is

$$Re = \frac{U_o D}{\nu} \quad (D.1.1)$$

where U_o is the free stream velocity, D is the circular cylinder diameter and ν is the kinematic viscosity. This assertion of structural resonance is possible due to the Strouhal number, St , having the value of 0.2 for a wide range of Re of up to 10^5 for a circular cross-section [Blevins 2009; Griffin and Ramberg 1982; Blevins 1990]. The definition of Strouhal number for the circular cylinder is

$$St = \frac{f_{vo} D}{U_o} \quad (D.1.2)$$

where, f_{vo} is the vortex shedding frequency. The viscous damping coefficient, c , was chosen to represent a critical viscous damping ratio, ζ , of 1%, where

$$\zeta = \frac{c}{2(km)^{1/2}} \quad (D.1.3)$$

Numerical investigations were performed with FLUENT[®] (ANSYS 2009) for a stationary circular cylinder in cross-flow, in order to confirm the Strouhal number. The value of St obtained was approximately 0.21, in good agreement with Blevins (1990, 2009) and Griffin and Ramberg (1982).

As flow travels over the elastically mounted circular cylinder, unsteady pressure fluctuations act on its surface as a result of vortex shedding, causing it to oscillate in the y -direction. FLUENT[®] is capable of simulating the fluid dynamics around static structures by default, but requires an additional source code to implement a moving boundary. To obtain the flow field predictions with the moving boundary of the elastically mounted cylinder, a user defined function (UDF) was written in C++ language (ANSYS 2009). The objective of this UDF is to communicate with FLUENT[®] to determine the position of the SDOF system using the equation of motion

$$F_L = m\ddot{y} + c\dot{y} + ky \quad (D.1.4)$$

In equation D.1.4, F_L is the sum of the pressure and viscous forces acting on the cylinder boundary in the y -direction. Over-dots represent time derivatives. The UDF calculates y in response to the fluid loading, F_L , at every time step. This is performed by rearranging equation D.1.4 to give the instantaneous change in velocity as

$$d\dot{y} = \frac{(F_L - c\dot{y} - ky)}{m} dt \quad (\text{D.1.5})$$

The resulting velocity calculated in equation D.1.5 is interpreted by FLUENT[®] to update the position of the cylinder boundary. The computational domain is re-meshed in response to the new position of the boundary at each time step.

The full computational domain for the numerical simulations is presented in Figure D.2(a). The domain is similar to that used by Tutar and Holdo (2000), as it extends from the center of the cylinder a distance of $7D$ both upstream and along the y -direction and a distance of $15D$ downstream. This domain ensured sufficient space for the downstream wake development, as well as minimising blockage effects due to boundaries in the y -direction.

The velocity inlet boundary condition was set for Re ranging from 800 to 1100. Pressure inlet boundary conditions were applied to the top and bottom boundaries and a pressure outlet boundary condition was applied to the downstream boundary, as shown in Figure D.2(a). This arrangement of boundary conditions allowed the flow to be directional from left to right while avoiding a wall bounded flow condition.

The mesh used is an unstructured triangular mesh of 36338 cells, to allow for a fixed-grid configuration during the simulations, as the mesh moved with the cylinder motion. This approach is similar to the fixed-grid approach implemented by Blackburn and Karniadakis (1993). The fixed-grid configuration is achieved by assigning a spring constant factor and a boundary node relaxation factor to the edges of each triangular cell within the mesh, which allowed a smoothing function to be applied for the re-meshing sequence during each time step. As the cylinder boundary moves in the vertical direction, it exerts a deformation in the edges of the near boundary layer cells, causing the adjacent edges to react outwards in a wave propagation pattern. Therefore, the mesh

elements behave as interconnecting springs. The application of suitable input variables for the spring constant factor and boundary node relaxation factor allow the mesh to follow the path of the moving cylinder boundary.

A size function was used starting from the cylinder wall, in order to ensure a fine enough mesh to sufficiently resolve the boundary layer, while having a large enough mesh in the surrounding wake region to minimise the effect on computational time. This mesh sequence is shown in Figure D.2(b). In order to capture the vortex shedding accurately, the time step, dt , was set at 0.001 s, to ensure that at least 600 time steps were used per shedding cycle.

In order to verify the present numerical model, comparisons were made with the numerical results of Lu and Turan (2000) and the experimental results of Griffin and Ramberg (1982). These works focused on the response amplitude of an elastically mounted circular cylinder. As a test case, they chose a spring-damper mounted cylinder in water having a mass ratio, m^* , of 7.6, and a damping ratio, ζ , of 5%. The mass ratio is given as

$$m^* = \frac{m}{m_f} \quad (\text{D.1.6})$$

where: $m_f = \rho\pi a^2$ (D.1.7)

In equation D.1.7, m_f is the added mass of the entrained fluid, and a is the cylinder radius. The simulation of Lu and Turan (2000) and the experiment of Griffin and Ramberg (1982) were replicated using the UDF approach discussed previously. At resonance, the maximum cylinder displacement, y/D , was within 10% of the maximum displacement given in both Lu and Turan (2000) and Griffin and Ramberg (1982). Due to the close agreement between the results of the present numerical procedures and that in Lu and Turan (2000), as well as the validation with Griffin and Ramberg (1982), the UDF approach was considered to be acceptable.

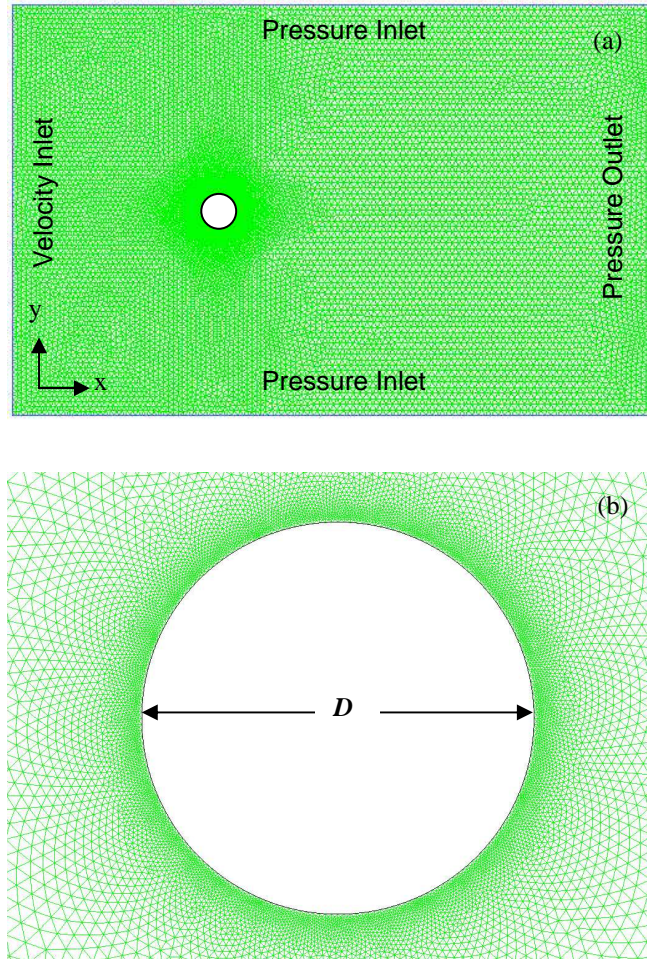


Figure D.2: Showing (a) full computational domain with imposed boundary conditions and (b) enlarged view with concentrated computational nodes.

D.2 Numerical Observations

D.2.1 Uncontrolled Vortex-Induced Resonance

Simulations were conducted with the elastically mounted circular cylinder for Re of 800, 850, 900, 1000 and 1100, in order to determine the free stream velocity at which vortex-induced resonance occurred. A Re of 1000 is designed to correspond to structural resonance, without considering the effect of the added mass of the entrained fluid, m_f (Blevins 2009). The simulations required a reasonably significant fluid density, ρ , of 150 kgm^{-3} , in order to observe the fluid-structure interactions. As a result, it is expected that the effect of added mass on the cylinder to be a factor in causing the

vortex resonance to occur at a smaller Re than 1000. The variation of Re from 1000 can also be interpreted as a frequency ratio of excitation, f_{vo}/f_n , where f_n is the structural natural frequency in vacuum. The ratio f_{vo}/f_n therefore corresponds to 0.8, 0.85, 0.9, 1 and 1.1, for the range of Re .

In Figure D.3, the displacement histories for the uncontrolled circular cylinder are given. Non-dimensional time, t/T_n , is shown along the horizontal axis, where T_n is the undamped natural period of the structure. Vertical axes indicate both the lift coefficient, C_l , and the non-dimensional displacement magnitude, y/D . Simulations are performed for 25 natural periods to maintain reasonable computational times.

Oscillations of the elastically mounted circular cylinder generally occur simultaneously at the vortex shedding frequency and the structural frequency. Therefore, the close existence of the forced response and transient response frequencies creates a beat envelope of different periods, depending on the value of the frequency ratio, f_{vo}/f_n . In Figures D.3(a) and D.3(c), the beat period is approximately $15T_n$ in Figure D.3(d) it is $7T_n$ and finally in Figure D.3(e) it is $4T_n$. A long beat period indicates two spectral components of comparable magnitudes at close frequencies, whereas a short beat period is the result of these frequencies moving away from each other.

In Figure D.3(b) no beat is observed, as there is close agreement between the vortex shedding and structural frequencies, therefore, suggesting the presence of structural resonance. This suggestion is supported by the existence of the growing envelope of the displacement history and the consistent quarter cycle phase lead between the lift coefficient and cylinder displacement histories (Dimarogonas and Haddad 1992). Hence, vortex-induced resonance is observed at a frequency ratio f_{vo}/f_n of 0.85, not at 1. A shift in the structural resonance frequency of approximately 15% can be attributed to the added mass of the fluid. Relatively large displacement magnitudes of the cylinder also contribute to this effect.

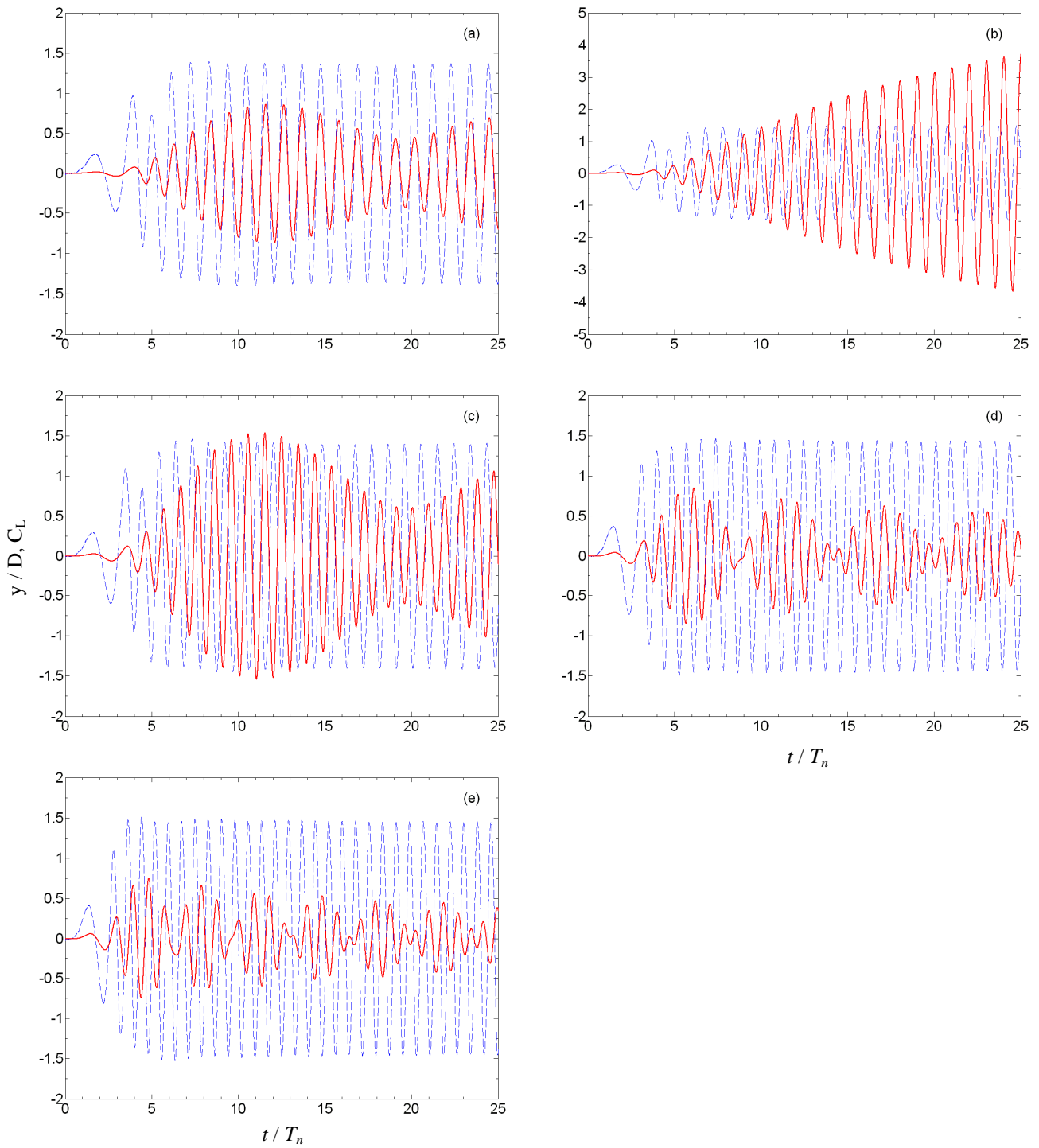


Figure D.3: Histories of the uncontrolled lift coefficient C_L (---) and cylinder displacement (---) for ζ of 0.01 and Re of (a) 800, (b) 850, (c) 900, (d) 1000 and (e) 1100.

D.2.2 Proposed Semi-Active Control

The implementation of the control involves applying fluctuations the structural stiffness, $k(t)$, in a square wave fashion, at a pre-determined control period, T_c . The choice for the square wave is purely for simplicity, which may well be altered during the later development stages. It is believed this application should provide an effective suppression technique, as it interferes with the organisation of vortex induced resonance. Simply changing the structural resonance frequency instead of fluctuating it, will only allow the problem to occur at another free-stream velocity and Re .

The proposed control is a semi-active parameter control technique (Antiohos *et al.* 2009). It contains a significant simplification, such that the actuation period is decided as part of design, not as part of flow or oscillation conditions. Therefore, no sensing or computing would be required for actuation of the control. For this reason, it is important to determine the most practical magnitude and period of actuation as key design variables.

Simulations were performed with variations in the spring constant from k , as the starting point, up to a magnitude of αk . The smallest α to provide a significant enough suppression of vortex induced resonance was determined to be 2. It is beneficial to have a small value of α to maintain the structural stiffness as near to its original value as possible, therefore, obtaining effective control with only small changes to the system. This ensures the practicality of the application.

For practical applications, it is also desirable that the actuation frequency of the stiffness fluctuations is small, while still maintaining effectiveness in control. Therefore, different control periods, T_c , were analysed, in order to determine the largest period suitable to achieve control. The displacement history of the controlled response for control intervals T_c of $T_n, 2T_n, 3T_n, 4T_n, 5T_n$ and $6T_n$ at the frequency ratio, f_{vo}/f_n of 0.85 is shown in Figure D.4. The axes are the same as in Figure D.3. The sharp peaks shown in the lower half of the C_l history indicate the actuation of the control. An initial delay of $5T_n$ was applied before the first actuation, in order to let the initial transients of the numerical solution to settle.

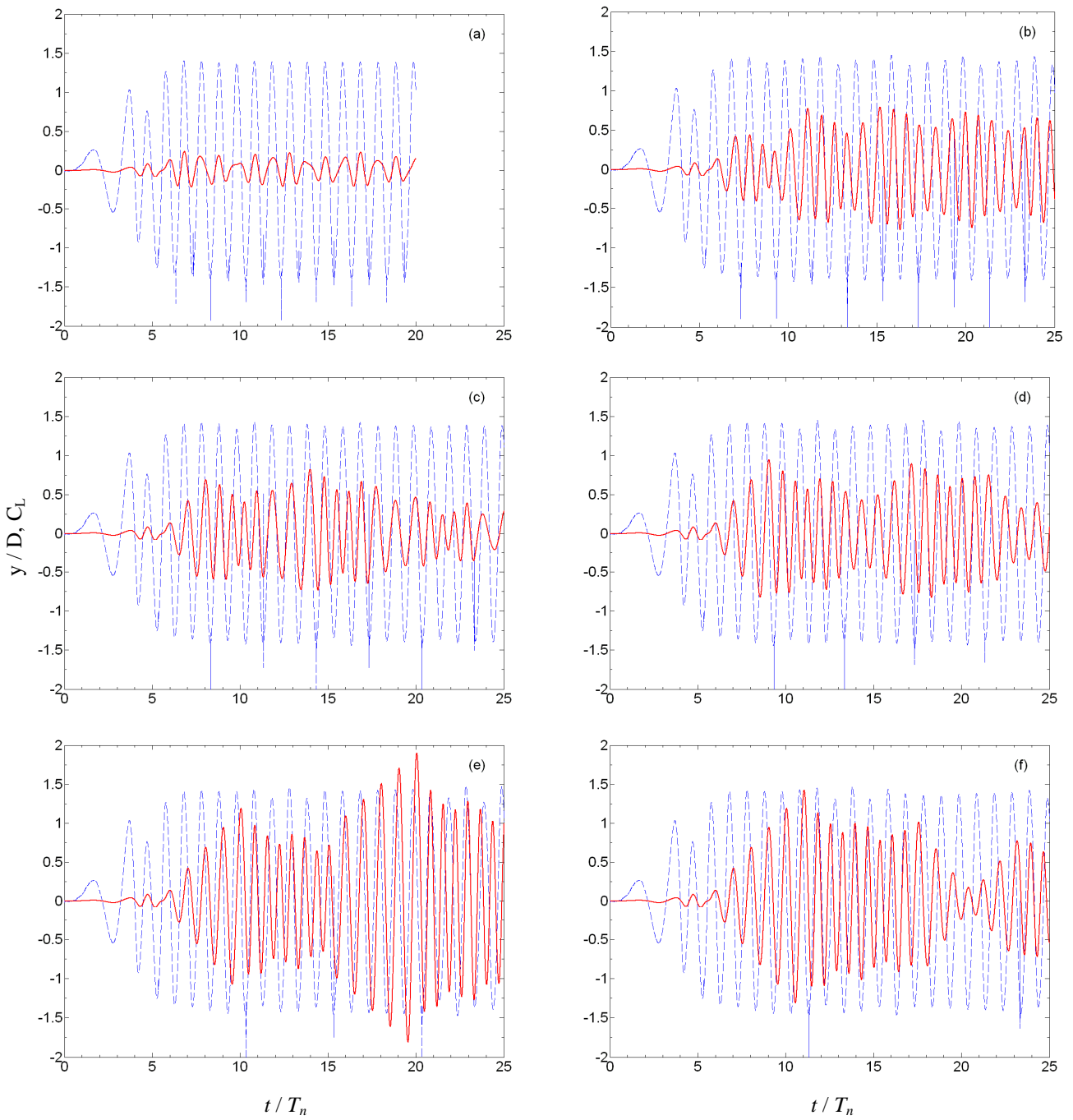


Figure D.4: Histories of the controlled lift coefficient C_l (---) and cylinder displacement (—) for ζ of 0.01, Re of 850 and for actuation periods, T_c of (a) T_n , (b) $2T_n$, (c) $3T_n$, (d) $4T_n$, (e) $5T_n$ and (f) $6T_n$.

It can be seen in Figure D.4 that applying a fluctuation to the stiffness prevents the organised resonance structure, as the amplitude ratio, y/D is significantly smaller than that of the uncontrolled case in Figure D.3(b). The most effective case is presented in

Figure D.4(a) with the control applied at every natural period, T_n , with the largest y/D of 0.25. As the displacement and C_l histories shown in Figure D.4(a) are now in-phase, as compared to the quarter cycle phase lead in Figure D.3(b), the structural resonance is prevented successfully. However, an actuation period equal to the natural period of the structure may be too rapid for a mechanical system to operate reliably.

In Figures D.4(b), D.4(c) and D.4(d), corresponding to T_c of $2T_n$, $3T_n$ and $4T_n$, respectively, the maximum magnitudes of oscillation for the elastically mounted circular cylinder are comparable. The displacements do not increase and the motion is non-resonant. Therefore, a control period as long as $4T_n$ can still be an effective solution.

The reduced amplitudes, y/y_o , for different control periods are shown in Figure D.5. Here, y_o is the uncontrolled cylinder displacement at f_{vo}/f_n of 0.85, obtained at t/T_n of 25. As the maximum uncontrolled cylinder displacement does not occur at 25 natural periods, these reduced amplitudes should represent conservative estimates of effectiveness. The envelope indicates the variation between the maximum and minimum amplitudes observed for each case after 10 natural periods. The vertical axis represents the effectiveness of control, as values of 1 and 0 represent an uncontrolled cylinder and the perfectly controlled cylinder, respectively. As expected, effectiveness in control decreases gradually for an increasing control period. In addition, the envelope of controlled displacements fluctuates by wider margins for increasing control periods, indicating a less consistent response.

It is noted in Figures D.3 and D.4 that the C_l histories display very similar patterns for all simulations. The maximum amplitude of lift is approximately 1.5 for both the uncontrolled and controlled cases. Similar C_l history is obtained for the stationary cylinder simulations. This suggests that there may be significant similarities in the vortex wake pattern for all these cases.

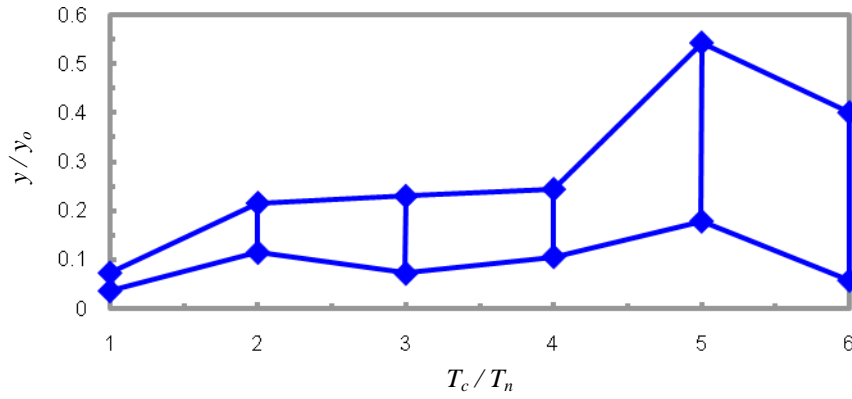


Figure D.5: Variation of the amplitude ratio, y/y_0 with control period, T_c .

Contours of vorticity magnitude for the uncontrolled and controlled cylinder at f_{vo}/f_n of 0.85 are presented in Figure D.6. The uncontrolled cylinder vortices are represented in Figure D.6(a). In Figures D.6(b) and D.6(c), vorticity contours for the controlled cylinder at a control period, T_c , of T_n and $4T_n$ are presented, respectively. Each illustration in Figure D.6 is obtained near t/T_n of 20. This instance corresponds to when a vortex is about to shed from the top of the cylinder. The colour scale represents the magnitude of vorticity. The largest magnitude of vorticity is located along the leading edge surface of the cylinder, near the stagnation point. The vortex pattern shown in Figure D.6 remains almost constant for all uncontrolled and controlled cases. This is also similar to that of a stationary circular cylinder, not shown for brevity. This suggests that the shedding of vortices occurs for the same cylinder position during oscillations in the vertical direction. The shedding occurs when the cylinder reaches zero displacement and the vortices are developed as the cylinder experiences peak displacements.

The vortex pattern shown in Figure D.6 corresponds to the 2S vortex wake mode defined as two single vortices per cycle of motion by Williamson and Govardhan (2004). They show experimentally that the 2S mode occurs for amplitude ratios y/D between 0.2 and 0.4. Numerical observations for the controlled cylinder are in close agreement, as the maximum amplitude ratios shown in Figure D.4 are between 0.25 and 0.85 for T_c of T_n to $4T_n$, respectively. However, for the uncontrolled case at f_{vo}/f_n of 0.85 the cylinder displacement is significantly larger than the suggested range of y/D , yet the same 2S vortex wake pattern is predicted numerically. This anomaly is currently under investigation.

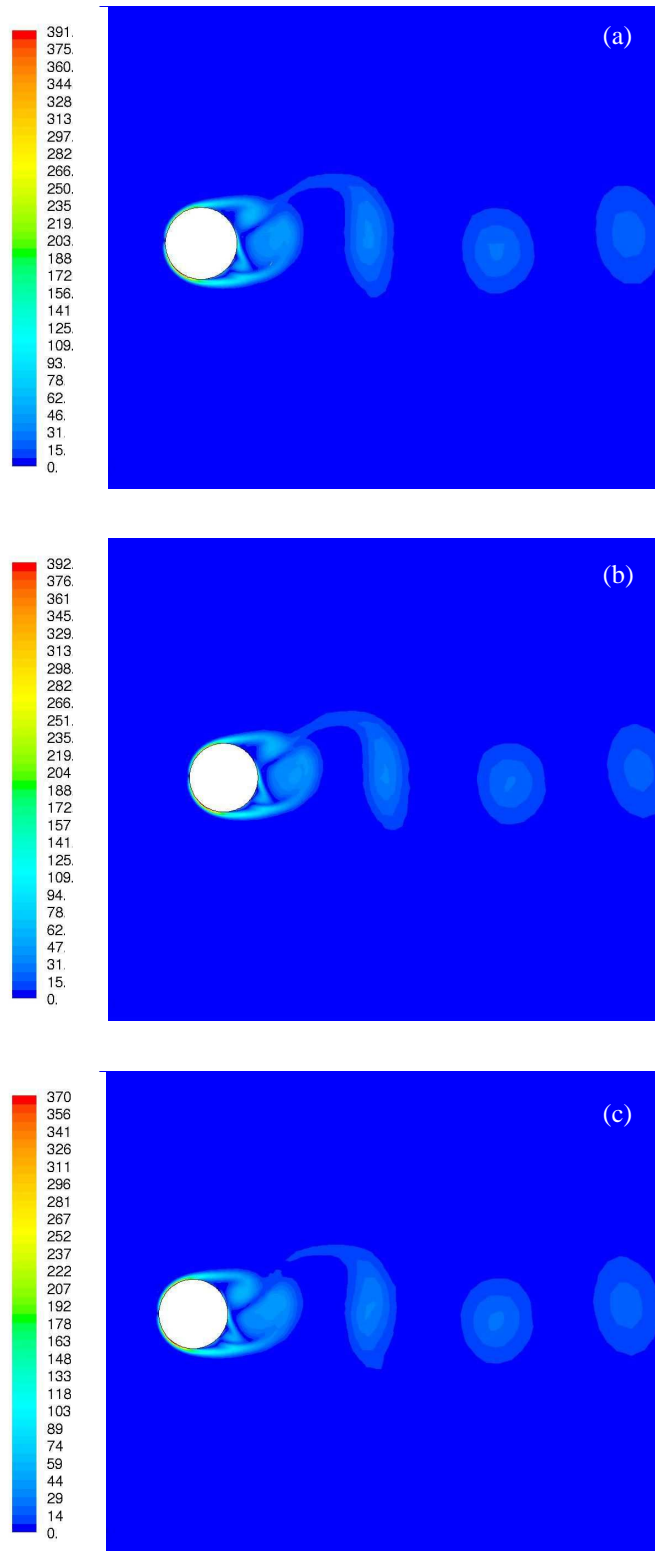


Figure D.6: Contours of vorticity magnitude for ζ of 0.01 and Re of 850 near t/T_n of 20; (a) Uncontrolled cylinder, (b) $T_c = T_n$ and (c) $T_c = 4T_n$.

The frequency distributions of the predicted cylinder displacement at f_{vo}/f_n of 0.85 for the uncontrolled and controlled cases at T_c of T_n and $4T_n$ are presented in Figure D.7. The uncontrolled cylinder predominantly oscillates at a peak frequency of 1.36 Hz, close to the vortex shedding frequency of 1.33 Hz for a St of 0.2. For the controlled cases, a dominant frequency is not as clear to identify as many spectral components co-exist with comparable magnitudes. This behaviour is a result of successfully preventing an organised structural resonance with the implementation of stiffness variations. As discussed earlier in relation to Figure D.4, a control period of T_n results in significantly smaller displacements than those for $4T_n$.

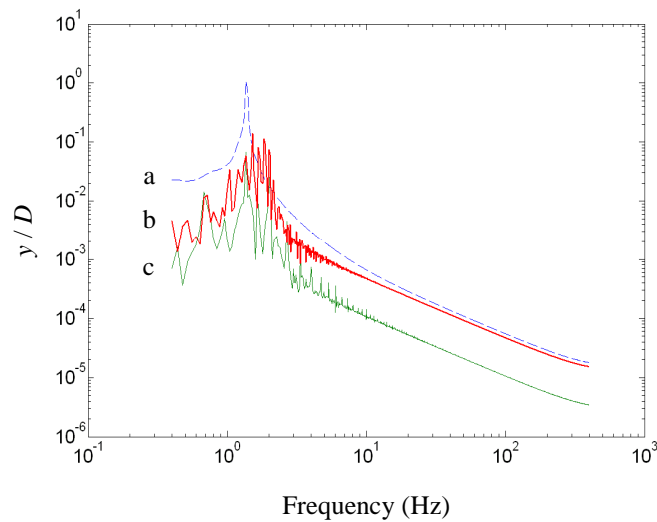


Figure D.7: Frequency distribution for the uncontrolled cylinder (a, ---) and controlled cylinder at T_c of $4T_n$ (b, —) and T_n (c, —).

D.3 Practical Implementation

The proposed control could benefit a cantilevered structure, or a structure with a significant free span between supports, for example, a tower or marine riser that is exposed to vortex induced resonance. A mechanical system could implement the control, possibly by applying and removing a support to change the effective free length, therefore, varying the effective stiffness. The location and the timing of the clamp are pre-determined as part of the controller design and not from flow or

oscillation conditions. Therefore, no sensing or computing would be required for actuation.

D.4 Summary

A numerical investigation to avoid the organisation of vortex induced resonance through a semi-active parameter control principle is presented in this paper. An elastically mounted circular cylinder exposed to cross-flow was modelled using FLUENT[®] to investigate both uncontrolled and controlled vibration conditions.

The proposed control is implemented practically by varying the effective stiffness at resonance. It has been observed that a square wave fluctuation between the original and doubled structural stiffness and an actuation period equal to the structural natural period provides the best control for resonance. The proposed application effectively prevents the organised resonance structure due to vortex shedding.

Numerical observations show similar vortex wake patterns for all studied cases with a 2S vortex wake mode. This mode is in good agreement with published experimental results for the controlled cases. However, the uncontrolled case at resonance also contains the 2S mode with a significantly larger amplitude ratio than what has been reported in literature. It is considered at this point that this anomaly may be due to not reaching a steady state pattern of oscillations at the time of the comparison, as computational requirements were considered.

The observations presented in this paper are encouraging for the continuation of the investigation to consider the aerodynamic performance, cost and practicality of the proposed control of vortex induced resonance.